Electron Transfer Dynamics in Halobenzenes at Ice and Metal Interfaces

Der Fakultät für Physik
der Universität Duisburg-Essen vorgelegte

Doktorarbeit

zur Erlangung des akademischen Grades eines Doktors der Naturwissenschaft
(Dr. rer. nat.)

von
Ishita Agarwal
aus Neu Delhi, Indien

Referent: Prof. Dr. Uwe Bovensiepen
Korreferent 1: Prof. Dr. Karina Morgenstern
Prüfer: Prof. Dr. Martina Schmid
Vorsitzender des Prüfungsausschusses: PD Dr. Markus Gruner
Tag der mündlichen Prüfung: 27. November 2017

Abstract

Electron transfer reactions manifest themselves in many physical, chemical and biological processes at a fundamental level, for example photosynthesis. Past studies have shown that dissociative electron attachment (DEA) cross sections of halogenated organic molecules are enhanced on polar solids as compared to in the gas phase. Despite its important implications, such as catalysis of ozone depletion, a rigorously proven model is still missing. This work aims to understand the mechanisms for this enhancement.

Halobenzenes (C_6H_5X, X = F, Cl and Br) coadsorbed on amorphous D_2O ice on Cu(111) are studied with two-photon photoemission spectroscopy, whereby changing the halogen, the energetics of the system is changed systematically. The C_6H_5X are shown to be ionised/dissociated by photoexcited excess electrons in the ice conduction band via DEA. The photoinduced reaction rate constants can be measured by surface workfunction changes, which is due to a build up of the negative charge at the surface. The dependence of the rate constants on incident photon flux, photon energy and different electron environment (C_6H_5X film thickness and solid phase of ice) are studied. By performing comparative analysis, it is shown that the enhancement of DEA cross section is due to pre-existing electron traps and delocalised electrons, which is in agreement with recent theoretical studies. An important implication of this study is that a spectroscopic signal from the transient ionic state is seen in the form of workfunction change.

Electron transfer mechanisms at metal-organic interface have also been investigated, as it is interesting from a fundamental view point and is important to molecular electronics. A molecular derived spectroscopic signature of C_6H_5F/Cu is observed with non-linear photoemission and compared to C_6H_6/Cu and C_6F_6/Cu (from past studies). Additionally, electron transfer efficiency is studied by performing coverage dependent workfunction studies of C_6H_5X/Cu. Together, these experiments show that the LUMO of the substituted benzene molecules shift to lower energies for less electronegative substitution on adsorption on Cu, reflecting the gas phase trend. This provides with a neat systematics to tailor metal-organic interface energies.

Deutsche Kurzfassung

Elektronentransferprozesse manifestieren sich in vielen physikalischen, chemischen und biologischen Prozessen auf fundamentalem Niveau, z.B. in der Photosynthese. Bisherige Studien haben gezeigt, dass die Wirkungsquerschnitte für dissoziativen Elektronenanhang (DEA) von halogenierten organischen Molekülen für polare Festkörper höher sind als in der Gasphase. Trotz der Relevanz, wie z.B. im katalytischen Kreisprozess der Bildung des Ozonloches, fehlt noch immer ein rigoros bewiesenes Modell. Diese Arbeit zielt auf ein Verständnis der Mechanismen für die Verstärkung der Wirkungsquerschnitte.

Koadsorbierte Halobenzole C_6H_5X auf amorphem D_2O-Eis auf Cu(111) werden mit Hilfe der Zwei-Photonen-Photoemissionsspektroskopie untersucht, wobei die Energetik systematisch durch Austausch der Halogene verändert werden. Es wird gezeigt, dass die C_6H_5X durch optisch angeregte Überschuss elektronen im Eis-Leitungsband via DEA ionisiert/dissoziiert werden. Die photo-induzierten Reaktionsraten werden durch Änderung der photoelektrischen Austrittsarbeit bestimmt, welche durch den Aufbau von negativen Ladungen an der Oberfläche verursacht wird. Die Abhängigkeit der Raten vom einfallenden Photonenfluss, der Photonenenergie und der unterschiedlichen elektronischen Umgebung (C_6H_5X Schichtdicke und Phase der Eisschicht) werden untersucht. Durch vergleichende Auswertungen wird gezeigt, dass die Verstärkung der DEA Querschnitte sich aus existierenden "Elektronenfallen" und delokalisierten Elektronen ergibt, in Übereinstimmung mit jüngsten theoretischen Untersuchungen. Eine wichtiges Ergebnis dieser Untersuchungen ist, dass eine spektroskopische Signatur des transienten ionischen Zustandes in der Form einer Änderung der Austrittsarbeit beobachtet werden kann.

Elektronische Transferprozesse an Grenzflächen zwischen Metallen und organischen Molekülen wurden ebenfalls untersucht, da sie von grundlagenwissenschaftlicher und technischer Interesse sind, bspw. in der molekularen Elektronik. Eine molekülspezifische Signatur von C_6H_5F/Cu wurde durch nicht-lineare Photoemission beobachtet und mit früheren Ergebnissen an C_6H_6/Cu und C_6F_6/Cu verglichen. Zudem wurde die Effizienz des Elektronentransfers in C_6H_5X/Cu durch die Schichtdickenabhängkeit der Austrittsarbeit untersucht. Zusammen zeigen diese Experimente, dass das niedrigste unbesetzte Molekülorbital (LUMO) der substituierten Benzolmoleküle bei der Adsorption auf Cu zu niedrigeren Energien für niedrigere Elektronegativität schiebt, was dem Trend in der Gasphase entspricht. Diese gründlichen und systematischen Studien liefern eine Basis zur Kontrolle der Energetik von Grenzflächen zwischen Metallen und organischen Molekülen.

List of Figures

List of Tables

Abbreviations

2PPE	two photon-photoemission
3d	three dimensional
ARPES	angle resolved photoemission spectroscopy
BBO	β-barium-borate
BL	bilayer
Bz	benzene (C_6H_6)
BzBr	bromobenzene (C_6H_5Br)
BzCl	chlorobenzene (C_6H_5Cl)
BzF	fluorobenzene (C_6H_5F)
BzF_6	hexafluorobenzene (C_6F_6)
BzX	halobenzene (C_6H_5X)
CB	conduction band
CCD	charge coupled device
CD	chromatic dispersion
CFC	chlorofluorocarbon
DEA	dissociative electron attachment
e_s^-	solvated electron
EA	electron attachment
EE	excess electrons
FROG	Frequency-resolved optical gating
FWHM	full width half maximum
GVM	group velocity mismatch
HOMO	highest occupied molecular orbital
HREELS	high resolution electron energy loss spectroscopy
HT	high temperature
Ic	conical intersection
I_h	hexagonal ice structure
IP	image potential
LED	light emitting diode

LEED	low energy electron diffraction
LT	low temperature
LUMO	lowest unoccupied molecular orbital
MCP	micro channel plate
ML	monolayer
NEXFAS	near edge X-ray absorption fine structure
NOPA	non-collinear optical parametric amplifier
OPA	optical parametric amplifier
pToF	position sensitive time of flight
QMS	quadrupole mass spectrometer
RegA	regenerative amplifier
SHG	second harmonic generation
SS	surface state
STM	scanning tunnelling microscopy
TDS	thermal desorption spectroscopy
ToF	time of flight
tr-2PPE	time resolved - two photon-photoemission
tr-ARPES	time resolved - angle resolved photoemission spectroscopy
TS	transition state
TST	transition state theory
UHV	ultra high vacuum
UV	ultra violet
VIS	visible
XC	cross correlation

Contents

Dedicated to my father, Akhil Kumar Agarwal, who was always supportive

Chapter 1

Introduction

Chemical reactions play a crucial role in our everyday world. From solar energy conversion to oxidation of haemoglobin in the blood, they drive the basic cogs of life. Amongst the different chemical processes, an electron transfer is the simplest charge transfer process and constitutes many rudimentary processes. For example: electron transport is an important regulation mechanism in **biochemical** activities like respiration, photosynthesis and nitrogen fixation. Biomedicine and biological radiation damage (DNA) are other important examples [7–10]. **Surface physics** phenomenon like chemisorption and atomic-molecular collisions also involve electron transfer. Electron transfer is at the heart of the **electronics** industry. Thus, electron transfer reactions, especially in the framework of electron-molecular interactions, are significant for fundamental research and optimising chemical, electrical and biological industrial processes. Due to their importance, electron transfer processes have been studied in depth and their significance is reflected by the Nobel Price in chemistry awarded to Rudolph A. Marcus for deriving the rate at which an electron is transferred from the reactant to the products (Marcus theory).

These reactions are very versatile and depend on many internal and external parameters like the reaction environment and reactant's physical state. Therefore, in the present study we investigate electron transfer mechanisms, but focus our research on polar solvents, where one finds that the dissociative electron attachment (DEA) cross section is enhanced compared to in the gas-phase [9–13]. We also study dynamics at metal organic interfaces, as it is of interest to electronic applications.

An important problem in atmospheric chemistry is the depletion of the ozone layer, where the halogen radicals are believed to be one of the main culprits in reducing O_3 to O_2 [14] in the stratosphere and halogenated hydrocarbons like chlorofluorocarbons (CFCs) are their ready source. Fascinatingly, it has been shown that the

rate of formation of $Cl^{\bullet}$ via DEA in CFCs is enhanced on ice surfaces in comparison to its gas-phase [11,15]. Electron transfer in polar environment is of interest not only to atmospheric chemistry, but also to other sciences like biology where water plays a crucial role in transport and regulation and to astrochemistry where ice covered dust particles are linked to prebiotic chemistry [16]. It has industrial significance as well, where air filters and air purifiers design can be improved with a better understanding of the mechanism behind the enhanced DEA cross section of impurities like hydrocarbons. As a result, EA and DEA reactions in the presence of polar medium has attracted a lot of interest in the past and still to date [10, 12, 17, 18]. For example, studies have been performed with respect to various solvent parameters like the solvent thickness [19] and the type of solvent [11,15]. Lu and Madey [11] showed for the first time that the dissociation of halogenated organic molecules is catalysed on polar surfaces and that it depends on both the concentration of the polar solvent and the reactant. They used an *electron stimulated desorption ion angular distribution* detector to study the yield of Cl^- dissociated from CF_2Cl_2/Ru(0001) with water and ammonia over layer via DEA. In the work by Ryu et al. [19], time resolved two photon photoemission (2PPE) spectroscopy was used to approach this problem. They studied the change in workfunction as a function of photoexposure time on $CFCl_3$ co-adsorbed with and without water on Ag(111) and verified their observations with thermal desorption spectroscopy measurements.

To date, there is only one model proposed to explain for this phenomenon [11], though it has not yet been rigorously verified. The model is based on the fact that polar solvent molecules can energetically stabilise excess electrons [17] through polarisation and form electron-solvent complexes [20] by solvent re-orientation. The electrons are thus self-trapped in attractive potential energy wells. Due to their high reactivity [10,12,21,22], longer lifetime and localised nature, these solvated electrons (e_s^-), or rather pre-solvated electrons, are believed to enhance the DEA cross sections.

Since the model has never been confirmed, we address the questions how and why localised electrons in polar environments enhance the EA and DEA yield and if it is indeed due to e^- solvation. Therefore, in contrast to aforementioned studies, we study charge transfer dynamics with respect to the dissociating molecule (reactant). To this end, we use halogenated benzenes C_6H_5X, X = F, Cl and Br (referred to as BzX henceforth) and can systematically tune the system energetically. As we go down the periodic table from F→Cl→Br, the electronegativity of the halogen progressively decreases, changing the overlap between the π electron cloud of the benzene and the halogen lone pair. This changes the energetics of the substrate-adsorbate system like the DEA cross section, surface coupling and dipole effect, consequently tuning the efficiency of the DEA process.

Such methodical studies have been performed with halobenzenes [23] and other molecules in the gas-phase [2,23–26] where the DEA probability was found to increase with increasing electronegativity. However, no known study has used the halogen series on polar surfaces to investigate charge transfer dynamics. Although Borodin, et al. [27] employed similar systems, they studied the mobility of adsorbates on ice and Yang, et al. [28] studied the adsorption geometry on a metal substrate.

In this work we study the efficiency of electron transfer to the reaction site (BzX molecule) by a comparative analysis of the reaction kinetics of the different BzXs. A good model system for this is coadsorbed BzX with D_2O ice on Cu(111), sketched in Fig.1.1, where the BzX molecules are adsorbed on ice covered Cu(111) interface. This system mimics electron transfer in the upper atmosphere, where an electron in atmospheric ice can dissociatively attach to hydrocarbons adsorbed on them. These electrons can be generated either by solar-UV photoexcitation of electrons into ice from, for example dust particles on which the ice adsorbed, or on impact with other molecules. In the laboratory frame of reference (Fig.1.1), the Cu(111) metal substrate acts as the source of electrons which can be photoexcited into the intermediate ice layer with suitable photon energies. The electrons in ice can either localise and get trapped due to solvation[1] or the delocalised electrons can dissociatively attach to the organic molecule via wavefunction overlap between the molecules and the metal substrate. Thus, the organic molecules may ionize into a $C_6H_5X^-$ anion or dissociate into a benzene radical $C_6H_5^\bullet$ and a halogen anion X^- on photoexposure. The negative charge will alter the surface dipole and hence the workfunction of the system. The rate of change in workfunction finally reflects the yield of the ionized/dissociated molecules giving the efficiency of the process.

The key to our approach is to use femtosecond two photon-photoemission spectroscopy, where the first photon pulse excites electrons in ice and the second photon probes the consequent changes. While there are other techniques to study DEA in molecules like, electron stimulated desorption and electron beam spectroscopy[2], photoemission is particularly suitable for this as we have energetically good control on the accessibility of photoexcited excess electrons in the polar environment. Additionally, by using photon energies not absorbed by the halogenated benzenes and ice, we ensure that the organic system is perturbed only by the excess electrons in ice.

We thus observe that the enhancement of the DEA cross section on ice was un-

[1]The existing model for DEA enhancement proposes that the pre-solvated but localised electrons dissociatively attach to BzX.

[2]a complete review of different techniques used to study polar medium electron attachment can be found here [12]

likely due to solvation of electrons, but instead due to delocalised electrons in the ice conduction band. This was supported by collaborative work with theory and scanning tunnelling microscopy (STM). Another important aspect of this study is that we probe a direct signature from the transient ionic state in a complex environment.

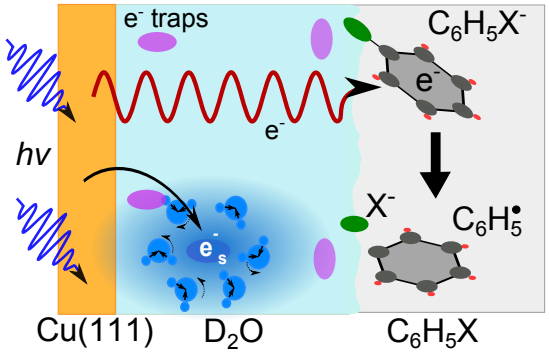

Figure 1.1: Illustration of electron transfer to C_6H_5X in $C_6H_5X/D_2O/Cu(111)$, where a photoexcited electron from the Cu(111) metal substrate is solvated in ice at pre-existing electron traps. The photoexcited electron may alternatively attach to C_6H_5X via delocalised Bloch-wave overlap between the metal and the organic molecule to either dissociate it into a benzene radical $C_6H_5^{\bullet}$ and a halogen anion X^- or ionize it into a $C_6H_5X^-$ anion, depending on the electron energy.

Collaborators : We conducted this research in joint collaboration with Michel Bockstedte[3] and his PhD student Philipp Auburger from FAU Erlangen-Nuremberg, Erlangen and Karina Morgenstern and her PhD student Cord Betram from the Ruhr University Bochum. Bockstedte and Auburger calculated the potential energy surfaces for BzX in the gas-phase and on the ice surface (pristine ice surface and trapping sites) in the framework of density functional theory and many body perturbation theory. By using this approach they did not need to include additional assumptions, contrary to the previous publications. Morgenstern and Betram performed low temperature STM measurements on $C_6H_5X/D_2O/Cu(111)$ before and after illumination with a frequency doubled super continuum laser and saw structural changes due to photoexposure. The work done by them is rather remarkable since STM on water surfaces is very challenging. One of the many reasons being water's tendency to adhere to every surface (due to hydrogen bonding) including the tip, which changes the water structure being measured. As the project was of a collaborative nature, we refer to their obtained results to support our drawn conclusions.

Another important aspect studied in this thesis is charge transfer at the metal-organic interface. The desire for smaller and more compact electronics has given birth to molecular electronics (like organic-LED, nano-junctions and nanotubes) which employ organic molecules as their fundamental building blocks. In addition to being cheap and the advantage of reduced size and structural control, they also provide the

[3]now at University of Salzburg

opportunity of tailoring the contact potential via suitable substitutions of the organic functional groups. Since in electronics the contact interface between the different components/materials set the performance limit of the devices, understanding the properties of these interfaces becomes crucial. Consequently, the growing need for molecular electronic in the past years has brought the metal-organic interface under the spotlight. Despite the plethora of research on the adsorption of organic molecules on coinage metals [28–33], there are still many open questions like the rules for energy level alignment, electron localisation and charge transfer at the interface.

Due to the interesting nature of π binding, which lies between hydrogen bonding and covalent bonding in strength, and due their wide manifestation as biomolecules [1, 34], π-molecular systems have been widely studied. Benzene is an ideal choice of molecule here since it is the simplest of the planar aromatic π-systems. Thus, benzene and benzene derivatives have been widely studied in the past. These studies [28, 35–38] revealed that the electronic structure of the π-system and its interaction with other planar π molecules and metal depends primarily on the substituted functional groups. For instance, a molecule with more electronegative functional group/s is weakly interacting compared to those with less electronegative substituents.

Halogenated benzene series have been extensively studied in the gas-phase, but there are not many systematic studies on the metal substrate. Therefore, in the context of molecular electronics, we address the question of energy level alignment and charge transfer at C_6H_5X/Cu(111) interface by exploiting the functional group based tailorability. As in the case of electron attachment in polar environments, here too we perform systematic studies and compare the charge transfer kinetics (work-function studies) in BzX/Cu(111) as a function of the halogen. This was complimented by thermal desorption spectroscopy, where the $\pi-\pi$ interactions between the molecular layers could be investigated. We also probed the molecular derived state of BzF and studied it in comparison to previously investigated C_6H_6/Cu(111) [3] and C_6F_6/Cu(111) [4, 39]. Together with these studies we showed that energy level alignment depends directly on the substitutional functional group, where a more electronegative functional group results in a weaker metal-π interaction. This corroborates with the various theoretical calculations in the gas-phase that predict the position of the molecular state on adsorption [28, 40, 41]. Because this topic is not at the heart of this thesis, we performed exploratory photoemission experiments on C_6H_5X/Cu(111) here, where we develop a feel and direction for future experiments. We therefore discuss only the preliminary analysis.

Overview

In chapter 2, we give an overview of the material systems used, photoemission technique and the theoretical models most pertinent to this work. In chapter 3, we walk through the experimental set-up, photoemission data analysis and characterisation of the adsorbate layers with thermal desorption spectroscopy. Some improvements were made to the laser set-up which are also described here. The experimental results and the subsequent analysis of DEA in $C_6H_5X/D_2O/Cu(111)$ is discussed in chapter 4. Here we show that the pre-existing electron traps in the polar medium is the reason for the enhanced dissociation cross section of organic molecules. Chapter 5 provides the first studies of BzX adsorbed on bare Cu(111). Here we investigate a molecular derived state of BzF with non linear photoemission and the dissociation/ionization kinetics of the $C_6H_5X/Cu(111)$. These studies show that the molecular level alignment can be determined by the extent of electronegativity of the substituted functional group, as in the gas-phase. In chapter 6 we briefly discuss the time resolved dynamics of electron solvation in water and the effect of BzF adsorption on it. We conclude the thesis with a summary and outlook in chapter 7.

Chapter 2

Theoretical Background

Here we give an overview of the material systems used and the theoretical models most pertinent to this work. We start of very general giving an introduction to the theory of electron transfer. Here we will discuss some important aspects such as the potential energy curve, Arrhenius equation, transient state theory and the Marcus theory of electron transfer. This is followed by an introduction to thermal desorption spectroscopy (TDS) which plays an important role in characterising the adsorbate coverages. So far we discuss very general concepts and if the reader is familiar with them, they can skip these parts. We then discuss the investigated system. Here we will discuss the metallic substrate Cu(111), its electronic properties and surface workfunction. This is followed by a discussion on free standing water, water ice/Cu(111) interface and electron solvation in amorphous ice. Lastly, we discuss the halogenated benzenes, the halogenated benzene series and potential energy maps, their dissociation and adsorption on the metal substrate.

2.1 Photochemistry and Stoichiometry

Since we are interested in studying e^- transfer in a polar medium via EA, it is pertinent to discuss the reaction rate constants for the dissociation of the halogenated benzenes. Thus, we briefly discuss different aspects of chemical kinetics in the following section. We first describe a potential energy curve, followed by the temperature Arrhenius equation. The Arrhenius equation, which is based on Boltzmann distribution, empirically describes the temperature dependence of chemical reactions and is in turn the foundation for the various other reaction models like the transition state theory and the Marcus theory. To calculate the reaction rate constants, one can use either the collision theory or transition state theory, amongst others. The transition

state theory predicts the reaction rate constants for reactions undergoing structural changes and can be used to describe the ionization/dissociation of BzX. The Marcus theory on the other hand is used to describe reactions where the reactants retain their individuality in the product state and is used to describe the solvation of electron in ice. In the end, we discuss some approximations used to describe chemical kinetics in complex reactions. These are all well established theories with a plethora of literature, so do not confine yourself only to the literature cited here.

2.1.1 Potential Energy Curve

The neatest way to describe a reaction is by using potential energy curves which describe a reaction mechanism by expressing the changing potential energy between the reactants and products as the reaction proceeds. In the framework of Born-Oppenheimer approximation, where the molecular electronic and nuclear motions are assumed to be decoupled, the potential energy curve shows the electronic potential energy as a function of the nuclear coordinates (rotation, vibration and translation) [42, 43].

For chemical reactions, the reaction coordinate is usually given by the nuclear distance and the potential energy is a result of Coulombic interaction (usually approximated by Lennard-Jones potential), as shown in Fig. 2.1a) for dissociation of a hypothetical molecule AB. When the atoms are very close to each other, there is a strong Coulomb repulsion between the nuclei and and the potential energy goes to infinity. When they are very far away, the potential energy is the sum of the individual atoms. The minimum gives the equilibrium bond length and the most stable configuration of the reactants.

Thermodynamically also one uses the potential energy profile which consists of the minimum and maximum, along with the other features, as shown in Fig. 2.1b). Here the x-axis show the progression of the reaction. The minimum corresponds to the zero point energy of the pre-reacted reactants and products, and the maximum or saddle point is given by the activation energy E_a needed by the reactants to overcome to form the product. As the reaction proceeds, the reactants form a cluster of atoms called the supermolecule which at the maximum is called the activated complex. On the other side of the saddle point is the product state. Depending on the potential energy of the product with respect to that of the reactants, also known as the enthalpy of formation ΔH, the reaction is exothermic or endothermic. For example, the halobenzenes will ionise only if, after electron capture, the excited molecule-electron complex can cross the saddle point which is given by the electron attachment threshold energy.

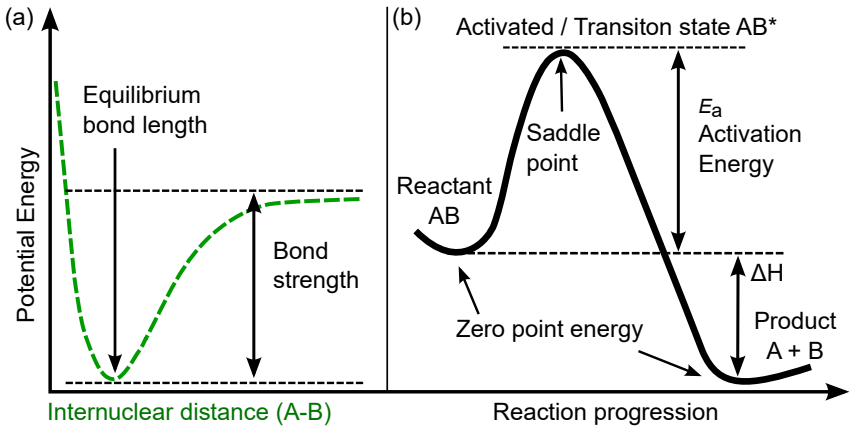

Figure 2.1: Exemplary potential energy curves describing a dissociative reaction of the molecule AB. Potential energy is plotted as a function of reaction coordinate and the reaction can be described in terms of a) its nuclear coordinates or b) thermodynamically. The latter is also used to describe the transition state theory. E_a is the activation energy or energy barrier that has to be crossed to form the products and ΔH is the enthalpy of formation and determines if the reaction is exothermic or endothermic and if it is reversible or irreversible.

2.1.2 Arrhenius Equation

One of the most important equations of chemical kinetics is the Arrhenius equation. It is an empirical formulation and a very powerful tool for describing the temperature dependence of reaction rates. It was developed by Svante August Arrhenius, who argued that the chemical equilibrium depends upon the reaction temperature. It is not restricted to only chemical reactions or diffusion like processes, but is applicable to temperature dependent physiological systems like the chirping of tree frogs [44]. It is expressed as:

$$k = A \exp^{-E_a/k_B T} \tag{2.1}$$

where k is the rate constant and A is the pre-exponential or frequency factor (same units as k). It is temperature dependent, contains the entropy terms and gives the number of times a reaction attempt is made. The exponential part gives the probability of the reaction to take place and can be described by Maxwell-Boltzmann distribution with temperature T, Boltzmann factor k_B and activation energy or threshold energy E_a in units of J/molecule. The Boltzmann factor can be replaced by the gas constant R, in which case, E_a is given by J/mol.

Arrhenius equation works well for most elementary and composite reactions. It is also the basis for TDS (§ 2.2,§ 3.6.2). Here the activation energy is the energy

needed to overcome the desorption/adsorption barrier for chemisorption or van-der Waal's force for physisorption. Though Arrhenius equation is quite robust, it breaks down for reactions and relaxation processes that are not described by Boltzmann distribution.

2.1.3 Determining Reaction Rate Constants

Although the Arrhenius equation is widely used, it doesn't describe the pre-exponential factor and thus cannot determine the reaction rate constants quantitatively. Therefore, other theories based on Arrhenius equation were developed to calculate the chemical rate constants like the collision theory or the transition state theory TST.

The collision theory (hard sphere collision theory) assumes that a reaction takes place if two colliding molecules have sufficient energy to cross the threshold energy and fulfil the reactions steric requirement (right collision orientation). It also takes the total number of collisions between the reactants into account. However, this does not hold for large molecules or heavy molecules as it doesn't take the internal molecular forces (or degree of freedom) into account.

The transition state theory (activated complex theory), on the other hand includes both the intermolecular and the intramolecular forces [45–48]. It is the basis of chemical kinetics and gives the reaction rate constants dependence on temperature and the reactant concentration. The theory makes use of potential energy surfaces where for a reaction to take place, the reactants have to climb up the potential energy barrier to reach the maximum or saddle point, where the reactants are in a transition state (TS) or activated complex, as shown in Fig. 2.1b). Crossing the saddle point, the potential energy drops and the reaction products are formed. It therefore requires knowledge of the potential energy surface of the reactants and the transition state. The excited molecules are given by Boltzmann temperature distribution. It is important to note that the TS is not a stable state but is a point on the potential energy curve.

The main assumptions of TST are [42]:

1) The overall rate is calculated by focussing on the transient state/activated complex species which lies at the saddle point of the potential energy surface.

2) The activated complex is in a quasi equilibrium with the reactants and are therefore independent of the product concentration. They are not in chemical equilibrium but in thermal equilibrium where the Boltzmann distribution of the products is given by the reaction temperature (reactant's Boltzmann distribution remains constant).

3) The motion of the system after the saddle point is described by kinetic theory, that is, once the reactants reach the saddle point, they will definitely form the product, since it is energetically downhill from there.

As mentioned before, TST includes all internal degrees of freedom of the reactants and the products and include the vibrational, rotational, translational and electronic molecular potential energies which are described by Q_v, Q_r, Q_t and Q_e partial partition functions, respectively. The canonical partition function q, which gives all the energy states available for the reaction at a temperature T and volume v, is simply the product of them all. From the second assumption, the partition function of the reactants and the products are in equilibrium at the saddle point and therefore, TST can be written as :

$$k = \frac{Q^{\mathrm{TS}}}{Q_{reactant1}Q_{reactant2}\cdot\cdot} \exp^{-E_a/k_BT} \tag{2.2}$$

where, k is the reaction rate constant discussed in Eq, 2.1. The expansion for the individual partition function can be found elsewhere [42, 43]. Eq. 2.2 is similar to the Arrhenius equation where the attempt frequency is given by the canonical partition functions. Transition state theory is applicable where there are structural changes involved as it assumes a strong coupling between the reactants and products. Since reaction takes place on the same potential energy curve (as opposed to Franck -Condon excitation), it is an adiabatic process. It gives a very good qualitative understanding of the reaction mechanism and thermodynamic and statistical-mechanical insight.

In this thesis, we study the ionization and the eventual dissociation of halobenzenes by electron transfer. The mechanism of both processes can be described by the transition state theory. Here after excitation of the molecules, they are ionised or dissociated only if the excitation energy is larger than the activation energy and the whole excited system can cross the saddle point (Fig. 2.1). For example, if the electrons that excite the molecule have less energy than the E_{a}, the molecules will not be able to ionise. Thus, the TST is used to give the formula for the reaction rate constants of ionization and dissociation.

2.1.4 Marcus Theory- electron transfer in solutions

Marcus theory was developed to describe electron transfer in a solutions where no bond breaking/making is involved, like ionization and solvation processes [49]. Here the reactant nuclei are weakly coupled to each other and the electron 'jumps' from the donor to the acceptor. He used the dielectric polarisation properties of solvents

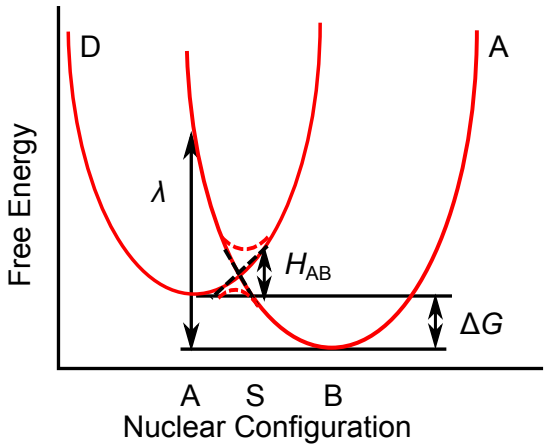

Figure 2.2: Potential energy curves of the reactant (R) and product (P) state crossing through the transition point T, shown as a function of free energy vs nuclear configuration. λ is the reorganisation energy, ΔG is the Gibb's free energy and H_{AB} is the electronic coupling between the reactants and products

and elegantly replaced the complicated reaction coordinate involving all the reacting atom coordinates with only the solvent's polarisation as the reaction coordinate.

The theory has widespread application to biological transport phenomenon where electron transfer takes place between biological molecules at a distance or with a single molecule. We use it to describe the solvation of electron in ice and thus discuss it conceptually and briefly. The mathematical development can be found in Marcus's papers [50–53].

On electron transfer, the solvent molecules will rearrange themselves in response to the charge. In Marcus theory, due to the weak coupling between the reactants, the solvent nuclei do not change before, during or after the charge transfer process (diabatic). This means that the solvent configuration for which electron transfer will take place cannot be that of the precursor (before electron transfer) or successor (after electron transfer) state, but somewhere in the middle. Therefore, it is assumed that the charge transfer or electron jump will take place when the solvents are in the transient configuration, that is, the solvent configuration for which the donor and the acceptor each have half the electron charge on it (hypothetically). Since the electron is an elementary particle, its splitting is not possible, but the solvents can attain the right polarisation while the electron is still at the donor site via thermal fluctuations in the solvent. Additionally, electronic and molecular (solvent) polarisation rates differ by several orders of magnitude and can be decoupled, thus decoupling the electron jump and the solvent rearrangement processes. Therefore, according to Marcus theory, the solvent molecules first reorganise themselves to be in the transient configuration and then the electron jump takes place. Fig. 2.2 shows the potential energy surfaces to describe it, where the left parabola describes the initial state (reactants) and the right describes the final state (products). The energy needed for

the solvent molecules to reorganise themselves is given by λ, and the charge transfer energy at the transition state is given by the Gibbs free energy of the reaction ΔG as shown in Fig. 2.2. The electronic coupling between the reactants and products is given by H_{AB}, depending on whether it is large or small, the reaction maybe adiabatic or non-adiabatic. The electron jump is described quantum mechanically.

Marcus theory is based on TST, where the activated complex is the solvent configuration if half an electron was transferred to it. The rate of electron transfer k_{ET} is thus given by Eq. 2.2, but with activation energy given by Gibbs free energy of activation $\Delta G^{\ddagger}$ according to:

$$k_{\mathrm{ET}} = A \exp^{-\frac{\Delta G^{\ddagger}}{k_B T}} = A \exp^{-\frac{(\lambda+\Delta G)^2}{4\lambda k_B T}} \tag{2.3}$$

A depends upon whether the process is adiabatic or diabatic in nature. This equation predicts that for very negative ΔG, the reaction rate actually slows, which is counter intuitive, but has been experimentally verified [54]. If the reactants and the products are strongly coupled (inner sphere electron transfer), the reaction proceeds adiabatically on the same potential energy surface. Here the reaction proceeds through chemical bonding and the reaction coordinate is described by vibrational states (harmonic approximation). In this case, the Marcus theory can no longer be treated classically and the Marcus-Hush theory was developed to describe it. For this work, the classical Marcus theory is sufficient as the solvated electron state retains its electronic nature. Marcus theory describes the electron solvation process in water ice. It also justifies using transition state theory to describe the ionization reaction rate constant.

2.1.5 Chemical Kinetics- reaction approximations

The equation Eq. 2.4 (also Eq. 4.3) is a commonly occurring reaction mechanism. These reactions with an intermediate state are classified as complex reactions.

$$[\mathrm{A}] \underset{\beta}{\overset{\alpha}{\rightleftharpoons}} [\mathrm{B}] \xrightarrow{\gamma} [\mathrm{C}] \tag{2.4}$$

Their differential rate equations can be written as:

$$\begin{aligned}\frac{d[\mathrm{A}]}{dt} &= -\alpha[\mathrm{A}] + \beta[\mathrm{B}] \\ \frac{d[\mathrm{B}]}{dt} &= \alpha[\mathrm{A}] - (\beta+\gamma)[\mathrm{B}] \\ \frac{d[\mathrm{C}]}{dt} &= \gamma[\mathrm{B}]\end{aligned}$$

Due to the coupled differential equations, it is not possible to solve them analytically. Therefore, various approximations have to be made. The two most common approximations are the steady state and the pre-equilibrium approximations [43].

In the steady state approximation, we make the assumption that the concentration of the intermediate state [B] rapidly reaches a constant. In the above equation, this condition will be achieved if $\gamma >> \beta, \alpha$, so that any [B] being formed will be simultaneously converted to [C]. Here, [A] $\underset{\beta}{\overset{\alpha}{\rightleftharpoons}}$ [B] become the rate limiting steps. The following differential equations are based on this:

$$\begin{aligned}\frac{d[\mathrm{B}]}{dt} = 0 \;\Rightarrow [\mathrm{B}] &= \frac{\alpha}{\beta+\gamma}[\mathrm{A}] \\ \gamma >> \beta, \alpha \;\Rightarrow \frac{d[\mathrm{C}]}{dt} &= \alpha[\mathrm{A}]\end{aligned} \tag{2.5}$$

In the pre-equilibrium approximation, we assume that the reactants [A] and [B] quickly come into 'equilibrium', with a part of [B] slowly leaking to [C]. This is not a true equilibrium since more products than reactants are being formed continuously. However, we neglect the leak and get equality between the forward and the backward reactions. This condition can be achieved when $\beta >> \gamma$, then the leak will be very small and most of [B] will relax back to [A], reaching a fast equilibrium. The simplified differential equations can be written as:

$$\begin{aligned}\alpha[\mathrm{A}] = \beta[\mathrm{B}], \;\Rightarrow \frac{\alpha}{\beta} &= \frac{[\mathrm{B}]}{[\mathrm{A}]} \\ \frac{d[\mathrm{C}]}{dt} &= \frac{\alpha\gamma}{\beta}[\mathrm{A}]\end{aligned} \tag{2.6}$$

Thus, if $\gamma >> \beta, \alpha$, then the steady state approximation can be used and the differential rate equation of the product is given Eq. 2.5. If $\beta >> \gamma$, the pre-equilibrium approximation is applicable and the product is given by Eq. 2.6.

2.2 Thermal Desorption Spectroscopy

For an atom or molecule (adsorbate) to adsorb on a surface (substrate), the attractive potential energy between the adsorbate and the substrate has to overcome the disordering thermal motion of both the surfaces (substrate and adsorbate). Adsorption maybe a physical process (physisorption) if the interaction is primarily van-der-Waals forces and the desorption energy is less than 50 kJ/mol [55]. Or it may involve formation of chemical bonds (chemisorption) like covalent bonds. In chemisorption, there is usually an activation barrier that must be overcome to bind to the substrate and adsorb. The vertical force (force between the adsorbate and the substrate) is often stronger or comparable to the lateral force (between the adsorbate particles themselves) and determines the chemisorption activation barrier. The vertical forces also play an important role of keeping the atoms/molecules in a 2D lattice and ensure good registry with the substrate. For the molecules to desorb from the substrate, they need to overcome the desorption activation barrier, which is larger for chemisorbed molecules than physisorbed ones.

We perform thermal desorption spectroscopy (TDS) to determine the adsorbed coverage and characterise it. Also known as temperature programmed desorption, it is used here predominantly to determine the adsorbed coverage Θ as a function of temperature T. Usually a TDS series is performed for different adsorption dosage amount to determine the adsorbed coverage and its characteristics. Since adsorption/desorption is a thermally activated process, the desorption rate constant is given by an Arrhenius equation, see § 2.1.2. With a constant heating rate β, the rate is given by the Polanyi-Wigner equation [56, 57]

$$I(T) = -\frac{d\Theta}{dT} = \frac{A}{\beta}\Theta^m \exp\left(\frac{-E_d}{RT}\right) \tag{2.7}$$

where *I(T)* is the observed desorption intensity as a function of T, E_d is the desorption activation energy, A is the Arrhenius frequency factor and m is the desorption order. The desorption yield is a convolution of the surface coverage and rate of desorption, so while the desorption rate increases exponentially, the coverage drops, giving a peak in the desorption curve.

Depending on m, the shape of the desorption curve changes. Zero order desorption ($I(T) = \frac{A}{\beta}\exp\left(\frac{-E_d}{RT}\right)$)is independent of coverage (unlimited supply of particle), has a common leading edge and the TDS peak shifts to higher energies for higher coverage due to intermolecular interactions. It is usually seen for sublimation and is related to multilayer coverages. In first order desorption, the desorption curve is linearly dependent on the coverage and is therefore observed for molecules that

desorb without dissociating or recombining to the substrate. The desorption curve is asymmetric, but with coverage independent desorption T. The second order desorption ($I(T) = \frac{A}{\beta}\Theta^2 \exp\left(\frac{-E_d}{RT}\right)$) is usually observed when there is recombination at the surface. Here the TDS curves are symmetric with overlapping trailing edge and the peak T moves to lower values with increasing coverage.

Thus, in this way, one can characterise desorption kinetics, surface coverage and structure (by identifying the order of desorption), total number of adsorbed molecules from intensity calculations, the adsorption/desorption activation energy and the rate of desorption. If the total number of incident molecules are known, one can even determine the sticking probability.

2.3 The Investigated Systems: Cu(111), Water-Ice, and Halobenzenes

2.3.1 Metal substrate: Cu(111) properties

Noble metals like copper, silver and gold belong to group 11 of the periodic table and are known for their excellent metallic properties like ductility, diamagnetic, low reactivity, and thermal and electrical conductivity. This makes them an ideal metallic substrate for photoemission experiments. Their photoemission spectra [58–61] are well studied, both experimentally and theoretically, and still attract a lot of interest [62–65]. In this work, we use copper as our metallic substrate and hence discuss it briefly.

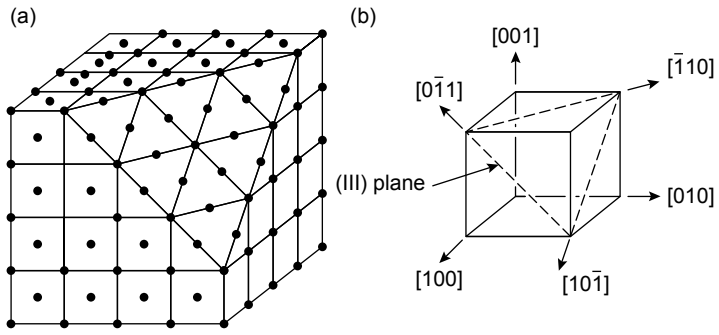

Figure 2.3: a) FCC structure of Cu showing the (111) crystallographic plane. b) Different crystallographic planes of copper. Image taken from [66]

Cu crystallises in a face centred cubic structure and has four equivalent hexagonal closed pack Cu(111) plane [66, 67], as shown in Fig. 2.3. It has a lattice constant

a=3.61 Å and density $\rho = 8.93\,\mathrm{g\,cm^{-3}}$ [67].

The density of states and the electronic band structure $E(\vec{K})$ [68] of copper is shown in Fig. 2.4. Close to the Fermi level E_F, there are two bands: the d-band and the sp-band. The d- band is fully occupied and lies 2-5 eV below the Fermi level. The sp-band ranges from states above the vacuum level E_vac to 8.6 eV below E_F with an orientational band gap from 0.85 eV below E_F to 4.15 eV above E_F at the $\bar{\Gamma}$ point. The sp- band is partially filled and has a parabolic dispersion of a quasi-free electron gas. In comparison, the d-band electrons are more localised and the band is flatter compared to the sp-band. The distinct colour of copper is due to interband scattering from the d-band into the sp-band. Cu thus absorbs photons > 2 eV and mostly reflects those with lesser energy.

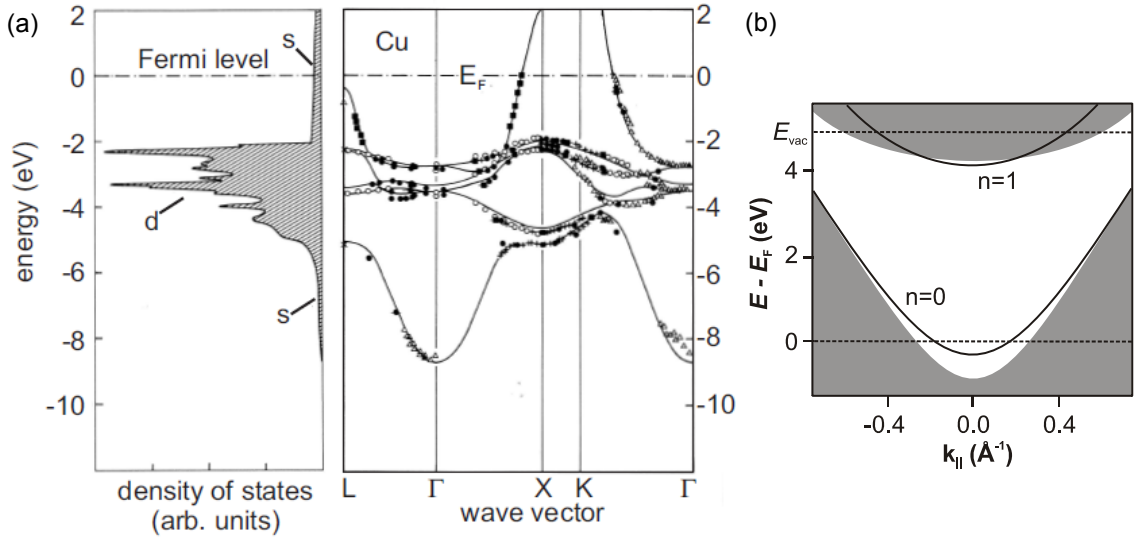

Figure 2.4: a) Calculated density of states [68] and the calculated and experimental band structure of Cu(111)- Image adopted from [69]. b) Projected surface band structure in the sp-band gap and the first image potential state. Image taken from [70].

Due to truncation of the crystal lattice, there is symmetry breaking in the out of plane direction which gives rise to a new set of states called surface states. The sp-surface state is of Shockley type and lies in the projected band gap of the sp-bulk states. In the photoemission spectrum such surface states show up as pronounced lines due to their two-dimensional character. The peak linewidths are given by the electron-electron and electron-phonon scattering and is calculated to be 22 meV at 0 K for the Shockley surface state [61]. Spectroscopically, it has been measured to be as narrow as 65±15 meV in a photon range of 2.1 to 2.3 eV by Wallauer and

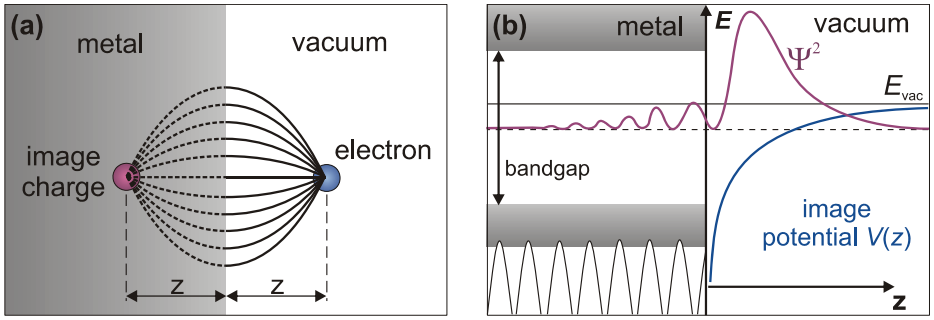

Figure 2.5: a) Schematic sketch of the image potential (IP) state in front of the metal at a distance z from the surface. The image charge in the metal is at a distance $-z$ from the surface. b) Energy level diagram showing exponential decay of the IP state wavefunction in the metal band gap. Image taken from [70].

Fauster [71]

In addition to the bulk and surface states, there are image potential states which are unoccupied states lying in the band gap and bound to the vacuum level E_{vac}. An electron in front of the metal surface at a distance z_0 from it, induces an electric field which causes the charge density at the metal surface to rearrange. They are rearranged such that there is no electric field component parallel to the surface, but only perpendicular to the surface, as shown in Fig. 2.5. This is equivalent to an electric field between the electron in front of the surface and an 'image' charge at a distance $-z_0$ below the metal surface. This gives rise to long range hydrogen like states and can thus be described by Rydberg series as:

$$\begin{aligned} V_{\text{IP}}(z) &= -\frac{e^2}{16\pi\epsilon_0(z-z_0)} \\ E_n &= E_{\text{vac}} - \frac{Ry}{(n+a)^2} \end{aligned} \tag{2.8}$$

where, V_{IP} is the image-potential and z_0 is the position of the image plane. E_n is the binding energy of the image states in the Rydberg series with quantum number n. Ry is the Rydberg unit of energy = 13.605 eV and a = 0 for Cu(111) is the so called quantum defect [72].

Both the surface state and the image state are 2-D bands and their dispersion in the $k_{\parallel}$ plane can be calculated. The surface state has a similar dispersion to the bulk band and are parabolic. The n=1 image state has a dispersion of a free electron and is mostly flat, since its probability density lies in the vacuum (Fig. 2.5).

At room temperature, the clean Cu(111) surface has a workfunction of 4.9 eV, the surface state at 0.39 eV below E_F and the first image state, n=1, at 4.1 eV above E_F [71].

2.3.2 Metallic Workfunction

'The work function may be defined as the difference in energy between a lattice with an equal number of ions and electrons, and the lattice with the same number of ions, but with one electron removed', E. Wigner and J. Bardeen [73]. The work function arises due to Coulomb interaction and many body interaction. It is a feature of symmetry breaking at the surface, where the fixed atomic lattice is suddenly terminated, but the valence electrons are allowed to 'spill' into the vacuum (*Jellium model).* The system can be considered as a parallel plate capacitor with the positive atomic core on one side and the spilled out electrons on the other with the vacuum between them as the dielectric medium (see for example, Fig. 4.3). A resulting electric field or dipole moment between the two plates is set up pointing towards the metal substrate. Therefore, for an electron to escape the metal surface, it has to overcome this retarding potential V [30, 55, 74]. Thus the workfunction $\Phi = e^{-}V$ and determines the vacuum level of the material. Since the 'spill out' depends upon the atomic lattice, the workfunction (and the vacuum level) is specific to the crystallographic plane. The image potential charge (§ 2.3.1) is also responsible for the workfunction, enhancing the surface dipole effect. As the electron leaves the surface, it experiences an attractive potential V_{IP} (Eq. 2.8) from its image charge in the metal, giving a contribution to the workfunction.

Since in this simple dielectric model the workfunction is determined by the surface dipole, any changes at the surface like structural changes or impurities at the surface will change the workfunction. On adsorption of molecules, a charge transfer between the metal and the adsorbate or polarisation of the adsorbate's charge density by the substrate will give rise to additional dipoles at the surface [30, 74]. Depending on how the adsorbates bind to the surface, Φ may increase or decrease, for example [30]:

- adsorption of alkalis like Cs on W(001), decreases work function: On the one hand, the Cs valence (6s) electrons get polarised towards the tungsten giving rise to a counter dipole field, on the other hand, the core Cs electrons are counter polarised giving rise to an aligned dipole field which enhances the original dipole potential. The net result is an overall decrease of work function (push-back or pillow effect).

- weakly adsorbed species like Xe or benzene, decrease in work function: The

workfunction decreases through the same mechanism as for Cs but with π-electrons in benzene and valence electrons in Xe. Pauli-repulsion between the metal spill-out electrons and the closed shell valence electron can also lower the surface dipole field.

- adsorption of highly negative species like halogens: increase in work function. Here the adsorption involves charge transfer from the metal to the halogen species which gives rise to a dipole in the direction of the metal spill-out dipole field enhancing the original dipole and increasing the work function.

The Smoluchowski-effect states that a rough surface has a lower workfunction [74]. In addition to the above, if there was a charging of the surface for example dissociation of an adsorbate, this too gives rise to additional dipole whose direction will depend on the sign of the charge. A negative charge will increase the dipole as it will enhance the retarding potential, while a positive charge will decrease the workfunction. We use this chain of arguments to explain the increase in Φ on photoexposure of $C_6H_5X/D_2O/Cu(111)$.

Though workfunction is a local effect, in photoemission spectroscopy we observe the macroscopic or average workfunction of the surface under the laser beam and often measure the global workfunction.

2.3.3 Water and Amorphous Ice

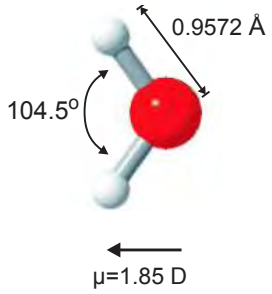

Figure 2.6: Water molecule and its dipole moment are shown here. Due to the oxygen lone pair, the two hydrogen atoms (white spheres) are at an angle, which together results in a dipole moment from the oxygen (red sphere) towards the hydrogen. Image is taken from [75].

In the water molecule, an oxygen atom is bound to two hydrogen atoms via sp^3 hybridisation involving a 2s and a 2p oxygen orbitals. The remaining two hybridised orbitals are occupied by the oxygen lone pair. The water molecule therefore has a tetrahedral geometry with the H-O-H bond angle = 109° and O-H bond length of 0.97Å in the liquid state, shown in Fig. 2.6. The non-linear configuration and the presence of a lone pair gives the water molecule its polar nature with a dipole moment of 1.85 D [76]. The oxygen lone pair can bind with other water molecules through their hydrogen atoms via O-H$\cdots$O bonds via H-bonding. Since H$\cdots$H lie in between

van der Waals and covalent bonding, the hydrogen bond strength in water is typically 240 meV.

Water exists in many phases of which the most abundant solid phase is the hexagonal crystalline ice I_h [77, 78]. The crystalline structure is with respect to the O atoms as they form a hexagonal lattice, despite the disordered orientation of the H atoms. The Bernal-Fowler rules [79] also known as ice rules which describe the atomic orientation in water ice, require only one H between two O neighbours and two hydrogen to be near an oxygen. These conditions are satisfied by the I_h ice phase. A detailed description of the various condensed phases of water can be found here [77, 80]. Deviation from the ice rules results in point defects which break the potential energy surface of the ice layer. As a result, local protonic defect sites [77, 78] are created which act as trapping centres for electron capture, some of which are shown in Fig. 2.7. For example, an ionic defect: $H_3O^+OH^-$ is when a proton is transferred to the neighbouring water molecule or a Bjerrum defect where no hydrogen atom (L-defect) or two hydrogen atoms (D-defect) are located between neighbouring O atoms. A full water molecule might also be missing from the lattice giving rise to a vacancy (DV). All these defects play an important role in the catalysis of DEA processes on atmospheric ice surfaces [5, 6, 81].

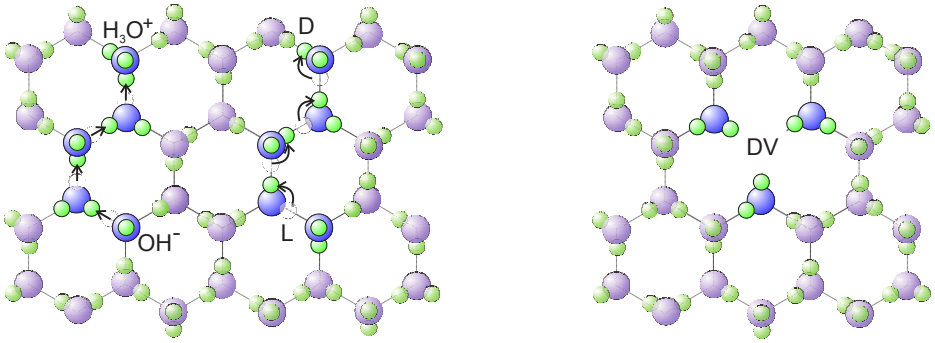

Figure 2.7: The various protonic defects in hexagonal ice I_h are shown and their description can be found in the text. Image is taken from [82].

In amorphous ice, the long range O order is lost, however, both the crystalline ice and amorphous ice behave like large band gap semiconductors with a band gap of 11 eV [83]. Amorphous ice is formed by fast cooling of water to below 130 K [84]. Depending on the preparation conditions, one may have low density (porous when $T < 70$ K and non-porous when < 70 K$T < 120$ K), high density ice or very high density ice. The latter are formed by warming ice under pressure. Since amorphous ice is formed at $T < 130$ K, which is lower than that needed to form crystalline

ice, their study is important with respect to extraterrestrial studies. Amorphous ice too has defects which along with its amorphous structure give rise to Anderson localisation. Thus, there are potential minima in its potential energy surfaces which act as the initial trapping sites in electron solvation.

2.3.4 Ice/Cu(111) Interface and Electron Solvation in Amorphous Ice

Water adsorption on Cu(111) Water molecules adsorb on metal surfaces in a bilayer (BL) configuration. Here, the first layer consists of half the water molecules with the O atom bound to the metal via its lone pair. The second layer consists of the other half of the water molecules bound via hydrogen bonding. This gives rise to a buckled structure [85]. The charge transfer between the metal and the first layer of O, and the water dipole moment pointing towards the metal causes the surface workfunction to decrease [82]. On adsorption of ice, the workfunction constantly decreases with increasing coverage and saturates at 3.9 eV [6, 82] for 3 BL, giving a maximum in workfunction of 1 eV. This means that ice doesn't grow in a closed layer configuration and a flat surface is obtained only after 3 BL of adsorption. This was further verified by STM where a smooth water surface is seen for 3 BL [86, 87]. Water has been found to desorb from Cu(111) via zero order desorption kinetics [6] commencing at 150 K.

e^- solvation in water Solvated electron (e_s^-) is the smallest anion in nature and hence the simplest quantum mechanical solute [17, 88]. Due to their high reactivity, they manifest themselves in many physical, chemical and biological [10, 12, 21, 22] processes at a fundamental level. Since water is a universal solvent and a medium to many vital reactions and processes, it is an important solvation system. Being polar, water can energetically stabilise excess electrons [17] by forming electron-solvent complexes with a solvation shell of ≈ 3 Å [20], localised by ≈ 6 water molecules [89].

Gahl, et al. [5, 6] performed detailed studies of electron solvation in amorphous ice on Cu(111) with tr-2PPE experiments, which we summarise here. Fig. 2.8a) shows the population decay of the unoccupied states in a classic tr-2PPE image for 4 BL D_2O adsorbed on Cu(111) [5, 6] and the 2PPE intensity is given by the false colour scale. The image details two distinct features; the solvated state (e_s^-) at $E-E_F = 2.9$ eV with a relatively long lifetime of upto picoseconds and, the ultrashort living e^- in the ice conduction band (CB) with a broad peak between the Fermi cut-off and e_s^-. The elementary steps involved in this photoexcited solvation process are shown in an energy level diagram, in Fig. 2.8b). Step 1) is the photoexcitation of an

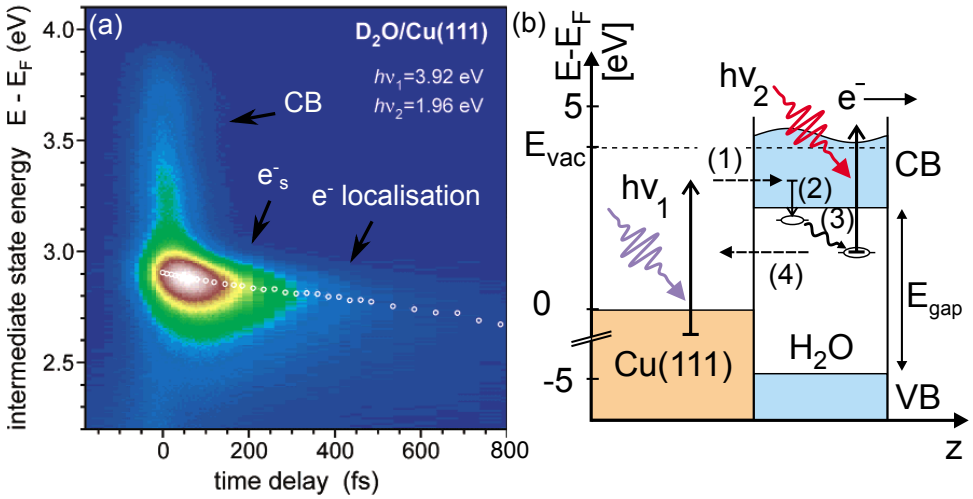

Figure 2.8: Electron solvation in water ice studied with 2PPE spectroscopy. a) Shows the time-resolved dynamics of the solvation state and is taken from [6]. e_s^- is the solvated electron spectral feature, and CB corresponds to the ice conduction band. b) Sketches the solvation process schematically and the image is taken from Gahl, et al. [5]. The various steps are explained in detail in the text.

electron from the Cu(111) into the ice CB due to wavefunction overlap between the delocalised metal states and the CB states. In step 2), the potential band minima below the CB and pre-existing e^- traps localise the excess electron in ice, which also explains why the solvated state is seen below the CB in the 2PPE spectrum. The time resolved spectrum also shows that the binding energy of the solvated electron progressively decreases with time and stabilises after a few hundred fs. This is a fingerprint for solvation and corresponds to step 3) where the water molecules reorient themselves due to polarisation and localise the excess electron or solvated electron. The decreasing peak intensity of the e_s^- peak is due to its continual back relaxation to Cu and this makes for step 4). Despite the back relaxation, the e_s^- has a lifetime of a few picoseconds because of screening by the water molecules which decreases the probability to relax back. Recent studies in bulk water > 15 BL by King, et al. [90] have shown that solvated electrons are stabilised at the ice-vacuum interface. They observed that the e_s^- are long living with a lifetime of 15 ± 1 s for 23 BL D_2O/Cu(111) at 50 K. Fascinatingly, they also found that these localised electrons are capable of reacting with the surrounding water molecule.

The ultrashort lifetime of the CB state is due to the strong coupling between the metal and itself. This also ensures the population of the CB on photoexcitation, provided the photon energy is large enough. Stähler, et al. [91] recently measured

the excess electron dynamics in the conduction band. They found that the electrons localise very fast towards the band bottom at a rate 27 meV/ps and the localisation from excess electron state to the birth of the solvated electron state occurs within 22 fs. From past angle-resolved 2PPE studies [6], the ice conduction band has an effective mass of $1m_e$ and displays a quasi free electron like character, while the e_s^- shows decreasing dispersion with pump-probe delay time implying time dependent localisation of the solvated state.

A natural question arises, where is the solvated electron, near the metal ice interface or ice-vacuum interface. This was answered by performing experiments in the presence of dielectrics like Xe [92, 93] which changes the electrostatic environment of the substrate surface resulting in a shift in states. Interestingly, for > 3 BL of ice, no change is observed implying that e_s^- lives near the metal-ice interface [92]. For $<$ 2 BL, shift in the binding energy is seen suggesting that the e_s^- lives near the vacuum interface [92, 93], but the surface is open and corrugated.

2.3.5 Halobenzenes C_6H_5X and their Ionization

Halobenzenes (BzX), chemical formula C_6H_5X, are benzene molecules with one hydrogen atom replaced with a halogen, as shown in Fig. 2.9.

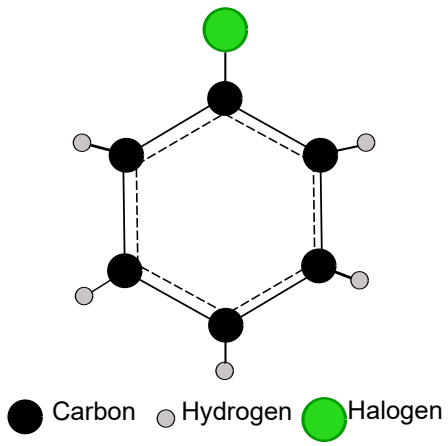

Figure 2.9: Structural figure of halobenzene where one hydrogen is replaced by a halogen atom, X .

In the present work, we consider only the first three halogens, that is X = F, Cl and Br. All the three molecules exist in the liquid state at ambient conditions, while BzF and BzCl have a characteristic aromatic smell, BzBr has a pungent smell. The molecules like benzene are planar with C-C-C bond angle of 120° and with equal C-C bond lengths (1.30Å in benzene) and C-H bond lengths (1.09Å in benzene). These molecules are flammable and have a toxicity level of category 2 or above and thus, should be handled with care.

The electronic structure of the halobenzenes can be explained by delocalised model of benzene [96,97] as shown in Fig. 2.10. Before discussing the structure of the halogenated aryl molecules, let us first discuss the structure of the hexagonal benzene ring in Fig. 2.10a). The C atoms undergo sp^2 hybridisation and bind to a

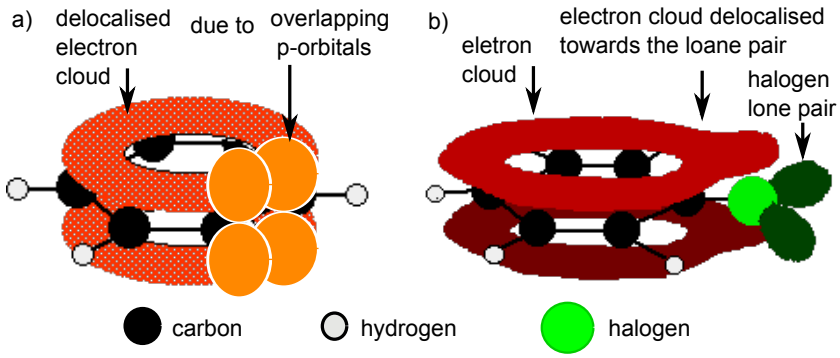

Figure 2.10: Electronic structure of a) benzene and b) halobenzene. The overlapping p-orbitals of the carbon atom result in two delocalised electron clouds. This cloud is pulled towards the halogen lone pair. Image adapted from [94, 95]

hydrogen atom as well a neighbouring carbon atom via σ bonds. The 3rd p orbital on the carbon does not hybridise and overlaps with the neighbouring C atom's 3rd p orbital, resulting in six delocalised π electrons (Fig. 2.10a)). This forms a delocalised π ring, with 6 electrons being shared by 6 carbon atoms. In halobenzenes, one hydrogen is substituted with a halogen which binds to the carbon via the lone pair sharing. The halogen lone pair pulls the delocalised p-electron cloud towards it, which further strengthens the C-X bond [97, 98] (Fig. 2.10b)). The extent of pull depends on the electronegativity of the halogen which is the highest for F = 4 and lowest for Br = 2.96. This means, as we go down the periodic table (F→Cl→Br), the C-X bond strength decreases, giving a systematic change in the chemical properties (Fig 2.12, discussed later).

The effect of the halogen on the aromatic ring is shown in Fig. 2.11 [1, 99], where the electrostatic potential surfaces calculated for benzene (Bz), BzBr, BzCl, BzF and hexafluorobenzene (BzF_6) are shown as false colour maps. A more negative potential is shown by red and a positive one by blue. We see that for Bz, the red centre is the most electronegative part of the ring while the green frame is comparatively positive due to the lower electron density. Since every C atom is identical (C-H bonding), each C has the same electrostatic potential on it and the electron density in the centre is a symmetric circle. On substituting one of the hydrogen atoms with a bromine atom, the electronegative halogen pulls the π electron cloud towards it. We see that the molecule and its potential energy surface is asymmetric, the electronegativity at the centre is reduced, and the Br end of the ring and the ring centre is more electronegative than the carbon framework. Since Cl and Br have similar electronegativity, on substituting with Cl we get a similar potential surface

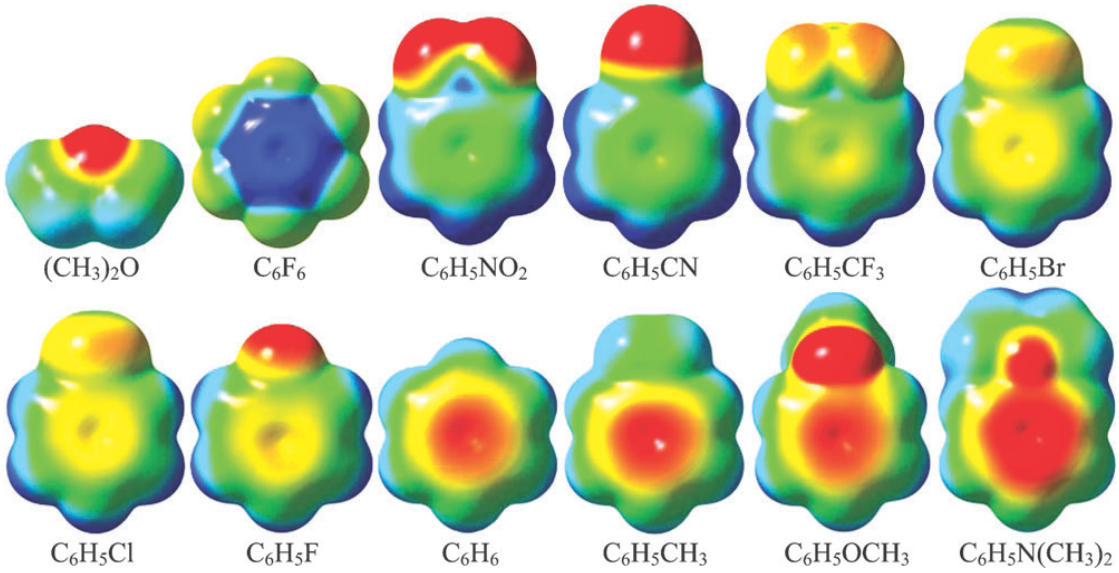

Figure 2.11: Potential energy surfaces of the different benzene substituted molecules, calculated by Amicangelo, et al. [1], showing the effect of substitution on the $\pi-$electron density at the ring centre. Negative potential is shown by red, positive by blue and green lies in between them.

map. Fluorine, which is the most electronegative halogen and also the smallest, attracts the π electrons more towards itself than bromine. As a result, the aromatic ring centre is comparatively less electronegative than that of BzBr and Bz and the electrostatic potential is no longer symmetric. The carbon in the C-F bond now has a larger electron density compared to the other C's and the electron density at the centre is also not symmetric (antisymmetric yellow circle). In the case of hexafluorobenzene, due to strong electron attraction at all the C's due to the C-F bond, the ring frame has a higher electron density than the centre (blue centre). Since all the hydrogen are substituted by F, the effect is symmetric and we see that the electrostatic potential surface of Bz and BzF_6 is opposite to each other. Therefore, depending on the substituent, the electrostatic potential surface changes.

This is also reflected in the electronic structure of the molecule where the molecular energy levels shift according to the above systematics. The HOMO (highest occupied molecular orbit) and LUMO (lowest unoccupied molecular orbit) levels for the mono-halogen series are shown in Fig. 2.12. These levels correspond to the ionization potential and the electron attachment levels and reflect the electrostatic potential surface systematics. With increasing electronegative substitution, the HOMO-LUMO gap decreases, that is the electron attachment level and the ionization energy

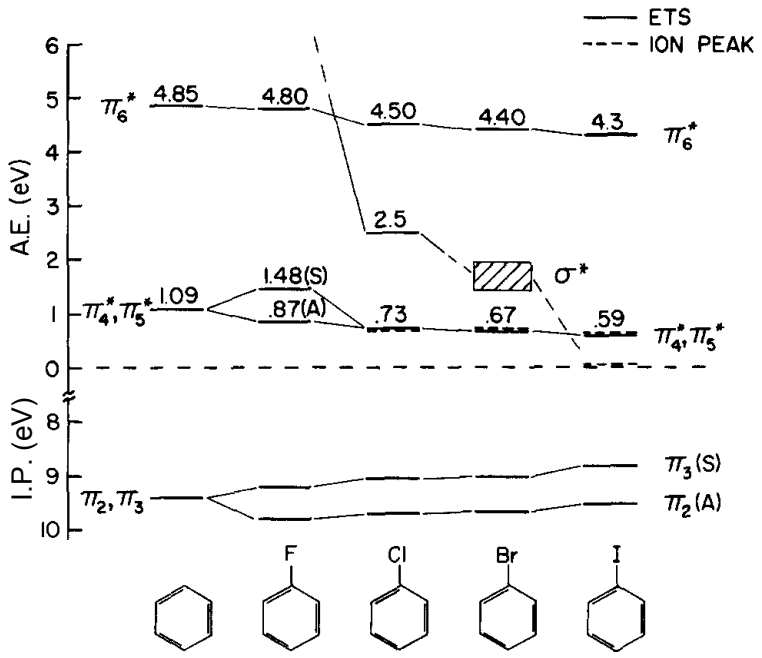

Figure 2.12: Electron attachment energies (A.E.) at the LUMO and ionization potential energies (I.P.) at the HOMO of gas-phase halobenzenes measured by electron transmission spectroscopy (ETS) by Olthoff, et al. [2]. Ion peak data correspond to measurements by photoemission spectroscopy. A decreased electron attachment energy and ionization potential energy is seen with increasing halogen size (going down the periodic table), showing the effect of substitution. Image taken from [2]

moves to lower energies [2, 100]. Experimental studies in the gas phase like electron scattering measurement and inverse photoemission spectroscopy [24, 38, 40] support these calculations. On adsorption on coinage metals, the HOMO-LUMO gap becomes smaller due to repulsive interaction between the metal e^- cloud density and the halogen lone pair and due to polarisation of the LUMO state by the metal's IP state [31, 33, 38, 101, 102], but the trend remains the same [103]. For example, Dudde, et al. [38] performed systematic studies of benzene, n substituted chlorobenzene and hexafluorobenzene on Cu(111) with inverse photoemission spectroscopy which showed that the antibonding orbitals shift to lower energies and the extent of the shift and the total shift depends on the substitute (more shift more less more electronegative substitution). Photoemission studies showed that the molecular state is localised for 6-fold symmetric molecules like Bz [3] and BzF_6 [4].

Since we would like to study the charge transfer dynamics at different coverages

of the halogen series, it becomes important to know how the π-rings are bound and oriented to each other. Due to the importance of $\pi - \pi$ and π-lone pair interactions in biochemistry and molecular electronics [36], they have been widely studied in the past. These studies revealed that the interaction strength depends primarily on the substituent group, for example a cation binds stronger with a less electronegative substituent than a more electronegative one. The electrostatic model is one of the proposed mechanism[1] to explain for this, where the interaction along a series can be explained primarily on the basis of electrostatic potential of the interacting molecules, shown in Fig. 2.11. For instance, comparing Bz and BzF_6, BzF_6 has a 'positive' core and a 'negative' frame, while Bz has a 'negative' core and 'positive' frame, thus changing the nature of interaction with, for example, a cation. Electrostatic potential surfaces are thus very intuitive and useful in understanding and predicting $\pi - \pi$ and $\pi-$lone pair interactions. We will therefore refer to them frequently for comparative analysis.

Some characteristic properties of the BzX's are compared in Table 2.1

Table 2.1: Physical and Chemical Properties of C_6H_5X in the gas-phase

Parameter	C_6H_5F	C_6H_5Cl	C_6H_5Br
molecular weight (g/mol)	96.1	123.56	157
electronegativty at X in C_6H_5X [104]	12.43	10.19	9.65
C-X bond length (Å) [105, 106]	1.34	1.735	1.85
C-X bond dissociation energy (eV) [24]		3.73	3.04
partial charge at X (e.u.) [104]	-0.17	-0.08	-0.05
dipole moment (Debye) [105]	1.66	1.54	1.55
polarisabilty of X ($Å^3$) [104]	9.98	12.19	13.09
solubility in water at 25°C (g/l) [107]	1-10	0.49	0.41
DEA(Experimental) (eV)	-	0.7 [23]-0.6 [24]	0.3 [23]-0.5 [24]
Photodissociation (Experimental) (eV)	6.42 [108]	4.66 [109, 110]	4.66 [111]

As we can see from Table 2.1 the electronegativity of the halogen in the benzene ring decreases from BzF to BzBr. This explains the trend of decreasing partial charge at the halide and the C-X bond dissociation energy, but an increasing polarizability from BzF to BzBr. Due to the larger size of the latter halogens, the dipole moment also increases from BzF to BzBr (Fig. 2.11).

[1]The other model is the quadrupole momentum model which considers the interaction via the ring's quadrupole moment only.

Dissociation

It is well known that the aryl halides can dissociate at energies lower than direct dissociation energies via a pre-dissociation channel [112,113]. In Fig. 2.13a), we show the potential energy curves of the ground state HOMO state π, the LUMO state π^* and the dissociative σ^* start on C-X bond length reaction coordinate. The lower lying non dissociative resonant π_a^* and π_s^* states (green dotted line in Fig. 2.13a)) are coupled to the higher lying dissociative resonant σ^* states (black solid line in Fig. 2.13b) through a conical intersection, Ic [114,115]. In the figure, $E_{ionization}$ is the ionization energy needed to excite the molecule into the π^* level and E_B is the energy needed to reach Ic. Since the (π, π^*) state are mostly delocalised over the aryl ring, they do not dissociate the C-X bond, however, the (σ, σ^*) states are localised over the C-X bond and mediate its dissociation. If the EEs in ice have sufficiently large energy, they can ionise C_6H_5X to $C_6H_5X^{*-}$ (excitation to π^* state) and dissociate it into benzene radical $C_6H_5^{\bullet}$ and halogen anion X^- (via intersystem crossing to σ^* state), shown in Fig. 2.13a).

Many photodissociation studies have been performed for the gas phase BzX molecules [25, 41, 109–111, 116]. For example, BzCl photodissociates at 193 nm via internal conversion from the lowest π^* state (after an internal conversion from the third singlet state) to the continuum of the σ^* state, shown by Freedman, et al. [113] by performing photo-fragmentation studies. Ichimura, et al. [110] further go on to suggest that the coupling to the triplet state is via the vibrational states and that at lower energies (248 nm) this can also happen through a hot mechanism, which is a vibrationally excited ground state. Dissociation via low energy electron attachment also proceeds in a similar way, that is by electron transfer to the π^* system which excites the molecule to the dissociative σ^* states. In Fig. 2.13b) we pictorially show a possible dissociation mechanism in BzX. Here the ground state singlet state is excited to the third singlet state $S_n(\pi, \pi^*)$, shown in the left wing. The third singlet state, via internal conversion, is coupled to a triplet state $T(\sigma, \sigma^*)$, shown in the central wing. Once in the excited triplet state, the molecule dissociates (right wing) by the various mechanism mentioned above, since this triplet state is dissociative.

2.3.6 Organic Molecule/Metal Interface

Halobenzene Adsorption on Metal and Ice Ming Xi, et al. [29] studied benzene adsorption on Cu(111) with NEXAFS, HREELS and TDS. They found that benzene adsorbs as a whole with its ring parallel to the metal substrate when the coverage is less than $1x10^{-14}$ molecules/cm^2, which corresponds to a close-pack layer. A coverage between this and three times this results in the tilting up of the ring,

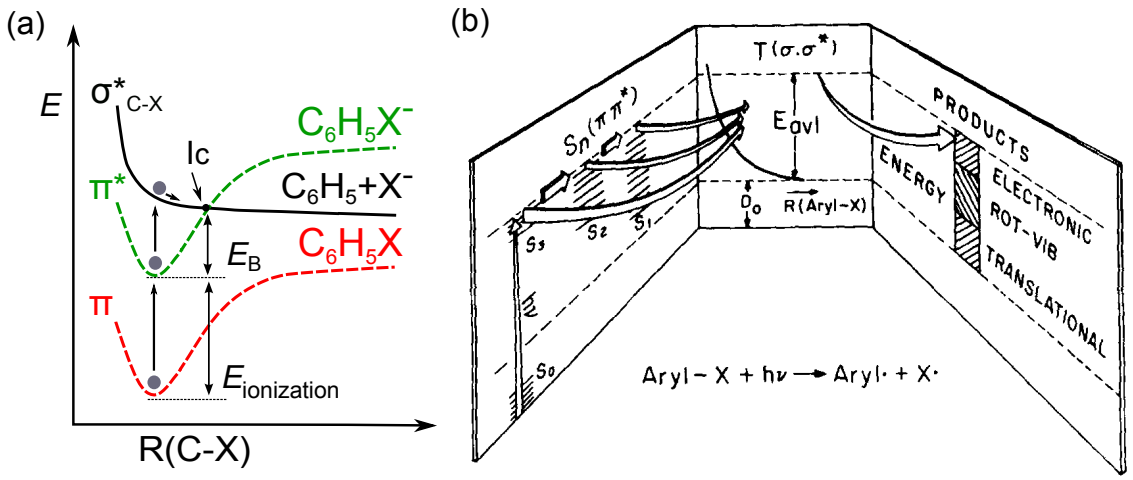

Figure 2.13: Dissociation mechanism in halobenzenes. a) The energy of the ionised/dissociated halobenzene state is shown as a function of the reaction coordinate, which is the carbon-halogen bond length here. The ionization and dissociation potential energy curves are schematically shown to cross at conical intersection Ic. $E_{\text{ionization}}$ is the threshold energy needed to ionise the neutral halobenzene to anionic halobenzene and E_{B} is the energy needed by the ionised molecule to reach Ic. b) Coupling between the singlet $S_n(\pi, \pi^*)$ and triplet state $T(\sigma, \sigma^*)$ which results in the dissociation of the halobenzene molecules, image taken from [113]. A detailed explanation of the mechanism can be found in the text.

with the tilt increasing for greater coverage. The molecules absorb in bilayer with the first monolayer chemisorbed and flat lying, while the second layer is tilted up and physisorbed. These observations and conclusions were also later supported by the 2PPE measurements performed by D. Velic, et al. [3] who found a shift in the binding energy of the image potential derived molecular state with coverage and explained it as a result of changing benzene orientation. A year after the Ming Xi, et al. paper [29] was published, Michael Yang, et al. [28] published NEXAFS and TDS study of chloro/iodobenzenes on Cu(111). They showed that halobenzenes too adsorb as a whole with their ring plane facing the surface, which for near monolayer coverage (0.7-0.8 ML) tilts up at an angle of 45±5° and near saturation of a monolayer, decreases to 43±5°. Recent near infra-red spectroscopy and STM [117] studies too show that at submonolayer coverage the BzX molecules physisorb flat lying on the metal and at some higher coverage (still under investigation) start to tilt up. The STM study found that even at 11 K, the submonolayer halobenzene molecules on bare Cu(111) are mobile. Not much is known about how halogenated benzenes adsorb on ice except that they form agglomerates with water which are partially embedded in the ice cavity [27] and that benzene acts as a proton acceptor [118].

Chapter 3

Experimental Tools and Techniques

To study the charge transfer dynamics between interfaces, we study the surface electronic structure with two-photon photoemission spectroscopy. Since we would like to investigate surface properties, we need an extremely clean sample surface and well characterised adsorbate films. Therefore, the experiments are performed in an ultra high vacuum chamber to provide the clean environment needed by surface studies. The Cu(111) is used as the metal substrate and is prepared by sputter-anneal cycles, while the adsorbed molecular (D_2O and C_6H_5X) layers are characterised by thermal desorption spectroscopy. We use two-photon photoemission (2PPE) spectroscopy to probe the system. Femtosecond pulses are generated by an amplified Ti:Sa laser. To match the different experimental wavelength requirements, an optical parametric amplifier (OPA) or a non-collinear optical parametric amplifier (NOPA) is used to tune the photon energy. A time of flight detector detects and analyses the kinetic energies of the photoemitted electrons. The resulting 2PPE spectrum is subsequently analysed using Igor procedures written by Laurenz Rettig and Patrick Kirchmann during their PhD theses [119,120]. The laser setup and the ultra high vacuum chamber were already setup and functioning before the start of the thesis. However, we improved on the NOPA setup which is explained in quite some detail at the end of the chapter. Since most of the topics discussed below are already well described in a lot of details in past theses, we strongly urge the readers to refer to the suggested text for clarification and in depth understanding of the setup.

3.1 UHV Chamber

To perform surface sensitive studies, a very clean surface is the first requirement for which we need a clean sample environment [121]. Therefore, we worked in an ultra high vacuum (UHV) chamber with a background pressure of $< 3 \cdot 10^{-10}$ mbar. To get an idea of the importance of ultra high vacuum consider this: at this pressure, it takes ≈ 10 hrs to form a monolayer of residual gas atoms, but with a background pressure of 10^{-6} mbar, the residual gas density is $3 \cdot 10^{16}$ molecules/m^3 and it takes only 1 s to form a monolayer.

The UHV chamber is mounted on an air-damped laser table to avoid unwanted vibrations and is divided into two parts by a gate valve. The upper part is pumped with a turbo-molecular pump (Pfeiffer) which is pre-pumped with a multi-stage membrane pump (VacuBrand). It is dedicated to sample preparation and characterisation. Accordingly, the upper chamber is equipped with a sputter gun, lead evaporator, electron gun, low energy electron detector (LEED), quadrupole mass spectrometer (QMS) and a pinhole doser. The upper chamber is also connected to a vacuum sample storage magazine and a transfer line. The sample can be shuttled in and out of the chamber from the magazine without venting the whole chamber. The bottom part of the chamber is pumped with a titanium sublimation pump (Riber) and an ion getter pump (Riber) and is dedicated to spectroscopy. It is equipped with an Auger spectrometer, a time of flight (ToF) spectrometer, and a position sensitive ToF (pToF) spectrometer home built by Patrick Kirchmann [120]. The ToF and the pToF are described in some details in subsection 3.2.

We use a motor controlled manipulator with four degrees of motion (x, y, z, and rotation around vertical axis) to manoeuvre the sample. The top of the sample holder is connected to the bottom of a 400 mm long helium cryostat (CryoVac) and can be cooled by lq. He or lq. N_2. The lower legs of the sample holder are coated with gold and have two tantalum wires (0.4 mm thick) stretched across it. These wires hold the Cu(111) monocrystal (9 mm diameter and 3 mm thick) between them. In addition to the contact with the cryostat, the sample holder is also connected to an electrical connection to enable resistive heating. In this way, the Cu(111) crystal via the tantalum wire and the copper legs can be heated or cooled. The copper legs are electrically insulated from each other and the sample holder (at the cryostat end) with a sapphire plate. Sapphire has good heat conductivity and does not hinder with the sample's heating and cooling. For a precise temperature read out at the sample, a Type K (NiCr/Ni) thermocouple in inserted into a hole in the thickness of the Cu(111) crystal. For this reason, while inserting or removing the Cu crystal, we don't use the transfer line, but have to remove the cryostat and vent-bake the

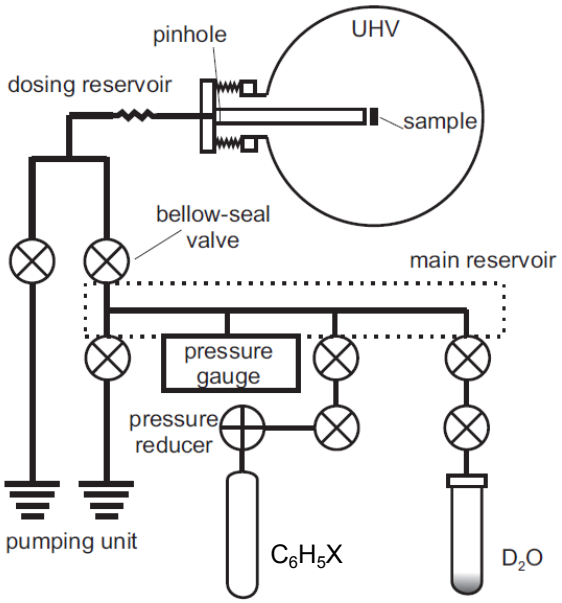

Figure 3.1: Schematics of the gas system which is connected to the ultra high vacuum (UHV) chamber through a pinhole doser. The different C_6H_5X are connected at different valves. Figure adapted from the PhD thesis of Michael Meyer [122].

chamber.

The preparation chamber is connected to the gas system via a pinhole doser and a leak valve. A schematic representation of the gas system is shown in Fig. 3.1. It consists of two independent gas reservoirs, which are nothing but 6 mm diameter steel pipes. The gas system is pumped by a cube pump (Pfeiffer) and the dosing molecules are attached to it via test tubes. Compressed noble gasses like He, Xe and Ne can also be attached via mini gas-cans. The pressure in the gas reservoir can be controlled with a series of valves at the test tubes and at the pump connections. The water and halobenzene (BzX) molecules were dosed on the sample via a pinhole doser which consists of a 50 μm pinhole and a long steel pipe. A uniform molecular beam is ensured because of the constant collision amongst the molecules and with the doser walls. The pinhole doser is also being continuously pumped by a turbo pump, except while dosing. This turbo pump is the same one which creates prevacuum for the chamber's main turbo pump. As opposed to the leak valve, which adsorbs molecules via background dosing, this method is more reproducible and the chamber's background pressure never rises above $5 \cdot 10^{-9}$ mbar. A detailed description of the chamber and its various home built instruments can be found in past theses: [82, 119, 120, 122–124]

3.2 Two-Photon Photoemission Spectroscopy

Two-photon photoemission (2PPE) spectroscopy and time resolved two-photon photoemission (tr- 2PPE) spectroscopy are well established surface techniques. Here an electron is pumped from the occupied state to above the vacuum level with the help of two photons and are detected by an electron spectrometer. By delaying one photon with respect to the other, the dynamics of the unoccupied state can studied. One can even perform tr- angle resolved photoemission (tr-ARPES) measurements or detailed workfunction studies with this technique. In this section we discuss two-photon photoemission (2PPE) and time resolved two-photon photoemission (tr- 2PPE) spectroscopy. Then we go on to discuss how a 2PPE spectrum can be analysed. We also include the description of the light source and beamline.

3.2.1 Photoemission Spectroscopy

Photoemission spectroscopy or photoelectron spectroscopy is a powerful spectroscopic technique to study the electronic structure of solids, surfaces and adsorbates. The sample absorbs a photon of energy $h\nu$ and excites a photoelectron above the vacuum level E_{vac} with a kinetic energy E_{kin} given by :

$$E_{\text{kin}} = h\nu - (E_i - E_{\text{F}}) - \Phi \tag{3.1}$$

where, Φ is the workfunction of the system, E_i is the binding energy of the photoexcited state and E_{F} is the Fermi energy. The photoemitted electrons are detected by a time of flight detector (ToF) in our setup and a distribution of the measured kinetic energy as a function of detected electrons gives us the photoemission spectrum. If the kinetic energy is measured as a function of the emission angle, its surface parallel momentum component and the electronic dispersion of the photoexcited state can be determined from Eq. 3.4 and Eq. 3.5, which we'll discuss shortly.

The photoemission process is rather complicated, but can be treated mathematically with the help of approximations. The two most important approximations are: 1) considering a one-electron picture (single electron states in the initial state in a system of non-interacting electrons) and 2) considering the dipole approximation. Another important approximation worth mentioning is the sudden approximation which considers the photoemission process as two decoupled processes, one the photoexcitation from the initial N particle state to final $N-1$ particle state (one-electron picture) and the other as the relaxation of the excited $N-1$ state (many body interaction). This is because it assumes that the photoemission process is much faster

than the electronic response of the system and one therefore probes the ground state spectral function.

Three- step and One-step models: There are two models to describe the photoemission process; *one-step model* and *three-step model*. The three step model [125, 126] approaches the problem in three independent steps: 1) The incident photon is absorbed by an electron which is excited to an unoccupied vacuum level state within the crystal. 2) The excited electron is propagated to the crystal surface and 3) finally escapes the crystal surface into the vacuum. However, these steps are not truly independent of each other and for a more rigorous approach, we consider the one -step model. The one-step model considers the optical excitation of an electron from an initial state of the crystal's Bloch wave to a final state in the vacuum level, which is a freely propagating wave outside the crystal but exponentially damped inside it. Since this is phenomenologically similar to LEED (treated as inverse LEED) [127–129], the one-step model is mostly considered for theoretical calculations as it can make use of the pre-existing theoretical formalisms used in LEED. Since we perform 2PPE at the surface, the one-step model is more appropriate.

The inelastic scattering in the three step model and the damped vacuum wave in the crystal in the one step model account for the energy dependent finite penetration depth in the photoemission spectroscopy given by the universal curve for electrons. It also gives rise to a background in the photoemission spectrum [121, 130].

In direct- or 1- photon photoemission, only one photon is needed to excite the electron from below E_{F} to above E_{vac}. Thus, an important condition for direct photoemission is that $h\nu > \Phi$. Here, one can probe the complete occupied electronic band and gain information on binding energies of surface states, valence state of ions and band dispersion. In this work, we do not perform direct photoemission measurements, but primarily perform 2PPE and hence discuss that in some details.

2PPE: While photoemission spectroscopy is limited to occupied and final states, 2PPE technique can probe both the occupied and the unoccupied states simultaneously [58, 60], like the image potential state in metals and the LUMO (lowest unoccupied molecular orbital) levels of the adsorbate. 2PPE is a two photon pump-probe technique where, the pump photon ($h\nu_1$) excites an electron from the initial state (occupied band) to an intermediate state (unoccupied) lying between E_{F} and E_{vac}. Next, the probe photon ($h\nu_2$) excites the electron from the intermediate state to above the vacuum level (final state) where the electron can propagate freely and

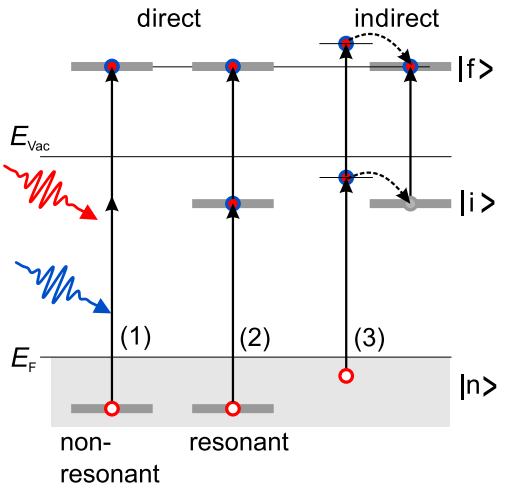

Figure 3.2: The different photoexcitation schemes possible in two-photon photoemission spectroscopy, where $|\ n\rangle$ is the initial state (occupied), $|\ i\rangle$ is the intermediate state (unoccupied) and $|\ f\rangle$ is the final state. E_F and E_{vac} represent the Fermi level and the vacuum level, respectively. The different excitation channels are explained in the text. Figure taken from PhD thesis of Cornelius Gahl [82].

is detected by an electron spectrometer. Hence, an important condition is:

$$h\nu_{1,2} < \Phi \quad \text{and} \quad h\nu = h\nu_1 + h\nu_2 > \Phi \tag{3.2}$$

i.e., the pump and probe photons together should have enough energy to be able to excite the electron above E_{vac}, but should not do so individually.

Since in 2PPE, an electron is excited from an $|\ n\rangle$ initial state to the final state (continuum states in vacuum) $|\ f\rangle$ via an intermediate state $|\ i\rangle$, there are three different excitation channels possible. In Fig. 3.2, we show an energy level diagram for the three different excitation channels. Channel 1 (initial state) is a non-resonant excitation from the initial state to the intermediate state, i.e. there is no resonant real intermediate state accessible by the initial state and the excitation occurs via a virtual intermediate state. This happens due to transient second order polarisation, possible in the presence of strong laser fields, and can be visualised as the absorption of two photons simultaneously. In channel 1, the electronic properties of the occupied states (or final states) are probed. Channel 2 sustains excitation from the initial state to a real intermediate state. Here, there is resonant excitation and the electronic properties of the intermediate state can be probed. The third channel, channel 3, is when there is an indirect and non resonant excitation of a real $|\ i\rangle$ via inelastic scattering processes (electron-electron, electron-phonon or electron-defect) from other intermediate states. Here the parallel momentum $\vec{k}_{\|}$ is not conserved due to scattering.

Since the photoemitted electron from the initial, intermediate or final state can be detected with the same E_{kin}, to distinguish them, we either rely on the tr-2PPE data or by playing with the photon energy $h\nu$. If we consider monochromatic 2PPE

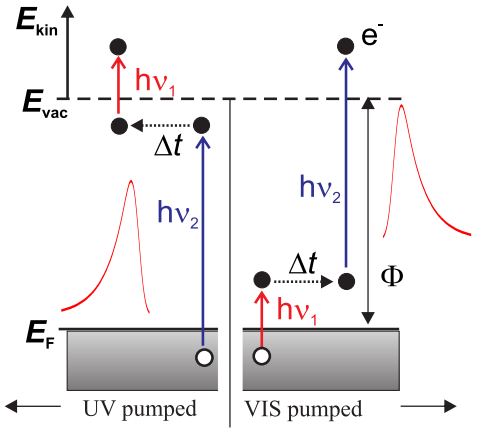

Figure 3.3: Energy level diagram schematically showing the tr-2PPE pump-probe scheme. The x-axis shows the two pump-probe axis, UV pumped (VIS probe) and VIS pump (UV probe). State near the vacuum level are pumped with the UV, while states near the Fermi level are pumped with the VIS. Figure adapted from Patrick Kirchmann [120].

where $h\nu_1 = h\nu_2$ and the observed state corresponds to an occupied state, then on changing the photon energy, the kinetic energy of the new state would shift by twice the difference between the new and the old photon energy, once because of the excitation to the intermediate virtual state and once for exciting it above the vacuum. If the observed state corresponds to an unoccupied energy level, then its kinetic energy with the new photon energy shifts by only once the difference between the old and new photon energies, corresponding to the difference between the probe pulses. For the final state, no shift in the kinetic energy is seen on changing the photon energy. By plotting the shift in E_{kin} of the observed spectroscopic peak with respect to $h\nu$ and measuring the slope, one can determine to which state the observed spectroscopic signal corresponds to depending on the slope, according to:

$$|\, n\rangle : \text{slope} = 2, \quad |\, i\rangle : \text{slope} = 1, \quad |\, f\rangle : \text{slope} = \text{no change} \tag{3.3}$$

tr- 2PPE and ARPES We introduce time-resolved two photon photoemission (tr-2PPE) and angle resolved-2PPE (ARPES) briefly since, they are not the main focus of this work. By time delaying the pump and probe pulses with respect to each other, one can study the time resolved population dynamics of the intermediate state. While the pump excites the electron into the intermediate state, the probe is delayed by $\Delta\tau$ with respect to the pump, giving a temporal evolution of electron relaxation of the excited intermediate state. In our setup, $\Delta\tau$ is varied by changing the VIS beam path with respect to the UV beam by a computer controlled delay stage. If a state lies near the vacuum level, it will be pumped by UV and probed with VIS, and *vice-versa* if the state is near the Fermi level (Fig. 3.3).

Since in photoemission the parallel momentum is conserved (if there is no scattering in the final state) and the photon momentum is small compared to the electron's momentum, the surface parallel dispersion component $\vec{k}_{\parallel}$ can be determined by:

$$\vec{k}_{\parallel}(\alpha, E_{\text{kin}}) = sin(\alpha)\sqrt{\frac{2m_e}{\hbar^2}E_{\text{kin}}} \tag{3.4}$$

where α is the electron emission angle and m_e is the free electron mass. If the 2PPE spectrum is measured for different emission angles, by either rotating the sample or using the position sensitive ToF (pToF)[1], the binding energy of the state with respect to the Fermi level ($E-E_{\text{F}}$) can be plotted as a function of $\vec{k}_{\parallel}$. This gives the electronic band structure of the photoexcited state (Eq. 3.5) and the electronic dispersion.

$$(E - E_{\text{F}})(\vec{k}_{\parallel}) = \frac{\hbar^2\vec{k}_{\parallel}^2}{2m_{\text{eff}}m_e} \tag{3.5}$$

where m_{eff} is the effective mass of the electron in terms of m_e. Since $\vec{k}_{\parallel}$ depends on E_{kin}, a wider k-space can be accessed by using higher photon energies, however, care should be taken to avoid direct photoemission, while performing 2PPE ARPES.

3.3 Data Acquisition and Analysis

3.3.1 Data Acquisition

The kinetic energy of the photoemitted electrons is measured by an electron time of flight (ToF) spectrometer. The spectrometer was home-built at the Fritz-Haber-Institute of the Max Planck Society and its detailed sketch can be found in [123, 131] and [120] for English. To describe it briefly, it consists of a long field free aluminium drift tube and a chevron stack of micro-channel plates (MCP). The photoemitted electrons enter the ToF tube through an aperture at its canonical tip. At the other end of the tube, the electrons are accelerated via a grid towards the MCP. Each accelerated electron causes an electron avalanche at the MCP and generates an electron cloud whose voltage signal is out-coupled with a capacitor at an anode and serves as the *stop* signal. The ToF spectrometer is housed in a μ metal shielding to block all external residual magnetic fields. It has openings for the manipulator and the laser beam, and enough space to allow the sample to rotate by $\pm 16^{\circ}$ for

[1] or using a hemispherical analyser with 2D detection

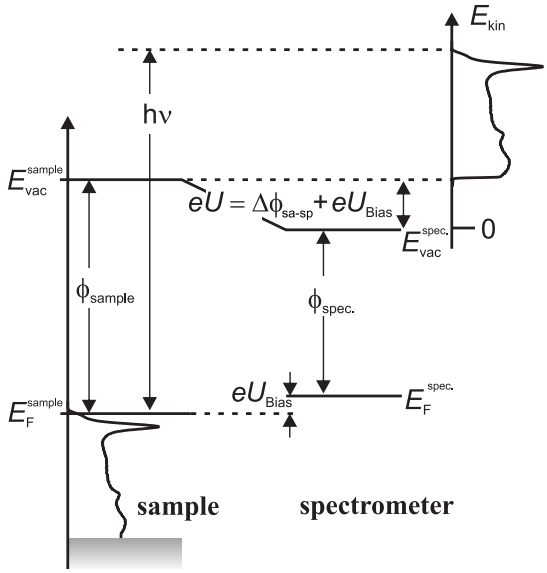

Figure 3.4: Energy level diagram schematically showing the need for a bias voltage U_{Bias} and how the bias helps the energy level alignment between the sample and the spectrometer. The 2PPE spectrum is measured with respect to the spectrometer's vacuum energy $E_{\text{vac}}^{\text{spec.}}$. If eU is the energy difference between the sample and the spectrometer and $\Delta\Phi_{\text{sa-sp}}$ is the workfunction difference between the two, eU_{Bias} is set $= \Delta\Phi_{\text{sa-sp}}$ such that eU is zero. This condition ensures that the photoemitted electrons travel in field free region from the sample to the spectrometer. Figure taken from Patrick Kirchmann's PhD thesis [120].

ARPES measurements. The sample surface is orientated parallel to the ToF tip aperture so that the beam enters the ToF spectrometer at a 45° angle with respect to the spectrometer axis. Additionally, to ensure an unperturbed acceleration of the photoemitted electrons in the drift tube, all the spectrometer parts like the tip, drift tube and the grids are coated with graphite and have a homogeneous workfunction of 4.3 eV. The time of flight t_{m} is calculated as the difference between the MCP's *stop* signal and a *start* signal. The *start* signal is usually a small signal from the laser head (RegA) detected by a fast photo diode. The in-depth summary of the signal processing can be found in the afore mentioned theses. The kinetic energy of the photoemitted electrons can be determined from its time of flight with the help of Eq. 3.6:

$$E_{\text{kin}} = \frac{1}{2} m_e \left(\frac{L}{(t_{\text{m}} - t_0)} \right)^2 - (\Delta\Phi_{\text{sa-sp}} + eU_{\text{bias}}) \tag{3.6}$$

where, $t_{\text{m}} - t_0$ is the actual time of flight and t_0 is the delay or offset in *start* signal due to system electronics. $L = 30$ cm is the drift length of the electron, $\Delta\Phi_{\text{sa-sp}}$ is the difference in workfunction of the sample and the spectrometer and eU_{bias} is the bias voltage applied to the sample. In Fig. 3.4 an energy level diagram for the sample and the detector before and after applying the eU_{bias} voltage is shown.

The photoemission spectrum is measured with respect to the vacuum level E_{vac} of the spectrometer. Since, the sample and the spectrometer are connected to each

other electrically via a contact potential (bias connection), they are equilibrated to each other via their E_{F}, before applying the bias voltage. Depending on the sign of $\Delta\Phi_{\text{sa-sp}}$, the potential difference between the vacuum energies might accelerate the electrons or decelerate them, for example, if the samples workfunction is higher than the spectrometers, then the photoemitted electrons will feel the potential difference and be accelerated. A negative or a positive bias voltage eU_{bias} thus has to be applied to the sample in order to compensate for $\Delta\Phi_{\text{sa-sp}}$. It can also be done to separate the sample's secondary edge from the detectors. For ARPES measurements, it is important that the sample and the spectrometer vacuum level are aligned to ensure a field free electron trajectory to the detector and hence the condition $eU_{\text{bias}} = \Delta\Phi_{\text{sa-sp}}$ becomes important.

pToF We also used the position sensitive time of flight spectrometer pToF which was built by Patrick Kirchmann [120, 132] and later modified (pToF tip) by Laurenz Rettig [119] during their respective PhDs. The pToF is capable of resolving the momentum dispersion parallel to the surface $\vec{k}_{\parallel}$ in both the x ($\vec{k}_x$) and y ($\vec{k}_y$) directions without rotating the sample. This is possible because the photoexcited electron cloud is detected by 3 sets of wires oriented 60° to each other and wound around a hexanode, giving a total of 6 voltage pulses collected at the wire ends. The impact position (x, y) on the MCP and the time of flight of the electrons can be determined from the relative arrival times of the six hexanode signal and the MCP impact signal, thus giving both energy and momentum resolution. If the pToF is used to perform tr-2PPE, we can study the photoemitted electron and the photoexcited state with any combination of these parameters: $E_{\text{kin}}, \vec{k}_x, \vec{k}_y$ and $\Delta\tau$.

3.3.2 Data Analysis

The 2PPE spectrum obtained by us shows the photoemission intensity as a function of the calculated kinetic energy (Eq. 3.6). A typical photoemission spectrum consists of a Fermi edge which is the high energy cut-off, and a secondary edge which is the low energy cut-off. The Fermi level E_{F} is the highest occupied state in metals at equilibrium and hence electrons with the highest kinetic energy $E_{\text{kin(Fermi)}}$ will be excited from it, giving the Fermi edge. The lower energy limit is given by the workfunction Eq. 3.8, where the electrons that just managed to escape the sample have the lowest kinetic energy E_{sec}.

The 2PPE signal from different energy states are seen as spectral peaks lying between these limits. Once we have determined the nature of the state corresponding to a spectral feature (§ 3.2.1 and Eq. 3.3), we can appropriately determine its binding

energy. Usually, the initial/occupied states ($\mid n\rangle$) are referenced to E_{F} and the intermediate/unoccupied ($\mid i\rangle$) state is referenced to E_{vac}. However, one can reference both to E_{F} on an intermediate or internal energy scale as:

$$\begin{aligned} E_{\mathrm{n}} - E_{\mathrm{F}} &= E_{\mathrm{kin(n)}} - E_{\mathrm{kin(Fermi)}} \\ E_{\mathrm{i}} - E_{\mathrm{F}} &= E_{\mathrm{kin(i)}} + \Phi - h\nu_{\mathrm{probe}} \end{aligned} \tag{3.7}$$

where, E_{kin} corresponds to the kinetic energy of the spectral feature under discussion. Here E_{F} coincides with the pump photon energy. Since in 2PPE both the VIS and UV photons can excite electrons from the Fermi level, we get two intermediate scales, one for VIS pumping and one for UV pumping. A second commonly used energy scale is the final state energy scale where the Fermi edge coincides with the sum of both the photons (or one photon in case of direct photoemission) according to: $E_{\mathrm{final}} - E_{\mathrm{F}} = E_{\mathrm{kin}} + \Phi - E_{\mathrm{kin(Fermi)}}$. In this work, we will only use the intermediate energy scale.

The kinetic energy of the peaks can be determined by fitting them with a Lorentzian function. The Fermi edge is determined by fitting it with a Fermi-function convolved with a Gaussian, since its width is determined by the sample temperature and the laser pulse bandwidth. The secondary edge was determined with the help of an error function.

Tr- data: The time resolved data is given by a false colour map showing E_{kin} vs $\Delta\tau$ on the *x-y axis* and the intensity on the colour scale. Since tr-measurements are usually performed with two different photon energies (pump and probe), we have two energy scales giving the same spectrum. For example red pump-blue probe and vice versa will excite and probe different states like hot electrons and the image state, respectively, but they can have the same photon energy. Therefore, depending on where the state is located energetically, the tr-2PPE spectrum can be referenced to two different energy scales. Cuts can be taken along the time or energy axis, giving 2-D spectra of the energy distribution at a constant delay or of time delayed intensities at constant energy, respectively. The time resolved data can be analysed by fitting the decay peaks with an exponential function convolved with the pump-probe cross-correlation (XC) § 3.4.2 giving us the exponential decay lifetimes of that state. The analysis of time resolved data will be discussed in more detail in chapter 6.

Workfunction Change : The basis of the following work is the analysis of change in surface workfunction because of the accumulation of negative charge due to photoinduced reactions. The workfunction of the sample can be determined with the following formula:

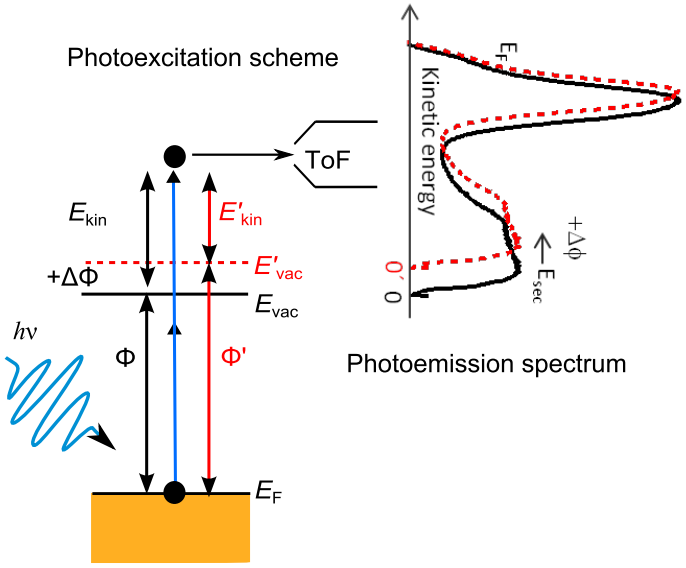

Figure 3.5: A schematic energy level diagram showing a change in workfunction from Φ to Φ' which is results in a shift of the secondary edge E_{sec} of the 2PPE spectrum and a narrowing of the 2PPE spectrum width. A larger workfunction Φ' is represented here as E'_{vac} at a higher energy and E_{sec} cut-off is seen at a larger kinetic energy.

$$\Phi = h\nu_1 + h\nu_2 - (E_{\text{F}} - E_{\text{sec}}) \tag{3.8}$$

where, $h\nu_1$ and $h\nu_2$ are the photon energies.

If the workfunction of the system increases, electrons will now need more energy to escape the surface. Hence, the lower energy electrons that could previously escape the system cannot and the low energy cut-off of the escaped electrons is higher. Since in our setup E_{F} is the reference between the sample and the spectrometer, the surface workfunction changes will be seen as a shift in E_{sec} in the 2PPE spectrum, given we do not change the bias. This is shown in an oversimplified schematic energy level diagram and the comparable 2PPE spectra in Fig. 3.5. Here an increase in workfunction by $\Delta\Phi$ is represented by a shift in E_{vac}[2] to a higher energy $E'_{\text{vac}} = E_{\text{vac}} + \Delta\Phi$. This means that the lowest energy electron ($E_{\text{kin-0}} \to 0$) that could earlier leave the surface cannot now, and the electrons that had kinetic energy $E_{\text{kin-0}} + \Delta\Phi$ just escapes. If the experimental parameters like $h\nu$ and bias remain unchanged, the measured E_{sec} shifts to higher energies. For a decrease in workfunction the opposite is true, that is E_{vac} level lowers allowing lower kinetic energy electrons to escape the sample and be detected, giving the E_{sec} signal at a lower energy. From this point on, we will use E_{F} and $E_{\text{kin(Fermi)}}$ interchangeably.

[2]Strictly speaking, E_{vac} is not changing with workfunction.

3.4 Laser System

In the following section we will briefly describe the already functioning laser setup and its incoupling to the chamber. A short report on characterisation and optimisation of the laser pulses is given later in this section. For a fundamental background in femtosecond lasers, standard laser textbooks like [133–135] should be referred to. Fundamentals of OPA/NOPA can be learned from any optics textbook on ultrafast optics and supplementary papers like [136–139] and non linear optics [140–143]. Since no major changes were done to the laser system, for a detailed description we would like to suggest earlier thesis [122]. However, we upgraded the NOPA and optimised it, and this is explained in the next section 3.5. The detailed description of the design and operation principles of the Coherent laser system can be found in [144–147].

3.4.1 Generation and Amplification of fs- Laser Pulses

In order to perform the 2PPE experiments, we used a commercially available Ti:Sa femtosecond laser system (Coherent) and the corresponding beam line is shown in Fig. 3.6. Here, the Verdi (V-18) laser (diode laser) produces continuous laser waves with central wavelength of 530 nm, and pumps the oscillator (Mira SEED) and a regenerative amplifier (RegA 9050). The Micra uses a Ti:Sa crystal as its active laser medium and produces broad band (spectrum) femtosecond pulses with central wavelength from 750-850 nm. We used 800 nm Micra output which is first stretched before entering the RegA for amplification. The RegA also uses a Ti:Sa crystal as its active laser medium and generates amplified pulses with central wavelength between 800-830 nm and a repetition rate of 250 kHz. The stretched and amplified RegA output is compressed in the time domain with a 4 grating compressor unit. We thus get **55 fs short laser pulses, with central wavelength 800 nm, pulse power of 6 μJ per pulse (beam power of 1.5 W and repetition rate of 250 kHz) and repetition rate of 250 kHz**.

To study the different electronic systems and excitation channels, we need to tune the pump and probe photon energies according to the experimental requirements. Therefore, we use a commercially available OPA (Coherent OPA 9450) and NOPA (HORIBA NOPA-Ultra). For all our measurements, we used the outputs from the OPA/NOPA which were driven by 50% of the laser power ($\approx 650 - 700$mW). The main advantages and disadvantages between the OPA and NOPA application lies in the bandwidth and time resolution of their output pulses. While the OPA produces VIS pulses from 460-760 nm, NOPA's output range is smaller, ranging from 480 - 650 nm. In addition, the spectral bandwidth of the OPA is ≈50 nm which is narrower

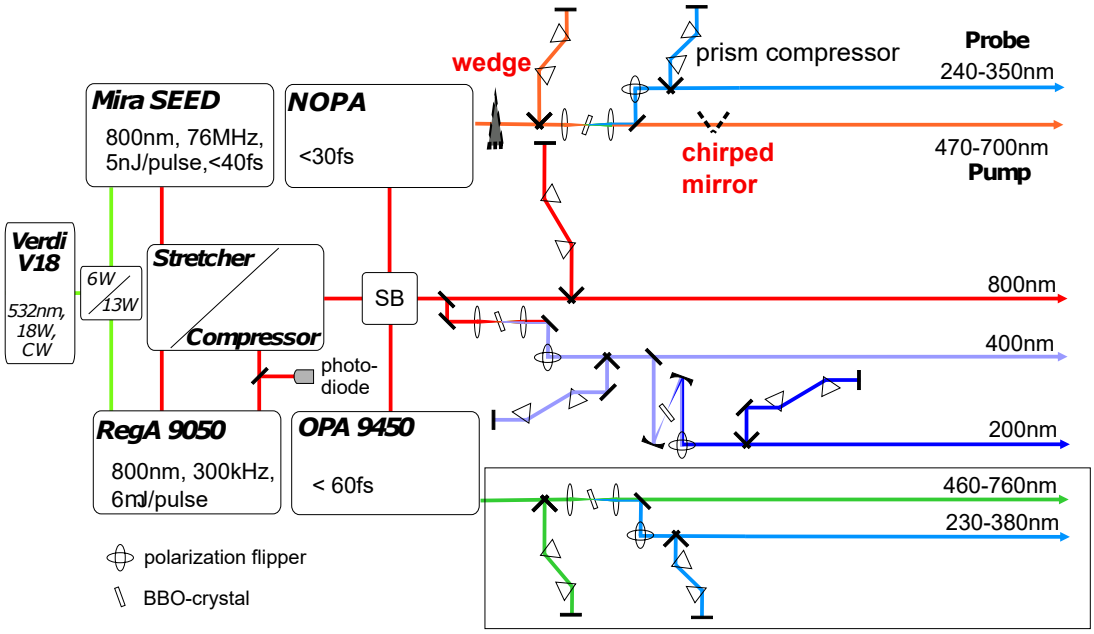

Figure 3.6: Line diagram of the optical beam path. The wedge and the chirped mirrors have been added for the current work. Additionally, SF11 prism in the VIS prism compressor was replaced by BK7 prisms. A detailed description can be found in the text. Figure taken from Laurenz Rettig's PhD thesis [119].

than the NOPA's ≈80 nm. This makes OPA more suitable for experiments with good energy resolution requirement. However, the NOPA has a better time resolution of <30 fs, while the OPA has ≈60 fs, making NOPA more suitable for experiments where time resolution is of paramount importance.

The OPA/NOPA output (VIS output) is frequency doubled (second harmonic generation, SHG) by a BBO crystal to give an UV output. To perform VIS-UV pump-probe experiments, the two are separated by a dichroic beam splitter, after which a periscope is used to convert the s polarised UV light back to p polarised. Two 4-pass prism compressors, one each for the VIS output and the UV output, are used to optimise the chirp in the OPA's/NOPA's beam paths. Both the beams are guided to the chamber with a series of mirrors and lenses and enter the chamber through a CaF_2 glass window, shown in Fig 3.7.

To perform **tr-2PPE** experiments, we need temporal and spatial overlap between the pump and probe pulses, and be able to delay them with respect to each other. A computer controlled delay stage (Pi505) is placed in the VIS beam path to delay the VIS pulse with respect to the UV pulse. To achieve spatial overlap between the

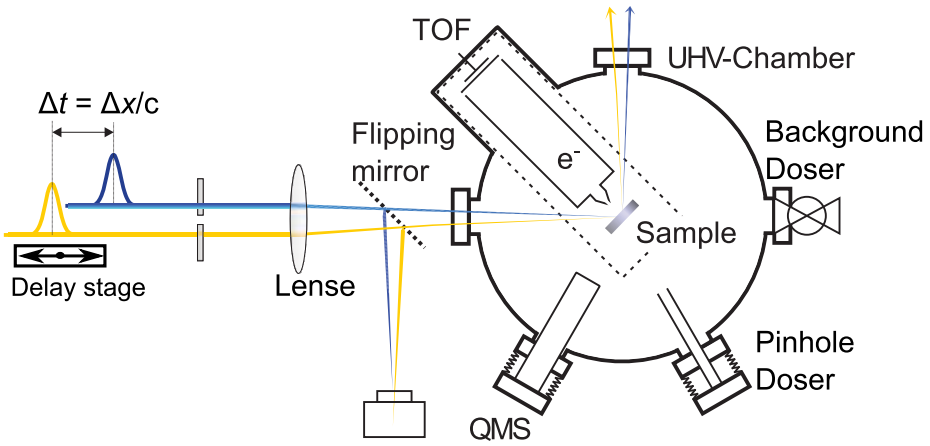

Figure 3.7: Incoupling of the laser beam into the chamber. The fundamental beam (shown in yellow) is guided onto the delay stage and can be delayed by Δt with respect to the SHG beam, by moving the delay stage by a distance Δx. A flipping mirror is used to take the beam profile on a CCD camera. Figure adapted from PhD thesis of Cornelius Gahl [82].

VIS and UV pulses, a pinhole and a flipping mirror are used. A majority of the experiments were performed in the one colour 2PPE configuration where only the UV output was used.

3.4.2 Laser Pulse characterisation

The spectrum of the laser pulse is determined by using OceanOPtics (HR4000CG-UV-NIR) spectrometer, which has a range of 200-1200 nm. To characterise the beam profile, a CCD camera is placed near the chamber such that, with the help of flipping mirrors, the beam could be imaged at the same distance as the sample in the chamber. The captured beam profile was fitted with two Gaussian fits to determine the horizontal and vertical FWHM (a and b) of the beam. The beam power P was measured near the chamber window in Fig. 3.7 with a power meter. The fluence of the beam could then be calculated with the following formula:

$$F = \frac{TP}{R} \frac{\cos\alpha \, \cos\beta}{\pi \, a \, b} \tag{3.9}$$

where, $T = 0.95$ is the transmission of the chamber window, $R = 250\,\text{kHz}$ is the repetition rate of the laser and $\alpha = 0°$ and $\beta = 45°$ are the azimuthal and polar angles of the sample with respect to the beam.

The temporal evolution of an occupied state is free of any population dynamics

as the excitation is via a virtual intermediate state. Thus, a tr-2PPE spectrum of the highest occupied state (to avoid relaxation from higher lying states) gives us the cross correlation (XC) or the convolution between the pump and probe pulse. Since the laser pulses are described by a Gaussian function, the FWHM of the XC is determined by a convolution of two Gaussian functions. To improve the time resolution of both the pulses, we try to reduce the XC width, by adjusting the prism compressors, grating compressors and the spatial overlap between the pump and probe beams.

In time resolved measurements, to accurately determine the lifetime of the intermediate state, we need to precisely determine the zero delay between the pump and probe pulses. This too is done by determining the zero delay for the occupied state, again due to its excitation via a virtual state.

3.5 NOPA Redesigning and Optimisation

In the following section, we will discuss the basic principle of the OPA/NOPA briefly. Since this is a standard technique, there is a lot of literature available on the detailed working principle and the mathematical construction for parametric amplifiers including [140–142]. Comparing to NOPA, OPA delivers longer pulse duration of about 60 fs [146], while NOPA can reach a pulse duration of less than 20 fs [143]. However, due to the short pulses, the NOPA spectral bandwidth is very large. This results in an energy resolution of larger than 100 meV compared to the OPA's 50 meV. In addition, one of the major restrictions we experienced with the NOPA is the wide chromatic dispersion in its output. This leads to different time resolutions at different spots on the sample, making the tr-studies tricky. We thus need a NOPA with better time resolution and acceptable bandwidth, which was not provided by the current NOPA configuration. By introducing glass plates into the NOPA, we reduce the bandwidth and compensate for dispersion both in the horizontal and vertical directions. The optimisation and redesigning were done by introducing wedges, chirped mirrors and glass plates in its beam path and changing the prism compressor, explained in detail in the following subsections. The NOPA finally reached a pulse duration of 40 fs and energy resolution of 60 meV.

3.5.1 Basic Principles

Non-linear optical processes become significant when strong incident electric fields interact with material. In this case, the higher order polarisation terms cannot be ignored and the induced polarisation *P(z,t)* in the material is given by:

$$P(z,t) = \epsilon_0 \mathcal{X}^{(1)} E(t) + \epsilon_0 \mathcal{X}^{(2)} E^2(t) + \epsilon_0 \mathcal{X}^{(3)} E^3(t) + ...$$

where, $\mathcal{X}^{(n)}$ is the susceptibility of the material and is defined by an n^{th} order tensor of rank $(n+1)$.

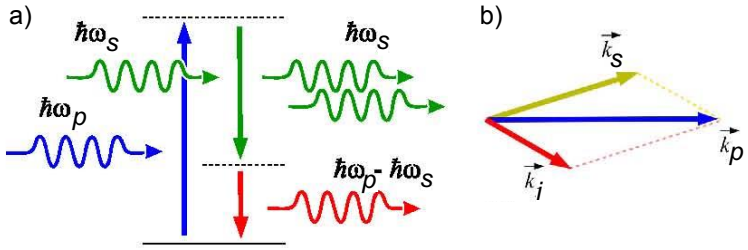

Figure 3.8: a) Energy scheme of optical parametric amplification process and b) the wave vector orientation in the non collinear geometry of the pump, signal and idler beams. Refer to text for details, adapted from Manzoni and Cerulla [139].

(Non collinear) Optical parametric conversion is a well established non-linear parametric amplification technique which enables us to tune the incident 400 nm beam to an output beam in the visible range. Here, a signal beam is amplified with the help of a pump beam (higher frequency and higher intensity) in a second-order ($\mathcal{X}^{(2)}$) non-linear crystal (BBO crystal), as shown in Fig. 3.8. The energy is transferred from the pump beam ($\hbar\omega_p, \vec{k}_p$) to the signal beam ($\hbar\omega_s, \vec{k}_s$), and a third beam called the idler beam ($\hbar\omega_i, \vec{k}_i$) is generated to fulfil the energy and momentum conservation law. Since parametric amplification takes place throughout the length of the crystal, the resulting signal and idler waves produced at different spots should interfere constructively to give an amplified signal outside the crystal. To achieve this, the phase-matching conditions must be satisfied. Thus, the two important criteria for phase-matching are given as follows:

$$\hbar\omega_p = \hbar\omega_s + \hbar\omega_i \tag{3.10}$$

$$\hbar\vec{k}_p = \hbar\vec{k}_s + \hbar\vec{k}_i \tag{3.11}$$

where, $\vec{k}$ is the wave vector.

In addition to the phase matching conditions, there should be minimum group velocity mismatch (GVM) in order to have a longer non-linear interaction between the pulses. The spectral gain bandwidth $\Delta\nu$ inversely depends upon the GVM and is given for the collinear geometry in the following equation [139]:

$$\Delta\nu = \frac{2\sqrt{\ln 2}}{\pi}\sqrt{\frac{\Gamma}{L}}\delta_{12}$$
$$\delta_{12} = \frac{1}{\nu_{g1}} - \frac{1}{\nu_{g2}}$$

where $\nu_g = \partial\omega/\partial k$ is the group velocity and the δ_{12} is the GVM between the signal (ν_{g1}) and the idler (ν_{g2}), Γ is a coupling constant and L is the crystal length. For the non-collinear geometry also, the gain bandwidth is maximum for minimum GVM [139, 140].

Due to the symmetry between the idler and the signal, both act as a seed for each other resulting in an exponential amplification of the signal [139]. Since the idler's group velocity is always a bit faster than the signal's, the new idler seeded signal photons are added at the leading edge of the signal beam and the signal seeded idler photons are added to the trailing edge of the idler beam. In this way, an additional chirp is added to the amplified signal beam. In the non-collinear alignment, due to different distances travelled by the two beams, the signal photons produced from the idler are at the same horizontal position as the signal amplification. This prevents the extra chirp in the signal beam and is the reason for the sub-30 fs pulse duration. Another effect of the reduced GVM is that the signal and the idler have a broad phase matching allowing for the parametric effect over relatively longer distances. This results in a wide spectral range to be amplified [137, 139, 143] giving a broad bandwidth amplified signal beam. With suitable prism compressors or chirped mirrors, transform-limited sub-20 fs pulses can be obtained.

OPA/NOPA Architecture: OPA and NOPA work on the same principle, the only difference is that the signal and pump beam are collinear in the OPA, but are at an angle α to each other in the NOPA. A part of the incident 800 nm beam is frequency doubled to 400 nm [3] and serves as the pump beam. The remaining beam is converted into white light continuum after passing through a sapphire plate, and is used as the weak incident broadband signal beam. The two beams are spatially and temporary overlapped in the OPA crystal (BBO). Due to the wide temporal chirp in the white light continuum, by changing the delay between the white light and the 400 nm, a different visible wavelength is amplified. In our NOPA setup, the signal is delayed with respect to the pump, and in the OPA the pump is delayed with respect to the signal. Also, we use the NOPA in a single pass configuration (that is,

[3] power = $\approx$ 180 mW with incident power at the NOPA = 600 mW

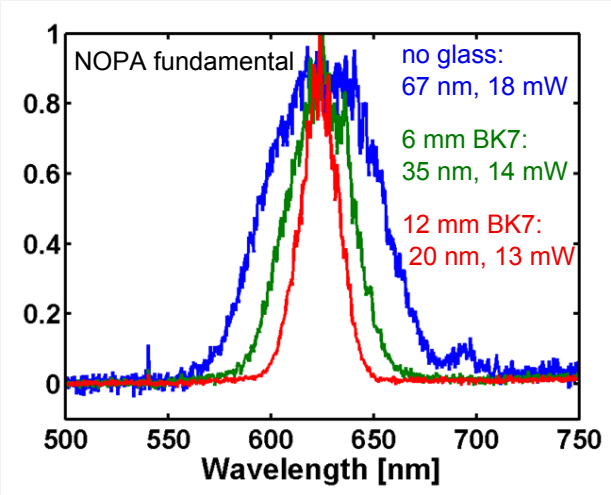

Figure 3.9: Spectra of 600 nm NOPA fundamental output measured with a spectrometer. Different glass thicknesses have been inserted in the signal beam path, before the BBO crystal.

the signal and pump pass through the BBO crystal once), while the OPA has two passes. The third and the most important difference between the two configurations is that the pump beam is at an angle with respect to the signal beam.

3.5.2 Optimising NOPA's broad Bandwidth

As explained previously, the NOPA has a very broad bandwidth. For experiments where energy resolution is of little importance, this does not pose a problem. But in many cases, there are unoccupied states lying very close to each other (for example image states) whose population dynamics are of interest. In this case, one needs a good energy and time resolution.

On adding glass in the beam path, the pulses are stretched in the time domain. This reduces the spectral bandwidth for which the temporal overlap holds and the interaction of the three beams after the white light generation is limited to a narrower bandwidth [148]. Subsequently, the phase-matching condition is valid for a longer time in the BBO crystal giving a higher signal power, thus partially compensating for the loss in total signal output power due to a narrower broadband.

We thus achieved a better energy resolution by using 8 mm (4x2 mm) BK7 glass plates in the white light continuum beam path. This is shown in Fig. 3.9 for NOPA central wavelength of 625 nm, where the normalised spectral intensity as a function of wavelength is shown for different amounts of glass. From the figure, a clear narrowing of the bandwidth can be seen on adding glass. With no glass, the FWHM is 67 nm

which decreases by 50% with 6 mm of glass, but the power also decreases 30%. On adding another 6 mm of glass, the FWHM decreases to 20 nm (another 20%) and the power drops further by 5%. The FROG measurements in Fig. 3.10 compares the two situations, before adding glass and after for the VIS NOPA output. We see that the autocorrelation (determined from the y-axis) increases from 55 fs to 110 fs on addition of glass, however, the beam is more symmetric implying that the bandwidth dispersion is less. Though we lose ≈35% power and ≈50% time resolution, we do gain in an improved spectral resolution by 70%. This makes it possible to perform energy resolved measurements. We don't get any side wings in the UV spectrum (NOPA SHG) and get a spectral resolution of 50 nm.

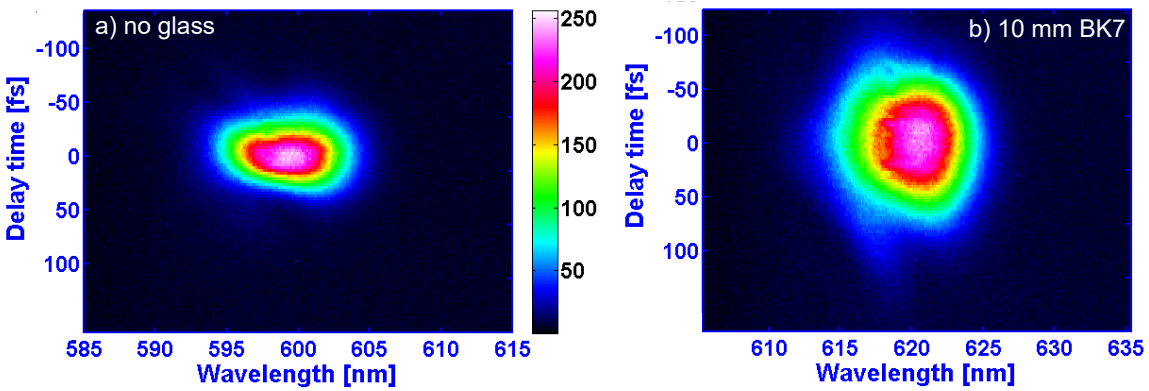

Figure 3.10: FROG image of 600 nm NOPA output with a) no additional glass and b) with 10 mm of BK 7 glass in the signal beam path.

3.5.3 NOPA Time Resolution Optimisation

We reduce the amount of glass to 6 mm since a bandwidth of 35 nm FWHM is sufficient for our experiments. With the reduced the NOPA SHG (UV) bandwidth, we have a moderate decrease of output power, however the drawback here is the long pulse duration of >100 fs. Hence, the NOPA should be further optimised. The main parameter for the long pulses is the lateral chromatic dispersion (CD). Due to NOPA's non-collinear geometry, the amplified signal pulses have a large lateral dispersion in the vertical axis. This results in a different time resolution at different parts of the beam. To correct for the dispersion, we first measured it by focussing the NOPA VIS beam on a spectrometer with a local focal length lens to a 5μm pinhole with the xy-translational stages. The positions of the stages were noted at the maximum intensity of the NOPA VIS spectrum. The stages were then moved

to the FWHM intensities of the maximum intensity and their position and central wavelengths were noted. We were thus able to determine the spatial extent of the CD in both the x and y directions. The same procedure was performed at the horizontal focus (focussed in the horizontal plane) and the vertical focus (focussed vertically) of the beam due to astigmatism, as shown in Fig. 3.11. We observe that the horizontal CD in and out of horizontal focus is almost negligible at $2.7\text{x}10^{-4}$°/nm. The vertical CD out of vertical focusing also show almost no dispersion. However, at vertical focussing, the dispersion is twice of this, of the order of $5.4\text{x}10^{-4}$°/nm. This suggests that the beam has less dispersion horizontally than vertically. Additionally, the CD is more pronounced at the focus.

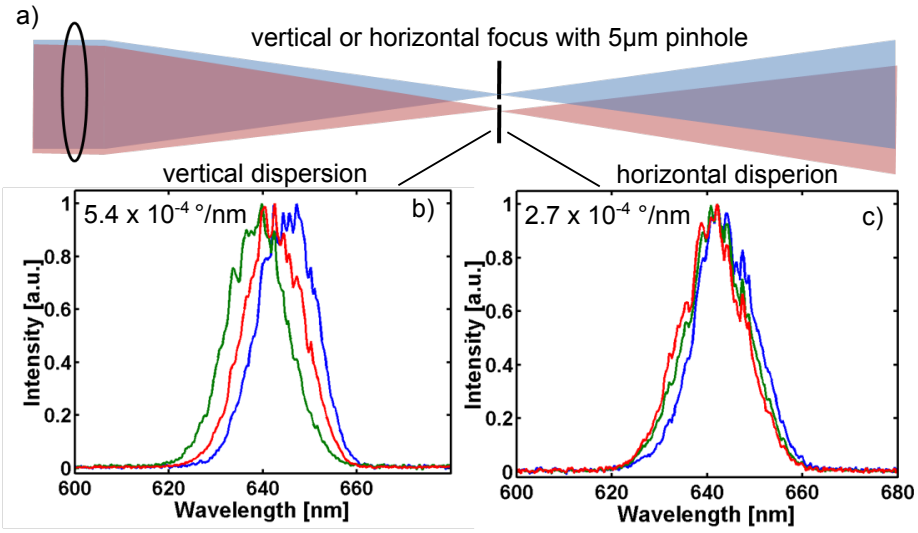

Figure 3.11: a) Measuring the chromatic dispersion of a focused beam with the help of a spectrometer, pinhole and a 3-directions delay stage at b) horizontal focus (dispersion in vertical axis) and at c) vertical focussing (dispersion in horizontal axis). Figure courtesy Ping Zhou.

Another test for the dispersion was by the orientation of the SHG crystal. The effect of lateral dispersion can sometimes be useful for the SHG generation, where the phase-matching condition needs the different incident angles for the different wavelengths. If the angular dispersion has the opposite sign as the phase-matching condition, all the wavelengths will be phase-matched and you will get more SHG output. For example in Fig. 3.12a) and b) we show the different crystal tilts with respect to the wavefront of the beam, which is tilted downwards here. By simple geometry, if the crystal face is parallel to the pulse wavefront (Fig. 3.12b)), the phase matching

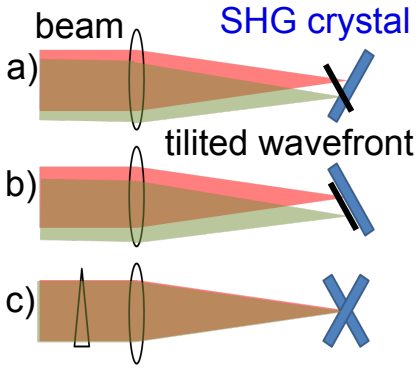

Figure 3.12: When the beam has lateral dispersion, the different crystal orientations with the crystal plane; a) 90° to the wavefront and b) parallel to the wavefront have different SHG output. c) On inserting a 5° wedge, the crystal orientation has no effect on SHG generation since the wavefront is no longer tilted.

condition will hold for a longer distance[4] in the crystal giving a larger SHG output. On the other hand, if the crystal face is away from the pulse wavefront (Fig. 3.12a)), the beams will soon walk out of phase matching giving destructive interference and a reduced SHG output. This was verified by comparing the maximum spectral intensities of the UV beam, which were 1800 units for case a) and 2800 units for case b), for the same FWHM of the beam.

Optimising Vertical Lateral Dispersion Another method to observe the lateral dispersion is by using single shot FROG [149, 150] measurements. In the single shot geometry, two beams cross each other and the time information is determined by the beam profile [151]. The lateral dispersion would give a tilting of the pulse front in the time domain [152] as different points of the beam will have different arrival times. We compensated this by inserting a BK7 5° wedge prism before compressing the NOPA fundamental output. For that part of the beam travelling through the thicker part of the wedge, the pulses will have a larger dispersion (positive chirp) compared to those travelling through the thinner part. Due to this differential dispersion imparted to the beam, all the spectral components now arrive at the same time and same point, giving a less dispersed beam at the sample (ideally).

After introducing the wedge, we observed no change in intensity on rotating the crystal by 180° (Fig. 3.12c)), suggesting less CD in the focussed beam than before. This also improves the pulse duration, which for 600 nm NOPA fundamental improves from 92 fs to 85 fs. This can be seen from the FROG trace in Fig. 3.13 where the beam is more symmetric and less tilted (indicating chirp) on using the wedge.

[4]since the faster travelling blue and the slower travelling red will reach the crystal at the same time

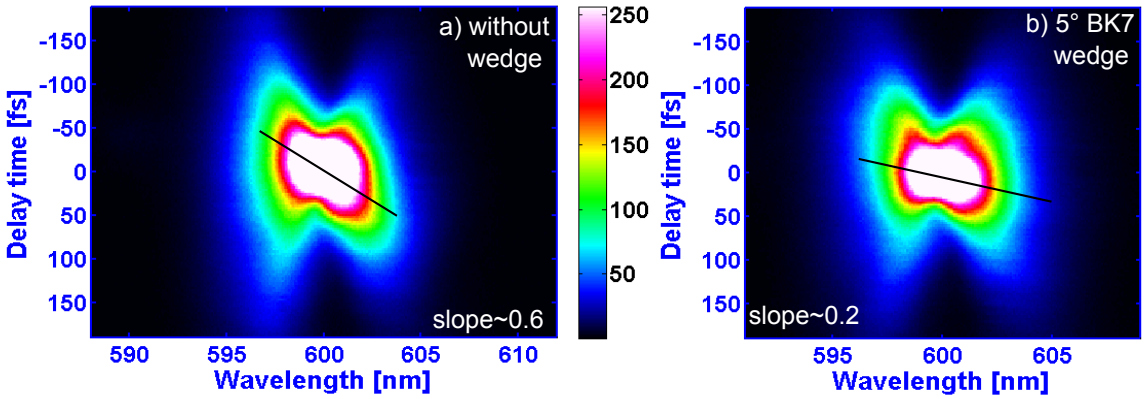

Figure 3.13: FROG images of NOPA fundamental at 600 nm a) without wedge and b) with 5° wedge. The tilt of the beam clearly decreases on inserting the wedge.

Optimising Horizontal Lateral Dispersion The dispersion in the horizontal axis can be compensated by using prism compressors which introduce a negative chirp in the beam [153]. By correcting the lateral dispersion in both the passes of the prism, we expect more or less transform limited pulses after the compressor. This was seen for 640 nm VIS NOPA wavelength using the SF11 prism compressor which was able to compress the pulse effectively upto 90 fs (more BK7 glass in the NOPA). However, on using less glass in the NOPA beam path (640 nm), the NOPA VIS was more dispersive and could not be properly compressed. We solved this problem by using a different prism material, because prisms can compensate for the high order group velocity dispersion and the extent of the compensation depends on the material of the prism. SF11 and SF10 have a large group velocity dispersion and are hence not able to compensate for the dispersion in the beam. BK7, which has the least group velocity dispersion, could be used to optimise the pulse duration. In Fig. 3.14, we show the FROG image for the BK7 prism compressors. We can clearly see that the BK7 prism compresses the beam more effectively and more uniformly.

Compression of the VIS pulse after SHG generation An additional problem was that to optimise the SHG process, we observed that the VIS pulses at the BBO crystal needed to be longer. Further, the CaF_2 window at the chamber, through which the beams have to pass before hitting the sample, add additional chirp. While the SHG pulse duration can be optimised with the help of prism compressors, the VIS pulse is uncompensated. As a result, we needed to make a trade-off between the SHG generation (UV power) and VIS pulse duration. This is a problem primarily for tr-2PPE measurements, where we need the shortest pulse duration and reasonable

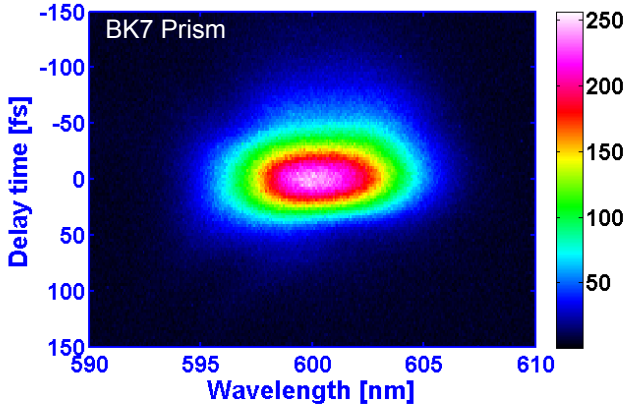

Figure 3.14: FROG image of NOPA fundamental at 600 nm with BK7 fundamental compressor.

UV power. One could use an additional prism compressor in the VIS beam path after the SHG generation or chirped mirrors. We chose to use the latter, as a 500 mm long prism compressor was not practical.

We measured the optimum prism position for the SHG generation (maximum UV only photoemission counts) and for the shortest pulse duration for the fundamental (VIS) NOPA. For the optimum VIS pulse duration, the second prism (P2) is at 24.8 mm and for the optimum SHG generation, P2 is at 23.15 mm, giving a difference of 3.8 mm of prism between the two processes[5]. This means that the fundamental pulses need a negative chirp after the SHG process. We therefore introduced two negatively chirped mirrors and reflected the fundamental beam multiple times off them. Due to its negative chirp, we gain a time resolution of 5 fs. This can be increased by increasing the number of reflections of the chirped mirrors, by either replacing all the silver mirrors with chirped mirrors after the SHG crystal or increasing the reflections between a pair of chirped mirrors. However, working with chirped mirrors is not straightforward since the mirrors have a wavelength dependent reflection profile, which restricts the flexibility of the NOPA wavelength regime. One could however use grating compressors or prism compressors at the risk of losing beam power.

Conclusion : By inserting a wedge and glass plates and by changing the prisms and some of the mirrors by chirped mirrors, we were able to optimise the NOPA in both the time and energy domain. By adjusting the amount of glass in the beam path and changing the prism compressor (to accommodate the new pulse duration), one can switch back and forth from NOPA-OPA output configurations.

[5]Additionally, we found that 6 mm of BK7 glass plate corresponds to 0.36 mm of SF11 prism.

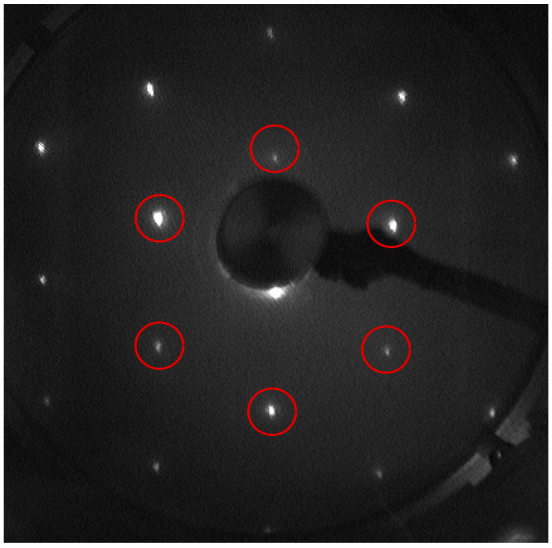

Figure 3.15: A LEED image of clean Cu(111) taken with 236 eV ionization energy and cooled to 100 K. The six spots marked by circles correspond to the first Brillouin zone.

3.6 Sample Preparation and Characterisation

Before we investigate the electronic structure and dynamics of the molecular adsorbates on the Cu(111) single crystal, the metal substrate needs to be cleaned and the molecular layers adsorbed on it in a UHV chamber. In the following subsections, we will describe the sample preparation techniques and their characterisation. The molecular films were calibrated and characterised by thermal desorption spectroscopy which is explained in detail here.

3.6.1 Cu(111) Preparation

We use a polished, 0.5 cm thick and 1 cm diameter round Cu(111) crystal as our metal substrate and it is cleaned by standard sputter-anneal cycles. While sputtering bombards and scatters away impurities at the surface, annealing helps to repair the consequently damaged surface. Each sputter cycle is performed with Ar^+ ions for 10 min at 1 μA sputter current and 1.2 kV energy. Succeeding annealing is performed for 25-30 min at 650-750 K. Annealing for too long or at very high temperatures mobilises impurities from the Cu bulk and contaminates the surface, hence a trade-off needs to be made between the two control parameters. The surface quality can be checked by measuring the workfunction with 2PPE spectroscopy, which for clean

Cu(111) surface is found to be 4.9 ± 0.3 eV [58,60] and by aiming for a high intensity and narrow linewidth of the surface state peak. LEED (low energy electron diffraction) can also be used to determine the surface quality and a LEED image of clean Cu(111) surface is shown in Fig. 3.15. The 2PPE spectrum of clean Cu(111) is not shown here since it is discussed in § 4.1. The LEED image shows a well resolved diffraction pattern with six well resolved and sharp diffraction points (indicated with red circles), indicating a well prepared surface. The six points correspond to the first Brillouin zone and the six-fold symmetry of the hexagonally closed packed structure of the Cu(111) lattice. The Cu(111) surface is prepared every time before adsorbing fresh molecules.

3.6.2 Preparartion of the Adsorbate layers, Thermal Desorption Spectroscopy (TDS)

The adsorbed molecules, halobenzenes (BzX, X = F, Cl and Br) and D_2O, are cleaned by freeze-pump-thaw cycles. The molecules are placed in individual test tubes which are frozen by dipping them in a Dewar of liquid N_2 till the molecules freeze. A pump valve is opened to allow the desorbing gaseous impurities to be pumped away by the cube pump. Once the molecules begin to thaw, the pump valve is closed and the molecules are allowed to melt completely. They are then frozen again and the freeze-pump-thaw cycle is repeated a number of times till there is no significant pressure rise during the pump-thaw part of the cycle. The molecular layer is prepared by simply adsorbing the clean molecules on the freshly cleaned Cu(111) substrate at 95 ± 5 K through a 50 μm pinhole doser. The coverage depends on the dosing time and the pressure in the gas reservoir. It is calibrated by performing a thermal desorption spectroscopy (TDS) series discussed next. Julia Stähler discusses the different ice structures and their annealing condition in her PhD thesis [70]. On the basis of her work, we annealed the amorphous ice surface at 148 K for 20 min which give us the crystallite ice structure needed in § 4.5.

Thermal Desorption Spectroscopy : In TDS, a distribution of the intensity of thermally desorbed molecules as a function of sample temperature is obtained by heating the sample at a constant heating rate (1 K/s) and detecting the desorbed species with a quadrupole mass spectrometer (QMS). From the desorption curve, one can gleam relevant adsorption information such as adsorption/desorption activation energy and coverage. A short background on TDS is given in § 2.2.

Before performing TDS, the characteristic charge-by-mass ratio **m/z** of the adsorbate needs to be determined. Accordingly, the cracking pattern of the halobenzenes

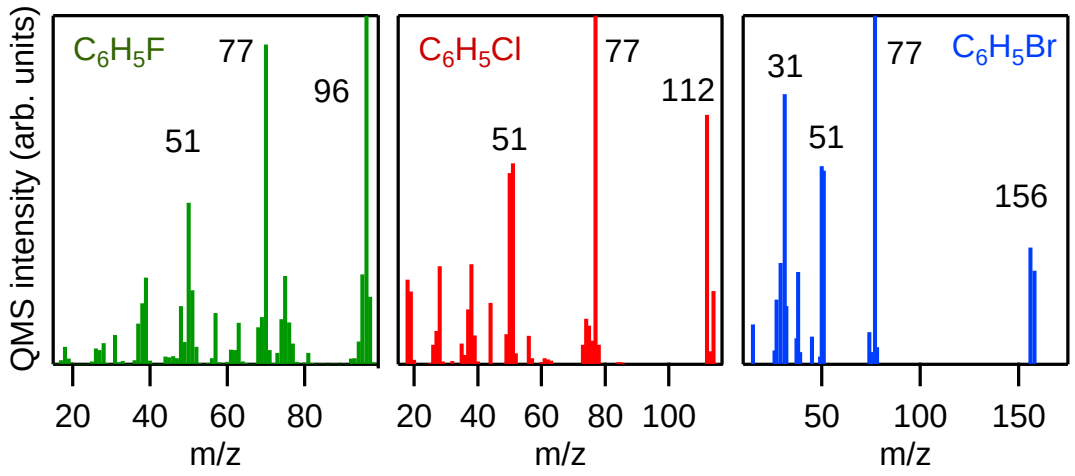

Figure 3.16: Cracking pattern for C_6H_5F (in green), C_6H_5Cl (in red) and C_6H_5Br (in blue) with characteristic peaks at m/z = 96, 112 and 156 respectively. Due to a significantly lower intensity of 156 in C_6H_5Br, we used 77 as the identifying mass in the TDS measurements.

were recorded at a background pressure of $\sim 10^{-8}$ mbar, shown in Fig. 3.16. Here the QMS intensities are plotted as a function of m/z ratios. We see that the peak QMS intensities at 96, 112 and 156 for BzF, BzCl and BzBr, respectively, which corresponds to their molecular masses. Mass 77 and 51 correspond to $C_6H_5^+$ and $C_4H_3^+$ ions, respectively and are fragments that are seen for all the halobenzenes. For BzBr, the intensity at 77 is at least twice that at 156 and is therefore used for the TDS series. For BzCl and BzF, signal at 112 and 96 are strong enough to be used for TDS.

In Fig. 3.17, we show the TDS series for BzX/Cu(111) where the corresponding m/z intensity is plotted as a function of temperature T. For all the halobenzenes, we see two peaks, a high temperature peak (HT) at ∼200 K and a low temperature peak (LT) at ∼150 K. In addition to the HT and LT peaks, we also see a peak around 170 K for BzF and double peaks in multilayer coverages for BzCl and BzBr. These desorption spectra, with the three peaks, are very similar to that of the well studied benzene on Cu(111) [3, 29, 31, 32] and BzCl adsorbed on Cu(111) [28] and Ag(111) [28,33,103] which are discussed in § 2.3.6. On the basis of these studies, we analyse our TDS spectra and characterise the peaks. The onset of HT peak shifts to lower temperatures with increasing coverage, while the peak position remains the same, thus characterising first order kinetics and is assigned to a monolayer coverage. We also observe that in the submonolayer coverages, as the coverage

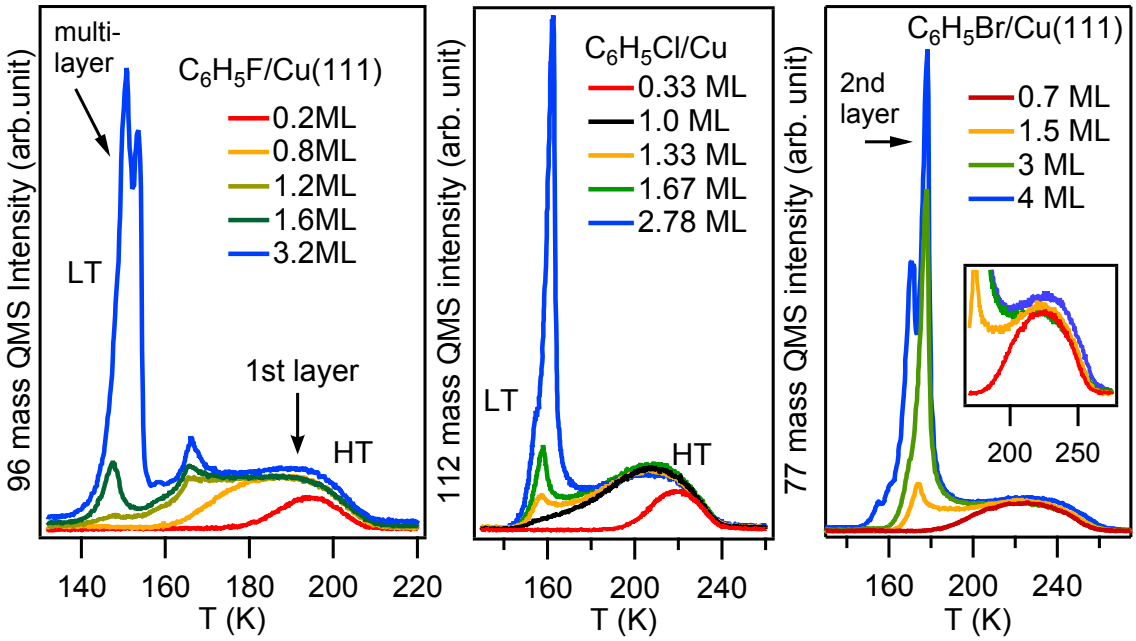

Figure 3.17: Thermal desorption spectroscopy of C_6H_5F, C_6H_5Cl and C_6H_5Br adsorbed on Cu(111). We see a high temperature peak (HT) and a low temperature peak (LT) for all the three halobenzenes. ML stand for a monolayer of the coverage defined as flat lying closed packing layer. Details in text.

increases, the peak gets broader towards lower temperatures. This indicates strong molecule-molecule interactions within the adsorbate layer [29]. The LT peak shows zero order kinetics (overlapping leading edge and does not saturate) and can be assigned to desorption from multilayer coverages.

From [117] we expect the BzX molecules to physisorb via their π electrons with their benzene ring parallel to the metal substrate, which tilts up near completion of a monolayer (ML), as discussed in § 2.3.6. The additional peaks observed by us are thus explained by a different adsorption geometry and the splitting of the LT peak at higher coverages for the BzXs[6] is argued in comparison to benzene adsorption on Cu(111) [3, 29]. Benzene adsorbs in bilayers with the first layer flat and the second standing up which is seen as the splitting of the LT peak towards lower temperature, where the old peak corresponds to the second layer and the new peak to the multilayers > 3. Thus the splitting of the multilayer observed by us hints towards bilayer adsorption geometry, where the first two layers have distinct binding

[6]Since the splitting occurs between 3-4 ML, we see only an onset of this for BzCl because the the highest coverage measured is 2.8 ML.

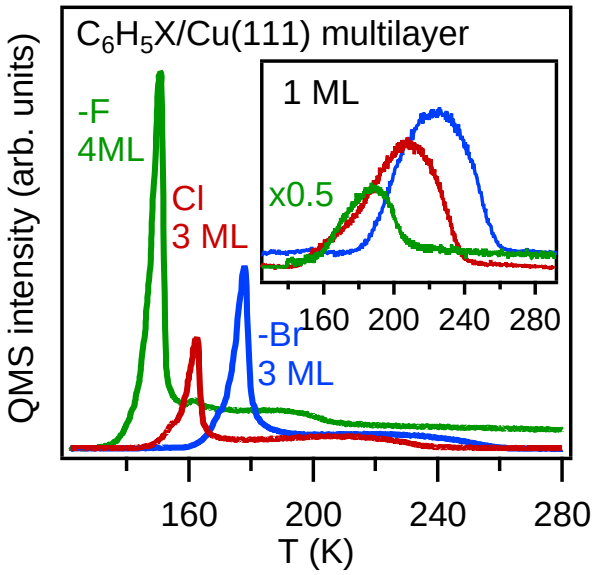

Figure 3.18: Comparing the TDS spectra of the different halobenzenes in a multilayer configuration and the monolayer configuration, the latter is in inset.

energies. According to this, the 3 ML in the TDS spectrum of BzBr and the 2.78 ML peak in BzCl in Fig. 3.17, should actually correspond to 2 ML. This discrepancy arises from our definition of a monolayer. We define a 1 ML coverage as the one just before the 160 K peak appears, that is, a closed flat lying coverage and the other layers are extrapolated linearly from this. However, the second layer which consists of tilted or standing molecules have a larger molecular density than the first layer. This implies that the actual 2 ML coverage is more than the calibrated 2 ML coverage and explains for the mismatch. Since we work mostly with monolayer and submonolayer coverages, we can use this calibration without any issues.

In Fig. 3.18, we compare the TDS spectra of the different BzX's for multilayer and monolayer (inset) coverages. We see that from BzF to BzBr the onset of desorption starts at a progressively higher temperature. The peak desorption temperature (within ± 3 K error margin) for the 1st ML increases from 191 K, 214 K and 222 K and for the multilayer peak from 144 K, 160 K and 174 K for BzF, BzCl and BzBr, respectively. This implies that the BzX binding to the Cu(111) substrate increases in strength from BzF to BzBr. Since the halobenzenes bind through the benzene ring π electrons and the halogen, the partial π electron charge over the benzene ring increases from BzF to BzBr, i.e. -0.16 e^-, -0.27 e^- and -0.26 e^- [104], respectively. Thus, the increasing binding strength from BzF to BzBr can be explained by

a stronger π electron polarisation towards the metal surface for BzBr than BzF. We can summarise from the TDS data that the binding of BzX is halogen dependent and the binding strength increases down the periodic table, i.e., from BzF to BzCl to BzBr.

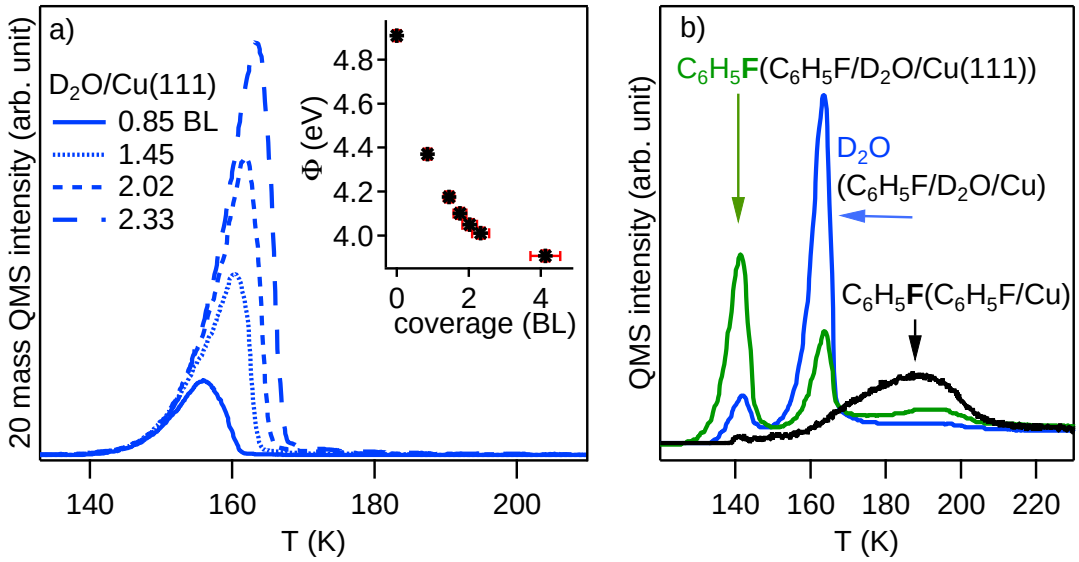

Figure 3.19: a) TDS series for D_2O/Cu and the corresponding workfunction change with coverage (inset). b) TDS spectra of C_6H_5F fromC_6H_5F/Cu(111) and C_6H_5F/D_2O/Cu(111) systems and of D_2O from $C_6H_5FD_2O$/Cu(111) system to show how both water and C_6H_5F desorption change when they are coadsorbed. The amount (dosing time and pressure) of C_6H_5F dosed is the same with and without coadsorbed water.

The TDS series of amorphous D_2O/Cu(111) at mass 20 is shown in Fig. 3.19a) where the intensity of the desorbed D_2O molecules are shown as a function of desorption temperature. Like the LT peak in BzX/Cu(111), water desorption also shows zero order kinetics. This makes it difficult to determine the coverage. However, the coverage of D_2O/Cu(111) has already been calibrated as a function of Φ by using a Ru(001) substrate in the past by Cornelius Gahl in his Diploma and PhD work [82, 154]. Since the workfunction decreases with increasing coverage and stabilises at 3.9 eV for 3 BL (bilayer), we calibrated our D_2O/Cu(111) coverage by comparing our coverage dependent Φ measurements (inset of Fig. 3.19) with the past D_2O/Ru(001) data. For 4 BL of amorphous D_2O/Cu(111), we dose water for 60 s at a water pressure of 0.1 mbar.

The TDS spectra of the different halobenzenes on ice are similar to each other and therefore we discuss only the C_6H_5F/D_2O/Cu(111) case in detail here. Fig. 3.19b)

shows the TDS spectrum of 1 ML C_6H_5F/Cu(111) and of C_6H_5F/D_2O/Cu(111) with 4 BL of D_2O. In both the cases (with and without coadsorbed water), the same amount of BzF is dosed, which corresponds to 1 ML on bare metal. The main differences compared to the desorption from bare Cu(111) are:

1) BzF desorbs at a much lower temperature from the ice surface than the metal surface, suggesting a weaker binding on the ice surface. Some of the possible reasons for a weaker interaction are: different interaction mechanism compared to on the metal substrate, screening of the molecules from the metal substrate by the ice layer, and stacked island type growth of molecules on the amorphous ice.

2) Additionally, a small D_2O signal, less than 15% of the main D_2O signal, is seen below its desorption temperature at 135 K along with the BzF signal. This leads us to believe that some D_2O molecules desorb with the above lying BzF molecules, possibly due to partial solvation of the smaller F halogen in ice. This was also suggested in [27], where BzCl and water molecules form clusters on the tungsten substrate.

3) The HT peak is seen at the same temperature on ice and on metal. This could correspond to the desorption of BzX from the metal surface, which is possible due to the thermally activated mix of D_2O and BzX resulting in the adsorption of some BzX on the metal [27].

4) Most BzX molecules desorb at 140 K and 160 K, where the later is the water desorption temperature from Cu(111). This suggests that the above lying BzX molecules are removed with the underlying water coverage, before they can be thermally desorbed. Due to a significant loss of molecules in this way, the HT peak has a smaller intensity on ice as compared to bare metal. Accordingly the **BzX coverage is calibrated on bare Cu(111) and is assumed to be the same on ice**.

We would like to point out that the adsorption of BzX on the amorphous ice surface is not expected to form closed layers, since the ice surface itself is not an equipotential surface due to its amorphous solid state.

In Fig. 3.20, we show the TDS spectra for 1 ML of BzX on D_2O. We see that most of the BzCl and BzBr molecules desorb with water, like BzF, but unlike BzF, we do not see a pronounced peak at 140 K before the water desorption starts. This can be explained on the basis of the size of the halogen atom and the effective charge on it. Since F is smaller than Cl and Br is the largest amongst the three, F can more readily

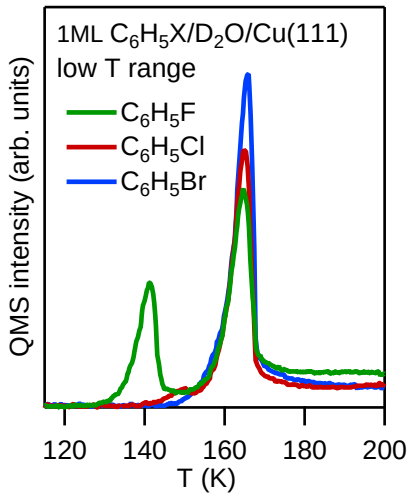

Figure 3.20: TDS spectra of 1 ML of the different halobenzenes adsorbed on water. Here only the low temperature part of the spectrum is shown.

(partially) solvate in the amorphous ice compared to the other two. Additionally, due to a larger electronegativity of the F atom, the partial charge on the F atom (= -0.17 e^-) is more compared to that on Cl (= -0.08e^-) and Br (= -0.05e^-) [104]. As a result, F atom can polarise the surrounding water molecules more efficiently than Cl and Br, further enabling its solvation. Thus, the efficiency of solvation[7] is expected to decrease from F→Cl→Br, with F solvation much more efficient than Cl and Br (reflected by their partial charge). Therefore, since the solvation of Cl and Br in ice is not as favourable as for F, we do not see a pronounced water signal from the 'solvation shell water molecules' for them as we do for F. However, Cl and Br can also bind stronger than F and thus desorb with water.

[7]Polarising of the surrounding water molecule depends on the charge on the halobenzenes and not its polarization. The polarization gives the extent to which the BzX molecule will get polarized and will be discussed in §4.1

Chapter 4

Photoinduced Electron Transfer Dynamics in $C_6H_5X/D_2O/Cu(111)$

Dissociative electron attachment (DEA) has been found to be enhanced on polar surfaces. In the past, it has been suggested that the enhancement is because of pre-solvated electrons arising due to polarisation of the solvent by the electron, as discussed in § 2.3.5. In order to verify this model, we performed two-photon photoemission (2PPE) experiments which are discussed in this chapter. Accordingly, we observe the rate of change in surface workfunction due to electron transfer from the D_2O/Cu(111) system to the halobenzene (BzX) C_6H_5X layer and determine the corresponding reaction kinetics. We thus probe the ionised molecular state indirectly and study the reaction efficiency. We show that it is the pre-existing electron trapping sites in ice that play a major role in catalysing DEA. With the collaborative contributions of theoretical calculations performed by Michel Bockstedte [1] and Philipp Auburger [2] proposing a new mechanism, STM images taken by Karina Morgenstern [3] and Cord Betram [4] giving a time resolved real space image of the process, and with our 2PPE measurements giving the reaction rates, we get a comprehensive picture of the charge transfer dynamics at polar surfaces in the presence of halogenated hydrocarbons.

The $C_6H_5X/D_2O/Cu(111)$ system was prepared by first adsorbing 4.0±0.5 BL of D_2O (amorphous ice) and then 1.0 ± 0.3 ML of C_6H_5X at 95±5 K. We performed monochromatic 2PPE spectroscopy with a photon energy of 3.79 eV (unless other-

[1] University of Salzburg, earlier Friedrich-Alexander University (FAU) Erlangen-Nuremberg
[2] Friedrich-Alexander University (FAU) Erlangen-Nuremberg
[3] Ruhr University of Bochum
[4] Ruhr University of Bochum

wise stated) and recorded the change in surface workfunction, due to photoelectron induced ionization/dissociation of BzX, as a function of time. The rate of workfunction change directly reflects the efficiency of the electron transfer process.

In order to understand the role of the trapping sites, we studied the dependence of the reaction dynamics on the incident photon flux, photon energy and BzX coverage, which are also discussed in detail below. We propose a simple chemical reaction to describe the EA reaction and verify it by simulating the observed workfunction change with photoexposure time.

We can consider the reaction to proceed under continuous photo-illumination despite using a pulsed laser source. This is because the photoexcitation is an instantaneous process and occurs only in the presence of the light, while the back relaxation processes occur over minute time-scales. A detailed description can be found in § 4.2.2.

4.1 2PPE Spectral Changes upon Adsorption of C_6H_5X on D_2O/Cu(111)

Adsorption of molecules on a surface changes the energetics of the system, for example its workfunction, molecular energy levels and the image and surface states of the substrate. Therefore, before looking into the dynamic changes of our system due to photoexcitation, we first study the changes in the 2PPE spectrum on adsorption of water and the halobenzenes on bare Cu(111). The main 2PPE spectral features and their corresponding changes on adsorption are discussed below.

The one colour ($h\nu = 3.78\,\text{eV}$) 2PPE spectra of clean Cu(111), ice- D_2O/Cu(111) and C_6H_5X/D_2O/Cu(111) [5] are shown in Fig. 4.1. The high energy cut-off in the 2PPE spectra corresponds to the Fermi edge E_F and is seen at $3.78 \pm 0.01\,\text{eV}$ for all the molecular systems. For clean Cu(111) surface, we see a peak at $E - E_F = 3.36 \pm 0.01\,\text{eV}$ which corresponds to the occupied Shockley surface state with a binding energy of $\approx$0.42 eV. Its linewidth of $150 \pm 10\,\text{meV}$ implies a uniform and adsorbate free surface [61]. The peaks at lower energies at $1.52 \pm 0.01\,\text{eV}$ and $1.98 \pm 0.01\,\text{eV}$ corresponds to excitations from the bulk valence d-band with binding energy $\approx$2.26 eV and $\approx$1.79 eV, respectively. Since it is a bulk feature, its spectroscopic signal can be seen even after adsorption of water and BzX. The photon energy here is too small to excite into Cu(111)'s image potential state. On adsorption of 4 BL of D_2O on clean

[5] The spectra of C_6H_5X/D_2O/Cu(111) appear to have a lower signal to noise ratio since they were recorded for only 15 s. This is because their workfunction increases with photoexposure, which is discussed in section § 4.2 onwards.

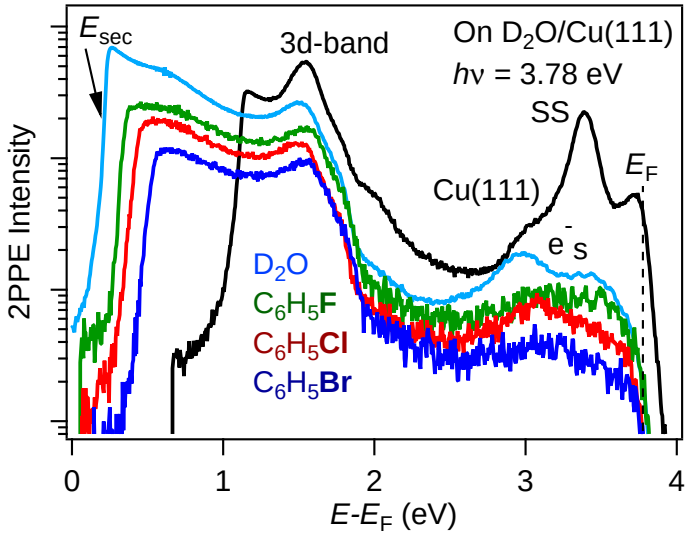

Figure 4.1: 2PPE spectra of Cu(111), 4 BL D_2O/Cu(111) and 1 ML C_6H_5X/D_2O/Cu(111) shown on a log-scale. Cu(111) is shown by the black line, D_2O/Cu(111) by the blue line, C_6H_5F by the green line, C_6H_5Cl by the red line and C_6H_5Br by the dark blue line. E_F and E_{sec} correspond to the Fermi edge and the secondary edge, respectively. SS, e_s^- and d-band refer to surface state, solvated electron and copper d-band spectral features, respectively.

Cu(111), the low energy cut-off E_{sec} shifts to lower energies and hence, Φ (from Eq. 3.8) decreases from 4.9 eV to 3.9 eV. Upon subsequent adsorption of BzX, Φ now increases for all the three Xs. In the 2PPE spectrum of amorphous ice, we see a peak at 2.97 ± 0.05 eV which corresponds to the solvated electron e_s^- in ice [5, 92]. The broader continuum at higher energy corresponds to the conduction band of ice § 2.3.4. The solvated electron state is found at 3.07 ± 0.05 eV after adsorption of the organic molecules.

The decrease in workfunction on water adsorption has been explained in § 2.3.4, where the internal dipole of the water bilayer suppresses the Cu(111) surface dipole. On adsorption of BzX, the workfunction is found to increase which can be explained by the polarisation of the organic layer by the underlying ice layer. Interestingly, the magnitude of the workfunction change increases down the periodic table, that is, it increases from BzF to BzBr by 0.10 ± 0.05 eV, 0.30 ± 0.05 eV and 0.33 ± 0.05 eV, respectively. There are two reasons for this: Firstly, the dipole moment of BzBr = 1.7 ± 0.03 Debye [105] and of BzCl = 1.69 ± 0.03 Debye are similar to each other, but larger than that of BzF = 1.6 ± 0.08 Debye. Despite the larger partial charge at BzF, due to the larger length of the C-X bond in Cl and Br, the dipole moment

of the later is larger. Secondly, as we go down the periodic table, the halogen's electronegativity decreases and the C-X bond strength weakens. Therefore, BzF has a lower polarisability of 9.98 Å^3 than that of BzCl and BzBr with polarisation of 12.19 Å^3 and 13.09 Å^3, respectively [104]. Hence, on adsorption BzF is polarised less than BzBr and the consequent change in the surface dipole of the system is less for BzF than for BzBr. Thus, a smaller workfunction change is seen as we go from BzBr→BzCl→BzF.

To conclude: on adsorption of water on the Cu(111) surface, the workfunction of the system decreases § 2.3.6 [85]. On further adsorption of the halobenzenes, the workfunction increases, more for BzBr than BzF.

4.2 Photoinduced Workfunction Change

We now discuss the evolution of workfunction with photoexposure time and the corresponding chemical kinetics. An energy level diagram describing the photoexcitation process is shown in Fig. 4.2. The mechanism and transfer dynamics of electron solvation in amorphous D_2O ice on Cu(111) has been analysed extensively in femtosecond time-resolved 2PPE [5]. We thus know that on photo-exposure, a metallic electron is photo-excited into the ice conduction band (CB), where they are called excess electrons and are attracted to preferential trapping sites. This is shown as step 1 in the energy level diagram. At the trapping sites, the pre-solvated electrons polarise the water molecule around them, getting localised and solvated, step 2, all the time relaxing back to the metal substrate. Now, on adsorption of halobenzenes, the delocalised photoexcited electrons can attach to the halobenzenes due to wavefunction overlap between the metal and the organic molecules, corresponding to step 3 in Fig. 4.2. These two scenarios, localised electron solvation and delocalised electron attachment (EA) to the molecules, are also shown schematically in Fig. 1.1. We are interested in the later where the delocalised excess electrons can ionise (green dashed line $C_6H_5X^-$) or dissociate (black solid line $C_6H_5^\bullet + X^-$) the organic molecules, depending on their energy and the position of the molecular LUMO level.

The formation of the ionised and dissociated species on the surface will result in an accumulation of negative charge. The system can be treated as a parallel plate capacitor with the water layer as the dielectric medium between the metal surface and the negatively charged molecular layer. On ionization, the charging of the molecular layer gives rise to an additional dipole moment $\vec{p}_{\text{ionize}}$ which points in the direction of the original surface dipole $\vec{p}$, as illustrated in Fig. 4.3. Thus, the dipole moment after photoexposure $\vec{p}' = \vec{p} + \vec{p}_{\text{ionize}}$ is enhanced and by the simple dielectric model § 2.3.2 the workfunction increases on photoexcitation. Since the kinetic energy of the

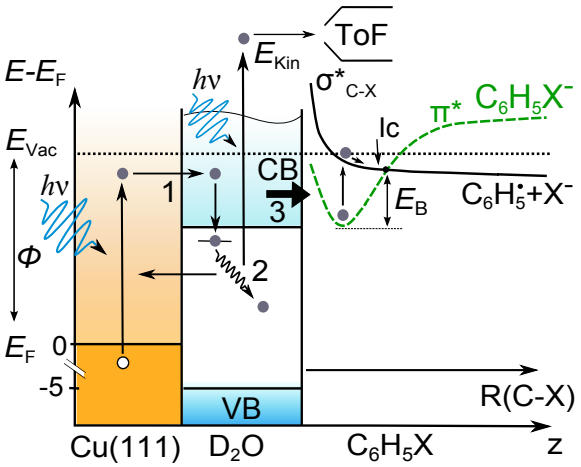

Figure 4.2: Energy level diagram showing 2PPE experiment on 1 ML C_6H_5X adsorbed on 4 BL D_2O covered Cu(111). The arrows show the occurring processes and are explained in the text. E_B is the energy required to reach the canonical intersection Ic. The green curve represents the ionization potential energy curve of the halobenzenes.

photoemitted electron depends upon the workfunction cut-off of the sample and the workfunction of the system changes due to ionization of the organic layer, we exploit this workfunction sensitivity in the following. By performing 2PPE spectroscopy, the first electron causes a change in the workfunction, which is measured by the second photon.

Hence, to study the excess electron induced surface changes as a function of photoexposure time, the 2PPE spectrum was recorded every few minutes with uninterrupted photoexposure. Fig. 4.4 a) shows the lower E_{kin} part of the 2PPE spectra recorded at different photoexposure times, as an example. We see a shift in E_{sec} to higher kinetic energies with increasing photoexposure time, implying an increasing workfunction (Eq. 3.8) with photon dose. The photon dose is calculated as the product of the incident photon flux and the photoexposure time.

Other than ionization/dissociation of the halobenzene, there could be various causes for the increase in workfunction. Like: photodissociation of the amorphous ice, sample ageing, surface diffusion of the organic molecule, change in their orientation (example, tilting of the molecular film) or space-charge effects. To check for photodissociation of the ice layer, a similar experiment was performed on bare D_2O/Cu(111), but, here no change in workfunction was observed (Fig. 4.4b)). We can thus exclude changes in the water surface as the source of increasing Φ. We work in a regime of low photoemitted electron count and can exclude space-charge effect from

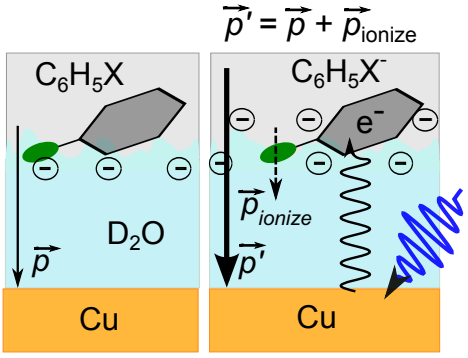

Figure 4.3: Schematic sketch showing the enhancement of the surface dipole when the surface is negatively charged. The left side shows the surface dipole $\vec{p}$ of the neutral system before photo-illumination. The right side shows the origin of a new dipole moment $\vec{p}_{\text{ionize}}$ because of ionization and charging of the organic layer. This results in an enhancement of the surface dipole according to $\vec{p}' = \vec{p} + \vec{p}_{\text{ionize}}$.

causing an artificial shift in E_{sec} and artificial workfunction changes. Further, the increasing negative dipole at the surface is not a consequence of sample ageing, since the same workfunction is recorded on different parts of the sample at different times after sample preparation. Thus, since there is no change in workfunction without an initial exposure to light, the increase in Φ is indeed a photo-driven process. Therefore, the possible causes for the increasing workfunction are DEA, photon dissociation, surface diffusion, and orientation changes. Unfortunately, it is difficult to directly disentangle these processes from each other experimentally, especially with our technique. However, we get hints throughout this chapter which suggest that surface diffusion and orientation changes are unlikely, based on the rate of change in workfunction of the BzX series. Low temperature STM measurements by Betram and Morgenstern (see Appendix C) further suggest that the change in workfunction is due to photoinduced dissociation. They observed structural changes on photo-illumination of submonolayer $C_6H_5Br/D_2O/Cu(111)$ and $C_6H_5Cl/D_2O/Cu(111)$, where the halobenzenes molecules were found to be more strongly bound to the ice layer after photoexposure. Thus, implying chemical changes due to photoexposure and hinting at their dissociation.

To better show the changes in workfunction, the evolution of Φ with photoexposure time is plotted for all the three BzX's in Fig. 4.4 b), where the time dependent workfunction is plotted on the y-axis and the corresponding photo-illumination time on the x-axis. We see that the workfunction of BzF saturates at longer time scales compared to BzCl and BzBr, while the later reach saturation in similar time scales to

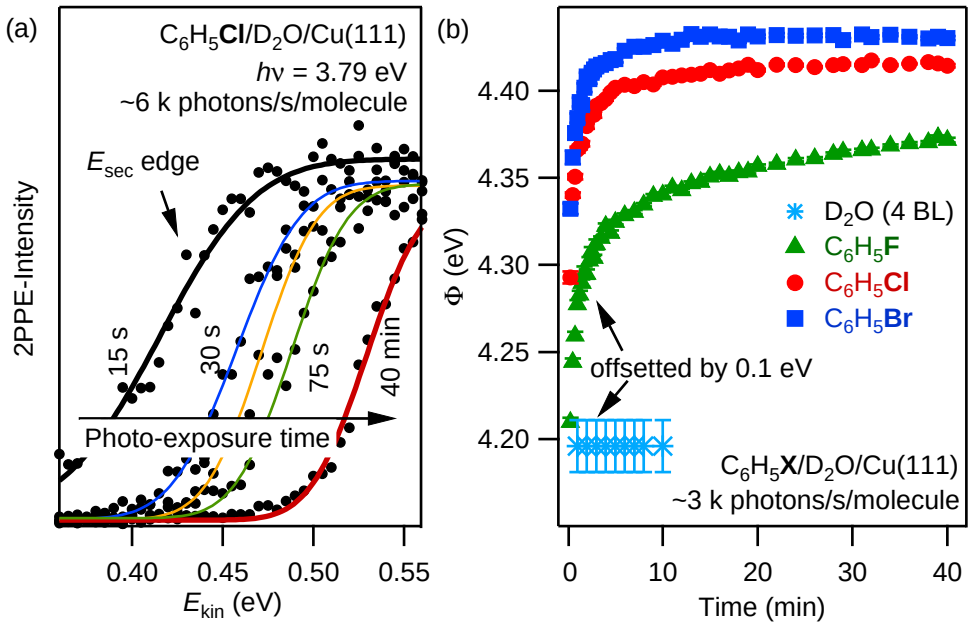

Figure 4.4: Increase in workfunction of $C_6H_5X/D_2O/Cu(111)$ with photoexposure time, measured with 3.79 eV photon energy. a) E_{sec} edge of the 2PPE spectrum which shifts to higher energies on photo-exposure, implying an increase in workfunction. The measurement was performed with a photon flux of ≈6000 photons/s/molecule. b) Evolution of workfunction Φ with photo-illumination time and hence photon dose. Photon flux used here was ≈3000 photons/s/molecule.

each other. The amplitude of workfunction change $|\Delta\Phi|$ is a product of the number of ionised/dissociated molecules (Eq. 4.8) and the individual workfunction contribution. That is, for the same $|\Delta\Phi|$, we can have a contribution from more molecules n with lesser individual $|\Delta\Phi_i|$ or with fewer molecules m with larger $|\Delta\Phi_j|$ as expressed below:

$$|\Delta\Phi| = n|\Delta\Phi_i| = m|\Delta\Phi_j|, n > m \text{ and } |\Delta\Phi_i| < |\Delta\Phi_j| \tag{4.1}$$

Therefore, we do not discuss the changes in the amplitude of the workfunction, but focus our analyses on the rate of change in workfunction, λ_Φ. Here $\Delta\Phi$ is defined as: $\Delta\Phi = \Phi(t) - \Phi(15\,\text{s})$, where $\Phi(15\,\text{s})$ is the workfunction of the first 2PPE spectrum recorded for 15 s and is taken as the reference spectrum. To discuss λ_Φ of the curves in Fig. 4.4 b), we plot it on a log-scale as shown in Fig. 4.5. The curves are first normalised, at maximum $\Delta\Phi$ (see Fig. 4.5 a)), that is to $\Delta\Phi_{max}$ and then subtracted by 1. Please note that due to normalisation, information on $|\Delta\Phi|$ is lost, allowing us to qualitatively discuss λ_Φ.

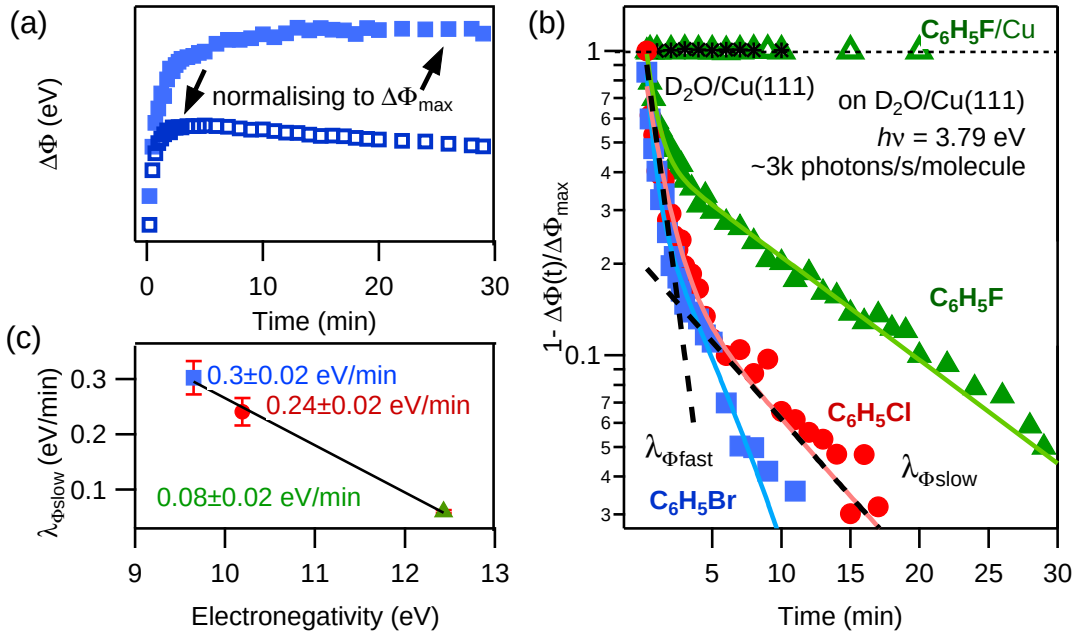

Figure 4.5: a) Change in workfunction as a function of photoexposure for two examples to show that $\Delta\Phi$ is normalised to maximum workfunction change $\Delta\Phi_{max}$. The data is normalised, subtracted by 1 and then plotted in b) on a logarithmic scale vs photoexposure time for all three $C_6H_5X/D_2O/Cu(111)$ systems. The rate of change in $\Delta\Phi$ is fitted with a multi exponential function, giving a large rate $\lambda_{\Phi fast}$, a small rate $\lambda_{\Phi slow}$. c) Linear dependence of $\lambda_{\Phi slow}$ on the halogen's electronegativity [104].

For all the three halogens, we observe linear curves suggesting that λ_Φ is exponential. In fact, the curves show two slopes implying that the workfunction changes with two time constants giving a large rate constant $\lambda_{\Phi fast}$ and a small rate constant $\lambda_{\Phi slow}$. The first slope contains contribution from $\lambda_{\Phi fast}$ and $\lambda_{\Phi slow}$, the former saturates in the first few minutes, giving us the second slope which is nothing but $\lambda_{\Phi slow}$. We don't have a clear explanation for the origin $\lambda_{\Phi fast}$, however, due to its fast saturation and large rate, we speculate it to be photoelectron annealing of defects. $\lambda_{\Phi slow}$ shows a clear dependence on the halogen and increases from BzF to BzBr. We can extract these rates by fitting the data (solid lines) in Fig. 4.5b) with a multi exponential function:

$$\Delta\Phi(t) = |\Phi_1| \exp^{-\lambda_{\Phi slow} \cdot t} + |\Phi_2| \exp^{-\lambda_{\Phi fast} \cdot t} - |\Phi_3| \exp^{-\lambda_{\Phi slowtc} \cdot t} \quad (4.2)$$

where, $|\Phi_1|$, $|\Phi_2|$ and $|\Phi_3|$ are prefactors and $\lambda_{\Phi slowtc}$ is the rate of a decreasing workfunction contribution better resolved at higher fluences and identified in

§ 4.3, where we discuss high fluence measurements. At low photon flux (≈3000 photons/s/molecule), $\lambda_{\Phi slow}$ for BzBr reduces by only 20% for BzCl, but as much as 70% for BzF, that is, as we go down the periodic table, λ_{Φ} increases. We explain this trend by the halogen's electronegativity and hence the C-X bond strength. We thus plot the measured $\lambda_{\Phi slow}$ as a function of the halogen's electronegativity [104] in the benzene ring, shown in Fig. 4.5c). Here, one can clearly see a linear dependence (solid line) of the reaction rate constant on the electronegativity, where with increasing electronegativity λ_{Φ} decreases. This is because, the more electronegative halogen has a stronger C-X bond which is more difficult to ionise (and break) and hence a less efficient electron transfer process is expected. This in turn would result in a slower change in workfunction. **Thus, the dependence of $\lambda_{\Phi slow}$ on the halogen's electronegativity suggests that $\lambda_{\Phi slow}$ corresponds to photoinduced ionization (and dissociation) of the C-X bond.** This is really interesting, since similar trends have also been seen in the gas-phase, for example, electron capture cross section increases down the periodic table [23, 24]. Despite the highly polar and reactive ice surface, the gas-phase trend holds even in the condensed state. The change in workfunction directly reflects the rate of ionization and dissociation of the organic molecules, giving a direct signal from the transient ionic state. It means that with 2PPE spectroscopy, we can excite an electron into a molecular state and at the same time probe the transient ion state via workfunction dynamics. For example, the energy alignment of the ionic state with respect to the metal's Fermi level can be determined by step-wise decreasing the incident photon energy, till no change in workfunction is observed. This is very exciting, as we now have the means to study these ionic states, whose observation with 2PPE has been debated in the past.

The above observations also hint that orientation changes or molecular diffusion can be excluded as the main contributors to the workfunction change. This is because if the workfunction change was associated with any sort of transport phenomenon the rates would depend on molecular mass and size. For the bigger and heavier BzBr, one would expect a slower rate than that of the smaller and lighter BzF (almost 50% of BzBr), but we observe the opposite. This suggests that the mechanism involved in workfunction change is primarily independent of the molecular mass and size, and thus we can neglect diffusion.

The role of e^- traps

We have established that we see a direct signal of the ionization and dissociation of the organic molecules due to photoinduced excitations. We would now like to discuss the possible mechanisms responsible for ionization and show that e^- traps play an

important role. We will therefore compare our observations with the theoretical calculations of the ionization and dissociation energy levels.

The substituted benzene molecules can ionise into $C_6H_5X^{*-}$ via excitation into the metastable π^* state [112, 113]. From here, the molecule can either relax back to the ground state [25] or dissociate into the phenyl radical $C_6H_5^{\bullet}$ and the halogen anion X^- by entering the dissociative σ^* state via a canonical intersection, explained in detail in section § 2.3.5. The ionization and the subsequent dissociation can happen via electron attachment (EA) [11, 23, 24] or via resonant molecular excitation by direct photon absorption in the molecule [26, 108, 110].

Betram and Morgenstern found through STM measurements (Appendix C) that the BzX molecules preferentially adsorb at the defect sites in the crystalline ice surface. Further, Bockstedte and Auburger calculated the peak dissociation energy for the molecules in the framework of DFT and many body perturbation theory. A detailed description of their approach and the calculated values can be found in Appendix C. They performed calculations for both the DEA and resonant photoexcitation mechanisms for ionization/dissociation. They investigated three scenarios for the BzX molecules: 1) in the gas phase, 2) adsorbed on pristine (defect free) crystalline ice I_h and 3) adsorbed at trapping sites on I_h ice (like defects, dangling H-bonds and vacancies). The peak cross section energy for EA and the lowest photon energy needed for resonant photoexcitation were calculated with respect to the ice conduction band and are shown for all BzXs in Table 4.1 (also see Fig. 4.6, which will be discussed soon). To compare, experimentally found electron energies for EA at peak cross section and the lowest photon energies for photoexcitation in the gas phase, are also given in Table 4.1. They found that on adsorption, the π^* states are ionised by the ice conduction band and are lowered in energy. At electron trapping sites (like defects and dangling H-bonds) too there is a decrease in the ionization potential of the molecules but it is significantly more by $> \times 10$, as can be seen from Table 4.1(last two columns). Additionally, the adsorption probability increases at these trapping sites. These observations were also reported by D. Clary and L. Wang in [155], where they see an increased adsorption and ionization of HCl due to defect sites in ice. Along with the ionization potential, the dissociative energy barrier E_B (see Fig. 2.13) is also pulled down in energy. They also found that the first antibonding triplet state for BzF is actually not dissociative. Thus, for BzF the dissociation barrier is too high and low energy electron attachment to the π^* system leads to only ionization of the molecules.

In Table 4.1, we see that the experimentally found and theoretically calculated photon energies for photodissociation are similar to each other, except for BzF, where the experimental value is larger than the calculated one. For BzF, the theoretically

Table 4.1: Experimentally measured dissociation energies for C_6H_5X in the gas-phase and theoretically calculated ionization energies E_{EA} (leading to dissociation) for C_6H_5X in both gas phase and condensed phase (on crystalline ice).

C_6H_5X	Photodissociation (eV)			E_{EA} at peak cross section (eV)			
	Exp.	Theory		Exp. (DEA)	Theory (EA)		
	gas	gas	ice	gas	gas	ice	traps
F	6.42 [108]	4.99	4.92	-	1.06	0.81	0.22
Cl	4.66 [109, 110]	4.92	4.89	0.7 [23]-0.06 [24]	0.95	0.66	0.08
Br	4.66 [111]	4.92	4.92	0.3 [23]-0.5 [24]	0.89	0.59	0.05
I	4.46 [156]	4.85	-	∼0 [23]	0.78		

determined value for photodissociation is determined for excitation to the first σ^* LUMO level, which is non-dissociative. Thus, the experimentally determined value is larger than the calculated value. The calculated values for gas phase and condensed phase are almost the same at 4.92 eV within a window of 70 meV. Experimentally, the lowest energy for dissociation amongst all the three halobenzenes is 4.6 eV for BzBr. We can thus safely assume that the maximum photon energy of 3.8 eV used in our experiments is too low in energy to directly excite and ionise the BzX molecules. With the CB minima of ice at $E - E_F = 3.05 \pm 0.05$ eV and the photon energy of 3.79 eV, we have access to excess electrons with energy $\leqslant 750$ meV, sufficient for electron attachment in BzX on the pristine ice surface and at trapping sites. This is schematically shown in Fig. 4.6 where the EA threshold energies (pristine ice and at electron traps) are compared to the excess electron energy in the ice CB. We see that the ionization threshold energy in the BzF case is at a limit of excess electron energy, but BzBr and BzCl can very clearly be ionised, at pristine ice surfaces. At the traps, the EA energy is much below the excess electron energy for all the halogens. Please note that in the figure, the EA energy at the traps has been offset by +500 meV so that it can be shown along with the pristine surface values. **We can thus conclude that on photoexposure, the workfunction increases due to ionization of C_6H_5X via electron attachment of excess electrons in the ice film.**

In contrast, despite many experimental efforts, DEA in gas phase BzF has not yet been detected [41]. Theoretical modelling found the lowest σ^* state to be non-dissociative [157]. Therefore, we do not expect dissociation for BzF, but only ionization. Additionally, calculations predict 800 meV EA barrier on ice which is at a limit of the excess electron energy of $\leqslant 750$ meV, thus limiting EA process on pristine ice and its contribution to $\lambda_{\Phi slow}$. Nonetheless, calculations show that at trapping sites,

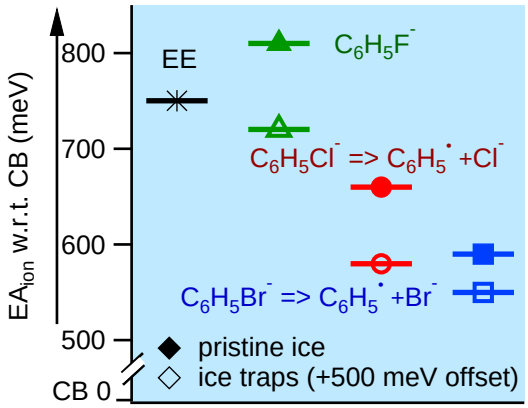

Figure 4.6: Schematic sketch of calculated threshold ionization energies at pristine ice surface and on low energy electron traps for the different C_6H_5X in comparison with the excess electron energy with respect to ice conduction band. The electron attachment energy at traps has been offset by +500 meV so that the trend at both the traps and on pristine ice surface can be seen in comparison.

the EA threshold energy for BzF drops significantly and can be as low as 220 meV, providing an energetically possible EA channel. Thus, for BzF the ionization is mediated via the trapping sites. This further supports our theory that the trapping sites play the central role in EA. Theory also predicts that the halogenated benzene molecules preferably adsorb at trapping sites, further enhancing their role in the EA process. In this context, $\lambda_{\Phi fast}$ is assigned to 'annealing', that is, ionization of BzX at very low energy traps (no EA threshold barrier defect sites) by photoelectrons in the ice CB.

Comparing BzF, BzCl and BzBr in Table 4.1, the EA threshold energies at traps decrease from BzF to BzBr, lowering the threshold energy by 78% for BzBr compared to BzF and 64% for BzCl compared to BzF. Since lower energy electrons can now participate in the EA process, the ionization rate increases (see Eq. 4.8) and a larger λ_Φ is expected. That is, we see that the reaction rate constant trend in Fig. 4.5c) follows the electron attachment threshold energy sequence in Fig. 4.6, where with lower threshold energy, there is larger gain and hence a larger reaction rate. In addition to this, EA is possible on pristine ice surface for BzCl and BzBr, further increasing the reaction sites and enhancing λ_Φ. This explains why a smaller λ_Φ is observed for BzF compared to BzCl, and is largest for BzBr.

To summarise, BzX in $C_6H_5X/D_2O/Cu(111)$ is ionised or dissociated via EA by excess electron which are photoexcited into the ice CB where the trapping sites play a central role. The overall reaction rate depends

on the halogen's electronegativity and increases from BzF to BzBr. Furthermore, we directly observe the transient ion state, excited by photoelectrons, as a change in workfunction.

4.2.1 Reaction Dynamics in the Absence of Light

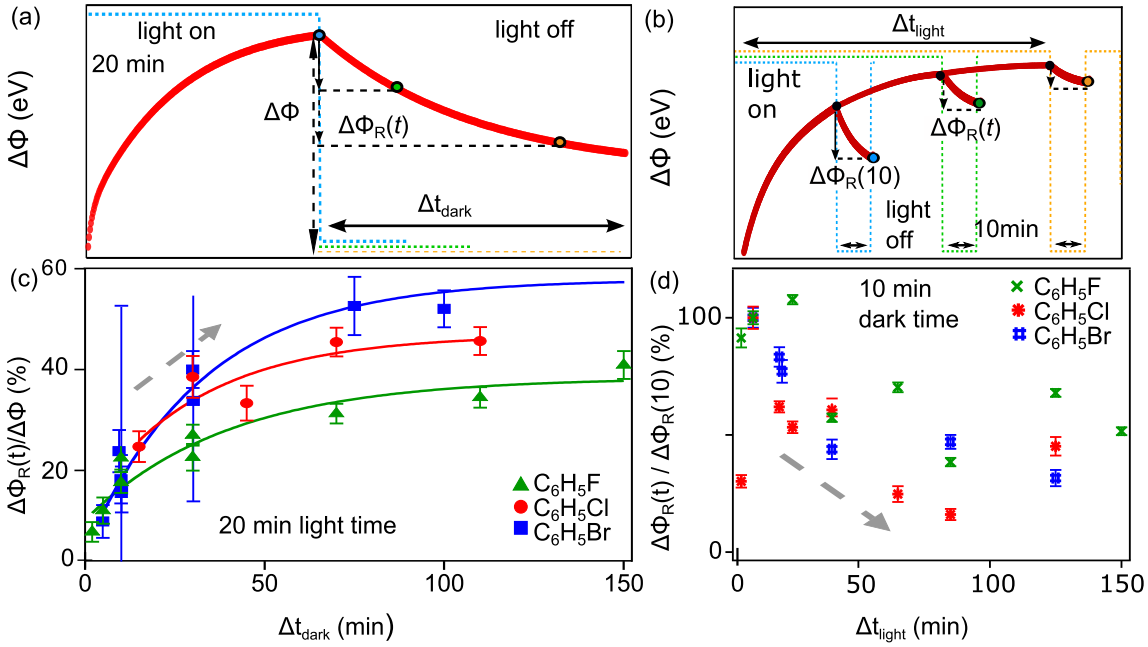

Figure 4.7: The workfunction recovers by $\Delta\Phi_R(t)$ when the laser exposure Δt_{light} is blocked for a certain time Δt_{dark}. This is shown schematically by a) dark-time and b) light-time experimental representation. In dark-time experiment Δt_{light}= 20 min is kept constant and Δt_{dark} is varied. In light-time experiment, Δt_{dark}= 10 min is kept constant andΔt_{light} is varied. c) Shows the measured $\Delta\Phi_R(t)$ for dark-time measurements, normalised to $\Delta\Phi$ measured just before blocking the laser. d) Shows the observed $\Delta\Phi_R(t)$ for light-time measurements, normalised to $\Delta\Phi_R(10)$. Each data point corresponds to a new experiment on a fresh spot.

In order to better understand EA reaction mechanism, we further investigated if the ionization/dissociation reactions are reversible or not. If a back reaction channel was active, it would take place even in the absence of light, while the ionization channel would proceed only in the presence of light. We thus performed 'dark time' and 'light time' measurements, shown in Fig. 4.7, where we see the role of light exposure and light blocking on workfunction recovery, by measuring a change in workfunction after blocking the laser light.

The dark time experiment is sketched in Fig. 4.7a), where we show how the workfunction would change as a function of blocking the light. Here, the light is exposed for a fixed photoexposure time of 20 min resulting in an increase in workfunction $\Delta\Phi$. The curve in the light off part of the figure represents the recovery of the workfunction in the absence of light. Blocking the light for some (variable) time Δt_{dark} and then taking a 2PPE spectrum (highlighted points), allows us to measure the recovered workfunction curve. If measurements for enough Δt_{dark} values are taken, then we can determine the recovery rate. The light time experiment was performed in a similar manner, but here the photoexposure time Δt_{light} is varied, the light off time is fixed to 10 min, and we measure the recovered workfunction (black curve) for different exposure time (red curve). We show the expected change in workfunction in Fig. 4.7b). Here we check if for different light exposure time, the amount of workfunction recovered on blocking the light is the same or not. In both the experiments, each 'dark time' and 'light time' data point after blocking the light is a new and identical experiment on a fresh spot, but with different Δt_{dark} and Δt_{light}, respectively. In these experiments, we analyse the recovered workfunction $\Delta\Phi_{\text{R}}(t)$ which is the change in workfunction after blocking the light, that is:

$$\Delta\Phi_{\text{R}}(t) = \Delta\Phi(\text{light}) - \Delta\Phi(\text{dark})$$

where, $\Delta\Phi$(light) is the change in workfunction just before blocking the light and $\Delta\Phi$(dark) is the change just after unblocking the light.

The percentage of the recovered workfunction, $\Delta\Phi_{\text{R}}(t)/\Delta\Phi\,(\%)$, is presented in Fig. 4.7c) as a function of Δt_{dark}. For all the three molecules, the amount of recovery increases with increasing light blocking time, as expected from Fig. 4.7a) and thus suggesting that there is an active back relaxation process, for example relaxation of the ionised species to the neutral state. A recovery in workfunction is also possible if the workfunction contribution of the dissociated species is less than that of the ionised species. Since, the amount of recovery depends upon the concentration of the ionised species, we fitted it with an exponential function and found the same recovery rate of 0.03 ± 0.01 /min for all three, suggesting $\lambda_{\text{relax}} + \lambda_{\text{dissoc}}$ is similar. Comparing the percentage of recovery in ≈ 100 min, BzBr was found to recover the most at $56 \pm 3\%$, followed by BzCl at $47 \pm 4\%$ and least for BzF at $36 \pm 2\%$.

In the light time measurement, Fig. 4.7d) we show the percentage of $\Delta\Phi_{\text{R}}(t)$ to the recovered workfunction after 10 min of darkness ($\Delta\Phi_{\text{R}}(10)$). Here we have to normalise since $\Delta\Phi$(light) is governed by light exposure. One can clearly see in the figure that the percentage of recovery decreases with longer photexposure times. That is, with increased exposure, fewer molecules are able to relax back. This suggests a stabilising process which limits the recovery.

With the 'dark' time and 'light' time experiments we found that the ionised species relax back to the neutral molecule and there is a stabilising forward process. On the one hand, the back reaction channel results in a loss of negative charge at the surface, which gives a decrease in workfunction. On the other hand, the dissociation channel would limit the back reaction, reducing the recovery of workfunction. The amount of recovery thus depends on how long the light is blocked (light off) and on how long the sample is photoexposed for (light on) before blocking it.

Surface diffusion of the intermediate and/or the dissociated species could also result in the decrease of workfunction. Again, the recovery rate is one for all BzXs, but due to larger mass and bigger size of BzBr molecule compared to the BzF molecule, the surface diffusion of $C_6H_5X^{*-}$ and X^{*-} should decrease from Br to F. One could argue that the radical benzene ring diffuses and causes this effect, but as mentioned before, due to the highly polar ice surface, both the dissociated species are expected to be stabilised quickly. Hence, diffusion is possible, but unlikely, corroborating our earlier statement.

4.2.2 Reaction Rate Constants

We can now write a simple chemical reaction to describe the photoelectron induced process as:

$$C_6H_5X + e^- \underset{\lambda_{\text{relax}}}{\overset{\lambda_{\text{ion}}}{\rightleftharpoons}} C_6H_5X^{*-} \xrightarrow[X=Cl,Br]{\lambda_{\text{dissoc}}} C_6H_5^{\bullet} + X^- \tag{4.3}$$

where, $\lambda_{\text{ion}}, \lambda_{\text{relax}}$ and λ_{dissoc} are the rate constants for the ionization, relaxation and dissociation reactions, respectively. We will discuss these rates and their relation to λ_Φ here. This form of chemical reaction is a commonly occurring reaction mechanism, where the reactants form the final products through an intermediate species, while both the final and intermediate reaction products can relax back. Here the organic molecule captures an electron to form the ionised halobenzene $C_6H_5X^{*-}$ (crossing the EA energy barrier), which can either relax back to the neutral molecule or dissociate into the halogen radical $C_6H_5^{\bullet}$ and the haloanion X^- (via intersystem crossing). A recombination of the dissociated species is also possible, but because this is a final product, λ_{dissoc} is simply the sum of the dissociation rate and recombination rate. Besides, due to the highly polar ice surface, the dissociated species will be 'stabilised' quickly and a recombination is unlikely. For BzF λ_{dissoc} is zero since its dissociation energy is too high. In this simplified chemical equation, we neglect secondary reactions between the ionised species, the dissociated species and other molecular species on the surface.

So far we have introduced two sets of rate constants: $\lambda_{\text{ion,relax,dissoc}}$ and λ_Φ. The different λ's in Eq. 4.3 are associated with the reaction at a molecular level and hence we call them the microscopic rate constants. They are the direct rates of the chemical reaction. The λ_Φ's give the rate of change in workfunction of the whole system and hence gives the macroscopic build-up of the negative charge at the surface. With 2PPE spectroscopy we cannot directly measure the individual microscopic rates since we are sensitive only to the macroscopic build-up of the workfunction, λ_Φ. Since λ_Φ is a function of the microscopic rates, we try to extract them by modelling the dissociation curves according to the above Eq. 4.3 and discuss it in § 4.6. The microscopic and macroscopic rates are discussed in more details in the following.

Microscopic Rates- Differential Rate Law In order to discuss the microscopic rates, let us first look at the first part of Eq. 4.3: $C_6H_5X + e^- \underset{\lambda_{\text{relax}}}{\overset{\lambda_{\text{ion}}}{\rightleftharpoons}} C_6H_5X^{*-}$. Here the concentration of $C_6H_5X^{*-}$ can either depend on the concentration of only C_6H_5X (first order) or on the concentrations of both C_6H_5X and e^- (second order). This dependence has to be determined experimentally. From the fluence dependent measurements (§ 4.3) of BzF, we find that the ionization process is a second order process depending on the concentration of C_6H_5X and e^-. Since the dissociation process depends on the concentration of the ionised species, we expect it to be a first order process. We can thus write the differential rate equations for all the three species as:

$$\begin{aligned} d[C_6H_5X]/dt &= dN_e/dt = -[C_6H_5X]N_e\lambda_{\text{ion}} + [C_6H_5X^{*-}]\lambda_{\text{relax}} \\ d[C_6H_5X^{*-}]/dt &= [C_6H_5X]N_e\lambda_{\text{ion}} - [C_6H_5X^{*-}](\lambda_{\text{relax}} + \lambda_{\text{dissoc}}) \\ d[C_6H_5X^{\bullet}]/dt &= d[X^-]/dt = [C_6H_5X^{*-}]\lambda_{\text{dissoc}} \end{aligned} \tag{4.4}$$

where, N_e is the density of electrons per molecule, $[C_6H_5X]$, $[C_6H_5X^{*-}]$, $[C_6H_5^{\bullet}]$ and $[X^-]$ are the concentrations of C_6H_5X, $C_6H_5X^{*-}$, $C_6H_5^{\bullet}$ and X^-, respectively.

The concentration of C_6H_5X and N_e are depleted due to the forward ionization reaction at a rate of λ_{ion}, while at the same time, they increases due to the relaxation of the ionised species $C_6H_5X^{*-}$. $[C_6H_5X^{*-}]$ changes in exactly the opposite manner, but has an additional depletion rate of λ_{relax} channel to the dissociated species. Lastly, the concentration of the dissociated species is always increasing with a rate of λ_{dissoc}. Since the dissociation process only depends on the concentration of the ionised species, we expect it to be a first order process, linearly depending on $[C_6H_5X^{*-}]$. As

mentioned earlier, λ_{dissoc} is the sum of the forward dissociation rate and the relaxation of the dissociated species, where the forward rate has to be larger than the backward rate. From these equations one can see that the rate of any of the reaction paths strongly depends on the concentration of each other. A simple implication of this is that on doubling the concentration of the C_6H_5X, the rate of formation of $C_6H_5X^{*-}$ would not simply double, but change by a factor depending on all the rates and concentrations in Eq. 4.4.

The microscopic rate constants $\lambda_{\text{ion,relax,dissoc}}$ can be described by the transition state theory § 2.1.3 as follows:

$$\lambda_{\text{ion,relax,dissoc}} = A_{\text{ion,relax,dissoc}} \exp^{-\frac{E_{\text{ion,relax,dissoc}}}{k_{\text{B}}T}} \tag{4.5}$$

where, k_{B} is the Boltzmann constant, $E_{\text{ion,relax,dissoc}}$ are the threshold energies for ionization, relaxation and dissociation processes and T is the reaction temperature. All these terms are seen in the exponent and give the probability of the reaction. $A_{\text{ion,relax,dissoc}}$ is the attempt frequency for the different reactions and includes all the partition functions for the internal degrees of freedom of the reactants and the steric requirements. From this equation we see that on decreasing $E_{\text{ion,relax,dissoc}}$, the reaction probability increases and hence the reaction rate constant will in turn increase. This explains why for BzBr, which has a lower ionization threshold, the reaction rate is faster than BzCl, with a comparatively larger E_{ion} and can also be seen by comparing Fig. 4.5c) and Fig. 4.6, where the decreasing EA threshold energy gives a faster reaction rate constant. In fact on changing $E_{\text{ion,relax,dissoc}}$, not only the reaction constant changes, but also the N_{e}, as is discussed below.

Another important parameter is the electron density per molecule N_{e} in ice, since the concentration of the ionised species depend on it. In the ice conduction band the electrons have a distribution of energy due to a finite bandwidth of the pulse, a continuous density of states in the metal below the Fermi level and preferential wave function overlap with the conduction band (example trapping sites). We can thus write:

$$N_{\text{e}} = \kappa N_{\text{ph}} = \int_{E_{\text{ion}}}^{h\nu-\text{CB}} N_{\text{e}}(E)dE \tag{4.6}$$

where, N_{ph} is determined by the photon flux per molecule and κ gives the quantum efficiency of photoexcitation process, that is, the fraction of incident photons that successfully excite the available excess electrons in ice. The lower limit of E_{ion} ensures

that only electrons with energies more than the ionization threshold are taken into account. The upper limit is given by the maximum energy of the excess electrons in the conduction band, which is given by $h\nu - \mathrm{CB}$, where CB is the conduction band minimum $= 3.05 \pm 0.05\,\mathrm{eV}$. Thus the excess electron density per molecule is also a function of energy, $N_\mathrm{e}(E)$. To be vigorous, N_e is also a function of femtosecond (fs) time as the excess electrons are continuously relaxing back to the Cu(111) substrate. But because we assume that EA takes place instantaneously on electron excitation, we can ignore this loss. For BzBr, where the EA threshold energy is lower than that BzCl, the acceptable energy bandwidth of N_e will be larger for the same flux and hence a faster reaction rate is expected for BzBr than BzCl.

To sum it up : λ_ion is found to be a second order process depending on the concentrations of the neutral organic molecule and the photon flux. λ_dissoc is expected to depend only on the concentrations of the ionised species. From the differential rate equations (Eq. 4.4), rate constant formalism (Eq. 4.5) and the energy dependence of N_e (Eq. 4.6), on decreasing the concentration of the reactants (example BzX coverage), photon energy, photon flux, or by increasing the EA threshold energy, the reaction rate will increase. We also see that the reaction rate is extremely sensitive to the ionization threshold energy.

Macroscopic rates (Photostationary state)- Integrated rate law To study the change in concentration as a function of the reaction time, we use the integrated rate law which can be obtained by solving the differential rate equations in Eq. 4.4. However, these equations need to be solved simultaneously and since they are interdependent, they give a very complicated solution. As an example, we solve for $C_6H_5X^{*-}$ in Eq. 4.4, assuming no back reaction and no dissociation channel and show it below in Eq. 4.7:

$$[\mathrm{C_6H_5X^{*-}}](t) = N_\mathrm{e} - ([\mathrm{C_6H_5X}] - N_\mathrm{e})\frac{N_\mathrm{e}}{[\mathrm{C_6H_5X}]}\exp^{-([\mathrm{C_6H_5X}]-N_\mathrm{e})\lambda t} \tag{4.7}$$

Where, concentrations $[C_6H_5X]$ and N_e are the initial concentrations at $t = 0$ and it is assumed that N_e changes with the same rate constant as $[C_6H_5X]$.

Now, going on to the slightly more complicated case of BzF where we have the back reaction, but no dissociation process. The equation is similar to Eq. 4.7, but

with the additional back relaxation rate constants and is given by:

$$\begin{aligned} [C_6H_5X^{*-}](t) &= \text{prefactors}(1 - \exp^{-\{([C_6H_5X]-N_e)\lambda_{ion}+\lambda_{relax}\}t} \\ \lambda_\Phi &= ([C_6H_5X] - N_e)\lambda_{ion} + \lambda_{relax} \\ \text{If, } [C_6H_5X] &>> N_e, \text{it can be simplified to} \\ \lambda_\Phi &= [C_6H_5X]\lambda_{ion} + \lambda_{relax} \end{aligned} \tag{4.8}$$

In the above equations, there is an exponential term depending on the difference of the initial BzX and the excess electron concentration in Eq. 4.7. However, we work in a regime where $[C_6H_5X] > 1000 \times N_e$, which means changing N_e by an order of 10 will not change the exponential term much and this term can be ignored. The prefactors are a function of the rate constants and initial concentrations. We can relate the macroscopic rate constant λ_Φ to the microscopic $\lambda_{ion,relax,dissoc}$. λ_Φ gives the rate of change in workfunction of the whole system. For BzF, there is only one negative species due to the ionization channel and therefore the change in workfunction would correspond to the build-up of only $C_6H_5F^{*-}$. This is given by the integrated rate law in Eq. 4.8 and hence $\lambda_\Phi = [C_6H_5X]\lambda_{ion} + \lambda_{relax}$, where $[C_6H_5X] >> N_e$.

The integral rate equation for BzBr and BzCl are very complicated due to the additional dissociation channel. We therefore try to explain it phenomenologically using the concept of a photostationary state, discussed as follows: Since we observe a time dependent workfunction change, it suggests that there is a build-up of the excited state, which is possible only if the ionised state is long living. This means that before the intermediate state completely relaxes back to the initial state, the next laser pulse arrives, exciting the system again and giving additional excited states, as shown in Fig. 4.8.

As a result, with each new laser pulse we get a build-up of the excited states. Such a state is called a *photostationary* state [70, 82] and the $\Delta\Phi$ we observe is a *macroscopic* effect of the build-up of the photostationary state. λ_Φ hence gives the time evolution of the photostationary state. In fact, since the adsorbed molecules are excited only in the presence of light and continue to relax back slowly in its absence, we can treat the system as if it were under continuous illumination and the integrated rate laws can directly describe our observations and give λ_Φ. Since we can solve it for BzF, we see that λ_Φ simply is the sum of the forward and back reactions. In the case of BzCl and BzBr, things get more complicated due to the dissociation process. Here the reaction rate of the dissociation channel depends on the concentration of $C_6H_5X^{*-}$, which in turn depends on the fluence. With increasing fluence, the rate of both $[C_6H_5X^{*-}]$ and $[X^-]$ will increase, but not linearly. Thus, the rate of

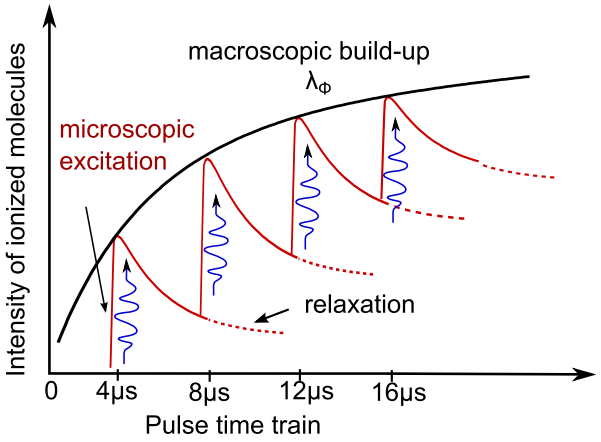

Figure 4.8: Build-up of photostationary state due to the long lifetime of the excited molecules. Before all the molecules can relax back, a new laser pulse (every 4 μs) excites more molecules, giving an accumulation of the excited state molecules.

accumulation of the dissociated species and consequently the ionised species becomes fluence dependent, making λ_Φ fluence dependent. Hence, while the individual rate constants $\lambda_{\text{ion,relax,dissoc}}$ are fluence independent, we observe a fluence dependent λ_Φ in § 4.3. λ_Φ can be defined for BzCl and BzBr as $f(\lambda_{\text{ion}}, \lambda_{\text{relax}}, \lambda_{\text{dissoc}}, N_e, [C_6H_5X])$. For BzF, $[C_6H_5X^{*-}]$ is fluence dependent, but its accumulation is given by Eq. 4.8, which we show is fluence independent.

4.3 Fluence Dependent Experiment

Since the concentration of the ionised species will depend on the concentration of the neutral species, we would like to see if it depends on the electron density as well. Therefore, to verify if the current reaction is of the first order or second order, as discussed in § 4.2.2, we performed fluence dependent measurements. This can be done by either changing the incident photon flux or by changing the photon energy as $N_e(E)$ is a function of electron energy. We did both, and performed measurements with photon flux ranging from ∼400 - 7500 photons/s/molecule at 3.78 eV and 3000 - 17,500 photons/s/molecule at 3.10 eV, shown respectively in the left and right panels of Fig. 4.9. Here we plot the normalised workfunction change on a log scale vs photoexposure time as a function of fluence. The top most panel (a and d) shows BzF, in the middle (b and e) is BzCl and BzBr is shown at the bottom (c and f). The 3.10 eV photon beam was obtained by frequency doubling the compressed

RegA output of 1.5 eV. That is why we have a much higher photon flux range at this energy as compared to 3.78 eV which is from the NOPA. Looking at the 3.78 eV data for BzF, we see that the curves at different fluences lie on top of each other and have the same slope, giving a fluence independent macroscopic rate constant. The 3.78 eV data for BzCl and BzBr show a clear and interesting dependence of λ_Φ on the photon flux. Firstly, both the slow and the fast rate constants get significantly larger (slope gets steeper) with increasing photon flux. This is qualitatively shown in Fig. 4.11, where we plot the corresponding $\lambda_{\Phi\text{slow}}$ from fitting the curves in Fig. 4.9, as a function of fluence for the three halobenzenes. We see that for both BzCl and BzBr, $\lambda_{\Phi\text{slow}}$ increases linearly but for BzF [6] no significant fluence dependence is observed. Returning to Fig. 4.9, the second observation for BzBr and BzCl is that at some critical photoexposure time t_c there is a reverse in dynamics, that is, after t_c the increasing Φ starts to decrease. BzBr also exhibits these trends, but t_c is seen at lower fluences and earlier times for BzBr compared to BzCl. It is to account for this change in trend that we use a three exponential fit routine in Eq. 4.2.

Before moving onto the energy dependent measurements, we would like to introduce Fig. 4.10, where we show the absolute change in E_{sec} on a linear scale vs photoexposure time for different fluences incident on the BzF layer. Here we can compare the absolute changes in workfunction, since for BzF we expect only one type of negative species $C_6H_5F^{*-}$. We see in the figure that with increasing fluence, the change in E_{sec}, which means $|\Delta\Phi|$ at time t increases. That is, with increasing fluence the density of $C_6H_5F^{*-}$ molecules increase. The fluence dependent curves for BzBr and BzCl on a linear scale are shown in the Appendix B.

The same experiment was performed at 3.10 eV, as shown in the right panel of Fig. 4.9. BzCl and BzBr are now fluence independent and behave similar to BzF at 3.78 eV. Both $\lambda_{\Phi\text{slow}}$ and $\lambda_{\Phi\text{fast}}$ are observed to be slower with $\lambda_{\Phi\text{slow}} = 0.02 \pm 0.02\,\text{eV/min}$, $0.06 \pm 0.01\,\text{eV/min}$ and $0.07 \pm 0.01\,\text{eV/min}$ for BzF, BzCl and BzBr, respectively for the highest fluence, which corresponds to $\times 4$ for BzF, $\times 10$ for BzCl and $\times 20$ for BzBr slower than that at 3.78 eV.

Fluence dependence of rate constant : As shown in Fig. 4.10, the $[C_6H_5F^{*-}]$ increases with increasing fluence. However, from Fig. 4.9 and Fig. 4.11, we see that λ_Φ, which is a function of λ_{ion} and λ_{relax} rate constants, remains the same [7]. These

[6] Note: for BzF a two exponential fit was used and negative component $\lambda_{\Phi\text{slowtc}}$ is ignored since there is no dissociation channel here. For BzCl, the best guess for Φ_3 was for the highest fluence and was used for all other fluences.

[7] A fluence independent rate constant hints that the N_e is not constant through the experiment even though N_{ph} is constant. This can be explained by the ionization of the molecular layer which

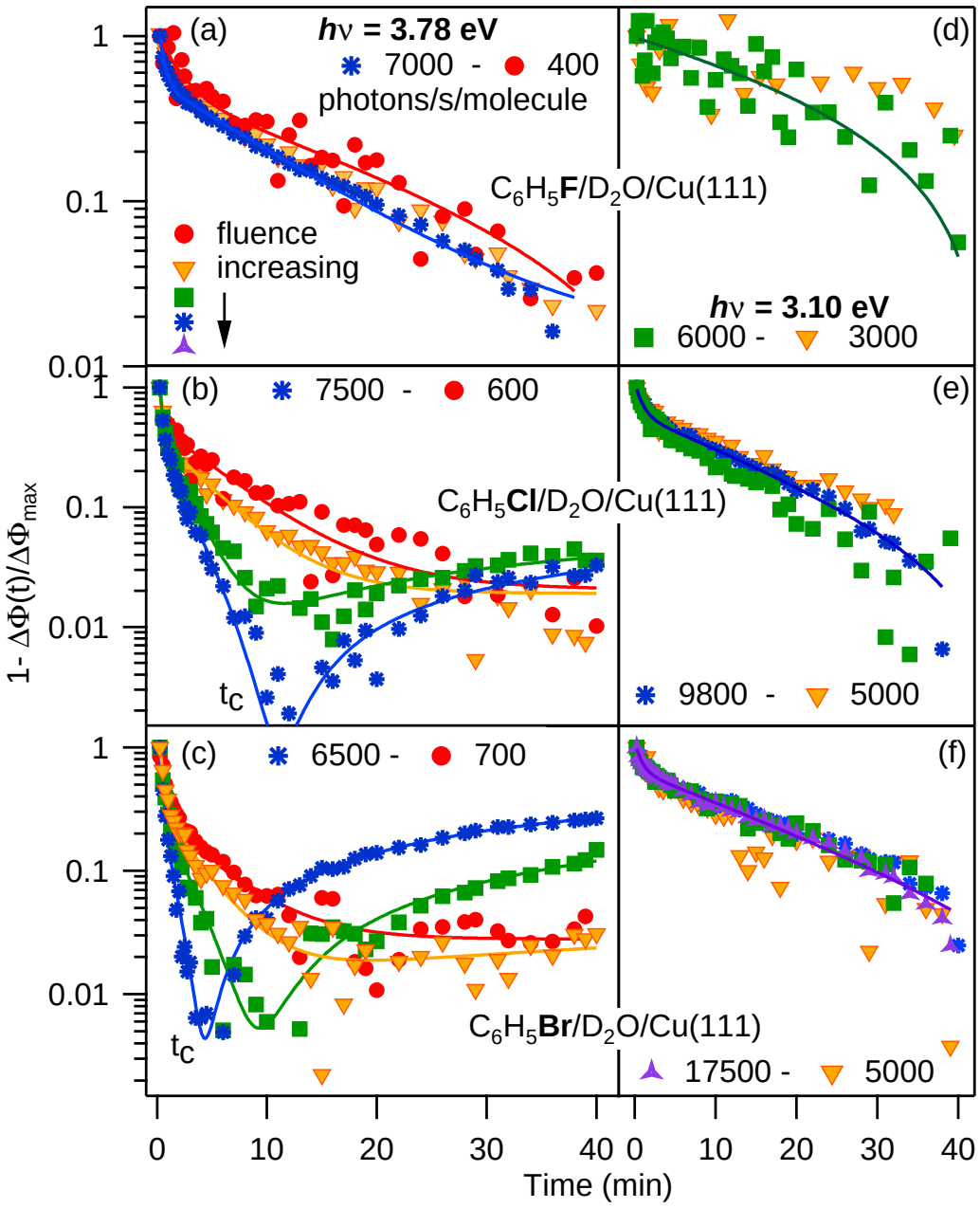

Figure 4.9: Normalised $\Delta\Phi$ vs photo-exposure time is plotted for different photon fluences (markers) on a logarithmic scale. The data is normalised to the maximum workfunction change $\Delta\Phi_{max}$. Measurements with 3.78 eV are shown in the left panel and those with 3.10 eV are shown in the right panel for BzF (top), BzCl (middle) and BzBr (bottom).

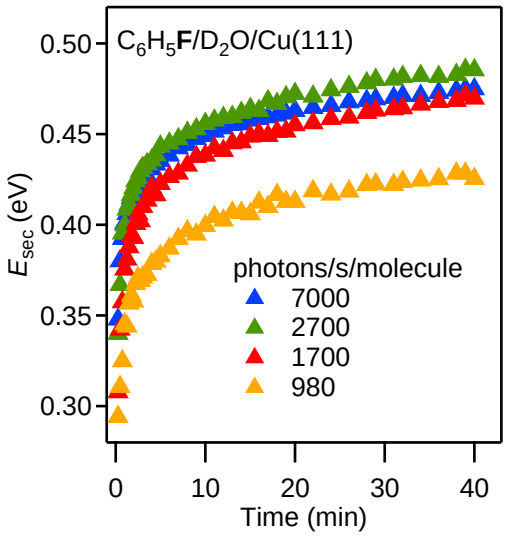

Figure 4.10: Photoinduced change in workfunction in $C_6H_5F/D_2O/Cu(111)$ for different fluences, shown as a shift in secondary edge E_{sec} vs photoexposure time. The absolute change in workfunction (or shift in E_{sec}) increases with increasing fluence.

two observations together suggest that the ionization process is a first order process since the reaction rate (do not confuse with reaction rate constant) increases linearly (because of change in concentration) with fluence and not exponentially (change in λ_Φ). BzCl and BzBr are not good examples to discuss the ionization process due to the dominance of the third exponential factor at higher fluences which results in a decrease in workfunction. This complication does not arise for BzF, since it has only one negative species. Anyhow, since the ionization mechanism is the same for all the three halogen's, BzF observations can be extended to BzBr and BzCl.

A very weak fluence dependence is seen for BzF rate constant. This is justified by the loss of a small percentage of the molecules to form some stable species (§ 4.2.1). The reaction rate constant for BzCl and BzBr are found to depend on the fluence, which is indeed expected because of its irreversible dissociation channel, as discussed in § 4.2.2. Here, the rate at which the dissociated species concentration builds up is given by the macroscopic rate constant which is fluence dependent even for the second order reactions.

Energy dependence : The energy dependent measurements provide the spectroscopic clue that the DEA process is not due to localised solvated electrons e_s^-, but

would have a different electron capture cross section that the neutral molecular layer.

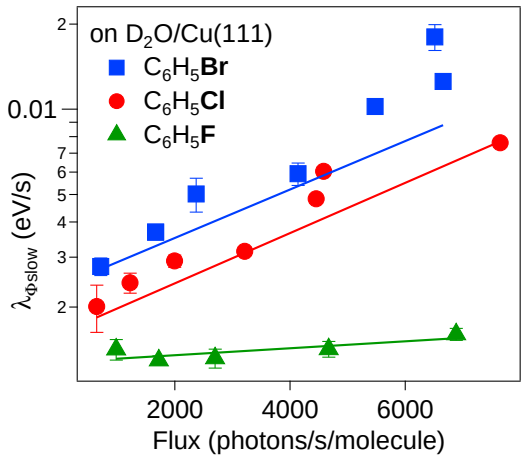

Figure 4.11: $\lambda_{\Phi slow}$ vs photon flux for C_6H_5F (green triangle), C_6H_5Cl (red circles) and C_6H_5Br (blue squares) adsorbed on $D_2O/Cu(111)$ is shown on a log-scale.

due to the delocalised electrons in the ice conduction band. Considering the solvated electrons, the solvated electron state lies at 2.97 ± 0.05 eV above the Fermi level which can be populated by the 3.10 eV photon energy used. However, we observe that at this reduced photon energy, the reaction rates are considerably slower from $\times 4$ for BzF to $\times 20$ for BzBr, compared to the 3.78 eV measurements. That we see such a strong effect on the reaction dynamics at 3.10 eV implies that e_s^- are not the main players in enhancing the DEA. In the case of excess electrons, photoexposure with 3.10 eV photons means that the excess electron energy (photon energy- conduction band energy) is drastically reduced by 680 meV compared to the 3.78 eV and hence the available excess electron density for EA (hence, the high fluences used). Additionally, these excess electrons have energies in the thermal energy range, making only the low energy traps accessible and switching off the EA channel at the pristine ice surface. Thus, the DEA at the lowest energy traps is the main contribution to $\Delta\Phi$. This would explain why we see lower saturation levels and slower rates for all the BzXs. In the case of BzF which was already driven by the trapping sites, the cross section is further reduced, giving a limited ionization probability.

Change in workfunction trend : A decrease in workfunction is associated with an effective loss of negative dipole at the surface § 2.3.2. This can happen either

due to a loss of the negative charge from the surface via the dissociation channel [8] or due to screening effects at the surface. These are discussed in the following three scenarios:

1) The first is that due to the negative nature of the halogen anions, one can expect them to be partially solvated in the ice layer. This would partially screen the anionic charge resulting in a lower $|\Delta\Phi|$ contribution from the dissociated species than the ionised species. Due to the dissociation channel, the system never comes into a true equilibrium. However, the intermediate species reach a maximum concentration $[C_6H_5X^{*-}]_{max}$ before being drained by the final product, similar to the pre-equilibrium approximation [9] discussed in § 2.1.5. Here, the condition $\lambda_{ion} > \lambda_{relax}, \lambda_{dissoc}$ holds and is verified from our numerical modelling in § 4.6. Therefore, the decrease in workfunction is argued to be due to the loss of the intermediate species to the final species. With increasing fluence or reaction rates, the intermediate species comes into quasi equilibrium sooner, reaching a maximum earlier, and hence an earlier t_c is expected.

2) The second explanation is that secondary reactions can take between the dissociated species at the surface producing final products with lower $|\Delta\Phi|$. We can not distinguish between these two processes and refer to them simply as the final products. When all the neutral molecules are used up and the secondary processes dominate, a decrease in workfunction will be seen. Like in the earlier case, with increasing fluence or reaction rates, the intermediate species get consumed faster and an earlier t_c is expected.

3) For the dissociable BzCl and BzBr, there is a large density of negative species at the surface, comprising of the ionised and dissociated molecules. At high fluxes, the concentrations of the reacted products increase and the negative charge density at the surface is larger. These charges can have a screening effect, effectively reducing the workfunction and giving a decrease in workfunction trend after some photoexposure time. The high concentration of the negative charge would be reached faster and an earlier t_c would be observed.

[8] Though the back reaction relaxes the intermediate $C_6H_5X^{*-}$ state to the ground state, from the rate equations, it brings the ionization channel into equilibrium, see § 4.6

[9] The steady state approximation doesn't work here, because it is valid only where $\lambda_{dissoc} >> \lambda_{ion}$ and the intermediate state reaches a constant concentration early on in the reaction. Hence, only the final state concentration will change, giving an ever increasing workfunction (or saturation for $|\Phi_{dissoc}| << |\Phi_{ion}|$). When $\lambda_{dissoc} > \lambda_{ion}, [C_6H_5X^{*-}]$ is not in steady state but the final product dominates and again only an increase in workfunction is seen.

Since BzF doesn't dissociate, a reversible trend is not expected and is not observed. Additionally, this would also explain why BzCl and BzBr appear to saturate faster than BzF. In all the three scenarios, at higher fluences or faster reaction rates, t_c is expected earlier.

Determining t_c as a function of incident photon flux The above discussion hints that the system would reach t_c when a certain concentration of the molecules are consumed. To verify this, we check if the total number of incident photons in t_c is the same for the different fluences.

Table 4.2: Total photons incident on C_6H_5Br and C_6H_5Cl in time t_c, estimated for different photon fluxes.

C_6H_5X	Flux ±1000 (photons/s/molecule)	t_c (min)	Total photons in time t_c $\times 10^6$(photons/molecule)
C_6H_5Br	6600	5±1	2.0±0.5
	6500	5±2	1.6±0.8
	5500	6±1	2.0±0.5
	4100	11±2	2.7±0.8
C_6H_5Cl	7600	13±2	6.0±1.3
	4600	16±2	4.4±1.1
	4400	16±2	4.3±1.1

This is shown in Table 4.2, where we tabulate the photon flux, t_c and the total number of incident photons at t_c for BzBr and BzCl. We see that the total incident photons are the same within error limits for the different fluences and can be approximated to $\approx 2.1 \pm 0.7 \times 10^6$ photons/molecule for BzBr and $\approx 5.1 \pm 1.2 \times 10^6$ photons/molecule for BzCl. This verifies that t_c depends on the number of ionised molecules. On the basis of this observation, we should be able to predict t_c for lower fluences. For example, for ≈2500 photons/s/molecule, we expect to see $t_c = 15 \pm 1$ min, which we do see in Fig. 4.9. Here we see that around 15 min, the data gets a little noisy but the workfunction starts to increase slowly. For ≈1700 photons/s/molecule, we expect $t_c = 21 \pm 1$ min and here too we see a loss of exponential character around 15 min. Due to the short time scale of the experiment, the effect is not as pronounced as for higher fluences. Nevertheless, we can predict t_c within error limits, ensuring that t_c depends only on the number of the ionization events.

From Table 4.2 we notice that BzCl needs at least twice as many photons as BzBr to reach t_c. This can explained by higher ionization and dissociation threshold

energies of BzCl compared to BzBr.

4.4 Coverage Dependent Workfunction Dynamics in $C_6H_5Cl/D_2O/Cu(111)$

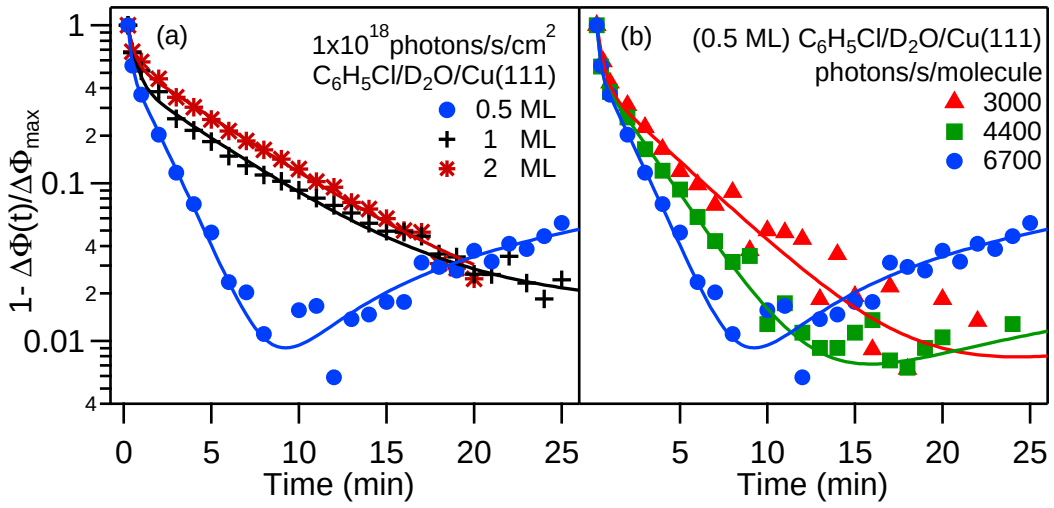

Figure 4.12: Normalised $\Delta\Phi$ (to maximum workfunction change $\Delta\Phi_{max}$) vs photoexposure time is plotted as a function of a) coverage and b) photon flux (0.5 ML coverage) on a semi-logarithmic scale for $C_6H_5Cl/D_2O/Cu(111)$. A multi-exponential function is used to fit the data points and is shown by the solid lines.

From Eq. 4.8, the ionization rate depends on the density of excess electron per molecule. This means, reducing the coverage or increasing the fluence will have the same ionization rate. That is, for the same photon flux, by decreasing the coverage we have a larger photon density per molecule and hence a faster DEA process. Thus, we performed coverage dependent measurements for 0.5 ML, 1 ML and 2 ML of BzCl, and fluence dependent measurement for the 0.5 ML coverage. In Fig. 4.12, both the measurements are shown as a normalised change in workfunction on a log scale vs photoexposure time.

The coverage dependent measurements are shown in Fig. 4.12a), where a similar fluence of 1×10^{18} photons/s/cm^2 was used for all the coverages. This corresponds to 6700, 3400 and 1700 photons/s/molecule for 0.5 ML, 1 ML and 2 ML, respectively. We observe that with decreasing coverage, the slope gets steeper.

On fitting the curves with a multi-exponential fit function, we find that $\lambda_{\Phi slow}$ increases with decreasing coverage, that is, from 2 ML to 0.5 ML $\lambda_{\Phi slow}$ increases from 0.17 ± 0.02 eV/min to 0.2 ± 0.1 eV/min to 0.51 ± 0.02 eV/min (shown in Fig. 4.13 in blue). For the 0.5 ML coverage, we observe the inversion of $\Delta\Phi$ at $t_c = 11$ min. Here, at a flux of 6700 photons/s/molecule, the total number of incident photons in 11 min are $4.6 \pm 0.8 \times 10^6$ photons/molecule. Within error limits, this is in accordance with our earlier observation for 1 ML coverage (Table 4.2), where we expect to see a t_c for total $5.1 \pm 1.1 \times 10^6$ photons/molecule. For the other coverages, the effective photon flux is not large enough to see t_c within the experimental time scales.

We performed fluence dependence measurements to further confirm that the reverse in trend at t_c is indeed in accordance to Table 4.2. The corresponding fluence dependent measurement for the 0.5 ML coverage at 6700 photons/s/molecule, 4400 photons/s/molecule and 3000 photons/s/molecule are shown in Fig. 4.12b). We see that with increasing fluence, the slope gets steeper, suggesting $\lambda_{\Phi slow}$ increases with fluence. The multi-exponential fits give $\lambda_{\Phi slow} = 0.24 \pm 0.01$ eV/min, 0.36 ± 0.02 eV/min and 0.51 ± 0.02 eV/min with increasing fluence. We thus see the same fluence dependent trend as for the 1 ML coverage, where $\lambda_{\Phi slow}$ increases with increasing photon flux, shown in Fig. 4.13 in red. Due to the increased photons/molecule at lower coverages, t_c is observed at 27 min for the lower fluence, 3000 photons/s/molecule, and at 17 min for 4400 photons/s/molecule. Both these cases along with t_c at 11 min for 6500 photons/s/molecule, correspond to a total incident photons of $4.6 \pm 0.8 \times 10^6$ photons/molecule in t_c.

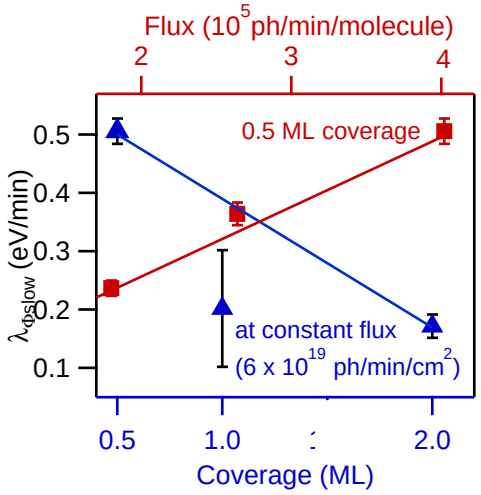

Figure 4.13: $\lambda_{\Phi slow}$ as a function of different coverage at $\approx 1 \times 10^{18}$ photons/s/cm^2 (blue markers) and as a function of flux for 0.5 ML of $C_6H_5Cl/D_2O/Cu(111)$ (red markers).

$\lambda_{\Phi slow}$ corresponding to the different coverages (blue) and different fluences (red) are shown in Fig. 4.13. The coverage is shown on the bottom axis and the fluence is on the top axis. Here, we can clearly see that with decreasing coverage $\lambda_{\Phi slow}$ becomes larger and with decreasing fluence, the rate decreases. The change in $\lambda_{\Phi slow}$ with flux for BzCl at 0.5 ML (Fig. 4.13) and 1 ML (Fig. 4.11) is the same $1.3 \pm 0.1\mu$eV/photons/molecule. This is similar to the change in $\lambda_{\Phi slow}$ with coverage equivalent to $1.52 \pm 0.08\mu$eV/photons/molecule, showing a dependence of the reaction rate on the density of the incident photons.

From these measurements we see that the changes in workfunction (a decrease in amplitude and increase in rate with decreasing coverage) directly depend on the density of the halobenzenes. This supports our claim that these changes are due to charging [10] of the adsorbate layer due to photoelectrons and that we see a signal from the transient ionic state.

4.5 Workfunction Dynamics on Crystalline Ice Surface

In order to compare our data with the STM measurements and the theoretical calculations, which were performed on crystalline ice, we repeated $C_6H_5Br/D_2O/Cu(111)$ with the crystalline ice surface. Julia Stähler discussed the different ice structures and their annealing condition in her PhD thesis [70]. On the basis of her work, we annealed the amorphous ice surface at 148 K for 20 min which should give us the crystallite ice structure. The proof of crystallisation can be seen in Fig. 4.14 where we show the TDS spectra and the 2PPE spectra (inset) for the amorphous and crystallite ice morphologies. The desorption of the amorphous ice starts at 146 K, which after annealing increases to 157 K. For the crystalline structure, due to the long range order, additional energy is needed to break the ordered structure and therefore a higher desorption temperature is expected. Thus, this increase in temperature suggests that we have successfully crystallised the ice layer. However, we can not say anything about the quality of crystallisation. One also notices that the peak of the annealed ice surface plateaus at the maximum. This is a technical mistake, where the detection range was set too low and the measurement went over it, loosing information between 168 K and 173 K. Regardless, we can characterise the ice layer as we are primarily interested in the onset of desorption. Looking at the 2PPE spectra, we observe that the electron solvation peak e_s^- and E_F remain

[10] One would expect an increase in rate and amplitude of workfunction change for lower coverages if it was due to diffusion.

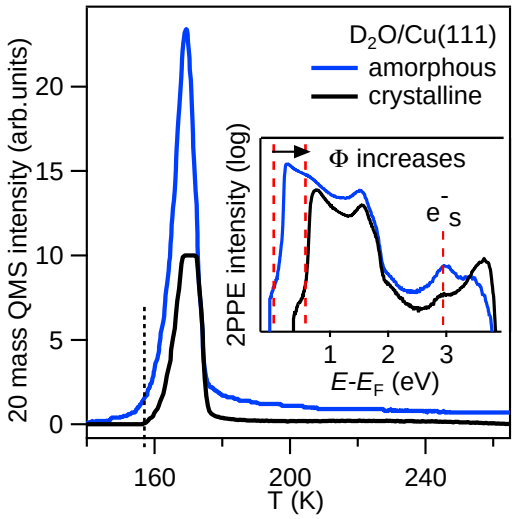

Figure 4.14: Thermal desorption spectra of 4 BL amorphous ice and of crystalline ice. The inset shows the corresponding 2PPE spectra on a log-scale, where, e_s^- is the solvated electron state. The crystalline ice surface desorbs at a higher temperature and has a larger workfunction compared to amorphous ice.

unchanged, but Φ increases by 40 meV. These changes were also reported in [5, 82], where 4 BL of amorphous D_2O were polycrystallised by flashing to 155 K, further confirming crystallisation of our ice layer. Due to annealing, some water is lost from the surface, and so we cannot comment on the thickness of the crystalline ice layer or the size of the crystals.

We adsorbed 1 ML of BzBr on the crystalline ice surface and performed fluence dependent measurements, shown in Fig. 4.15, and compared our observations with that on amorphous ice. In Fig. 4.15a) we show normalised $\Delta\Phi$ on a log scale as a function of photoexposure time for amorphous and crystalline ice. There are two main observations: Firstly, there is no change in $\Delta\Phi$ trend, that is, $\Delta\Phi$ continues to increase even at high fluences. This can be seen clearly in Fig. 4.15c), where we show $\lambda_{\Phi\text{slow}}$ as a function of fluence for both the ice surfaces. For crystalline ice, $\lambda_{\Phi\text{slow}}$ increases at a rate of $0.16 \pm 0.02 \mu$eV/(photons/molecule), which is very small compared to the amorphous ice case, where it increases at a rate of $4.1 \pm 0.5 \mu$eV/(photons/molecule). Here we consider a linear fit because from Eq. 4.8, there is a linear dependence on electron density. In Fig. 4.15a) we also observe that the slow process is slower than that on amorphous ice. For example, at a flux of $\approx$4400 photons/s/molecule, $\lambda_{\Phi\text{slow}}$ for crystalline ice is 12% of amorphous ice. The second observation is that the fast process saturates very fast (from the smaller amplitude at early times), while the

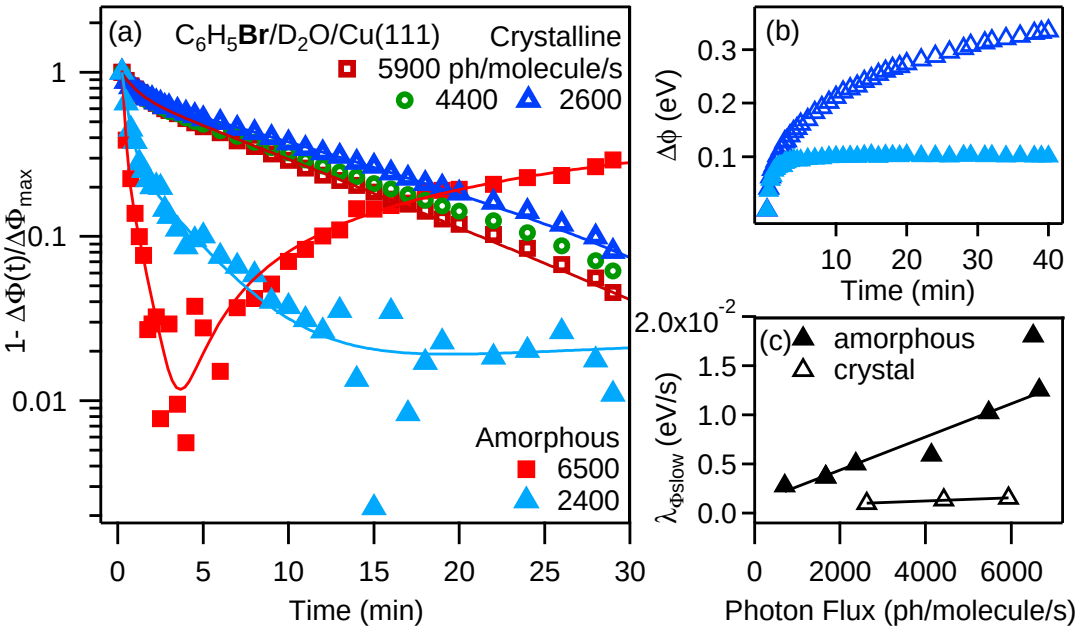

Figure 4.15: Comparing reaction dynamics for crystalline ice (hollow markers) and amorphous ice (solid markers) sublayer in $C_6H_5Br/D_2O/Cu(111)$. a) Shows the normalised change in workfunction as a function of fluence on a log-scale. b) Compares the absolute change in workfunction at $\approx$ 2500 photons/s/molecule for both the ice surfaces. c) Shows the rate of change in workfunction, $\lambda_{\Phi slow}$ with incident photon flux.

slow process takes very long. This is obvious from Fig. 4.15b) where we show $\Delta\Phi$ on a linear scale vs photoexposure time at a low fluence of $1.8\mu J/cm^2$ and $2.04\mu J/cm^2$ on amorphous ice and crystalline ice, respectively. While on amorphous ice, $\Delta\Phi$ saturates in the first 10 min of photoexposure, $\Delta\Phi$ for crystalline ice continues to increase even after 40 min of light. Another interesting observation is that the total workfunction change is more.

The smaller $\lambda_{\Phi slow}$, fluence independence and fast saturation of the fast process can all be explained by the fact that on crystalline ice surface, there are less defects and trapping sites § 2.3.4. As shown in section § 4.2, the trapping sites are the main contributors to EA process. The longer saturation time can be explained by the smaller λ_{ion} which now takes longer to come into 'equilibrium'.

The larger change in workfunction can be explained by a more ordered ice and BzBr layer. Due to a flatter and smoother crystalline surface [158], we can expect a more ordered BzBr layer. This will result in a more aligned BzBr dipoles at the surface and hence a larger dipole moment owing to a larger additive component.

Moreover, the crystalline ice surface has less dangling H-bonds and partial solvation of the reaction products is less likely. Therefore, for the crystalline ice, the workfunction contribution from the individual species is more and so is the cumulative dipole effect compared to the amorphous ice layer, thus showing a larger workfunction effect.

4.6 The Microscopic Fit Model

From Eq. 4.2, we can only determine the total rate (macroscopic rate) of workfunction change λ_Φ. However, we would like to know the individual rates (microscopic rates) $\lambda_{\text{ion}}, \lambda_{\text{relax}}$ and λ_{dissoc} in Eq. 4.3. This form of chemical reaction is common, but rather complicated to solve analytically due to the coupled differential equations. Therefore, we extract these rates by simulating the workfunction dependence on photoexposure time in Microsoft Excel. For each halogen, we take a high and low fluence case and assume λ_{relax} and λ_{dissoc} to be the same for both on account of Eq.4.8, where only λ_{ion} is fluence dependent. Eq. 4.3 can be rewritten as :

$$\begin{aligned} \text{w[C6H5X]} &\underset{-\lambda\_\text{relax}}{\overset{\lambda\_\text{ion}}{\rightleftharpoons}} \text{x}[C_6H_5X^{*-}] \xrightarrow{\lambda\_\text{dissoc}} \text{y}[C_6H_5^* + \text{X}-] \\ \text{w[C6H5X]} &\xrightarrow[\text{(fast)}]{\lambda\_\text{ion-fast}} \text{z}[C_6H_5X^*] \end{aligned} \tag{4.9}$$

where, $[C_6H_5X]$,$[C_6H_5X^{*-}]$,$[C_6H_5^* + X-]$ and $[C_6H_5X^*]$ are the respective concentrations with w, x, y and z their corresponding workfunction contributions or amplitudes. In the model, we assume that the unexcited C_6H_5X molecule has no contribution to the workfunction change and hence w = 1. Since we expect the workfunction contribution from $C_6H_5^* + X^-$ is less than $C_6H_5X^{*-}$, we can set the condition y<x. $\lambda_{\text{ion-fast}}$ is the fast reaction channel yielding excited (or even dissociated) $C_6H_5X^*$ species. For the sake of simplicity, we set $\lambda_{\text{ion-fast}}$ same for all fluxes and all halogens. Since there are a limited number of low energy defect sites and the process saturates, we set an arbitrary saturation limit of s = 0.5. The rest of the parameters are determined without constraints. We used time steps of 0.051 min.

We also introduce the light on - light off feature and take the recovery of the workfunction into account. That is, all the reaction processes take place continuously when the light is on, but on blocking the light, the back reaction and the dissociation channel are active and reduce the workfunction. Note: For simplicity, we assume that the dissociation channel is the final product, the secondary reactions are limited by the dissociation channel, and we don't distinguish between the secondary reaction products and the dissociation products.

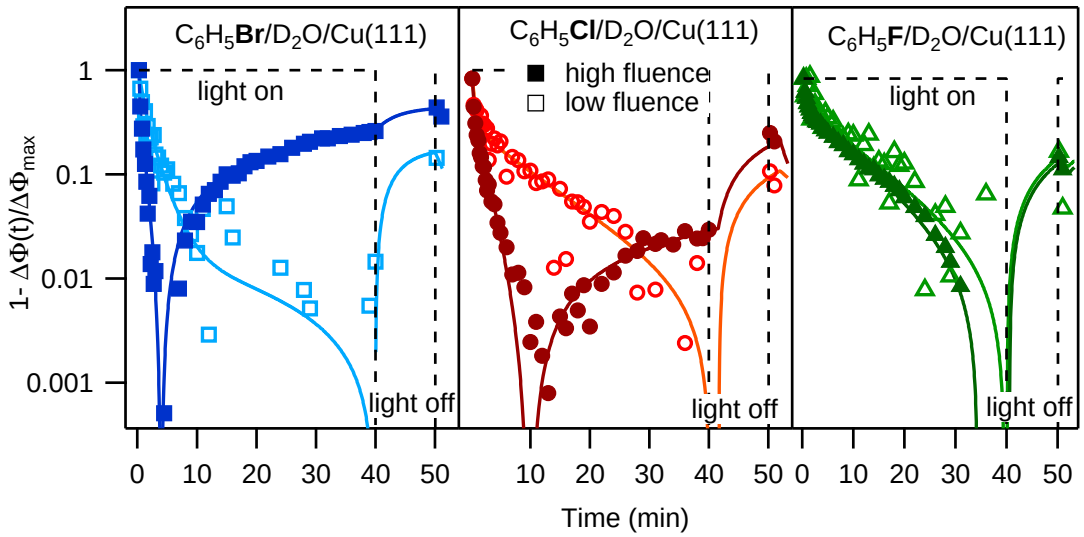

Figure 4.16: Shows the experimental data (markers) with modelled fits (lines) based on the proposed reaction model for a) C_6H_5Br b), C_6H_5Cl and c) C_6H_5F. The model fit and data are normalised in the vicinity of $\Delta\Phi_{max}$ so that the two are normalised by the same factor. Since the normalised data is subtracted by 1, it gives rise to a singularity and hence divergence at the maximum.

Table 4.3: Microscopic rates obtained by modelling the change in workfunction as a function (photons/s/molecule) of time according to Eq. 4.9. The modelling was done for a high and a low fluence data set for the three halogens.

Variable	C_6H_5F		C_6H_5Cl		C_6H_5Br	
Fluence (ph/s/molecule)	369	6883	643	7646	713	6655
λ_{ion} (events/min)	0.038	0.057	0.058	0.48	0.072	0.7
λ_{relax} (events/min)	0.035	0.035	0.057	0.057	0.19	0.19
λ_{dissoc} (events/min)	-	-	0.007	0.007	0.035	0.035
Φ_{ion} (eV)	0.335	0.212	0.209	0.1	0.28	0.082
Φ_{dissoc} (eV)	-	-	0.165	0.058	0.06	0.008

Fig. 4.16 shows the normalised workfunction change from the experimental data points and the corresponding modelled curves for high and low flux values for all the three halogens. Here we used the pre-equilibrium approximation where λ_{dissoc} is much slower than λ_{ion} § 2.1.5. In the figure, we first normalised the data and the modelled curve together to the maximum $\Delta\Phi$. Then this was subtracted by 1 and plotted on the log scale. Normalising and subtracting by 1 means generating a singularity at maximum workfunction change and the curves show an artificial divergence from the

data. We see that our proposed model describes the data well and it agrees with our conclusion that the ionization rate for BzF is much slower than the BzCl and BzBr. However, we found that the amplitudes are not unique solutions. The extracted $\lambda's$ and amplitudes are shown in Table 4.3. We see that the microscopic rates like the macroscopic rates increases from BzF to BzBr, as expected.

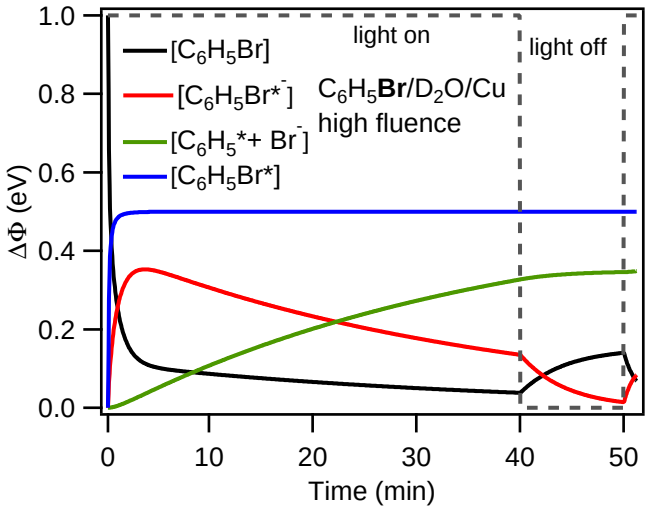

Figure 4.17: Modelled time evolution of the individual concentrations C_6H_5Br, $C_6H_5Br^{*-}$, $C_6H_5^* + X^-$ and $C_6H_5Br^*$ for high fluence $C_6H_5Br/D_2O/Cu(111)$ case.

The evolution of the individual concentrations is shown for the high fluence BzBr case, as an example, in Fig. 4.17. The concentration of species C_6H_5X decreases steadily as the reaction proceeds and the $C_6H_5X^*$ concentration saturates within a few minutes. From the pre-equilibrium approximation, the concentration of $C_6H_5X^{*-}$ also increases fast and reaches a maximum quickly, while slowly leaking into $C_6H_5^* + X^-$. The concentration of the dissociated species increases steadily.

In Fig. 4.18 we show a simulation where rate λ_{dissoc} is much faster than λ_{ion} (steady state approximation). Here it is clear that this situation does not explain the dark time dynamics. A larger λ_{dissoc} will ensure that the population of B remains small even in the presence of light. On blocking the light, only a small contribution to the workfunction change is stopped, and only a small $\Delta\Phi_R$ would be seen. Additionally, at lower fluences λ_{ion} would be smaller, but λ_{dissoc}, which is independent of fluence, will be the same. As a result, t_c would be expected sooner, which is not the case.

The role of the back relaxation - The back reaction depends upon the concentration of the intermediate state. In a simpler equation, that is the absence of the

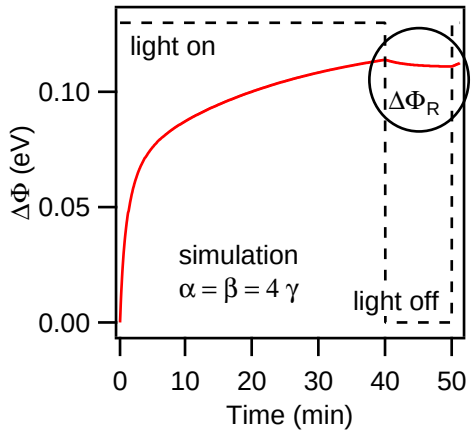

Figure 4.18: Simulation of steady state approximation where the $\alpha, \beta = 4\gamma$, in other words, $\lambda_{\text{ion}}, \lambda_{\text{relax}} = 4\lambda_{\text{dissoc}}$. A very slow recovery is observed on blocking the light.

dissociation channel, the ionization species (now the final species) keep increasing till the system comes into a chemical equilibrium, after which there is no change in the concentration of the reaction species (basic chemical kinematics). A faster back reaction would just result in a faster equilibrium and therefore, the back reaction does not result in an overall decrease of the ionised species. The number of molecules involved in the back relaxation channel depends on the concentration of the intermediate species. Therefore, with the dissociation channel, the back reaction is simply limited (because of the reduced intermediate species). Here the system doesn't come into equilibrium, but the intermediate species reaches a maximum.

Note: Water Coverage and Temperature Dependence

Water Coverage : In addition to the above, we also wanted to study the effect of water coverage on the efficiency of electron transfer to the molecules. If electron transfer from the metal substrate and the organic molecule is due to wavefunction overlap between them, on increasing the thickness of the ice layer, the substrate-molecular wavefunction overlap will be weakened and a smaller electron capture cross section would be expected. If this is not the case and the excess electrons are delocalised electron in the ice conduction band, a change in thickness should not have a significant effect on the reaction rate constants. However, we found that at ≈10 BL of water coverage, the water surface was unstable under light as we saw an increase in photoemitted electron counts in the first few seconds. One could go to lower coverages to avoid this problem, but below 3 BL, we do not have closed ice

layers and the water coverages will not be homogeneous. We would therefore suggest, performing this study in a coverage range from 3-5 BL, where they are known to be stable to photo-illumination [5]

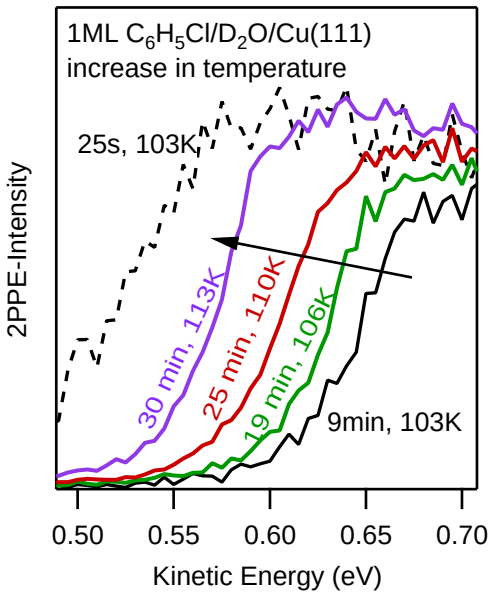

Figure 4.19: Shift of E_{sec} to lower energies (decrease in Φ) once substrate starts to warm up after 19 min.

Sample Heating : In the course of the experiments, we noticed that if the sample was heated slightly (for example, when the cooling is turned off), the increasing workfunction due to photoexcitation starts to decrease, as shown in Fig. 4.19 for $C_6H_5Cl/D_2O/Cu(111)$. Here we show the secondary edge of the 2PPE spectra measured at different photoexposure times and substrate temperature. In the first 9 min of illumination at substrate $T = 103$ K, E_{sec} increases by ≈ 100 meV. The cooling was turned off after 9 min of illumination, but it was only after 12 min that the substrate temperature started to increase at a rough rate of 0.7 K/min. The coloured curves correspond to the 2PPE spectra when the temperature was rising and show that E_{sec} shifts to lower energy, clearly indicating a decrease in workfunction. After 30 min of photo-illumination (18 min of warming), the temperature increases by 10 K and the workfunction decreases by ≈ 80 meV. A possible explanation for this is that the ice structure is sensitive to the substrate temperature. From 85 K to 120 K the porous amorphous ice transitions to compact amorphous ice [87]. Since we are in this en-

ergy window, the density of the amorphous ice may change with slight temperature increases. This would imply that the ice layer is thermally active and is now more mobile to better solvate the already charged species and screen them more efficiently.

4.7 Summary

Co-adsorbed halobenzenes (BzX) with water ice on a Cu(111) substrate was studied with 2PPE spectroscopy. It proved to be an elegant model system for studying charge transfer dynamics in polar environment. Due to ionization of the BzX surface by photoelectrons, a change in workfunction $\Delta\Phi$ with photoexposure time was observed, providing a direct signal of the electron transfer reaction dynamics. Detailed workfunction analysis showed that reaction dynamics like rate constants and (dissociative) electron attachment EA (DEA) probabilities depend on the reactant's electronegativity and electron affinity. The rate of change in workfunction (λ_Φ) was found to be exponential and with three time constants, $\lambda_{\Phi\text{fast}}$, $\lambda_{\Phi\text{slow}}$ and $\lambda_{\Phi\text{slowtc}}$. Though the interpretation of the larger rate constant $\lambda_{\Phi\text{fast}}$ is not clear, due to its saturation in the first few minutes of photoexposure, we assigned it to photo-annealing of or EA at very low energy traps. The smaller rate constant $\lambda_{\Phi\text{slow}}$ showed an inverse dependence on the halogen's electron negativity and decreased from BzBr to BzF. It was therefore assigned to the ionization/dissociation of the BzX molecules. While BzCl and BzBr are known to dissociate, BzF only ionises. The third rate constant $\lambda_{\Phi\text{slowtc}}$ was found only for the dissociating BzCl and BzBr molecules and account for the decrease in workfunction with photoexposure

Due to the long lifetime of the excited state, λ_Φ corresponds to a build-up of the workfunction (photostationary state). λ_Φ of BzF was found to be insensitive to fluence changes, hinting at a fluence independent build-up of the photostationary state. Here, the number of ionization events increase, but not the rate of build-up. Thus suggesting that the ionization process is a second order reaction and depends on the concentration of BzF molecules and excess electron density per molecule. For BzCl and BzBr, due to the dissociation channel, λ_Φ is expected to show a dependence on fluence since it is the macroscopic reaction rate constant. We observe that $\lambda_{\Phi\text{slow}}$ shows a linear dependence on the photon flux, where by decreasing the BzX coverage or increasing the fluence, λ_Φ was found to be larger for BzCl and BzBr. Here, not only a change in the reaction rates was observed, but also in the reaction trends. That is, at a higher photon flux per molecule, $\Delta\Phi$ first increases and then starts to decrease at a critical time t_c. This loss of exponential character was found to depend on the total number of incident photons per molecule in time t_c, suggesting that after a certain number of BzX molecules are consumed, a new reaction pathway dominates,

the ionised species concentration start to drop (pre-equilibrium approximation), or screening between the negative species become non-negligible. Therefore, for higher fluences, lower coverage or faster reaction rates, t_c was observed earlier.

In order to compare our work with theory calculation and STM measurements, which were conducted on crystalline ice surface, we annealed the amorphous ice surface to form crystallite ice phase surface and repeated the experiments on it. While here the dynamics were the same as on amorphous ice, the reaction rates decreased considerably. This could be explained by the drastically decreased electron trapping site on the crystalline surface.

The ionization and dissociation rates also depend on the energy distribution of the excess electrons. Consequently, on tuning down the photon energy to the lower edge of the ice CB, we were able to almost turn off the EA process. It strongly suggests that the enhancement of DEA on polar surfaces is due to pre-existing electron traps and not due to self trapping of electrons due to its solvation. This is because 3.10 eV photon energy is sufficiently large to excite an electron to the solvated electron state and should not affect its density. Other experimental observation support this conclusion, for example, for BzF we see a workfunction change comparable to BzBr and BzCl even though it can be ionised only via the traps, hinting that the traps play a significant role in ionization rate. Our observations are also supported by collaborative theory calculations and STM measurements.

The work also has implications to transient anionic state that have not yet been observed spectroscopically. In fact, it has been debated if they can be probed spectroscopically or not. Since we see workfunction changes due to ionization of the molecules, it implies that we have a direct signal from the transient ionic state allowing us to probe it.

Chapter 5

Electron Transfer Dynamic at C_6H_5X/Cu(111) Interface

With the advent of molecular electronics, understanding organic-molecule adsorption on coinage metals and charge transfer dynamics at metal-organic interface becomes important. Amongst the many organic systems, substituted benzenes are ideal for studying this because of their simplicity and because they serve as a model system for larger planar organic molecules. In § 2.3.5 we showed that the electronic properties of gas-phase halogenated benzenes change as a function of the substitutional group. A less electronegative substitution of the aromatic molecule results in lower LUMO levels and hence can be ionised or dissociated with a lower photoexcitation or electron attachment energy, compared to a -more electronegative substitutions [40]. We would like to check if this holds on a metal surface as well, if so, giving us a systematic tailorability of the energy level alignment. We therefore investigate the problem spectroscopically and follow two approaches. The first approach is to compare the energy level alignment of BzF with previously studied benzene (Bz) [3] and hexafluorobenzene C_6F_6 (BzF_6) [4], which includes identifying the observed unoccupied states in C_6H_6F/Cu(111). The second approach is similar to that in chapter 4, where we studied the charge transfer efficiency qualitatively by studying the chemical kinetics of the ionization/dissociation of the organic layer through workfunction analysis. We also perform coverage dependent studies to investigate the role of screening on charge transfer. The following measurements were performed at 95±5 K.

Since this topic is not the central aim of the thesis, we review here only the preliminary measurements and analysis of C_6H_5X/Cu(111) and lay the seeds for future experiments. In the following chapter, we discuss the first approach in section § 5.1 and the second approach in section § 5.2.

5.1 C_6H_5F/Cu(111): Characterising/Probing the Molecular State

In this section we discuss the role of the substitution functional groups on the molecular energy level alignment at the metal-organic interface by comparing 2PPE measurements of C_6H_5F/Cu(111) with those of Bz and BzF_6. Ideally, we would like to extend the study to BzCl and BzBr as well, however, we do not see any new spectroscopic features on their adsorption.

Two-Photon Photoemission Spectroscopy

Let us first look at spectral changes on adsorption of 1.6 ML of BzF on Cu(111), shown in Fig. 5.1a) and measured with $h\nu = 4.1$ eV. The 2PPE intensity is plotted on a log scale and is presented as a function of binding energy on the intermediate energy scale. We see that on adsorption, the secondary edge moves to lower energy and the workfunction of the system decreases from 4.9 eV (bare Cu(111)) to 4.4 eV. A more comprehensive workfunction dependence on coverage is shown in Fig. 5.1b). We see that for sub-monolayer coverages, the workfunction decreases with increasing coverage and at 1 ML (within error limits), the workfunction saturates to 4.4 eV for BzF. This is similar to benzene [3] and hexafluorobenzene [4] growth on Cu(111) and suggests that at 1 ML we have a mono 'closed' layer. Coming back to Fig. 5.1a), we see two peaks very close in energy at $E - E_F = 3.54 \pm 0.02$ eV and 3.69 ± 0.02 eV and with similar intensities. The Cu 3d-band states at 2.04-2.25 eV, being bulk states, remain unaffected by the adsorbate and are seen at the same energy.

In order to identify the nature of these twin peaks, we performed photon energy dependent measurements. By determining the slope of the peak's kinetic energy vs photon energy, we can determine whether the spectroscopic peak corresponds to an unoccupied, an occupied or a final state § 3.2.1. In Fig. 5.2a) we plot the 2PPE spectra of 1.6 ML C_6H_5F/Cu(111) measured with photon energies ranging from 3.9 eV to 4.15 eV and show only the higher energy part of the spectrum with the relevant binding energies. We observe three peaks (peak1, peak2, and peak3) and a shoulder labelled peak4[1]. To determine the energetic peak position, the peaks were fitted with Lorentzian functions, shown by the solid lines. The individual Lorentzian functions are illustrated for the spectrum at 4.1 eV with the filled area curves.

We now plot the kinetic energy of the peaks as a function of photon energy, shown in Fig. 5.2b). On fitting these curves with a linear function, the slopes of peak1 and peak2 are found to be ≈1 and of peak3 and peak4 ≈2. This implies that the twin

[1] To fit the Fermi edge and the twin peaks, it is important to consider the shoulder, peak 4

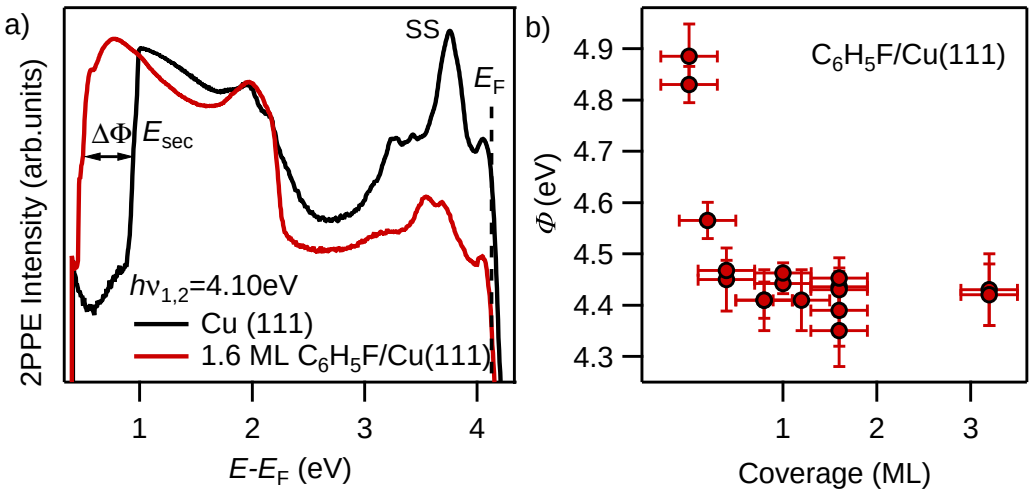

Figure 5.1: a) Photoemission spectrum of 1.6 ML C_6H_5F/Cu(111) in comparison to bare Cu(111), on a log intensity scale. The surface state (SS), E_{sec} and E_F are indicated and a decrease in workfunction $\Delta\Phi$ is observed upon adsorption. b) Decrease in workfunction Φ with increasing C_6H_5F coverage, which reaches a maximum workfunction change of 0.5 eV at 1 ML coverage.

peaks are spectroscopic signals from an unoccupied state, while peak3 and peak4 are from an occupied state. Peak3 has a binding energy of $E - E_F = 4.0$ eV with 4.1 eV photons, which is energetically very close to the Fermi edge binding energy of $E - E_F$ =4.1 eV. This suggests that it is a resonant excitation of E_F, which would explain the shift in the peak energy. The resonance is expected to be with the first image potential (IP) state of Cu(111) which is expected to be shifted to higher kinetic energy on adsorption of the molecules. For a resonant excitation with E_F, the IP state should have a binding energy of 4.07 eV (verified shortly). The binding energy of the shoulder corresponds to 3.84 eV, which corresponds to 0.2 eV below the Fermi and can be assigned to the surface state. A shift in the surface state is reasonable due to polarisation of the surface dipole by the adsorbate [159]. A suppressed surface state signal has been observed for Bz [3] and BzF_6 [4] as well for coverages up to 1 ML and 3 ML, respectively. The binding energy of the surface state in the case of BzF_6 was found to decrease by 50-100 meV, which is similar to what we observe. These observations suggest a weak interaction between the surface state and the benzene derivatives. For a photon energy of 3.88 eV, we see only one peak since there is a resonant excitation between the surface state and the unoccupied state at $E - E_F$ =3.7 eV. This results in a broadening of the resonant peak and primarily one peak is observed. With larger photon energies, we walk out of resonance and both the

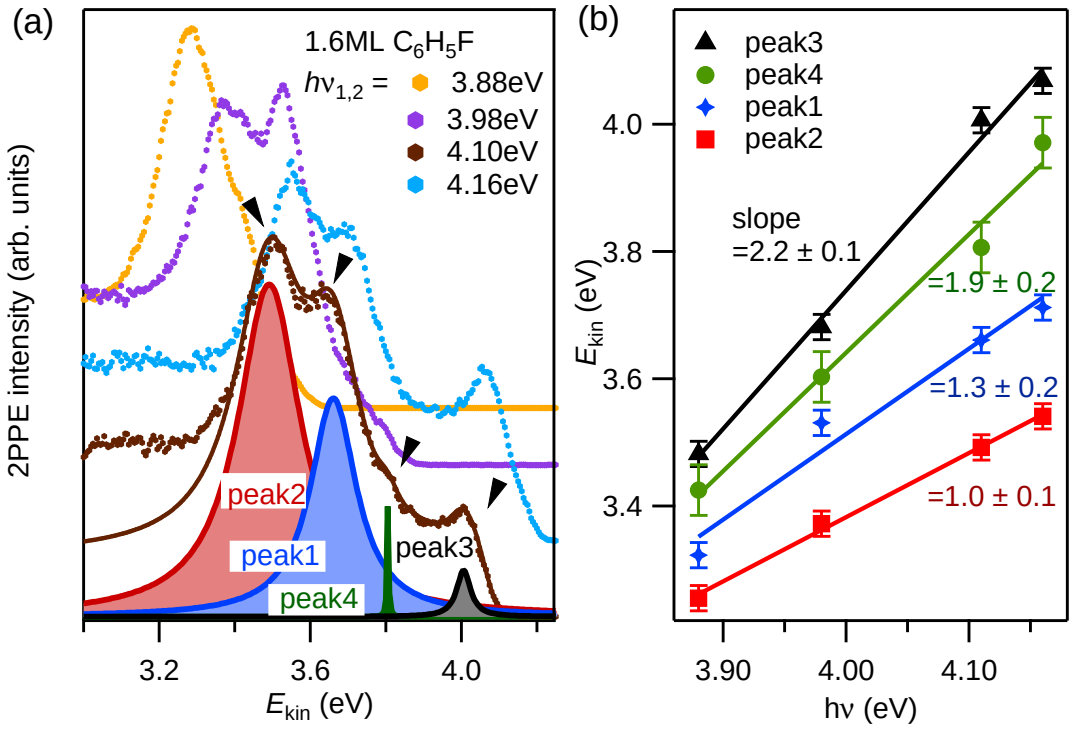

Figure 5.2: Spectral features of 1.6 ML C_6H_5F/Cu(111) are identified by performing photon energy dependent measurements. a) Photoemission spectra of 1.6 ML C_6H_5F/Cu(111) for different photon energies. Only the high energy part of the spectrum is shown where the new spectral features are observed. b) Kinetic energy of the corresponding spectral features are shown as a function of photon energy and are fitted with a linear fit function.

peaks are resolved. The twin unoccupied states could either correspond to modified image potential state of the metal, a LUMO level of the molecule, or a molecular derived state such as a hybrid of the image potential state and the molecular state. The exact origin is difficult to determine here, and so we look at their evolution as a function of coverage to get more information.

In Fig. 5.3 we show the 2PPE spectra of bare Cu(111) and of 0.8 ML and 1.6 ML adsorbed BzF, on a linear scale. These measurements were performed with 4.1 eV photons, large enough to pump the Cu(111) IP state at $E - E_F$ =4.06 eV. Note that the IP state is seen at the same binding energy with respect to the Fermi edge with and without the BzF adsorption. A similar observation was made in the case of BzF_6 in [4]. However, IP states are bound to the vacuum level and due to a decrease in Φ on adsorption, the IP states shift to lower binding energy in C_6H_5F/Cu(111).

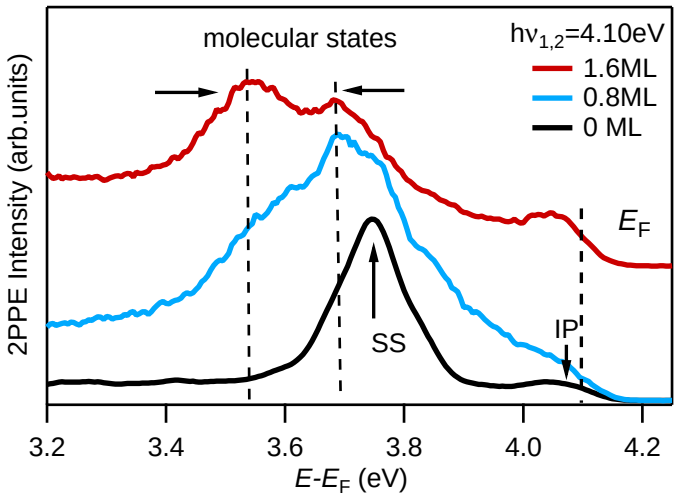

Figure 5.3: 2PPE spectra of different C_6H_5F/Cu(111) coverages. A molecular state is observed at 3.7 eV above E_F at 0.8 ML and an additional state is seen at 3.5 eV above E_F for 1.6 ML. IP refers to image potential state.

Comparing the 0.8 ML and 1.6 ML coverages, we see the higher energy unoccupied peak for both the coverages. The lower energy unoccupied peak is well defined only for 1.6 ML coverage and is seen as a shoulder for 0.8 ML coverage. Since the lower energy peak is seen only for incomplete coverage here, and has been observed for only incomplete coverages of Bz [3] and BzF_6 [4], suggests that its origin lies in the differently oriented molecules in the incomplete coverage which would have a different binding energy compared to those in the complete/closed layer. At 0.8 ML we don't have a closed monolayer coverage and all the molecules are expected to have the same orientation, hence giving a single peak.

2PPE: C_6H_5Cl/Cu(111) and C_6H_5Br/Cu(111) Though this section is dedicated to BzF, we would like to discuss a few aspects about BzCl and BzBr, before discussing BzF's observations in detail. 2PPE was performed for different coverages of C_6H_6Cl/Cu with 6 eV photon energy and the corresponding workfunction is shown in Fig. 5.4a) as a function of coverage. The direct photoemission spectra for the different coverages can be seen in the Appendix B.1. We see that with increasing coverage the workfunction decreases like for BzF and was found to be 4.37 eV for 1 ML, but stabilised at 4.32 eV at 1.5 ML. However, unlike C_6H_5F/Cu(111), no spectral feature was observed (we measured up to 2.8 ML). This is shown in Fig. 5.4b) where we show

the 2PPE spectrum for 1 ML BzCl adsorbed on Cu(111) on a log scale and measured with 3.79 eV photon energy. The data is noisy since it was recorded for a short time due to the photoinduced workfunction change. While we see the Cu 3d-band state in the 1.5 eV-1.7 eV energy range, the surface state $E - E_F = 3.63 \pm 0.05$ eV and a clear Fermi cut-off, no spectral feature is seen at higher binding energy, where we would expect a molecular state resonance. Like BzF, the surface state is shifted to higher binding energy by ≈0.23 eV, which is more than that in the case of BzF, suggesting a stronger surface-molecule interaction. A possible reason for not observing an adsorption induced new spectral feature is that the lowest antibonding molecular state π_4^* is dissociative for BzCl and it is found to be 0.4 eV below the vacuum energy [38]. With a workfunction of 4.3 eV and a photon energy of 3.9 eV this state should be accessible, but because it is dissociative, one can not detect it. Another possibility is that it is not spectroscopically accessible (due to the photoemission matrix elements). However, we have reason to believe that the state is being photoexcited due to a change in workfunction with photoexposure, discussed in the next section § 5.2. A similar observation was made for BzBr, where no spectral feature was observed. Here the workfunction was found to be the least compared to BzF and BzCl, corresponding to 3.95 eV for 3 ML.

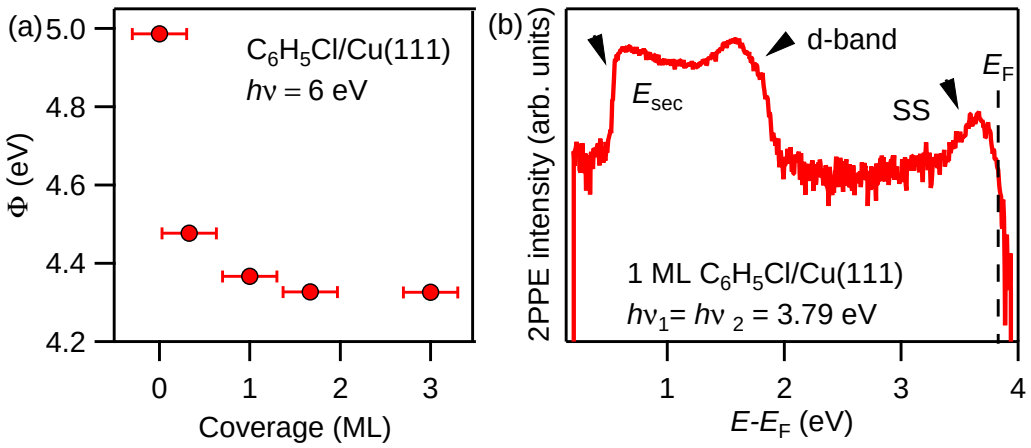

Figure 5.4: a) Change in workfunction on adsorption of C_6H_5Cl/Cu(111) as a function of C_6H_5Cl coverage. b) 2PPE spectrum of 1 ML C_6H_5Cl/Cu(111) on a logarithmic intensity scale.

Discussion: Comparison with C_6H_6 and C_6F_6

In order to discuss the above observations in more detail, we compare our observations with those of Bz and BzF_6 adsorbed on Cu(111), shown in Fig. 5.5 for different coverages. Here the 2PPE intensity is plotted as a function of final state energies where $E_{\text{final}} - E_{\text{F}} = E_{\text{kin}} + \Phi - E_{\text{kin(Fermi)}}$.

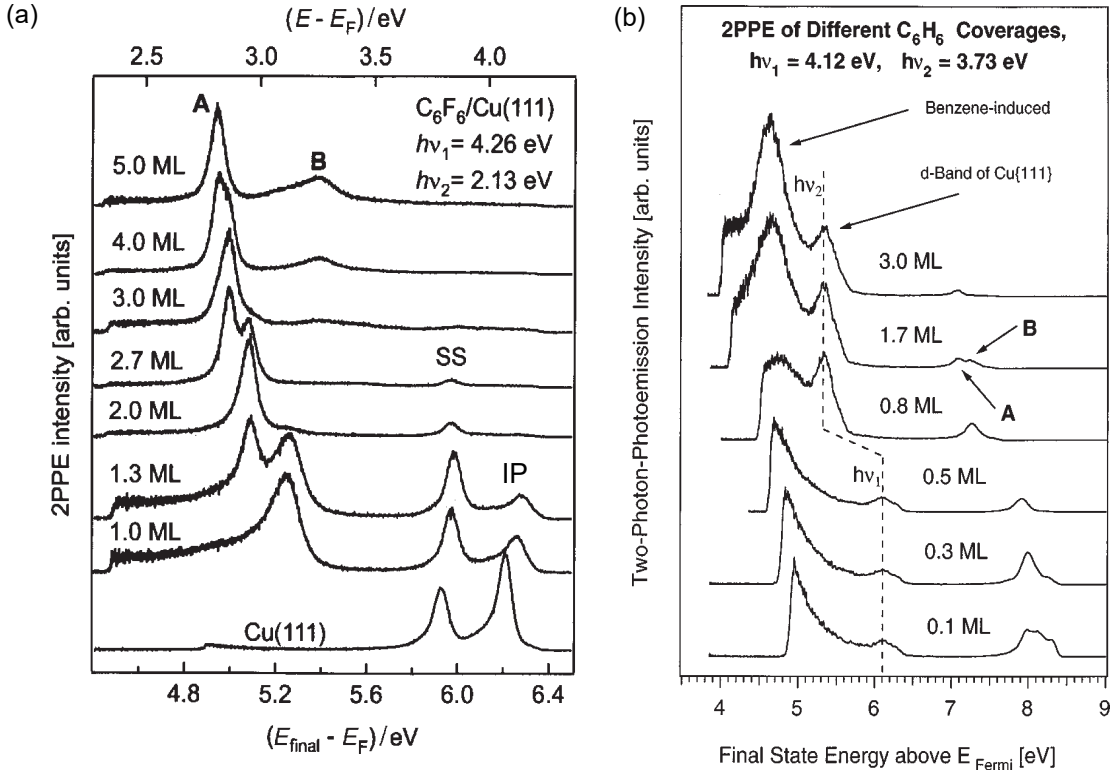

Figure 5.5: Coverage dependent 2PPE spectra of a) C_6F_6/Cu(111) [4] and b) C_6H_6/Cu(111) [3], taken from literature. The evolution of the molecule derived states, the modified IP state and SS are shown. States A and B refer to molecular derived LUMO states in the case of C_6F_6 and to molecule-derived image potential states in the case of C_6H_6.

For both Bz and BzF_6, the workfunction of the system decreases on adsorption and is 4.2 eV for Bz and 4.5 eV for BzF_6 for 1 ML coverage. The change in workfunction due to adsorption of 1 ML of BzF lies in between these two values and is ≈4.4 eV. Benzene molecules adsorb on coinage metals with their π electrons which results in a decrease in workfunction due to the push-back effect (or pillow

effect) [30, 74, 101, 102] § 2.3.2. Therefore, a larger change in Φ for Bz than BzF_6 is justified by the larger $\pi-$character of Bz which polarises the surface dipole more. In BzF the functional group substitution lies between Bz and BzF_6 in terms of electronegativity and hence the amount of π-character is also in between the two. This can also be seen from the potential energy maps in Fig. 2.11, where the negative potential at the ring centre (corresponding to π electrons) is more than that of BzF_6 but less than Bz. Thus, this explains the intermediate workfunction change in BzF. A similar Φ trend based on the electronegativity of the substitution is seen in the mono-substituted halogens BzX, where the change in workfunction increases from F$\rightarrow$Cl$\rightarrow$Br as 4.4 eV$\rightarrow$4.37 eV$\rightarrow$3.95 eV, in the order of decreasing electronegative substitution. Here too, the density of π electrons at the ring centre decreases more with more electronegative substitution, that is from F to Br. The systematic decrease in workfunction change with increasing electronegative substitution already shows that the gas-phase systematics holds even on adsorption on the metal surface. It also supports the electrostatic potential model (§ 2.3.5) and verifies that the benzene derived interactions can be explained qualitatively on its basis.

The twin peaks in 1.6 ML BzF are found at $E_{\text{vac}} - E = 0.9$ eV and 0.75 eV below the vacuum level. The two lowest antibonding states of BzF in the gas-phase are found to be at 0.8-0.9 eV [2, 40] (referred to as π_4^*) and 1.4 eV [40] (referred to as π_5^*) above the vacuum level. On adsorption, the molecular LUMO levels are expected to be polarised by the free electron gas of the metal due to Pauli's repulsion between the two and by the IP state [31, 33, 38, 101, 102]. We can estimate the shift of the lower LUMO state by the metal's electron cloud from Eq. 2.8, where $z = 2.5$ Å is the distance of flat lying benzene molecules from the metal surface (for flat lying Bz [103]) and ϵ_0 is the vacuum permittivity. This explains a shift of 1.44 eV and we can expect the 0.9 eV π_4^* state to be at 0.53-0.43 eV below the vacuum and the 1.4 eVπ_5^* state to be at the vacuum level. The observed unoccupied state is in this vicinity, suggesting that it is the lowest π_4^* molecular state. Alternatively, if the unoccupied state is the polarised π_4^* state, then a shift of 1.65 eV is expected for the higher bound state ($E_{\text{vac}} - E$ =0.75 eV), corresponds to $z = 2.18$ Å [2], which is reasonable. However, the permittivity should not be strictly considered as vacuum permittivity due to the molecules permittivity. For both Bz and BzF_6, we see that at coverages around 1 ML new spectroscopic features appear which were identified as unoccupied states. In the

[2]There is some uncertainty as to the orientation of the molecules, where Koch et al. [103] calculated submonolayer adsorption to be tilted by 45° and according to [117] it is found to be initially flat. If a tilted geometry is considered then $z = 2.2$ Å assuming the maximum radius of the molecule = benzene radius of 5.5/2 Å [3, 160] + radius of chlorine atom 1.75 Å.

case of Bz, these features were identified to be modified IP states and the LUMO state was observed as a final state [3]. For BzF_6, the new peaks were assigned to the σ^* molecular resonance state [159], which was considerably lowered compared to its gas-phase due to ionization by copper's IP state.

For Bz [3] and BzF_6 [4], two peaks are reported in literature for the intermediate coverages and a single peak for complete coverage. With the help of TDS measurements and angle resolved spectroscopy, authors of references [3] and [4] were able to determine that Bz and BzF_6 grow in complete layers. The molecules form islands before forming a closed film and for the intermediate/incomplete coverages, some of these islands have a higher coverage [3, 29]. The second peak arises due to a different binding energy of the bilayer islands in the incomplete layer (due to various reasons like distance from the substrate and polarisation effects). In the case of BzF_6, with increasing coverage (including the intermediate layer peak), the molecular state binding energy shifts to lower energies ($E - E_F$). This was explained by the broadening of the potential well at the metal surface (formed due to high electron affinity of BzF_6) due to larger coverage thickness. This causes the molecular states to shift to the bottom of the well, resulting in a lower binding energy. A similar lowering of the molecular state with increasing coverage was observed for C_6H_5Cl/Ag(111) [33]. We too observed that the second peak in intermediate coverage has a smaller binding energy, thus hinting that the second peak arises from bilayer island growths and is a molecular state. For Bz, the intermediate layer peak is seen at a higher binding energy (referenced to Fermi energy) compared to the closed monolayer peak, since they are IP states. This is because IP states are polarised to higher energies on adsorption of electronegative adsorbate [161] and for higher coverages, the polarisation is stronger due to a larger adsorbate concentration. This supports our earlier assumption that the second peak is a molecular derived state and not an IP state. Another supporting fact is that the twin peaks in our case are too close in energy (150 meV) to be consecutive IP states. Further, neither can it be a modified IP state of Cu(111) which is at 0.85 eV [71] below vacuum for bare Cu(111). This is because, on adsorption the IP state will be polarised towards the vacuum level by the molecules and an upward shift in the IP state is expected [161]. Therefore, we assign both the unoccupied states to the π_4^* molecular resonance state.

To conclude: The LUMO states for Bz, BzF and BzF_6 are thus 4.6 eV, 3.7 eV and 3.5 eV above the Fermi, respectively. Like for the workfunction, this shows clear systematics that with the decreasing π character of the benzene ring, less charge transfer between the metal and the molecule takes place which reduces the lowering of the LUMO level, thus following the same systematics as in the gas-phase [2, 26, 38, 40] and is in agreement with the theoretical models [1, 35, 99, 162], also discussed in § 2.3.5.

Static Angle Resolved 2PPE

To study the degree of localisation of an electron in the molecular derived LUMO state, we performed static angle-resolved 2PPE measurements and calculated the dispersion of the surface parallel momentum $\bar{k}_{\parallel}$ of the state $E(\vec{k}_{\parallel})$. We recorded the 2PPE spectra for different angles, θ between copper's surface normal and the ToF spectrometer tip by rotating the sample about the vertical axis, shown in Fig. 5.6a). The measurements were performed on the 1.6 ML BzF layer with 4.1 eV OPA pulses and the $E - E_F = 3.53$ eV molecular state was investigated. The peak position was determined by fitting them with a Lorentzian function. With the help of Eq. 3.4, we can calculate the surface parallel momentum component $\bar{k}_{\parallel}$ corresponding to the θ and plot the binding energy of the state as a function of $\bar{k}_{\parallel}$, as shown in Fig. 5.6b). We see that the momentum has a positive dispersion and to obtain the effective mass, m_{eff} of electrons in this state, we fit the curve with the parabolic function given in Eq. 3.5. This was found to be $0.8\pm0.3\ m_e$, which is less than the free electron mass. Conversely for 1 ML BzF_6, the electron in the molecular derived state has a larger effective mass of $m_{\text{eff}} = 1.9 \pm 0.2\, m_e$ and is more localised, which decreases with increasing coverage [4].

The difference in m_{eff} between the BzF and BzF_6 is tentatively assigned to the asymmetry in BzF, where BzF molecules have 2-fold (C_{2v}) symmetry [100] while BzF_6 have 6-fold symmetry (D_{6h}) [100]. Looking at the potential energy surface of BzF_6 in Fig. 2.11, a strong negative potential is on the ring backbone which would result in potential maxima and minima in the plane of the flat lying molecules, localising the electrons in the potential well [4]. However, in the case of BzF, the potential energy surface from the centre of the ring to F is smoother, due to the pull of the π electron cloud by the strong electronegativity of the fluorine atom. In a layer of flat lying BzF, the potential field is thus less corrugated than that in BzF_6, where the electrons can get trapped in well defined potential wells. A less corrugated potential surface will result in a more free electron like character. We also performed time- and angle- resolved 2PPE measurements to study the temporal evolution of the momentum dispersion of the molecular state. These are discussed in the Appendix A.2

Time resolved measurements with the optimised NOPA (60 fs cross correlation and 40 nm NOPA fundamental bandwidth) were performed for 1 ML coverage. Here we see a tail from the IP state which makes it difficult to discuss the molecular state features. Nevertheless, the data is discussed in the Appendix A.1. The tail of the IP state can also be partially due to a broader bandwidth of the NOPA fundamental beam and hence the NOPA pulses should be further improved.

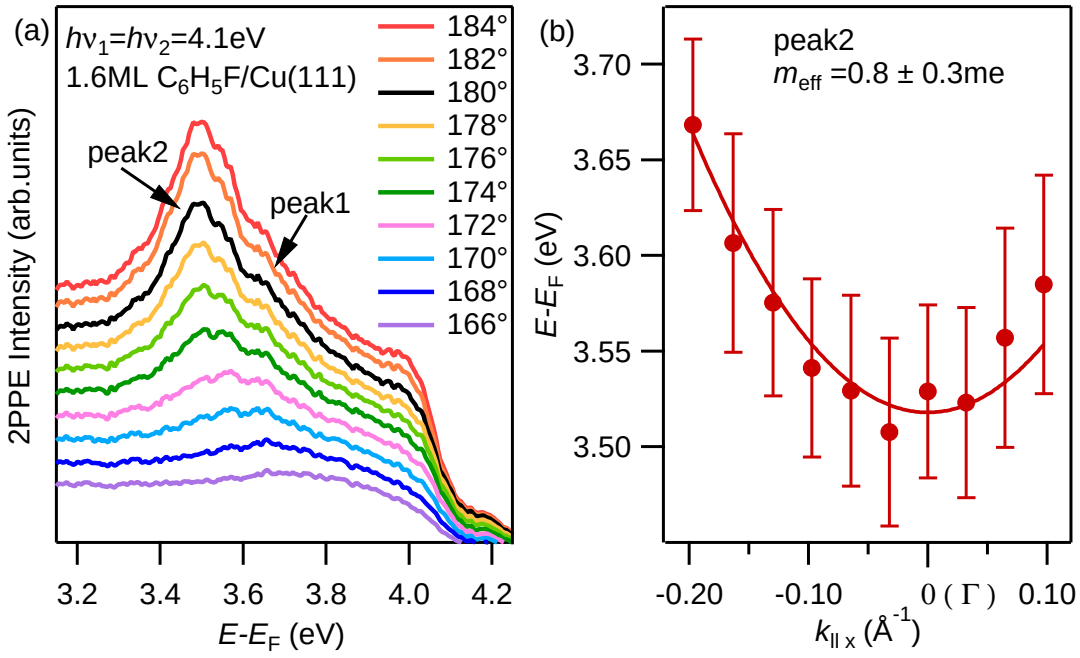

Figure 5.6: Static angle-resolved 2PPE measurement of 1.6 ML C_6H_5F/Cu(111), measured with the ToF. a) 2PPE spectra recorded at different sample rotation angle. The binding energy of peak2 corresponds to the molecular derived state in the bilayer and is b) plotted as a function of parallel momentum, which corresponds to the rotation angle. The solid line is a parabolic fit function giving the effective mass of this state.

5.2 C_6H_5X/Cu(111): Chemical Kinetics

We now study the chemical kinetics of the photoinduced ionization/dissociation of C_6H_5X/Cu(111) in a similar way as was done on the polar ice surface in chapter 4. We measure the corresponding change in workfunction on continuous photo illumination of the sample by performing monochromatic 2PPE spectroscopy and determine the reaction rates. Comparing the trend of workfunction change for the different halobenzenes and their coverage, we can study the role of halogen substitution on interface dynamics from a macroscopic point of view. We report here the first experiments performed towards this aim.

In Fig. 5.7 we show the change in workfunction as a function of total photoexposure time for the different halobenzenes adsorbed at 1 ML and 3 ML coverages. BzF was measured with 3.8 eV photon energy and is shown in Fig. 5.7a). We find that for 1 ML coverage, the workfunction of the system does not change. However for higher

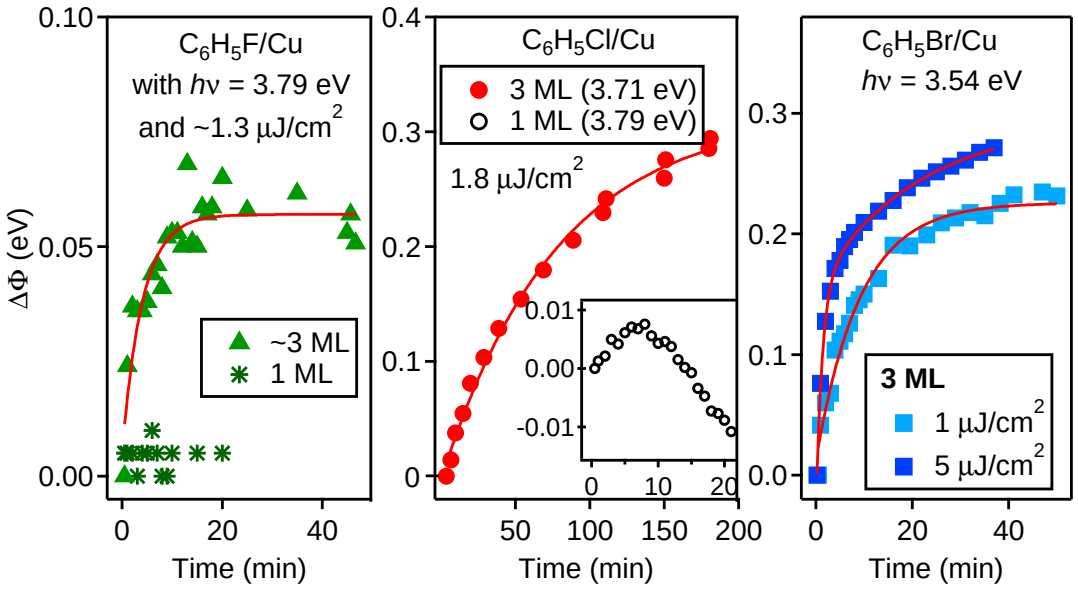

Figure 5.7: Change in workfunction of C_6H_5X/Cu(111) as a function of photoexposure time, for monolayer and multilayer coverages.

BzF coverages, like 3 ML, we see that the workfunction increases with increasing photon dose. This hints at an accumulation of negative charge at the surface as a consequence of formation of long living ionised states or due to electron trapping at the surface.

A change in workfunction for BzCl is also observed and is shown in Fig. 5.7b). The measurements were performed with 3.7 eV for both the monolayer and the multilayer coverages. Interestingly, the workfunction of the monolayer coverage first increases and then decreases, similar to high fluence measurements of BzCl, BzBr/D_2O/Cu(111). For the multilayer coverage a single exponential increase in workfunction is seen. We also see a workfunction increase for BzBr, however here we have measurements only for 3 ML coverage, shown in Fig. 5.7c). The measurements were performed with 3.54 eV photon energy and at two different fluences of $1\mu J/cm^2$ and $5\mu J/cm^2$.

Discussion:

The observation of a workfunction change for the multilayer coverage but an absence for the monolayer coverage for BzF is explained by a decreased metal-adsorbate wavefunction overlap for the higher coverages. Being spatially further away from the

metal substrate, molecules in the multilayer have a weaker wavefunction overlap with it. Further due to the screening of the multilayer coverages from the metal substrate by the monolayer coverage, wavefunction overlap between the two further decreases. As a result, electrons excited into the BzF multilayer are expected to have a longer lifetime (observed in the 1.6 ML tr-2PPE measurements in Fig. A.1). However, since we don't see any workfunction change on photoexposure of 1 ML, where we excite into the non-dissociative π_4^* molecular state, we argue that the workfunction changes in the multilayer is not due to a build-up of the ionised molecular state, but due to electron trapping in the film. Another possible mechanism is that since we are in the multilayer regime, partial solvation of the electrons in the polar BzF coverage is possible. If the electron lifetime in the 3 ML coverage is sufficiently large[3], a build-up of the negative charge will be observed as an increase in workfunction. On fitting the workfunction dependence on time, we find that the data can be described by a single exponential function with a time constant $\lambda_F = 0.25 \pm 0.05$ eV/min and saturates within 20 min which is much faster when compared to C_6H_5X/D_2O/Cu(111).

The change in workfunction for both BzCl and BzBr molecules can be explained by photoinduced excitation of their antibonding π^* state. On adsorption, the molecular LUMO levels are expected to be redshifted due to the IP state, as was in the case of BzF. The π^* state for BzCl and BzBr lie at 0.73 eV and 0.67 eV [2] above the vacuum in the gas-phase and are roughly expected to shift to 0.86 eV and 0.92 eV below the vacuum. Please note that this is only a rough estimate and many factors like size, angle and polarisation of the molecules will play a major role. With a workfunction of 4.36 eV for 1 ML BzCl, 4.32 eV for > 1.5 ML BzCl and 3.95 eV for 3 ML BzBr, the binding energies are $E - E_F = 3.45$ eV and 3.4 eV, respectively. In fact, inverse photoemission spectroscopy of multilayer C_6H_5Cl/Cu(111) by Dudde, et al. [38]found the π^* state to be at 0.4 ± 0.35 eV below the vacuum. Due to intersystem crossing of the π^* and dissociative σ^* states, the molecules can dissociate as well by excitation into the π^* state. Thus, these states can be populated by photoelectrons with the photon energies used, ionising and dissociating the BzCl and BzBr molecules. For BzBr, the σ^* state overlaps with the π^* states energetically[4], further enhancing the dissociation cross-section. In the case of BzCl, the σ^* state is ≈ 1.8 eV higher and cannot be populated. A resonant excitation from the molecular ground state to an antibonding state via photon absorption in the molecule

[3]The requirement is that not all excited electrons or excited molecules relax back before the next laser pulse, within 4 μs

[4]Do not confuse with the C_6H_5X/D_2O/Cu case, where the σ^* channel is ignored. Here the electron energy is referenced to ice conduction band and is less than 1 eV, much lower than electron energies involved in direct excitation from Cu to C_6H_5Br in C_6H_5Br/Cu.

is also possible[5]. For C_6H_5Cl/Ag(111), the low energy cut-off for this process was found to be at 350 nm (3.54 eV) by Zhou and White [33]. This cut-off is much lower than the gas-phase limit of 266 nm (4.66 eV) [109]. The redshift of the dissociation limit is explained by charge transfer between the metal and molecule, resulting in a repulsive interaction (Pauli's repulsion), which lowers the LUMO level [33, 102]. The neutral molecule can also be ionised by thermal electrons [24] like hot electrons and the anionic state can then be readily dissociated [33], giving a redshift of the gas-phase dissociation energy. Since gas-phase BzBr LUMO levels are lower than BzCl (by 60 meV), photoexcitation of the molecular resonance is expected. This implies that the ionization/dissociation of BzCl and BzBr is highly probable via electron attachment and resonant photoexcitation of the molecule. Thus, the change in workfunction in BzCl and BzBr coverage is due to a build-up of negative charge of the ionised and dissociated BzX species and the rate at which this build-up takes place reflects the macroscopic charge transfer rate from copper to BzX.

In the multilayer BzCl and BzBr case, like for multilayer BzF, a decreased coupling of the higher coverage molecules from the surface is expected, causing the ionised/dissociated species to have a longer lifetime and ensuring their build-up. Since both electron attachment and photoexcitation of the molecular resonance are probable, one would expect to see two exponential rate constants to describe both these processes. However, we see a single exponential build-up of the workfunction, suggesting either that the two processes cannot be distinguished from each other kinetically and both the processes have a similar rate constant (the two mechanisms are equally probable), or that one is more dominant that the other and we don't see a signal from the second process.

The mechanism for the decreasing workfunction trend in 1 ML BzCl is not clear, however, a possible reason can be a dominant secondary reaction between the dissociated species, similarly to C_6H_5Br/D_2O/Cu(111) in chapter 4. For example, the ionised species can bind to the metal substrate and get dissociated by the metals hot electrons [30, 33, 103, 163] giving a benzene radical and an halogen anion which binds to the metal to form a halogen-metal complex [30,163]. While the ionised/dissociated species result in an increase in workfunction, the secondary reaction products may decrease the workfunction. Since our monolayer is not compact, surface diffusion is possible. STM measurements [117] found that the BzX molecules are physisorbed on Cu(111) surface and are mobile even at 11 K. Therefore, it is reasonable to expect the dissociated species to recombine and form secondary products with an overall decrease in surface dipole. A good test for this hypothesis will be to measure the

[5]On adsorption, the molecules interact with each other and are hybridised by the metal which results in band formation of the molecular states

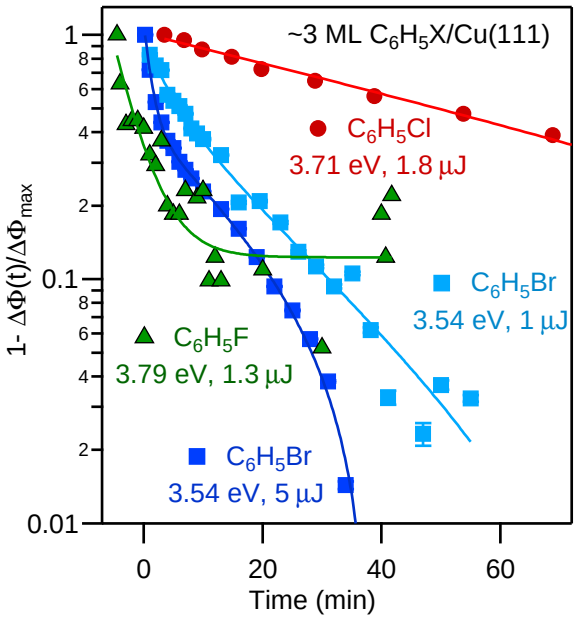

Figure 5.8: The change in workfunction of the multilayer coverage is plotted on a log-scale. The C_6H_5F curve lies on top of C_6H_5Br curve at earlier times and is thus offset by - 5 min. C_6H_5Br is described by two exponential functions, while C_6H_5F/Cl are described by a single exponent.

monolayer workfunction response of BzBr. Another speculation is the strong metal-molecule interaction, where the negative charge of the ionised halobenzene is screened by the metal's free electron gas.

We replot the multilayer curves for the three halogens on a log-scale after normalisation to the maximum workfunction change $\Delta\Phi_{max}$ in Fig. 5.8. For BzBr, the high and low fluence curves have an initial steep slope followed by a gradual slope and need two exponential functions to describe it. On fitting the curves with a double exponential fit function, we found $\lambda_{\Phi Br\text{-}slow} = 0.04 \pm 0.03\,eV/min$ and $\lambda_{\Phi Br\text{-}fast} = 0.2 \pm 0.1\,eV/min$ for the low fluence and $\lambda_{\Phi Br\text{-}slow} = 0.049 \pm 0.005\,eV/min$ and $\lambda_{\Phi Br\text{-}fast} = 0.77 \pm 0.03\,eV/min$ for the high fluence. For BzCl and BzF, a single slope is seen, suggesting a single exponential function which on fitting gives, $\lambda_{\Phi Cl} = 0.013 \pm 0.001\,eV/min$ and $\lambda_{\Phi F} = 0.25 \pm 0.05\,eV/min$ rate constants for BzCl and BzF, respectively. The order of magnitude difference between BzF and BzCl is explained by the different mechanisms responsible for the change in workfunction. That is, for BzCl we expect the increase in workfunction due to ionization/dissociation of the molecule due to excitation into a molecular state. However, for BzF the change in workfunction is expected to be due to electron trapping in

the molecular layer (for example by defect sites)[6]. In the case of BzBr, the fast rate constant is of the same order of magnitude as the rate constant of BzF, hinting that the fast rate constant is due to electron trapping by the molecular film. However, this leaves us with an obvious question as to why we don't see a fast component for BzCl, for which we don't have any clear explanation. The slower rate constant of BzBr is similar to that of BzCl and can be assigned to the build-up of the ionised/dissociated species via molecular excitation (electron attachment and photoexcitation), since this mechanism is highly probable for both BzCl and BzBr. The larger (slow) rate constant of BzBr compared to BzCl is justified by its lower LUMO level and the additional direct excitation channel into the σ^* state. In BzBr, we also observe that the fast and slow rate constants are larger for the high fluence measurements compared to the lower fluence one which is explained by an increased number of events due to increased photon density per molecule. This is similar to that observed in C_6H_5X/D_2O/Cu(111), where we see a linear dependence of the reaction rate constants on the fluence.

Conclusion: Charge transfer dynamics can be studied as a function of workfunction change. Screening plays an important role in charge transfer which is clearly seen in the case BzF and BzCl. Substitution based dependence of the charge transfer dynamics is observed in the case of BzCl and BzBr, which supports the comparative LUMO level alignment study of Bz, BzF and BzF6 in the previous section. An advantage of studying charge transfer dynamics through the macroscopic workfunction change is that we don't have to know the exact positioning of the energy levels to qualitatively discuss the efficiency of the process. Determination of the energy states can be difficult due to the strong metal molecule interaction which gives rise to new hybrid energy levels like the metal-molecule interface states [102]. We speculate a different mechanism for charging of the multilayer organic film for BzF from that of BzCl and BzBr.

5.3 Summary

On adsorption of C_6H_5X on Cu(111), we observe a decrease in workfunction which changes the most for BzBr at 4.0 eV (3 ML) followed by BzCl at 4.3 eV and least for BzF at 4.4 eV. A similar trend is observed on comparing BzF to literature values of Bz [3] and BzF_6 [4], where the change in workfunction decreases with increasing electronegative substitution, that is, from 4.2 eV for Bz [3], 4.4 eV for BzF and 4.5 eV

[6]This is similar to that in the C_6H_5X/D_2O/Cu(111) case, where the observed fast rate constant was assigned to electron attachment at preferential trapping sites.

for BzF_6 [4]. This is explained with the help of potential energy maps where a more electronegative substitution decreases the π character of the molecule and hence results in a weaker push back effect between the metal's electron cloud and the π electrons of the molecule.

With 2PPE spectroscopy, we observed a molecular derived spectroscopic feature for C_6H_5F/Cu(111) with a binding energy of 3.7 eV above the Fermi level, which we assign to the lowest LUMO state of the molecule with π-character and referred to as π_4^* state in literature [2, 40, 100, 164]. This modified molecular state lies in between the LUMO derived state observed for Bz and BzF_6 on adsorption on Cu(111), which were observed at 4.6 eV [3] and 3.5 eV [4] above the Fermi level, respectively. This too reflects a direct dependence of the polarizability of the molecular states by the free electron gas in the metal on the electronegativity of the functional group. This is very interesting since it reflects the gas-phase systematics and verifies the many models that describe π molecule adsorption on metal surfaces [1, 2, 26, 35, 38, 40, 99, 162]. We also showed that the molecules grow in closed layers and with increasing coverage the binding energy of the LUMO state decreases. We observed no new spectroscopic features for C_6H_5Cl/Cu(111) and C_6H_5Br/Cu(111) up to 3 ML of coverage. Angle-resolved 2PPE measurements showed that the molecular state at 3.53 eV above the Fermi, has $m_{\text{eff}} = 0.8m_e$, which is speculated to be due to the asymmetric potential energy surface of the BzF molecule.

We also studied the charge dynamics by determining the macroscopic photoinduced reaction rate constant, observed indirectly via workfunction measurements, similar to that in chapter 4. We were able to determine the macroscopic workfunction change rate constants which for multilayer coverage were $\lambda_{\Phi\text{Br-slow}} = 0.04 \pm 0.03\,\text{eV/min}$ and $\lambda_{\Phi\text{Br-fast}} = 0.2 \pm 0.1\,\text{eV/min}$ for the low fluence and $\lambda_{\Phi\text{Br-slow}} = 0.049 \pm 0.005\,\text{eV/min}$ and $\lambda_{\Phi\text{Br-fast}} = 0.77 \pm 0.03\,\text{eV/min}$ for the high fluence, $\lambda_{\Phi\text{Cl}} = 0.013 \pm 0.001$ and $\lambda_{\Phi\text{F}} = 0.25 \pm 0.05$. For BzBr, a double exponential workfunction change trend is observed with a fast and slow rate constant. The slow rate constant was found to be similar to BzCl and is tentatively assigned to photoinduced excitation of the molecule, while the faster rate constant was found to be similar to that of BzF and was assigned to electron trapping by the molecular film. For BzCl and BzBr, both resonant photoexcitation of the organic molecule and electron attachment are expected to be equally responsible for the workfunction change, since only a single exponential rate constant is observed for BzCl. A larger rate constant for BzBr compared to BzCl was explained by the lower π^* and σ^* LUMO levels. We hence showed that the π system interaction with other reactants/bodies depends primarily on the substituent group. This was further supported by comparative analysis of Bz, BzF and BzF_6 series.

We observe that screening (from the molecular layer and the free electron gas in the metal) plays a crucial role in determining the charge transfer rates. For BzF, we see no change in workfunction on photoexposure for 1 ML coverage, but an exponential increase for the multilayer coverage, justified by the screening of electrons in the multilayer by the molecular monolayer. In the case of BzCl, the monolayer coverage shows initially an increase in workfunction which quickly starts to decrease with photoexposure time, while the multilayer coverage shows a single exponential continuous workfunction increase. This is expected to be due screening by the metal's free electron gas and due to diffusion of the dissociated species.

Chapter 6

Time- and Angle- Resolved 2PPE of D_2O/Cu(111) and Decay Dynamics of C_6H_5F/D_2O/Cu(111)

When an electron is exited from the metal into the ice conduction band (CB), it can either get trapped and solvated at pre-existing e^- traps, or attach to the organic molecule. Solvated electrons are the smallest anion that can be realised in nature. Because of their small spatial extent and high reactivity, they have gained widespread interest [10]. Water is a universal solvent and the environment for many vital reactions and processes, making it an important medium for DEA. As a result, solvated electrons in amorphous ice (D_2O/Cu(111)) have been studied with 2PPE spectroscopy where their lifetime [5,93], energetic and momentum localisation [6,87] and relative position [92] in the ice layer were investigated. An interesting observation was that the m_{eff} of solvated electrons at larger delays was found to be negative. These measurements were performed with the ToF spectrometer. In order to verify this observation and as a comparison between the ToF and pToF, we performed trangle resolved measurements of 4 BL D_2O/Cu(111) with the pToF. We compare our results with those in [5,6], where they discuss their observations. We also studied the binding energy stabilisation and changes in its lifetime on coadsorption of C_6H_5F. We discuss these observations in this brief chapter below.

6.1 Time resolved 2PPE of D_2O/Cu(111) and C_6H_5F/D_2O/Cu(111)

In this section we investigate the time resolved dynamics of solvated electrons before and after the adsorption of the BzF. We performed tr-2PPE measurements with 1.95 eV and 3.79 eV photon energies and 55 fs pump-probe cross correlation on D_2O/Cu(111) and C_6H_5F/D_2O/Cu(111). We used the position sensitive pToF for these measurements to be sensitive to the dispersion (discussed in the next section § 6.2) as well. The respective 2PPE spectra are shown in Fig. 6.1 in the left panel as a false colour plot with the binding energy as a function of pump-probe delay and the photoemission intensity on the false colour scale. In both these cases, we see a short living state at higher binding energies $E - E_F > 3.05 \pm 0.05$ eV corresponding to the ice conduction band[1] and a long living state at 2.97±0.05 eV corresponding to the solvated electron e_s^- state. Another clear feature of the spectrum is that the binding energy of the e_s^- decreases with increasing probe delay, suggesting localisation of the state. The tr-2PPE image of bare water are similar to those by Gahl, et al. [5], shown in § 2.3.4 and by Stähler [87], which were measured by the ToF spectrometer.

On adsorption of C_6H_5F, there are some differences observed in the 2PPE spectrum. Firstly, the secondary edge shifts to higher energy, giving an increase in work-function, which is also shown in the one colour 2PPE spectrum in Fig.4.1. Secondly, the lifetime of the solvated state was found to decrease on coadsorption as shown in Fig. 6.1b). In the figure, the time evolution of the solvated state is extracted from the image plot by taking an energy cut in the range of 2.74 eV - 3.15 eV for water and 2.73 eV - 3.3 eV for BzF and plotting the 2PPE intensity as a function of pump-probe delay $\Delta\tau$ (constant energy range). The data was fitted with an exponential function convoluted with the Gaussian of the pump-probe cross-correlation (XC). We thus measured the lifetime of the solvated state for the two cases equivalent to 90 ± 8 fs for only water and 60 ± 7 fs for coadsorbed C_6H_5X, showing a faster relaxation on adsorption. This implies that there is some wavefunction overlap between the solvated electron and the molecular overlayer. This is reasonable as it has been found that the solvated electron complexes are formed at the ice-vacuum interface [87, 92] and a weak interaction between the early localised electrons and BzF is still possible. However, a large overlap is not expected since the wavefunction of the electrons gets confined with solvation and theoretically (Appendix C), we do not expect an

[1] We cannot determine a clear higher energy cut-off since our photon energy is not large enough. We use a photon energy of 3.79 eV which is the expected CB upper limit [165]

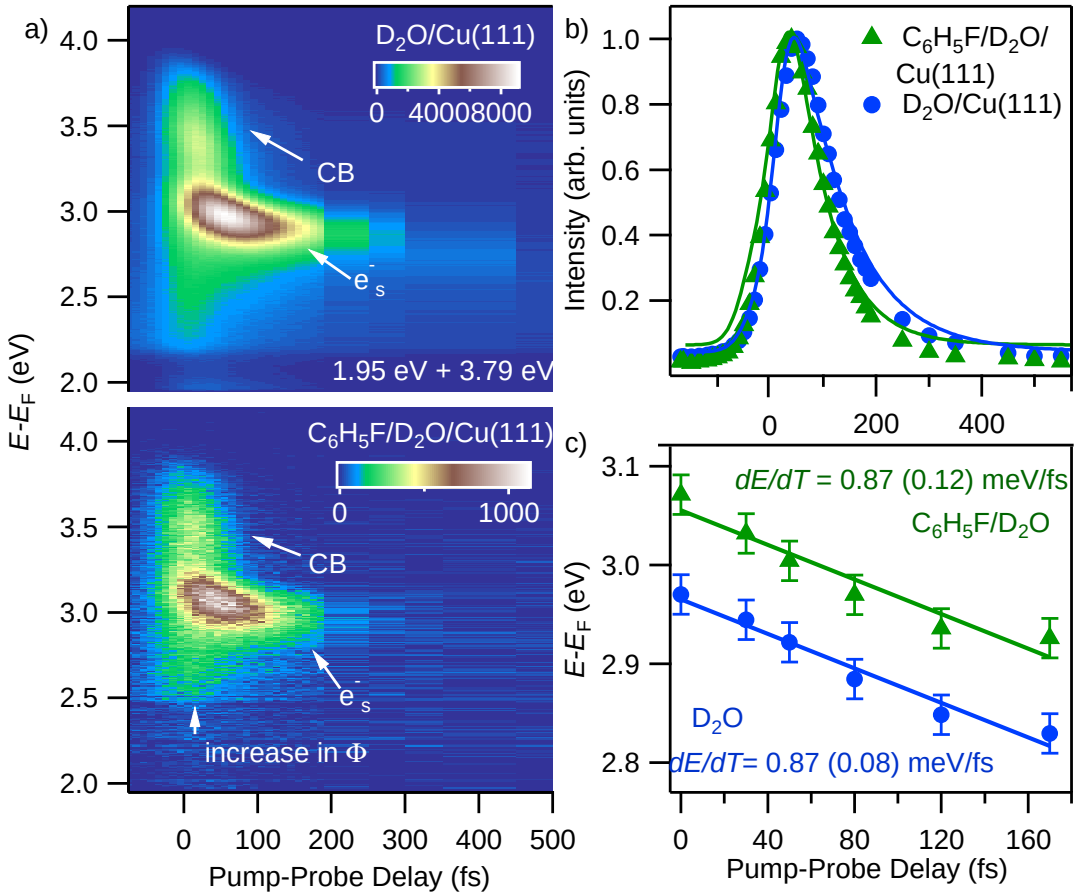

Figure 6.1: a) False colour plot showing the time resolved dynamics of solvated electrons in water with and without coadsorbed C_6H_5F. Binding energy (UV pump) as a function of pump-probe delay is shown on the x-y plane and the 2PPE intensity is shown on the false colour scale. CB refers to the conduction band of ice and e_s^- refers the solvated electron state. b) 2PPE intensity of e_s^- vs pump-probe delay, showing a shorter lifetime after adsorption of C_6H_5F. c) Binding energy as a function of pump-probe delay, showing the same rate of relaxation in e_s^- binding energy with time.

electron attachment below the ice CB, where the solvated electrons are energetically localised.

Lastly, we see that the C_6H_5F/D_2O/Cu(111) data is noisy compared to the D_2O/Cu(111). This is due to experimental constraints, where ionization of the organic layer results in a workfunction change (see chapter 4), the measurements were performed at a much lower incident flux than those used for D_2O/Cu(111).

We also compared the rate of localisation of the solvated state for the two cases and show it in Fig. 6.1c). The change in binding energy of the solvated electron as a function of time is the same with and without BzF, which is 0.87 ± 0.12 meV/fs. This means that the solvation shell is unaffected by BzF, similar to how it is impervious to the metal substrate, shown in [87].

At this point, we would like to point out that there are discrepancy's between our decay lifetime and energetic stabilisation of the solvated electron on pure ice and those measured by Stähler et al. [70, 87]. We can describe the solvated electron's decay dynamics with a single exponential. However, they found that the electrons initially decay with a time constant of 140 fs and after 150 fs with a slower 316 fs time constant. They also measured a much slower stabilisation rate of 0.27 meV/fs. We can explain the discrepancies by the lack of data points at later delays. Since the motivation behind these measurements was to perform excellent quality angle-resolved measurements, we measured fewer delay points at later times. Hence we used larger steps between the subsequent delays after 150 fs because of which the decay dynamics cannot be resolved well at later delay steps. Thus we do not have full information after 150 fs and the information on the slow decay channel and binding energy relaxation at larger delays is lost. It has been shown that the early time delays are more sensitive to changes in substrate or ice structure [87]. Therefore, because we are interested in the qualitative effect of BzF on the solvated electron, it is reasonable to look into only the early time delays of the relaxation dynamics.

To sum up: we see that on adsorption of BzF, the lifetime of the solvated state decreases but its stabilisation rate remains unchanged. This suggests that while BzF does not influence the solvated shell in anyway, it weakly interacts with the electron itself.

6.2 Tr- and Angle Resolved- 2PPE of D_2O/Cu(111)

In Fig. 6.1, we see a spectroscopic signal of electron solvation in amorphous ice which is its decreasing binding energy with delay. Another way to determine the localisation is to measure its band dispersion as a function of pump-probe delay.

We used the position sensitive pToF spectrometer for these measurements, because of its sensitivity to the electron's photoemission angle. One thus gains information on the band dispersion as well as the kinetic energy distribution (2PPE spectrum). The tr-2PPE spectrum is shown above in Fig. 6.1a). The corresponding dispersion cone of the in plane momentum (momentum component parallel to the surface axis) along the $\vec{k}_{\parallel x}$ direction is shown in Fig. 6.2. Here the y-axis gives the

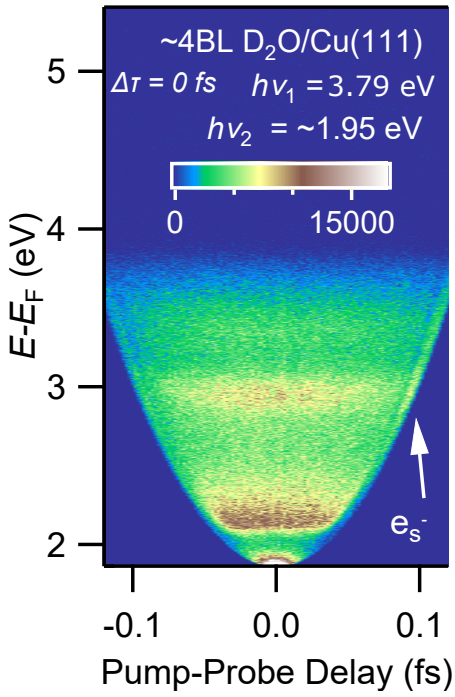

Figure 6.2: Time- and angle- resolved 2PPE of 4 BL D_2O/Cu(111) measured with pToF spectrometer showing the momentum dispersion cone measured by the pToF at 0 delay. Binding energy vs surface parallel momentum along the horizontal x-axis $\vec{k}_{\|x}$ are plotted in the x-y plane and the 2PPE intensity on the false colour scale.

kinetic energy, the x- axis gives the momentum and the false colour scale gives the intensity. Similar dispersion cones are obtained for the measured time delays and for the $\vec{k}_y$ direction. We only show the image for $\vec{k}_{\|x}$ direction and $\tau = 0$ fs.

One finds that the e_s^- peak at $E_{\text{kin}} = 3.1$ eV kinetic energy has some dispersion. In order to quantify this, the corresponding energy spectra at different momentum and different delay steps are extracted and the peak position is determined by fitting them with the Lorentzian function. As an example, the energy spectra for some of the momentum steps at 0 fs delay are shown in Fig. 6.3a). Here we can see the shift of the binding energy to higher-lower-higher values for momentum from left to right (or vice-versa). The corresponding dispersion curves for the different delays are shown to its right in panel b). We see that with increasing delay, the momentum dispersion curve gets flatter and the m_{eff} increase. This suggests that the electrons get heavier and hence more localised with time. At the 300 fs delay point, a negative dispersion is seen. This compares well with the past studies by Gahl, et al. [5, 6] which were performed with the ToF, shown in panel c). Here too a decreasing effective mass with increasing delay was observed and at delays larger than 100 fs a negative dispersion was seen. The broad energy peaks (solvated state and the conduction band), which need to be decoupled from each other to determine the dispersion of the solvated peak, and the finite bandwidth of the solvated electrons in the momentum space,

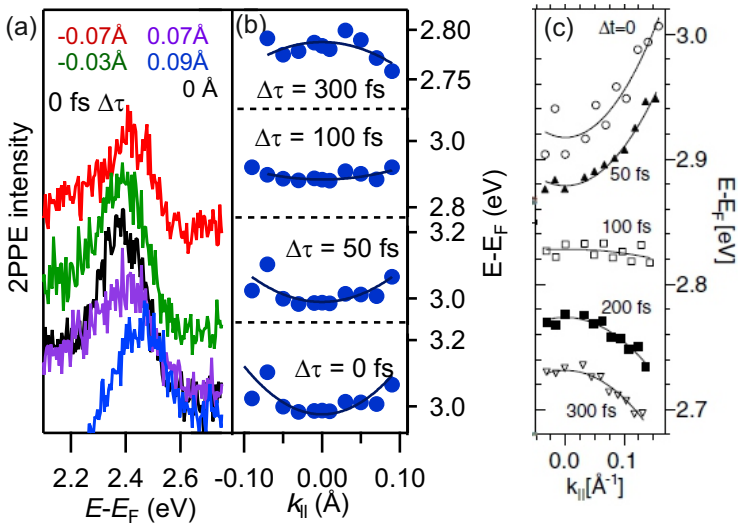

Figure 6.3: Time- and angle- resolved 2PPE of 4 BL D_2O/Cu(111) measured with pToF spectrometer. a) 2PPE spectra for different parallel momenta ($\vec{k}_{\|x}$) values at 0 delay, corresponding to Fig. 6.2 and measured with 1.95 eV+3.79 eV. b) Binding energy as a function of $\vec{k}_{\|x}$ and showing momentum dispersion curves at different delays. The curves are fitted with a parabolic function to determine the effective mass m_{eff}. c) m_{eff} at different delays measured by Gahl, et al. [5, 6] with ToF spectrometer.

gives rise to an apparent negative dispersion. A more detailed explanation can be found in [6]. Therefore, the similarities between our measurements and those by Gahl, et al. [6], verify that the negative dispersion in not a spectrometer artefact and that the pToF spectrometer is capable of reproducing ToF measurements.

6.3 Summary

To summarise, we studied electron solvation in 4 BL amorphous water ice adsorbed on Cu(111) with tr-2PPE and tr- and angle resolved- 2PPE. We identified the electron solvated state at $E - E_F = 2.97 \pm 0.05$ eV and the ice conduction band spectral feature, which were found to match the literature values [5, 87]. The lifetime of the solvated state was found to be 90 ± 8 fs, lower than literature value of a few picoseconds. The solvated state shows energy stabilisation, which is observed as decreasing binding energy of the solvated state with increasing probe delay. The rate of localisation was found to be 0.87 meV/fs in our measurements, which is faster than the literature value of 0.27 meV/fs. The difference in our measured lifetime and lo-

calisation rate of the solvated state from literature values is explained by the large delay steps after 150 fs. It was found that on adsorption of 1 ML BzF, the lifetime of the solvated electron decreases to 60 ± 7 fs, while the solvated state localisation rate remains the same. This suggests that though on adsorption the organic molecules interact with the metal substrate and the solvated electron, the solvation shell remains unaffected. We also performed tr-angle resolved measurements in the 2PPE configuration and used the pToF as an electron spectrometer. We compared our momentum dispersion measurements of the solvated electrons with those by Gahl, et al. [6] which were measured by the ToF. We thus verify their observation with a different electron spectrometer. We were able to reproduce their measurements and show that with increasing probe delay the band gets flatter, suggesting a localising electron with time. At higher delays, for example, 300 fs, the dispersion becomes negative. The apparent negative dispersion is observed due to the wide overlapping energy bandwidth of the solvated electrons and conduction band electrons spectral features and due to the finite bandwidth of the solvated electrons in the momentum space.

Chapter 7

Conclusion and Outlook

The present thesis investigated electron transfer probability and dynamics on a polar surface ($C_6H_5X/D_2O/Cu(111)$) and at a metal-organic interface. Studying charge transfer dynamics spectroscopically through workfunction measurements has many advantages. Not only does the photoemission technique provide flexibility in accessing the energy levels, one doesn't need to know the position of the resonant molecular state to qualitatively study the charge transfer efficiency. Literature shows that on polar surfaces, the DEA cross section of organic molecules is enhanced. Though a model has been proposed based on electron solvation and localisation due to self trapping of electrons in the polar environment [11], it has not been explicitly proven. With the aim to verify this model, this works shows that the enhancement on polar surface cannot be due to the pre-localised solvated electrons due to energetic constraints. Though ice indeed enhances DEA, it is found that the pre-existing electron traps are the main player in the enhancement and that the delocalised electrons are responsible for DEA of the organic molecules. The above work was done in collaboration with theory and STM groups.

$C_6H_5X/D_2O/Cu(111)$ Workfunction studies of coadsorbed halobenzenes on D_2O and Cu(111) were performed with the help of 2PPE spectroscopy, where the charging of the organic layer by photoelectrons results in an increase in workfunction. Therefore, by studying the rate of change in workfunction, the efficiency of DEA for the different molecules were determined and was found to increases from BzF to BzBr, reflecting the C-X bond strength and providing evidence for ionization/dissociation of the organic layer. The experiments were repeated under different experimental conditions like coverage, photon dose, excitation energy, and water structure. Through comparative analysis of all these studies, it was found that the catalysis of the DEA

on ice was unlikely due to solvated electrons, but instead due to delocalised electrons exited from the metal substrate. An important observation in support of this was that on using lower photon energies, a significant decrease in the reaction rate constants was seen, even though the photon energy was sufficiently large to photoexcite electrons into the pre-solvated state in ice. In addition, collaborative work with theory and STM showed that at pre-existing electron traps, the organic molecules are polarised and have a lower ionization threshold energy, hence suggesting that the enhancement is due to electron traps in ice.

Another important aspect of this study is that a direct signature from the transient ionic state in a complex environment is observed, since the transient ionic state results in a workfunction change. A spectroscopic signal from such states has not been seen in the past.

C_6H_5X/Cu(111) Fundamental processes like charge transfer, localisation, energetic stabilisation and electron back transfer at the metal-molecule interface is of great interest, in particular to the molecular organic industry. With this motivation, studies were also performed on bare Cu(111) surface. With two photon-photoemission spectroscopy, a molecular derived state of C_6H_5F/Cu(111) could be identified. It was found to have an energy of 3.7 eV above the Fermi and could be assigned to the lowest π^* LUMO level of BzF. In comparison to the literature values of the LUMO state of benzene (4.6 eV above the Fermi) [3] and hexafluorobenzene C_6F_6 (3.5 eV above the Fermi) [4] adsorbed on Cu(111), the LUMO of BzF lies in between. Thus a systematic dependence of metal-organic molecule interaction (polarisation) on the extent of electronegative substitution of the benzene molecule, similar to that in the gas-phase [40], is shown. Angle resolved 2PPE measurements further showed this molecular-derived state has an effective mass of $0.8m_e$. A molecular derived spectral feature was not seen in the case of BzCl and BzBr and could be explained by their dissociative nature.

Reaction kinetics of photoinduced ionization/dissociation of the halobenzenes were studied through rate of change in workfunction. It was observed that while the workfunction of monolayer BzF was constant on photoexposure, it increased for a multilayer coverage. The LUMO level is being populated for both the monolayer and multilayer coverages. This suggests that the build-up of the negative charge, which leads to the workfunction increase, is due to electrons trapped in the molecular layer. In addition to BzF coverage observations, monolayer BzCl showed a decrease in workfunction on photoexposure, while multilayer showed an increase. In the case of co-adsorbed ice layers also a photoexposure dependent workfunction increase is observed. These observations together highlight the role of screening by the metals

electron gas, the molecular layers and the ice bilayers, that is, a dominant signal of the increasing workfunction with photoexposure time is seen only when there is screening between the metal and the BzX molecules. Workfunction changes are also observed for multilayer BzBr and had a larger rate constant compared to BzCl, reflecting a dependence on the substitution group. Here, the change in workfunction is due to the ionised/dissociated species which can happen via electron attachment to the resonant molecular LUMO level. The ionization can also happen via direct photon excitation of the molecule (HOMO to LUMO excitation), unlike adsorption on ice, because of the strong metal-molecule interaction. Hence, the charge transfer mechanism at C_6H_5F/Cu(111) interface and the C_6H_5Cl/Cu(111) interface are different. For BzBr, a double exponential increase in workfunction is observed, where the fast rate constant is due to electron trapping by the molecular film (similar to BzF) and the slower rate constant is due to ionization/dissociation of the molecules (similar to BzCl).

We thus showed that as in the gas-phase, halogenated benzenes can be characterised by the extent of the electronegativity of the substituted group, where a more electronegative substitution is weakly reacting compared to a less electronegative substitution and can be explained by potential energy surfaces of the molecules. Not only the halogen, but also the number of halogens (as in the case of C_6F_6 from literature) and the thickness of the adsorbed layers effect the molecular level alignment and hence the charge transfer probability. Since these are first measurements of C_6H_5X/Cu which already show rich dynamics, it is worth exploring this system in more details.

Outlook

In the course of the detailed study of DEA of BzX on ice, many questions were answered, but many more arose. For one, it is curious to know if for fluences even higher than those used in this study the reaction rate constants λ increases or saturates. A saturation would suggest that there exist an optimal ratio of photons per molecule which has been reached and any more photons will not have an effect. Alternatively, one could enter a non linear regime and observe a more interesting behaviour. Another interesting study would be changing the amorphous ice thickness to determine if the DEA is via conduction band electrons or via 'direct' excitation of photoexcited electrons from the metal. That is, to see if the role of water in electron transfer is simply to decouple the organic layer from the metal or it it plays an active role. However, one would have to be careful with the coverage range they use, since coverages less than 3 BL are incomplete layers and higher coverages show photo reaction.

It is worthwhile to investigate how heating or annealing of the amorphous ice after photoillumination will effect the reaction rate constants. This would mean supplying activation energy to the dissociated species and the ice molecules allowing them to either diffuse faster or solvate better.

Since molecular energy level alignment is an important industrial question, $C_6H_5X/D_2O/Cu(111)$ 2PPE measurements may be repeated with systematically decreasing the photon energy. The cut-off energy where no more (or drastically decreased) workfunction change is observed will give the experimentally determined ionization energy level of the molecule. This is also a good check for the theoretical calculations of our collaborators. The same can be done on bare Cu(111) to determine the position of the LUMO of the molecules, especially for BzCl and BzBr, where we don't see a direct spectroscopic molecular feature. $C_6H_5X/Cu(111)$ measurements were preliminary, but they gave a glimpse of the rich dynamics at the metal substrate. It would therefore be interesting to learn the effect of submonolayer coverages in $C_6H_5X/Cu(111)$ on the workfunction change rate constants and if the interesting behaviour we see for 1 ML BzCl also hold for 1 ML BzBr. It is suggested that the future experiments also investigate the high fluence behaviour of BzBr and compare it to BzCl.

While we were able to identify the nature of the unoccupied state that appears up in BzF/Cu(111), time resolved measurements with better energy and time resolution pulses are suggested to be repeated and be performed for different coverages. This would help to confirm if the molecular derived state is indeed a LUMO level or a hybridised image potential state. Time- and angle- resolved measurements with the pToF show that the effective mass of the molecular-derived state is $0.8m_e$ and decreases with pump-probe delay. Since these are first measurements, the experiment should be repeated with the ToF spectrometer to confirm this trend. A possible explanation for this observation is that momentum dispersion of this state is polarised by the photons pulses and hence depends on the intensity. A suggested experiment to verify this hypothesis is fluence dependent time- and angle- resolved measurements, where a stronger response of the effective mass is expected for higher fluences.

Appendix A

Time Resolved and Angle Resolved 2PPE of C_6H_5F/Cu(111) using the NOPA

A.1 Time Resolved 2PPE of 1 ML C_6H_5F/Cu(111)

The tr-dynamics of 1 ML BzF/Cu(111) was studied with the optimised NOPA (with wedges and BK7 prism compressor) with 4.1 eV+ 2.05 eV photons, 60 fs pump-probe cross correlation (XC) and measured with the pToF spectrometer. The corresponding false colour map, the 2PPE spectrum with the decay lifetimes, and the molecular state decay curve with the XC are shown in Fig. A.1. Firstly we notice that the time resolution in the false colour map is quite good due to the short NOPA pulse duration giving a narrower XC. Secondly, due to the closed molecular layer, we see only the single molecular state at 3.7 eV energy. Thirdly, near E_F, there seems to be a state decaying in the blue pump-red probe region with a seemingly long lifetime. The lifetime of these states were determined by fitting the decay curve with a negative exponent and a positive exponent, as shown in the left panel. We show here the XC of the pump-probe pulse (decay curve of surface state on bare Cu(111)) and the population decay curves for the molecular state. We find that one needs both the exponential components to describe the data and a 20 fs minimum positive decay constant is seen for all the states, increasing as we go lower in energy. This is shown in the right panel where we plot the negative and positive decay components for various parts of the spectrum. This suggests that the positive decay component is from hot electron states lying near the Fermi edge which are red pumped (hence positive exponential decay) and energetically overlap with states lying the vacuum

edge which are blue pumped (hence negative exponential decay).

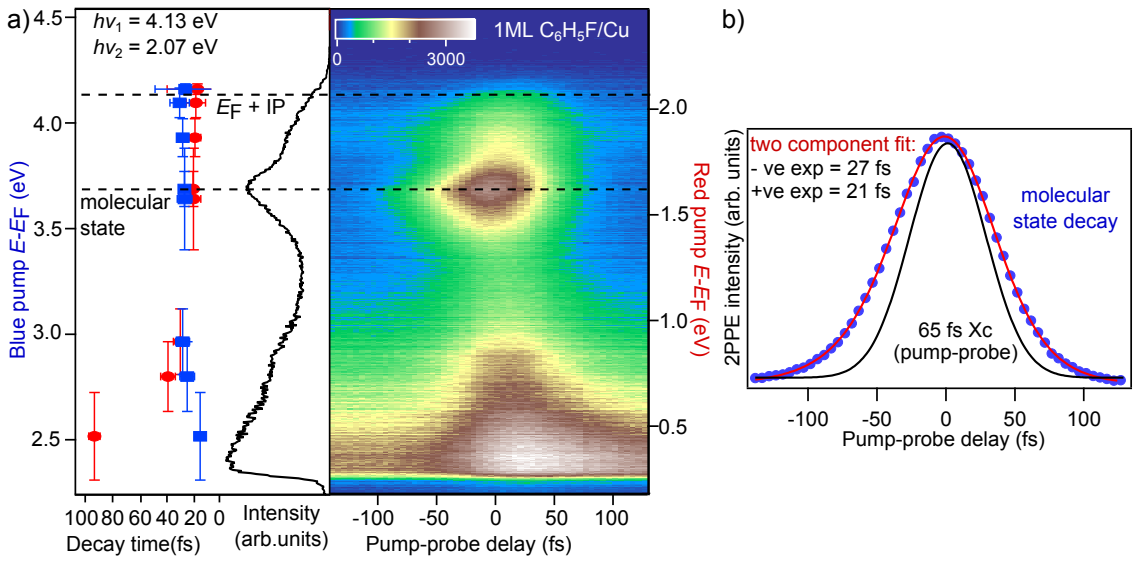

Figure A.1: Tr-photoemission of 1 ML C_6H_5F/Cu(111). a) False colour map showing binding energy on the y-axis as a function of pump-probe delay. The false colour scale gives the 2PPE intensity. The measured exponential decay constants are shown in the left panel along with the photoemission spectrum at zero delay. The blue markers correspond to negative decay constant and is referred to the blue pump energy scale. The red markers correspond to positive decay constant and refer to pump energy scale. b) Decay curve of the molecular state along with the cross correlation (XC). The negative pump-probe delay corresponds to blue-pump and red probe and vice-verse for positive pump-probe delay.

The IP state is expected to be at a lower kinetic energy (higher binding energy with respect to the vacuum) for 1 ML compared to 1.6 ML BzF adsorbed on Cu(111). This is because of a stronger polarisation by more adsorbate molecules in the later case. Therefore, the state at $E - E_F = 4.07 \pm 0.03$ eV is assigned to an IP state of Cu(111) (same distance from the Fermi as on bare Cu(111), similar to C_6F_6/Cu(111)) and has a negative decay component of 40 fs. The molecular unoccupied state decays faster with a time constant of 27 fs for 1 ML coverage. Interestingly, the occupied surface state also shows a negative decay component of comparable value. In fact, if we look at the negative decay component in the right panel, we see that below the IP state all states have this lifetime. This suggests that the 27 fs lifetime we observe is not the lifetime of the unoccupied state but a tail of a higher lying state like the IP state. However, it sets the upper limit of the lifetime of the electrons which is 27 fs.

A.2 Tr- and Angle Resolved- 2PPE of C_6H_5F/Cu(111)

In order to study the localisation of electrons in the π^* LUMO state dynamically, we preformed preliminary time- and angle- resolved 2PPE measurements of 1 ML C_6H_5F/Cu(111), shown in Fig. A.2.

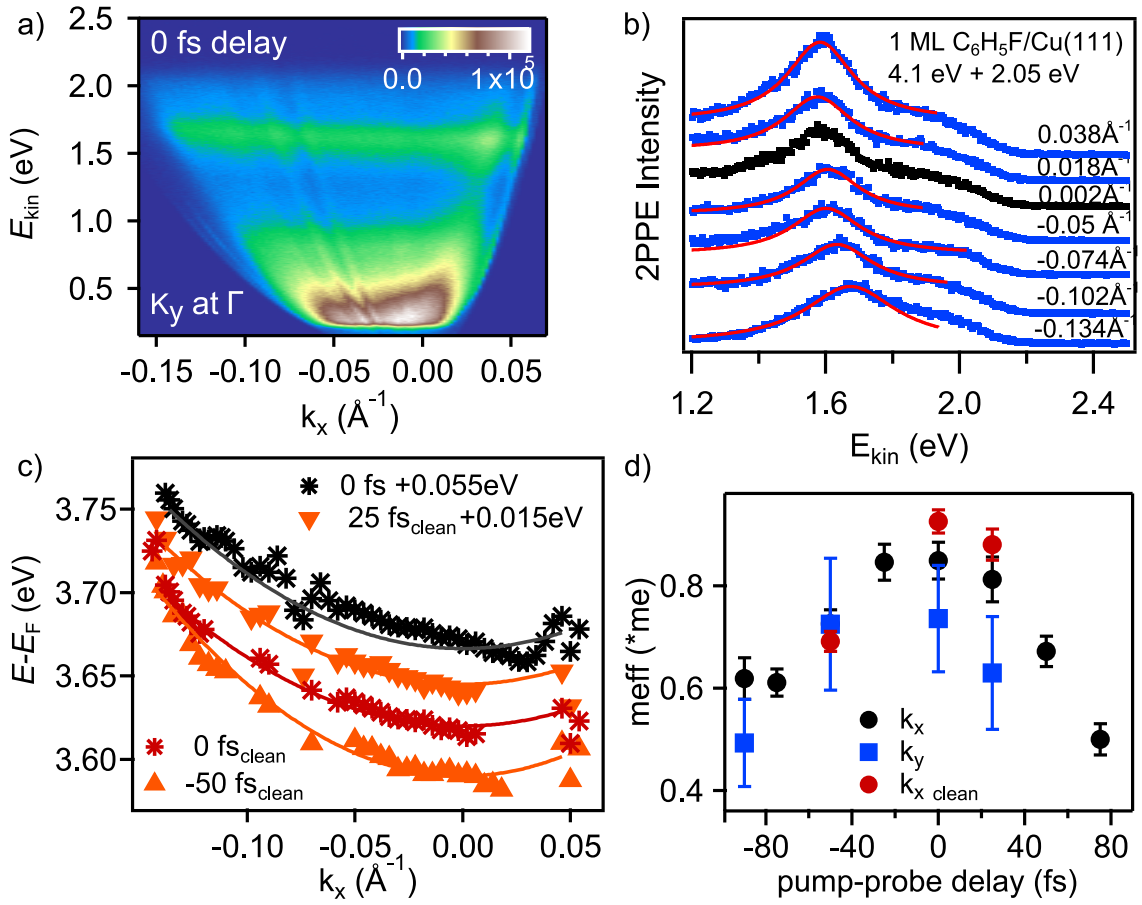

Figure A.2: Time- and angle- resolved 2PPE measurement of 1 ML C_6H_5F/Cu(111) measured with the pToF spectrometer. a) The desperation cone along the $\vec{k}_x$ as a function of kinetic energy and 2PPE intensity. b) Different 2PPE spectra corresponding to different momenta in a). c) Binding energy of the molecular derived state as a function of momentum, determined from fits in b). Parabolic fit of these curves give the effective mass m_{eff} of electron in that state. d) Effective mass as a function of pump-probe delay for the $\vec{k}_x$ and $\vec{k}_y$ parallel momentum, determined by in c).

The optimised NOPA (with the wedge and BK7 prism compressors) was used to generate pump and probe pulses of 4.1 eV and 2.05 eV and a XC of 60 fs. We

used the pToF spectrometer which has an electron acceptance angle of $\pm 11^\circ$ [132], measuring the surface in-plane dispersion along the x- and y- axis. In Fig. A.2a) we show the dispersion at $\tau = 0$ along the sample's x-axis (horizontal to the detector) as a false colour map showing the kinetic energy as a function of $\vec{k}_x$ and the intensity is plotted on the colour scale. Here $\vec{k}_y = 0$ is at Γ point of the Brillioun zone. A similar dispersion cone is also obtained as a function of $\vec{k}_y$ ($\vec{k}_x$ at Γ), but we only show and discuss the $\vec{k}_x$ case in this work. In the figure, at $E_{\text{kin}} < 1\,\text{eV}$, the observed intensity corresponds to the hot electrons, while at $\approx$1.6 eV a band is observed corresponding to the molecular unoccupied state. The band appears to have a positive dispersion and to determine this more accurately, energy cuts are taken for different momenta, shown in Fig. A.2b). Here we plot the 2PPE spectra corresponding to different momentum as a function of kinetic energy. One sees that at higher and lower momentum, there is a shift in the kinetic energy which can be quantised by plotting the peak binding energy (determined by Lorentzian peak fit function) as a function of the momentum, depicted in Fig. A.2c). The dispersion for different delays can be clearly seen here. The black markers shows the dispersion at $\tau = 0\,\text{fs}$, but we see at certain momentum values, the curve gets noisy. These momentum values correspond to the vertical stripes seen in Fig. A.2a), which are due to a technical problem with one set of pToF wires [1][2]. We therefore analyse the data without these point and label it as 'clean', shown in Fig. A.2c) as $\tau\,\text{fs}_{\text{clean}}$. For comparison, the 'clean' curves for $\tau = 25\,\text{fs}$ and $\tau = -50\,\text{fs}$ delays are also shown. The corresponding effective mass is determined from Eq. 3.5 and by fitting the dispersion curves. The respective m_{eff} at different delays for the $\vec{k}_x, \vec{k}_y$ and $\vec{k}_{x\text{clean}}$ are shown in Fig. A.2d). At $\tau = 0$, we measure an effective mass of $0.88\pm0.06\,m_e$ along the x-axis and $0.7\pm0.1\,m_e$ along the y-axis, which is similar to that measured with the ToF spectrometer and OPA pulses in Fig. 5.6. For all the three cases, $\vec{k}_x, \vec{k}_y$ and $\vec{k}_{x\text{clean}}$, we see a similar trend, that is at zero delay, the m_{eff} is maximum but decreases with pump-probe delay. This suggests that with increasing pulse intensity (the two pulses overlap at $\tau = 0$ and have maximum intensity), the electron is getting more localised. Since these are just the first analysis, we refrain from making definitive statements about the mechanism behind these observations. However, we speculate that the state has a fast response to the laser field and gets polarised with the laser intensity, as a result, the electron localisation follows the laser intensity. We therefore show, the band dispersion has interesting time dependent response which is worth

[1] It arises due to a possible impedance mismatch of wires 1 and 2, because of which the discriminator is set very high.

[2] The position of the electrons on the MCP plate and hence the momentum can be determined with two sets of wires alone and thus the signal from wires 1 and 2 can be ignored.

investigating in detail.

Appendix B

Additional Figures

Here we include some additional figures, which may be of relevance for future experiments.

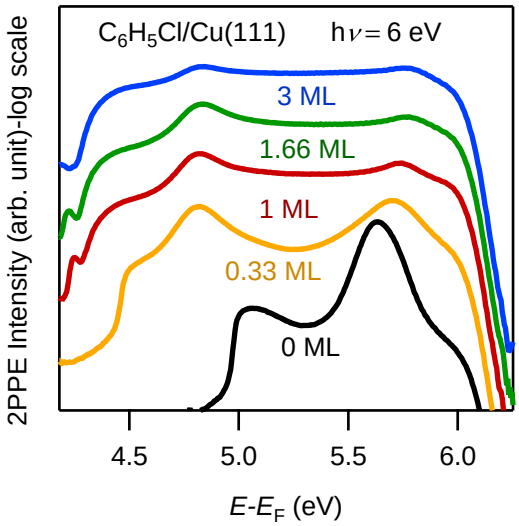

Figure B.1: Coverage dependent photoemission of C_6H_5Cl/Cu(111) measured with 6 eV photon energy. The direct photoemission curves show that with increasing coverage, the surface state (SS) is suppressed and the workfunction decreases, but no new spectral feature is observed. The surface state is also found to shift to higher binding energy by 70 meV.

In Fig. B.1, we show coverage dependent direct photoemission spectra of C_6H_5Cl/Cu(111) measured with $h\nu = 6$ eV and the ToF spectrometer. We see that the surface state

is suppressed on adsorption of molecules, it shifts to higher binding energy from $E - E_F = 0.39 \pm 0.05$ eV to 0.28 ± 0.05 eV and the workfunction decreases.

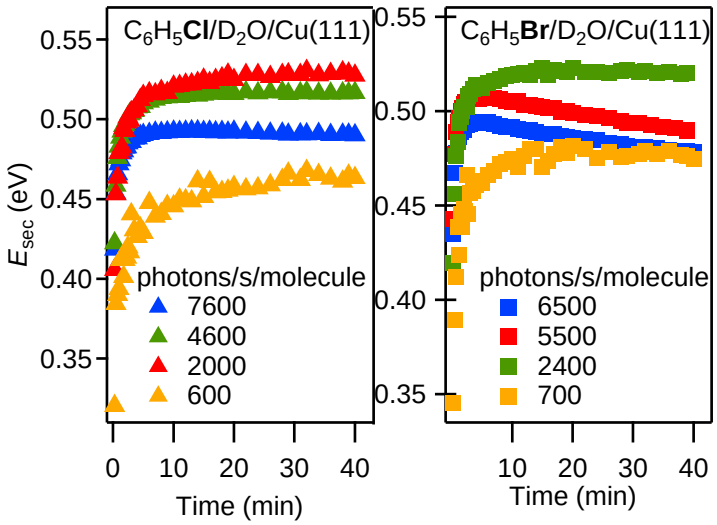

Figure B.2: A shift in the secondary edge as a function of photoexposure time for a) C_6H_5Cl and b) C_6H_5Br are shown for different incident photon fluences.

In Fig. B.2, we show the change in secondary edge, which corresponds to a change in workfunction, with photoexposure time, for different incident fluences. The measurements were taken with the ToF spectrometer and the NOPA was used to generate the 3.78 eV photon pulses. We see that at lower fluences the absolute changes increase with fluence. At higher fluences, when the third exponential contribution becomes stronger at earlier times (Table 4.2), a decrease in $|\Delta\Phi|$ is seen with increasing fluence. This can be associated with the reverse in workfunction trends which become prominent at higher fluences. This does not suggest that the rate of the ionization process is decreasing with increasing fluence, but simply that the total workfunction contribution (from two different charged species) decreases with fluence.

Appendix C

Current Paper

We are currently writing a joined paper with our collaborators. A copy of the current version of the manuscript can be found here. See next page!

How does ice mediate photochemistry in the atmosphere?

Authors: Ph. Auburger[1], I. Agarwal[2], C. Bertram[3], M. Ligges[2], M. Bockstedte[1,4]*, U. Bovensiepen[2]*, K. Morgenstern[3]*.

[1]Solid State Theory, Friedrich-Alexander University Erlangen-Nürnberg, Staudstr. 7B2, D-91058 Germany.

[2]Faculty of Physics, University of Duisburg-Essen, Lotharstr. 1, D-47057 Duisburg, Germany.

[3]Physical Chemistry I, Ruhr-Universität Bochum, Universitätsstr. 150, D-44801 Bochum, Germany.

[4]Department of Chemistry and Physics of Materials, Paris-Lodron University Salzburg, Jakob-Haringer-Str. 2a, A-5020 Salzburg, Austria.

*Correspondence to: Michel.Bockstedte@sbg.ac.at, Uwe.Bovensiepen@uni-due.de, Karina.Morgenstern@ruhr-uni-bochum.de .

Photochemistry in the earth's atmosphere is decisive for life, but has not yet been understood on a fundamental level. A variety of photochemical reactions were shown to be enhanced in the vicinity of naturally abundant ice-covered dust particles, in particular halogen dissociation from carbohydrates initiated by photo-excited electrons. Chlorine and bromine involving reactions impact concentration ratios of hydrocarbons, ozone and cloud concentrations. We establish the molecular-scale picture of enhanced reactivity on ice by combining local and spectroscopic probes with *ab initi*o theory. Our complementary approach reveals a combined action of electron attachment to molecular orbitals and electron solvation at pre-existing adsorption sites on the ice particles. The picture is corroborated by a clear dependence of reaction rate on halogen electron affinity. On a broader range, our results shed light on the influence of solvation on the propensity for dissociation.

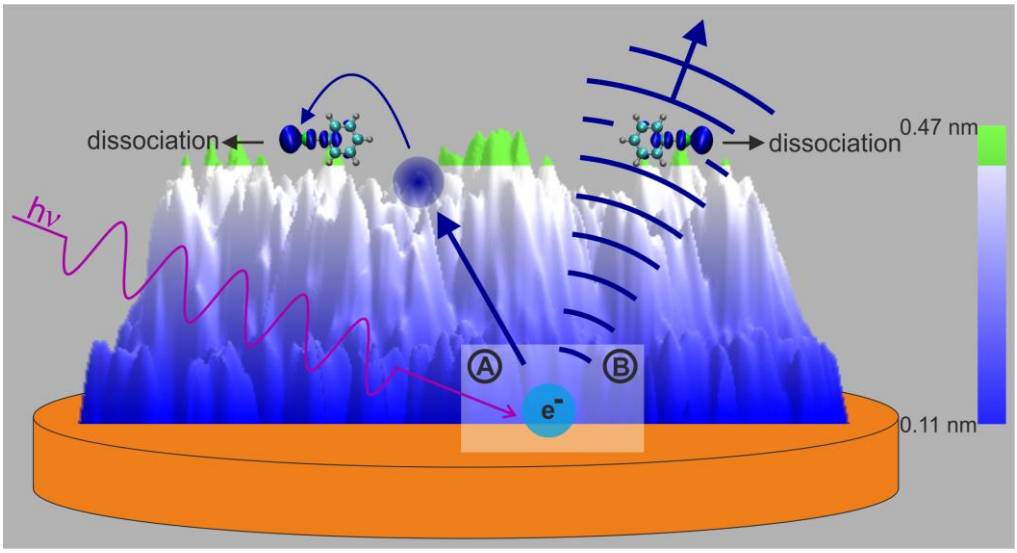

Fig. 1: Model system for atmospheric chemistry: Electron attachment via two pathways to dissociative orbital of chlorobenzene resulting from *ab initio* calculations superimposed on STM image of chlorobenzene colored in green on amorphous ice in blue (3D representation, color scale on right-hand side, 100 mV, 7.3 pA). (A) represents the model invoked so far; (B) represents the model developed here.

Photo-induced dissociation of gas phase molecules[1] is substantially enhanced on water-ice particles[2], a process which is highly relevant for atmospheric chemistry[3,4] and to snow photochemistry[5,6] as first observed on snow packs[7]. Despite its importance, no molecular scale picture exists that describes the interaction of adsorbed molecules with photo-excited excess electrons at the ice surface. A process has been proposed where the excited electrons in ice are solvated at specific sites at the ice surface via polarization of the surrounding water molecules and attach to the adsorbed molecules to induce their dissociation (see Fig. 1, path A). These electrons originate either from an impact of high energy particles with ice[2] or from photo-excitation of in-gap states in doped ice[8,9]. Though this model is largely accepted[10], it has never been challenged, in particular with respect to the interaction of the solvated electron with the adsorbate. Thus, the current understanding of the physical mechanisms at work remains rather incomplete. We here develop and proof a different model (see Fig. 1, path B), which generally sheds light on the active role of polar solvents in chemical reactions, as these represent a unique class of catalysts because of their ability to solvate charge carriers and excess electrons[11].

In the context of photochemistry, the dissociation of halocarbons is of large environmental relevance[5] as the released radicals impact atmospheric chemistry[12]. Such organic compounds have been shown to adsorb on ice via their interaction with dangling OH groups that are not engaged in ice related hydrogen bonding at the ice surface[13,14]. Such an adsorption leads to a measurable shift of the absorption spectrum for a variety of organic pollutants[6]. In this class of molecules, dissociation in the gas phase involves creation of a transient ion via electron attachment to an anti-bonding molecular orbital[1]. However, a similar attachment mechanism for these molecules on ice particles is incompatible with the bound solvated electrons[15,16] invoked in

the model discussed above unless the energy of the molecular orbitals changes drastically upon adsorption. To solve this issue, we here investigate adsorption and dissociation of halobenzenes on ice surfaces by the complementary methods of scanning tunneling microscopy, photoelectron spectroscopy, and *ab initio* theory. Our result will not only impact the understanding of the named issues, but also of the interplay between the electronic structure of solvated ionic molecules and their propensity for dissociation. This topic is thus related to the general area of photo-induced reaction in polar solvents[17] and the solvated electron.

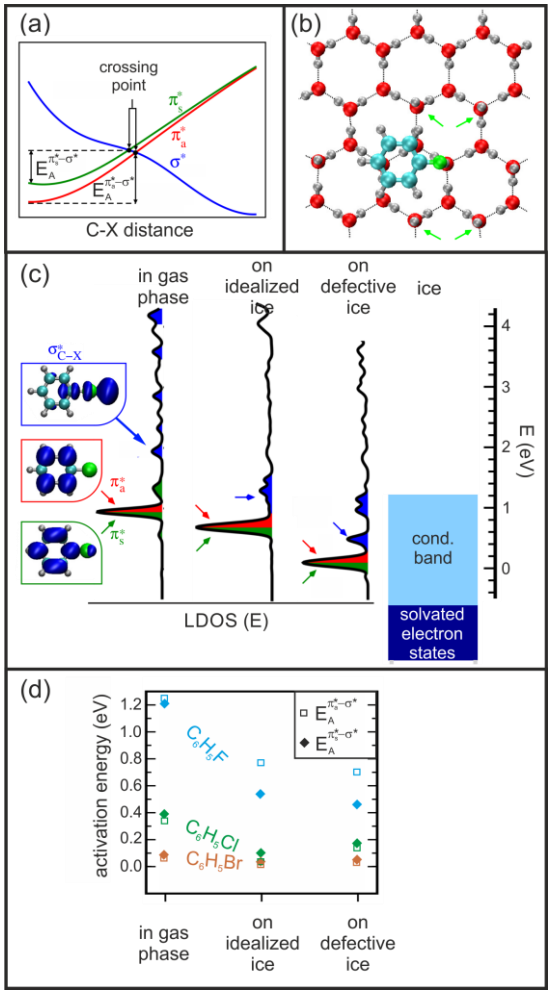

Fig. 2: **Modelling of halobenzene (C_6H_5X, X=Br, Cl, F):** (a) Potential energy surface of orbitals relevant for dissociation vs. C-X distance (b) adsorption geometry at orientational defects (as marked by arrows; top view) (c) LDOS for C_6H_5Cl in gas phase and adsorbed on ice with orbital shape as insets (d) activation energies E_A for different halobenzenes in gas phase and adsorbed on ice.

Results and discussion

First, *ab initio* theory is used to develop the microscopic mechanism of the reaction $C_6H_5X + e^- \leftrightarrow C_6H_5X^{*-} \rightarrow C_6H_5\cdot + X^-$ at the ice surface (X = F, Cl, Br) based on the dominant dissociation channel for chloro- and bromobenzene in the gas phase[18]. Subsequently, we substantiate this model by scanning tunneling microscopy (STM) and two-photon photoemission (2PPE).

In gas phase, the dissociation pathway is initiated by the formation of a meta-stable transient anion $C_6H_5X^{*-}$ via occupation of an anti-bonding electronic state, a symmetric or an anti-symmetric π*-state or a σ*-state (Fig. 2a). Note that the transient ion might either dissociate or the attached electron might spontaneously detach leaving the molecule intact. The dissociation of the halogen bond is facilitated by the position of a node of the σ*-orbital between the C-X bond (Fig. 2c, inset). As this dissociative σ*-orbital is quite high in energy, a low-energy pathway for dissociation proceeds via occupation of one of the π*-orbitals and subsequent transition to the σ*-orbital at the conical intersection between the σ*- and π*-potential energy surfaces after some bond elongation (Fig. 2a).

We model the halobenzenes in gas phase, on idealized ice surfaces and on defective ice surfaces using DFT-PBE0 and many-body perturbation theory within the GW approach. Prototypical adsorption sites are the so-called Fletcher stripe bilayer terminated surface for the idealized ice surface, in which neighboring rows of surface water molecules with dangling protons (OH groups) and flat-lying water molecules alternate[19,20] and orientation defects for the defective ice surface, e.g. with a cluster of four additional dangling OH groups (Fig. 2b). Vacancy formation[21] and point defects[22] on crystalline ice surfaces were characterized by *ab initio* methods before. Here, we calculate the propensity of such defects to solvate electrons. Indeed, these defects are strong electron traps that solvate electrons with energies up to 0.4 eV because of an attractive interaction with the positive partial charges of the dangling OH groups.

Upon adsorption of halobenzenes on such ice surfaces, anti-bonding orbitals are situated in the region of the ice conduction band, well above the solvated electron states (Fig. 2c). Solvated electrons are thus unable to initiate dissociation, at odds with the model of path A in Fig. 1. While the character of the anti-bonding orbitals is essentially unchanged upon adsorption, their energy depends largely on the exact adsorption site as evidenced by the local-density of states (LDOS). They are red-shifted in energy by adsorption on the idealized ice surface and even to a larger extent at orientation defects due to the attractive interaction of the polar molecule with the positive partial charges of the dangling OH groups. This red shift is expected to facilitate electron attachment and thus dissociation rates. Moreover, along the halogenated molecules series (C_6H_5X, X=F, Cl, Br), the red-shift of the anti-bonding orbitals increases (cf. supplementary material), that is the halogen of larger mass and with lower electron affinity possesses orbitals at lower energy. Moreover, the activation energy to the crossing point is reduced upon adsorption, again even more for halogens of lower electron affinity (Fig. 2d). We expect that this reduction in energy translates into halogen-specific dissociation rates being larger for heavier halogens. Our model calculations propose that the halobenzene molecules are trapped at those defect sites with an abundance of dangling OH bonds which also solvate electrons. However, dissociation is initiated in this case from delocalized electrons travelling through the conduction band of ice as sketched in Fig. 1, path B and not from the solvated electron.

In order to verify this theoretical picture experimentally, we adsorb halobenzenes on ice nanoparticles supported on Cu(111). The copper electrode serves as an electron source, which allows transferring delocalized electrons into the conduction band of ice[23]. Electrons created via illumination by UV light in such a system were shown to solvate at the surface of both amorphous[24] and crystalline ice[25] in particular at low temperature[26]. Here we excite this system by a photon energy that is too low to photo-excite and dissociate the molecules in gas phase and,

according to our calculation, also at the ice surface (see supplementary material) ensuring that no direct photodissociation falsifies our measurements and all processes reported below originate from electrons transferred to the conduction band of ice.

In order to confirm the selective adsorption of halobenzene at defects and the subsequent possibility of photoinduced dissociation experimentally, we adsorb chloro- and bromobenzenes on crystalline ice that has been prepared to exhibit a substantial number of intrinsic, but well separated dangling OH-bonds in the form of defects (cf.[27]). The high thermal and electronic stability of our STM gives direct information about the fate of individual molecules by imaging exactly the same spot of the ice surface before and after adsorption of the molecules (Fig. 3a-c) and before and after illumination with laser light (Fig. 3d,e), for details see supplementary material.

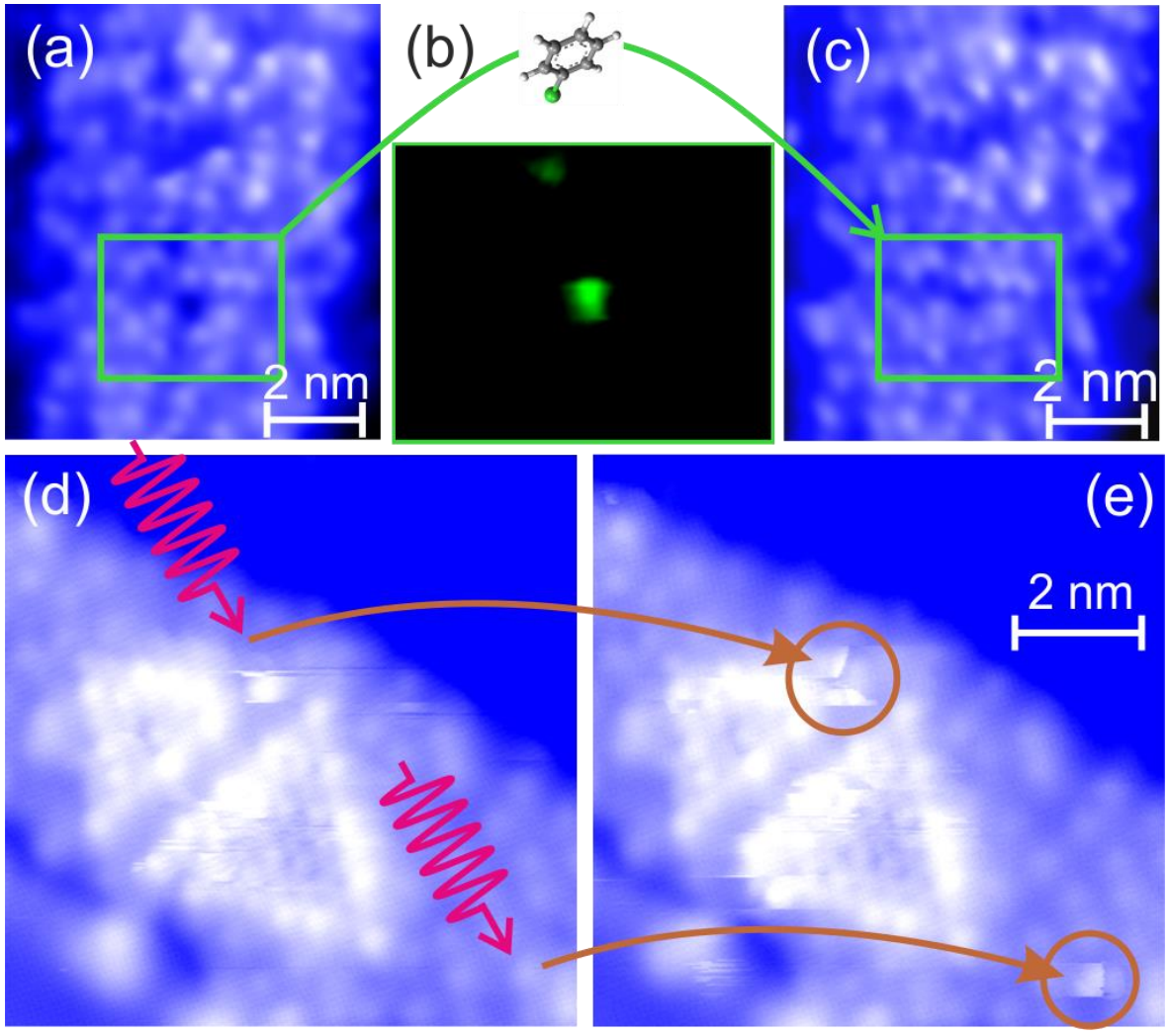

Fig. 3: Identification of individual adsorption and reaction events on crystalline ice by STM measured at 7.5 K with -100 mV and 1 pA: (a-c) adsorption of chlorobenzene (0.05 molecules/nm^2 at 11 K): STM image of crystalline ice (a) before and (c) after deposition of chlorobenzene molecules (b) difference in green enlarged by a factor of 4. (d,e) photo-reaction (photon dose $2.0 \cdot 10^5$ photons/molecule, 330 nm) of bromobenzene: STM (d) before illumination and (e) after illumination. Circles mark two of the photo-induced changes.

Before co-adsorption of the halobenzene, each protrusion corresponds to a single water molecule[28] As exemplified for adsorption of chlorobenzene in Fig. 3a-c, halobenzenes, imaged as slightly larger protrusions, adsorb exclusively either at defects on the ice surface or at the borders of the ice nanoclusters. This observation implies that the halobenzenes are mobile on top of defective ice surfaces during the adsorption process even at 11 K. It also confirms that molecules are trapped at energetically more favorable sites as predicted by theory (cf. Fig. 2b). The halobenzene mobility is expected to increase its dissociation yield since the defects shift the anti-bonding orbitals towards the bottom of the conduction band (cf. Figs. 2c,d).

Illumination of both adsorbed halobenzenes causes substantial changes to the imaging of the adsorbates, as demonstrated for bromobenzene in Fig. 3d,e. While the halobenzenes before adsorption are easily moved by the tip, this is no longer the case after illumination. In addition, this more tightly bonded species interacts characteristically with the tip in dependence on tip-sample distance. Such species are observed after illumination with both 400 nm and 326/330 nm wavelengths on both crystalline (Fig. 3d,e) and amorphous ice (Fig. 4a). They are neither observed before illumination nor after illumination of the native ice without halobenzene. The STM experiments thus imply that halobenzene molecules were dissociated upon illumination.

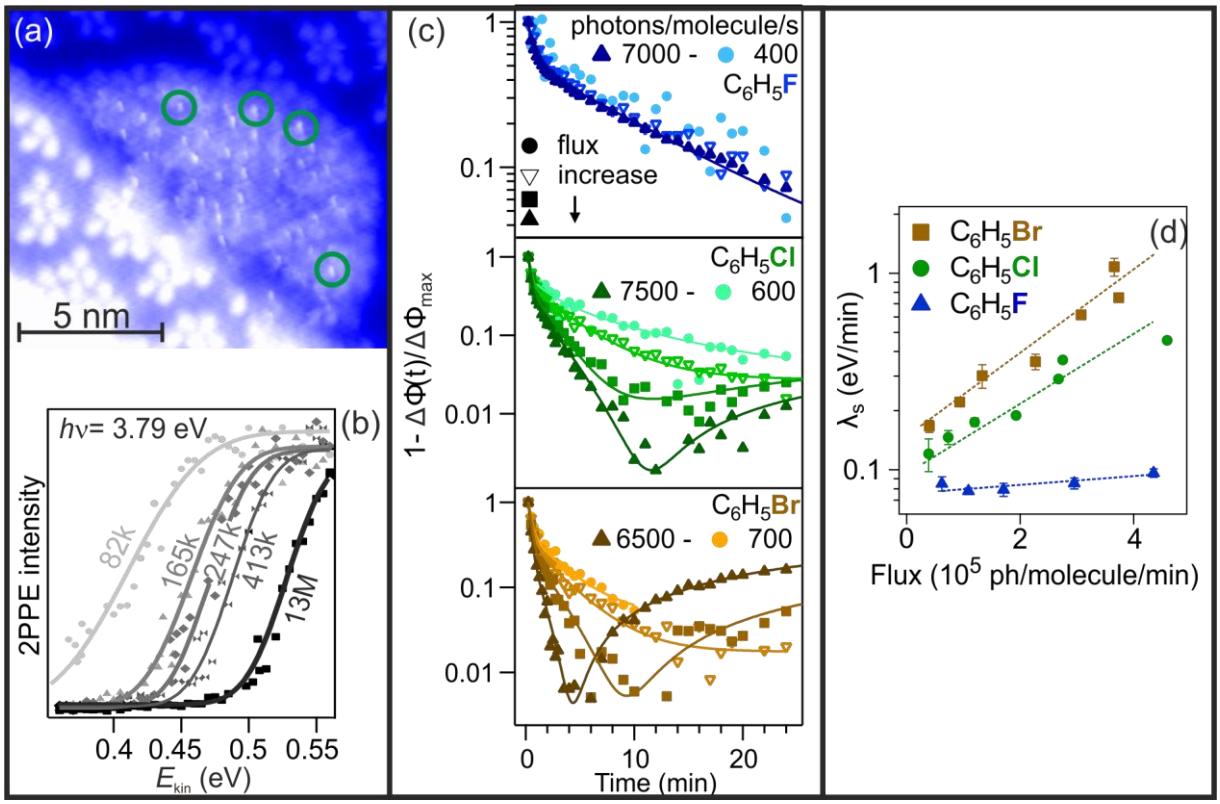

Fig. 4: Halogen specific reactivity on amorphous ice nanoclusters: (a) chlorobenzene after illumination at 326 nm with a photon dose of $5.2*10^5$ photons/molecule (100 mV, 5 pA), circles mark photo-induced changes. (b) low energy cut-off of two-photon photoemission spectra using 327 nm illumination for indicated photon dose; lines are fits of an error function for determination of the work function ϕ (c) relative change of the work function vs. illumination time on logarithmic scale obtained from low energy cut-off (see panel b) for different photon fluxes and halobenzenes; $\Delta\phi = \phi(t) - \phi(t=0)$; lines are multi-exponential fits to determine the rates

of change λ in $\Delta\phi$ (d) slow rate of change λ_S vs. flux for the series of halobenzenes; dashed lines guide the eye.

In order to prove that this modification is related to dissociation, we now measure the work function change induced by illumination of halobenzenes adsorbed on amorphous ice structures, shown in real space in Fig. 4a. The work function, measured as the low energy cut-off of the 2PPE spectrum, is a good indicator for the amount of halogen ions after dissociation, because it is determined by the charge distribution along the surface normal. Here, the low energy cut-off shifts to higher kinetic energy with photo-exposure time (Fig. 4b) giving a work function increase. As expected from our model (cf. Fig. 2), there are significant differences in work function change along the halogen series (Fig. 4c). While for the fluorinated benzene a biexponential increase in work function with illumination time does not change with flux, we observe flux-dependent variations for chlorinated and brominated benzenes. For the two heavier halogens, their initial work function change is accelerated with increasing photon fluxes and the direction of change inverses at later times.

Flux-independent photo-induced work function changes in time indicate in general a built-up of a photo-stationary state, in which for instance attachment and detachment of electrons to the adsorbate lead to an equilibrium density of transient ions ($C_6H_5X^{*-}$) without dissociation. For C_6H_5F, the fluence dependence of the slow rate of work function change λ_S is weak. This observation for C_6H_5F indicates the formation of such transient ions. In contrast, a flux dependence suggests a permanent change of the surface due to the formation of $C_6H_5\cdot$ and X^-, as observed for the two heavier halogens. The inversion of work function change at later times is related to the consumption of the available native halobenzenes by dissociation leading to a smaller amount of transient ions.

The multi-exponential fit of the time-dependent work function gives a slow molecule-dependent rate after an initial fast molecule-independent rate; the slow rate is plotted in Fig. 4d. The smaller dissociation rate of chlorobenzene as compared to bromobenzene is consistent with the calculated trend in activation energy (Fig. 2c). For fluorobenzene the activation energy is much larger than the thermal energy provided in the experiment, here 90 K, such that dissociation should not take place, as observed. All our experimental results thus confirm the molecular scale picture developed above.

Conclusion

Ice mediates photodissociation by lowering the energy barrier for at the conical intersection between anti-bonding orbitals in particular at defective regions with a large abundance of OH-bonds. We emphasize that electrons injected into the ice conduction band mediate the dissociation and not the electrons solvated at the ice surface (cf. Fig. 1, path B). However, the importance of electron solvation sites lies in their property to also trap adsorbates and alter the molecular orbitals to enhance the dissociation rate. Such a cooperative effect of adsorption, surrounding water molecules, and electron solvation onto a reaction probability should be a universal property of polar molecules and emphasizes the active role of polar solvents in chemical reactions. The proposed mechanism has further implications in fields as diverse as atmospheric chemistry, electrochemistry, astrophysics and biology. Moreover, our results might be of potential relevance to air purifiers, were a large number of trapping sites could improve their performance.

Methods: GEÜRZT sollte 800 WORTE, war 1100 Worte, jetzt 940; Kann in der Theorie noch etwas weg?

The **STM experiments** are performed in a STM with direct optical access to the tip-sample region, operated in ultra-high vacuum at 7.5 K. Cu(111) is cleaned by repeated cycles of sputtering with neon ions (1.3 keV, 45 min, 1μA at $3\cdot 10^{-5}$ mbar) and annealing at 900 K for 10-20 min. Around 0.9-1.0 BL (bilayers) of ice are deposited at a flux of 0.1 BL/min onto the sample at either 88 K for preparation of amorphous ice or at 77 K and subsequently annealed at 115 K for 10 min for crystalline ice[27], the same procedure as used for the 2PPE experiments. For identification of the adsorption site, 0.025 ML (monolayer) chlorobenzene is adsorbed *in situ* the STM at a rate of 0.024 ML/min. During deposition the sample temperature rises to a maximum of 11 K. For the photo-dissociation experiments, 0.4 ML halobenzene are adsorbed *ex situ* the STM at a rate of 1.5 ML/min at a deposition temperature of 77 K or 88 K.

The sample is illuminated for 10 h by a frequency-doubled super-continuum laser (NKT Photonics, ν = 77.8 MHz, 10 ps, p-polarised) focussed from outside the vacuum chamber into the tunneling junction at two wave lengths. At the lower wavelength, the fluence is 2.3 pJ/cm^2 for the halobenzenes adsorbed on amorphous ice at 326 nm and 20 pJ/cm^2 for those adsorbed on crystalline ice at 330 nm. At 400 nm, the same fluence of 230 pJ/cm^2 is used for halobenzenes adsorbed on both types of ice.

The tip is retracted from the tip by several 100 nm in order to avoid tip-induced near field effects during illumination. Control experiments ensure that the observed changes are due to illumination including temperature control at the position of the tip by a silicon diode and in-situ heating without laser illumination. In this case, no photodissociation is observed.

Large-scale images ensure that the images before and after deposition and before and after illumination correspond to exactly the same spot of the sample.

The **photo-emission experiments** are performed in a separate UHV chamber with the same facilities for sample preparation to ensure a similar sample preparation in both experiments. For sputtering, argon ions are used for 15 min followed by annealing at 750 K for 25-30 min. The amorphous ice layer is prepared by depositing D_2O at 90 K. Approximately 4 BL of ice are adsorbed at a flux of 4 BL/min. A coverage corresponding to 1 ML of halobenzenes on bare Cu(111) is adsorbed on D_2O/Cu(111) at a flux of 3 ML/min, 4 ML/min and 6 ML/min for C_6H_5F, C_6H_5Cl and C_6H_5Br, respectively. The photo-emission experiments are performed using a Ti:Sa laser (Coherent RegA9040, central wavelength: 800 nm, repetition rate: 250 kHz). A non-collinear optical parametric amplifier (NOPA) generates the wavelength of 327 nm (3.79 eV). A fluence range from 0.5-10μJ/cm^2 is used for the fluence dependent measurements. The two photon photoelectron spectrum is analysed by an electron time of flight spectrometer with an energy resolution of 25 meV.

The different fluences for the two different laser set-ups in STM and photo-emission experiments are compensated by adapting the illumination times. This is a reliable procedure because all photo-induced processes are linear in fluence.

Theoretical modelling employs density functional theory with gradient corrected (PBE) and hybrid (PBE0) functionals and many body perturbation theory within the GW and BSE approaches to address structural, electronic and photo-physical properties of the adsorbate-ice system. The hexagonal ice surface is represented by a slab model consisting of three bilayers in a 4x4 unit cell yielding converged electronic properties. Antiferroelectric proton order between the

bilayers reduces the complexity while protons within the bilayer are arranged for yielding a vanishing dipole moment. Electronic wave functions are represented by a projector augmented plane-wave basis set (energy cut-off of 400eV) as implemented in the VASP-package (cf. [29,30] and references therein). This approach enables a well-converged description of both extended states and localized orbitals. The geometry of the Fletcher-stripe bilayer-terminated ice surface and the orientation defect with an intact water bond network (cf. [25,31]) are optimized at the PBE-level without semi-empirical dispersion corrections (cf. **Fehler! Textmarke nicht definiert.**). The optimization of the adsorbate geometry includes an additional relaxation of the adorbate coordinates alone using D2-dispersion corrections. G0W0 calculations start from the PBE0-level electronic structure including virtual states up to 125 eV. The PBE0-level is superior to the PBE-level for the description of the transient ion, because of its better self-interaction cancelation. For the molecules in gas phase a large cubic super cell (side length 1.5 nm) is employed. Tests show that including self-consistency at the GW-level yields only minor corrections in the description of the relevant states. Photo excitations were treated at the BSE approach**Fehler! Textmarke nicht definiert.**. The dissociation of the transient ion is investigated by elongating the halogen-carbon bond by up to 50%, while keeping the halogen at its position. Note that the broad energy range of σ* orbitals found at the equilibrium distance collapses into one sharp σ* orbital in the region of the crossing point and beyond. Thus, the activation energies are well defined.

Data availability;

All data is available upon request from the corresponding authors; U.B. for photoemission data, K.M. for STM data, M.B. for theoretical data.

Acknowledgments

The authors acknowledge financial support by the Deutsche Forschungsgemeinschaft under grants BO1841/3-1, BO 1823/5-1, and MO960/18-1 and the Cluster of Excellence RESOLV (ECX 1069). For computer time we thank the Research Center Jülich (HER140) and the FAU Erlangen-Nürnberg (HPC-cluster of RRZE).

Author contributions

U.B., M.B., and K.M. conceived, designed, and led the project and co-wrote the article. P.A., I.A., C.B., and M.L. performed the experiments and anlyzed the data. I.A., M.L., and U.B. thereby performed the photoemission experiments, C.B. and K.M. the STM experiments, and P.A. and M.B. the calculations.

Additional information

Supplementary information is available in the online version of the article.

Competing financial interest

The authors declare no competing financial interest.

References

[1] O. Ingolfsson, F. Weik, E. Illenberger, The reactivity of slow electrons with molecules at different degrees of aggregation: gas phase, clusters and condensed phases, *Int. J. Mass Spect.* **155**, 1 (1996).

[2] Q.-B. Lu, L. Sanche, Effects of cosmic rays on atmospheric chlorofluorocarbon dissociation and ozone depletion, *Phys. Rev. Lett.* **87**, 078501 (2001).

[3] C. George, M. Ammann, B. D'Anna, D. J. Donaldson, and S. A. Nizkorodov, Heterogeneous photochemistry in the atmosphere, *Chem. Rev*. **115**, 4218 (2015).
[4] R. Vogt, P.J. Crutzen, R. Sander, A mechanism for halogen release from sea-salt aerosol in the remote marine boundary layer, *Nature* **383**, 327 (1996).
[5] A. M. Grannas et al., An overview of snow photochemistry: evidence, mechanisms and impacts, *Atmos. Chem. Phys*. **7**, 4329 (2007).
[6] T. F. Kahan, D. J. Donaldson, Benzene photolysis on ice: implications for the fate of organic contaminants in the winter, *Environ. Sci. Technol*. **44**, 3819 (2010).
[7] K. L . Foster, R. A. Plastridge, J. W. Bottenheim, P. B. Shepson, B. J. Finlayson-Pitts, C. W. Spicer, The role of Br2 and BrCl in the surface ozone destruction at polar sunrise, *Science*, **291**, 471 (2001).
[8] I. V. Hertel, C. Hüglin, C. Nitsch, C. P. Schulz, Photoionization of $Na(NH_3)_n$ and $Na(H_2O)_n$ clusters: a step towards the liquid phase, *Phys. Rev. Lett*. 67, 1767 (1991).
[9] T. Vondrak, J. M. C. Plane, S. R. Meech, Influence of submonolayer sodium adsorption on the photoemission of the Cu(111)/water ice surface, *J. Chem. Phys.* **125**, 224702 (2006).
[10] B. C. Garret et al., Role of water in electron-initiated processes and radical chemistry: issues and scientific advances, Chem. Rev. **105**, 355 (2005).
[11] A. D. Miller, I. Bezel, K. J. Ganey, S. Garrett-Roe, S. H. Liu, P. Szymanski, and C. B. Harris, Electron Solvation in Two Dimensions, *Science* **297**, 1163 (2002).
[12] I.J. George, J.P.D. Abbatt, Heterogeneous oxidation of atmospheric aerosol particles by gas-phase radicals, *Nature Chem.* **2**, 713 (2010).
[13] N. S. Holmes, J. R. Sodeau, A study of the interaction between halomethanes and water-ice, *J. Phys. Chem. A* **103**, 4673 (1999).
[14] A. Borodin, O. Hofft, U. Kahnert, V. Kempter, S. Krischok, M.O. Abou-Helal, The interface between benzenes (C_6H_6; C_6H_5Cl; 2-C_6H_4OHCl) and amorphous solid water studied with metastable impact electron spectroscopy and ultraviolet photoelectron spectroscopy (HeI and II), *J. Chem. Phys.* **120**, 5407 (2004).
[15] E. J. Hart, J. W. Boag, Adsorption spectrum of the hydrated electron in water and in aqueous solutions*, J. Am. Chem. Soc.* **84**, 4090 (1962).
[16] K. R. Siefermann, Y. Liu, E. Lugovoy, O. Link, M. Faubel, U. Buck, B. Winter, B. Abel, Binding energies, lifetimes and implications of bulk and interface solvated electrons in water, *Nat. Chem.* **2**, 274 (2010).
[17] J. Knorr, P. Sokkar, S. Schott, P. Costa, W. Thiel, W. Sander,.E. Sanchez-Garcia, P. Nuernberger, Competitive solvent-molecule interaction govern primary processes of diphenylcarbene in solvent mixtures, *Nat. Commun.* **7**, 12968 (2016).
[18] A. Modelli, Electron attachment and intramolecular electron transfer in unsaturated chloroderivatives, *Phys. Chem. Chem. Phys.* **5**, 2923 (2003).
[19] V. Buch, H. Groenzin, I. Li, M. J. Shultz, E. Tosatti, Proton order in the ice crystal surface, *Proc. Nat. Am. Soc.* **105**, 5969 (2008).
[20] D. Pan, Li-Min Liu, G. A. Tribello, B. Slater, A. Michaelides, E. Wang, Surface energy and surface proton order of ice Ih, *Phys. Rev. Lett.* **101**, 155703 (2008).
[21] M. Watkins, D. Pan, E. G. Wang, A. Michaelides, J. VandeVondele, B. Slater, Large variation of vacancy formation energies in the surface of crystalline ice, *Nat. Mater.* **10**, 794 (2011).
[22] M. Watkins, J. VandeVondele, B. Slater, Point defects at the ice (0001) surface, *Proc. Nat. Am. Soc.* **107**, 12429 (2010).
[23] J. Stähler, M. Mehlhorn, U. Bovensiepen, M. Meyer, D.O. Kusmierek, K. Morgenstern, M. Wolf, Impact of Ice Structure on Ultrafast Electron Dynamics in D_2O Clusters on Cu(111), *Phys. Rev. Lett.* **98**, 206105 (2007).
[24] C. Gahl, U. Bovensiepen, C. Frischkorn, M. Wolf, Ultrafast dynamics of electron localization and solvation in ice layers on Cu(111), *Phys. Rev. Lett.* **89**, 107402 (2002).
[25] U. Bovensiepen, C. Gahl, J. Stähler, M. Bockstedte, M. Meyer, F. Baletto, S. Scandolo, X.-Y. Zhu, A. Rubio, M. Wolf, A dynamic landscape from femtoseconds to minutes for excess electrons at the ice-metal interfaces, *J. Phys. Chem. C* **113**, 979 (2009).
[26] J.R.R. Verlet, A.E. Bragg, A. Kammarath, O. Cheshnovsky, D.M. Neumark, *Science* **307**, 93 (2005).
[27] M. Mehlhorn, K. Morgenstern, Faceting during the transformation of amorphous to crystalline ice, *Phys. Rev. Lett.* **99,** 246101 (2007).

[28] A. Michaelides, K. Morgenstern, Ice nanoclusters at hydrophobic metal surfaces , Nature Mater. 6, 597 (2007).
[29] M. Shishkin, G. Kresse, *Phys. Rev.* B **75**, 235102 (2007).
[30] T. Sander, E. Maggio, G. Kresse, *Phys. Rev. B* **92**, 045209 (2015).
[31] M. Bockstedte, A. Michl, M. Kolb, M. Mehlhorn, K. Morgenstern, *J. Phys. Chem. C* **120**, 1097 (2016).

Bibliography

[1] J. C. Amicangelo, B. W. Gung, D. G. Irwin, and N. C. Romano, "Ab initio study of substituent effects in the interactions of dimethyl ether with aromatic rings," *Physical Chemistry Chemical Physics*, vol. 10, pp. 2695–2705, 2008.

[2] J. K. Olthoff, J. A. Tossell, and J. H. Moore, "Electron attachment by haloalkenes and halobenzenes," *The Journal of Chemical Physics*, vol. 83, no. 11, pp. 5627–5634, 1985.

[3] D. Velic, A. Hotzel, M. Wolf, and G. Ertl, "Electronic states of the C_6H_6/Cu{111} system: Energetics, femtosecond dynamics, and adsorption morphology," *The Journal of Chemical Physics*, vol. 109, no. 20, pp. 9155–9165, 1998.

[4] C. Gahl, K. Ishioka, Q. Zhong, A. Hotzel, and M. Wolf, "Structure and dynamics of excited electronic states at the adsorbate/metal interface: C_6F_6/Cu(111)," *Faraday Discussions*, vol. 117, pp. 191–202, 2000.

[5] C. Gahl, U. Bovensiepen, C. Frischkorn, and M. Wolf, "Ultrafast dynamics of electron localization and solvation in ice layers on Cu(111)," *Physical Review Letters*, vol. 89, no. 10-2, p. 107402, 2002.

[6] U. Bovensiepen, C. Gahl, and M. Wolf, "Solvation dynamics and evolution of the spatial extent of photoinjected electrons in D_2O/Cu(111)," *Journal of Physical Chemistry B*, vol. 107, no. 33, pp. 8706–8715, 2003.

[7] A. Mozumder, *Fundamental of Radiation Chemistry*. Academic Press, 1992.

[8] A. Solovýov, ed., *Nanoscale Insight into Ion-Beam Cancer Therapy*. Springer International Publishing, Switzerland, 2016.

[9] E. Alizadeh, T. M. Orlando, and L. Sanche, "Biomolecular damage induced by ionizing radiation: The direct and indirect effects of low-energy electrons on DNA," *Annual Reviews of Physical Chemistry*, vol. 66, pp. 379–98, 2015.

[10] K. R. Siefermann and B. Abel, "The hydrated electron: A seemingly familiar chemical and biological transient," *Angewandte Chemie International Edition*, vol. 50, no. 23, pp. 5264–5272, 2011.

[11] Q. B. Lu and T. E. Madey, "Giant enhancement of electron-induced dissociation of chlorofluorocarbons coadsorbed with water or ammonia ices: Implications for atmospheric ozone depletion," *The Journal of Chemical Physics*, vol. 111, no. 7, pp. 2861–2864, 1999.

[12] Q.-B. Lu, "Cosmic-ray-driven electron-induced reactions of halogenated molecules adsorbed on ice surfaces: Implications for atmospheric ozone depletion and global climate change," *Physics Reports*, vol. 487, no. 5, pp. 141–167, 2010.

[13] D. Marchione, J. D. Thrower, and M. R. S. McCoustra, "Efficient electron-promoted desorption of benzene from water ice surfaces," *Physical Chemistry Chemical Physics*, vol. 18, no. 5, pp. 4026–4034, 2016.

[14] S. Solomon, R. R. Garcia, F. S. Rowland, and D. J. Wuebbles, "On the depletion of antarctic ozone," *Nature*, vol. 321, pp. 755–758, 1986.

[15] Q. B. Lu and L. Sanche, "Enhanced dissociative electron attachment to CF_2Cl_2 by transfer of electrons in precursors to the solvated state in water and ammonia ice," *Physical Review B*, vol. 63, no. 15-15, p. 153403, 2001.

[16] K. I. Öberg, "Photochemistry and astrochemistry: Photochemical pathways to interstellar complex organic molecules," *Chemical Reviews*, vol. 116, no. 17, pp. 9631–9663, 2016.

[17] B. Abel, U. Buck, A. L. Sobolewski, and W. Domcke, "On the nature and signatures of the solvated electron in water," *Physical Chemistry Chemical Physics*, vol. 14, pp. 22–34, 2012.

[18] A. Ribar, K. Fink, Z. Li, S. Ptasińska, I. Carmichael, L. Feketeová, and S. Denifl, "Stripping off hydrogens in imidazole triggered by the attachment of a single electron," *Physical Chemistry Chemical Physics*, vol. 19, no. 9, pp. 6406–6415, 2017.

[19] S. Ryu, J. Chang, H. Kwon, and S. K. Kim, "Dynamics of solvated electron transfer in thin ice film leading to a large enhancement in photodissociation of $CFCl_3$," *Journal of The American Chemical Society*, vol. 128, no. 11, pp. 3500–3501, 2005.

[20] L. Kevan, "Solvated electron structure in glassy matrices," *Accounts of Chemical Research*, vol. 14, no. 14, pp. 138–145, 1981.

[21] R. Laenen, T. Roth, and A. Laubereau, "Novel precursors of solvated electrons in water: Evidence for a charge transfer process," *Physical Review Letters*, vol. 85, no. 1-3, p. 50, 2000.

[22] A. T. Shreve, M. H. Elkins, and D. M. Neumark, "Photoelectron spectroscopy of solvated electrons in alcohol and acetonitrile microjets," *Chemical Science*, vol. 4, no. 4, pp. 1633–1639, 2013.

[23] H. Shimamori, T. Sunagawa, Y. Ogawa, and Y. Tatsumi, "Low-energy electron attachment to C_6H_5X (X =Cl, Br and I)," *Chemical Physics Letters*, vol. 232, no. 1-2, pp. 115–120, 1995.

[24] L. G. Christophorou, R. N. Compton, G. S. Hurst, and P. W. Reinhardt, "Dissociative electron capture by benzene derivatives," *The Journal of Chemical Physics*, vol. 45, no. 2, pp. 536–547, 1966.

[25] M. Kadi, J. Davidsson, A. N. Tarnovsky, M. Rasmusson, and E. Åkesson, "Photodissociation of aryl halides in gas phase studied with femtosecond pump-probe spectroscopy," *Chemical Physics Letters*, vol. 350, no. 1-2, pp. 93–98, 2001.

[26] T. D. Scarborough, J. Strohaber, D. B. Foote, C. J. McAcy, and C. J. G. J. Uiterwaal, "Ultrafast REMPI in benzene and the monohalobenzenes without the focal volume effect," *Physical Chemistry Chemical Physics*, vol. 13, no. 30, pp. 13783–13790, 2011.

[27] A. Borodin, O. Höfft, U. Kahnert, V. Kemter, S. Krischok, and M. O. Abou-Helal, "The interface between benzenes (C_6H_6;C_6H_5Cl;$_2$−C_6H_4OHCl) and amorphous solid water studied with metastable impact electron spectroscopy and ultraviolet photoelectron spectroscopy (HeI and II)," *The Journal of Chemical Physics*, vol. 120, no. 11, pp. 5407–5413, 2004.

[28] M. X. Yang, M. Xi, H. Yuan, B. E. Bent, P. Stevens, and J. M. White, "NEXAFS studies of halobenzenes and phenyl groups on Cu(111)," *Surface Science*, vol. 341, no. 1-2, pp. 9 – 18, 1995.

[29] M. Xi, M. X. Yang, S. K. Jo, B. E. Bent, and P. Stevens, "Benzene adsorption on Cu(111): Formation of a stable bilayer," *The Journal of Chemical Physics*, vol. 101, no. 10, pp. 9122–9131, 1994.

[30] X.-Y. Zhu, "Electronic structure and electron dynamics at molecule-metal interfaces: Implications for molecule-based electronics," *Surface Science Reports*, vol. 56, no. 1-2, pp. 1–83, 2004.

[31] A. Kahn, N. Koch, and W. Gao, "Electronic structure and electrical properties of interfaces between metals and π-conjugated molecular films," *Journal of Polymer Science Part B: Polymer Physics*, vol. 41, pp. 2529–2548, 11 2003.

[32] X.-L. Zhou, M. E. Castro, and J. M. White, "Interactions of uv photons and low energy electrons with chemisorbed benzene on Ag(111)," *Surface Science*, vol. 238, no. 1-3, pp. 215–225, 1990.

[33] X.-L. Zhou and J. M. White, "Photon- and electron-induced chemistry of chlorobenzene on Ag(111)," *The Journal of Chemical Physics*, vol. 92, no. 9, pp. 5612–5621, 1990.

[34] M. Egli and R. V. Gessner, "Stereoelectronic effects of deoxyribose O4' on DNA conformation," *Proceedings of the National Academy of Sciences*, vol. 92, no. 1, pp. 180–184, 1995.

[35] M. O. Sinnokrot and C. D. Sherrill, "Unexpected substituent effects in face-to-face π-stacking interactions," *The Journal of Physical Chemistry A*, vol. 107, no. 41, pp. 8377–8379, 2003.

[36] S. Mecozzi, A. P. West, and D. A. Dougherty, "Cation-pi interactions in aromatics of biological and medicinal interest: electrostatic potential surfaces as a useful qualitative guide," *Proceedings of the National Academy of Sciences*, vol. 93, no. 20, pp. 10566–10571, 1996.

[37] B. W. Gung and J. C. Amicangelo, "Substituent effects in C_6F_6-C_6H_5X stacking interactions," *Journal of Organic Chemistry*, vol. 71, no. 25, pp. 9261–9270, 2006.

[38] R. Dudde, B. Reihl, and A. Otto, "π^* and σ^* molecular orbitals of condensed films of chlorobenzenes and hexafluorobenzene observed by invserse photoemission," *The Journal of Chemical Physics*, vol. 92, no. 6, pp. 3930–3934, 1990.

[39] P. S. Kirchmann, P. A. Loukakos, U. Bovensiepen, and M. Wolf, "Ultrafast electron dynamics studies with time-resolved two-photon photoemission: Intra- and interband scattering in C_6F_6/Cu(111)," *New Journal of Physics*, vol. 7, p. 113, 2005.

[40] J. R. Frazier, L. G. Christophorou, J. G. Carter, and H. C. Schweinler, "Low-energy electron interactions with organic molecules: Negative ion states of fluorobenzenes," *The Journal of Chemical Physics*, vol. 69, no. 8, pp. 3807–3818, 1978.

[41] Y.-J. Liu, P. Persson, and S. Lunell, "Theoretical study of the fast photodissociation channels of the monohalobenzenes," *The Journal of Physical Chemistry A*, vol. 108, no. 12, pp. 2339–2345, 2004.

[42] K. J. Laidler, *Chemical Kinetics*. Harper and Row, 3rd ed., 1987.

[43] K. A. Connors, *Chemical Kinetics: The Study of Reaction Rates in Solution*. John Wiley and Sons, VCH, 1990.

[44] K. J. Laidler, "Unconventional applications of the arrhenius law," *Journal of Chemical Education*, vol. 49, no. 5, p. 343, 1972.

[45] M. G. Evans and M. Polanyi, "Some applications of the transition state method to the calculation of reaction velocities, especially in solution," *Transactions of the Faraday Society*, vol. 31, pp. 875–894, 1935.

[46] H. Eyring, "The activated complex and the absolute rate of chemical reactions.," *Chemical Reviews*, vol. 17, no. 1, pp. 65–77, 1935.

[47] E. Wigner, "The transition state method," *Transactions of the Faraday Society*, vol. 34, pp. 29–41, 1938.

[48] J. C. Polanyi, "Energy distribution among reagents and products of atomic reactions," *The Journal of Chemical Physics*, vol. 31, no. 5, pp. 1338–1351, 1959.

[49] R. A. Marcus, "Electron transfer reactions in chemistry: theory and experiment (nobel lecture)," *Angewandte Chemie International Edition*, vol. 32, no. 8, pp. 1111–1121, 1993.

[50] R. A. Marcus, "On the theory of oxidation-reduction reactions involving electron transfer. I," *The Journal of Chemical Physics*, vol. 24, no. 5, pp. 966–978, 1956.

[51] R. A. Marcus, "On the theory of oxidation-reduction reactions involving electron transfer. II. applications to data on the rates of isotopic exchange reactions," *The Journal of Chemical Physics*, vol. 26, no. 4, pp. 867–871, 1957.

[52] R. A. Marcus, "On the theory of oxidation-reduction reactions involving electron transfer. III. applications to data on the rates of organic redox reactions," *The Journal of Chemical Physics*, vol. 26, no. 4, pp. 872–877, 1957.

[53] R. A. Marcus, "Chemical and electrochemical electron-transfer theory," *Annual Review of Physical Chemistry*, vol. 15, no. 1, pp. 155–196, 1964.

[54] G. L. Closs, L. T. Calcaterra, N. J. Green, K. W. Penfield, and J. R. Miller, "Distance, stereoelectronic effects, and the marcus inverted region in intramolecular electron transfer in organic radical anions," *The Journal of Physical Chemistry*, vol. 90, no. 16, pp. 3673–3683, 1986.

[55] H. Lüth, *Solid Surfaces, Interfaces and Thin Fillms*. Springer Science & Business Media, 5th ed., 2010.

[56] A. de Jong and J. W. Niemantsverdriet, "Thermal desorption analysis: Comparative test of ten commonly applied procedures," *Surface Science*, vol. 233, no. 3, pp. 355–365, 1990.

[57] M. Polanyi and E. Wigner, "On the interface of characteristic vibrations as the cause of energy fluctuations and chemical changes," *Zeitschrift Fur Physikalische Chemie-Abteilung A*, vol. 139, p. 439, 1928.

[58] H. Petek and S. Ogawa, "Femtosecond time -resolved two-photon photoemission studies of electron dynamics in metals," *Progress in Surface Science*, vol. 4, no. 4, pp. 239–310, 1997.

[59] E. Knoesel, A. Hotzel, and M. Wolf, "Ultrafast dynamics of hot electrons and holes in copper: Excitation, energy relaxation, and transport effects," *Physical Review B*, vol. 57, no. 20-15, p. 12812, 1998.

[60] T. Fauster and W. Steinmann, "Two-photon photoemission spectroscopy of image states," *Electromagnetic Waves : Photonic Probes of Surfaces vol.2,*, vol. 2, pp. 347–411, 1994.

[61] P. M. Echenique, R. Berndt, E. V. Chulkov, T. Fauster, A. Goldmann, and U. Höfer, "Decay of electronic excitations at metal surfaces," *Surface Science Reports*, vol. 52, no. 7-8, pp. 219–317, 2004.

[62] M. Janczarek, Z. Wei, M. Endo, B. Ohtani, and E. Kowalska, "Silver- and copper-modified decahedral anatase titania particles as visible light-responsive plasmonic photocatalyst," *Journal of Photonics for Energy*, vol. 7, no. 1, p. 012008, 2017.

[63] K. Chen and D. Xue, "Materials design towards high performance Cu-based electrodes for electrochemical energy storage devices," *Science of Advanced Materials*, vol. 7, no. 10, pp. 2037–2052, 2015.

[64] S. A. Paknejed and S. H. Mannan, "Review of silver nanoparticle based die attach materials for high power/temperature applications," *Microelectronics Reliability*, vol. 70, pp. 1–11, 2017.

[65] R. Ahmed, J. Fu, N. Y. He, and S. Li, "Advanced gold nanomaterials for photothermal therapy of cancer," *Journal of Nanoscience and Nanotechnology*, vol. 16, pp. 67–80, 2016.

[66] D. Hull and D. J. Bacon, *Introduction to Dislocations*. Elsevier Ltd., 5th ed., 2011.

[67] C. Kittel, *Introduction to Solid State Physics*. Wiley, 8th ed., 2004.

[68] H. Eckardt, L. Fritsche, and J. Noffke, "Self-consistent relativistic band structure of the noble metals," *Journal of Physics F: Metal Physics*, vol. 14, no. 1, pp. 97–112, 1984.

[69] H. Ibach and H. Lüth, *Festkörperphysik: Einführung in die Grundlagen*. Springer, Berlin Heidelberg, 2009.

[70] A. J. Stähler, *Freezing Hot Electrons*. PhD thesis, Fachbereich Physik der Freien Universität Berlin, 2007.

[71] W. Wallauer and T. Fauster, "Two-photon excitation process and linewidth of surface and image states on Cu(111)," *Surface Science*, vol. 374, no. 1-3, pp. 44–50, 1997.

[72] P. Echenique and J. B. Pendry, "Theory of image states at metal surfaces," *Progress in Surface Science*, vol. 32, no. 2, pp. 111–159, 1989.

[73] E. Wigner and J. Bardeen, "Theory of the work functions of monovalent metals," *Physical Review*, vol. 48, no. 1, p. 84, 1935.

[74] H. Ibach, *Physics of Surfaces and Interfaces*. Springer, Berlin Heidelberg, 2006.

[75] R. Ludwig, "Water: From clusters to bulk," *Angewandte Chemie International Edition*, vol. 40, no. 10, pp. 1808–1827, 2001.

[76] S. A. Clough, Y. Beers, G. P. Klein, and L. S. Rothman, "Dipole moment of water from stark measurements of H_2O,HDO, and D_2O.," *The Journal of Chemical Physics*, vol. 59, no. 5, pp. 2254–2259, 1973.

[77] T. Bartels-Rausch, V. Bergeron, J. H. E. Cartwright, R. Escribano, J. L. Finney, H. Grothe, P. J. Gutiérrez, J. Haapala, W. F. Kuhs, J. B. C. Pettersson, *et al.*, "Ice structures, patterns, and processes: A view across the icefields," *Reviews of Modern Physics*, vol. 84, no. 2, p. 885, 2012.

[78] V. F. Petrenko and R. W. Whitworth, *Physics of Ice*. New York: Oxford University Press, 1999.

[79] J. D. Bernal and R. H. Fowler, "A theory of water and ionic solutions, with particular reference to hydrogen and hydroxyl ions," *The Journal of Chemical Physics*, vol. 1, no. 8, pp. 515–548, 1933.

[80] G. Malenkov, "Liquid water and ices: understanding the structure and physical properties," *Journal of Physics: Condensed Matter*, vol. 21, no. 28, p. 283101, 2009.

[81] U. Bovensiepen, C. Gahl, J. Stähler, M. Bockstedte, M. Meyer, F. Baletto, S. Scandolo, X.-Y. Zhu, A. Rubio, and . M. Wolf, "A dynamic landscape from femtoseconds to minutes for excess electrons at ice-metal interfaces.," *Journal of Physical Chemistry C*, vol. 113, no. 3, pp. 979–988, 2009.

[82] C. Gahl, *Elektronentransfer- und Solvatisierungsdynamik in Eis adsorbiert auf Metalloberflächen*. PhD thesis, Fachbereich Physik der Freien Universität Berlin, Mai, 2004.

[83] T. Shibaguchi, H. Onuki, , and R. Onaka, "Electronic structures of water and ice," *Journal of the Physical Society of Japan*, vol. 42, no. 1, pp. 152–158, 1977.

[84] P. Jenniskens and D. F. Blake, "Structural transitions in amorphous water ice and astrophysical implications," *Science*, vol. 265, no. 5173, pp. 753–756, 1994.

[85] P. A. Thiel and T. E. Madey, "The interaction of water with solid surfaces: Fundamental aspects," *Surface Science Reports*, vol. 7, no. 6-8, pp. 211–385, 1987.

[86] M. Mehlhorn and K. Morgenstern, "Height analysis of amorphous and crystalline ice structures on Cu(111) in scanning tunneling microscopy," *New Journal of Physics*, vol. 11, no. 9, p. 093015, 2009.

[87] J. Stähler, U. Bovensiepen, M. Meyer, and M. Wolf, "A surface science approach to ultrafast electron transfer and solvation dynamics at interfaces," *Chemical Society Reviews*, vol. 87, no. 10, pp. 2180–2190, 2008.

[88] B. Abel, "Hydrated interfacial ions and electrons," *Annual Reviews of Physical Chemistry*, vol. 64, pp. 533–552, 2013.

[89] O. V. Prezhdo and P. J. Rossky, "Solvent mode participation in the nonradiative relaxation of the hydrated electron," *The Journal of Physical Chemistry*, vol. 100, no. 43, pp. 17094–17102, 1996.

[90] S. B. King, D. Wegkamp, C. Richter, M. Wolf, and J. Stähler, "Trapped electrons at the amorphous solid water/vacuum interface as possible reactants in a water splitting reaction," *The Journal of Physical Chemistry C*, vol. 121, no. 13, pp. 7379–7386, 2017.

[91] J. Stähler, J.-C. Deinert, D. Wegkamp, S. Hagen, and M. Wolf, "Real time measurement of the vertical binding energy during the birth of a solvated electron," *Journal of The American Chemical Society*, vol. 137, no. 10, pp. 3520–3524, 2015.

[92] M. Meyer, J. Stähler, D. O. Kusmierek, M. Wolf, and U. Bovensiepen, "Determination of the electron's solvation site on D_2O/Cu(111) using Xe overlayers and femtosecond photoelectron spectroscopy," *Physical Chemistry Chemical Physics*, vol. 10, no. 32, pp. 4932–4938, 2008.

[93] J. Stähler, C. Gahl, U. Bovensiepen, and M. Wolf, "Ultrafast electron dynamics at ice-metal interfaces: Competition between heterogeneous electron transfer and solvation," *The Journal of Physical Chemistry B*, vol. 110, no. 19, pp. 9637–9644, 2006.

[94] J. Clark, "Electronic structure of benzene." http://www.chemguide.co.uk/basicorg/bonding/benzene2.html#top, March 2013.

[95] J. Clark, "Electronic structure of halobenzene." http://www.chemguide.co.uk/organicprops/arylhalides/background.html, March 2016.

[96] D. B. Cook, *Quantum Chemistry: A Unified Approach*. Imperial College Press, 2008.

[97] M. Clugston and R. Flemming, *Advanced Chemistry*. Oxford University Press, Oxford, 2000.

[98] S. Fujisawa, K. Ohno, S. Masuda, and Y. Harada, "Penning ionization electron spectroscopy of monohalogenobenzenes: C_6H_5F,C_6H_5Cl,C_6H_5Br and C_6H_5I," *Journal of the American Chemical Society*, vol. 108, no. 21, pp. 6505–6511, 1986.

[99] M. Alonso, B. Pinter, T. Woller, P. Geerlings, and F. D. Proft, "Scrutinizing ion-π and ion-σ interactions using the noncovalent index and energy decomposition analysis," *Computational and Theoretical Chemistry*, vol. 1053, pp. 150–164, 2014.

[100] R. P. Frueholz, W. M. Flicker, O. A. Mosher, and A. Kuppermann, "Electronic spectroscopy of benzene and the fluorobenzenes by variable angle electron impact," *The Journal of Chemical Physics*, vol. 70, no. 6, pp. 3057–3070, 1979.

[101] G. Witte, S. Lukas, P. S. Bagus, and C. Wöll, "Vacuum level alignment at organic/metal junctions:"cushion" effect and the interface dipole," *Applied Physics Letters*, vol. 87, no. 26, p. 263502, 2005.

[102] P. C. Rusu, G. Giovannetti, C. Weijtens, R. Coehoorn, and G. Brocks, "First-principles study of the dipole layer formation at metal-organic interfaces," *Physical Review B*, vol. 81, no. 12-15, p. 125403, 2010.

[103] D. B. Kokh, H.-P. Liebermann, and R. J. Buenker, "Photodissociation of CH_3Cl,C_2H_5Cl,andC_6H_5Cl on the Ag(111) surface: Ab initio embedded cluster and configuration interaction study," *The Journal of Chemical Physics*, vol. 132, no. 7, pp. 074707–10, 2010.

[104] ChemAxon, "Chemical and physical properties of halobenzenes." http://www.chemicalize.org/structure/#!mol=Clc1ccccc1&source=calculate, August 2016.

[105] D. R. Lide, *Handbook of Chemistry and Physics*. CRC press, 85th ed., 2004.

[106] R. Kalescky, W. Z. amd Elfi Kraka, and D. Cremer, "Quantitative assessment of the multiplicity of carbon-halogen bonds: Carbenium and halonium ions with F, Cl, Br, and I," *Journal of Physical Chemistry A*, vol. 118, no. 10, pp. 1948–1963, 2014.

[107] R. Stenutz, "Structure and physical data for bromobenzene." http://www.stenutz.eu/chem/solv6.php?name=bromobenzene.

[108] S.-H. Lee, C.-Y. Wu, S.-K. Yang, and Y.-P. Lee, "Photodissociation dynamics of fluorobenzene (C_6H_5F) at 157 and 193 nm : Branching ratios and distributions of kinetic energy," *The Journal of Chemical Physics*, vol. 125, no. 14, pp. 144301–7, 2006.

[109] G.-J. Wang, R.-S. Zhu, H. Zhang, K.-L. Han, G.-Z. He, and N.-Q. Lou, "Photodissociation of chlorobenzene at 266 nm," *Chemical Physics Letters*, vol. 288, no. 2-4, pp. 429–432, 1998.

[110] T. Ichimura, Y. Mori, H. Shinohara, and N. Nishi, "Photofragmentation of chlorobenzene: Translational energy distribution of the recoiling Cl fragment," *Chemical Physics*, vol. 189, no. 1, pp. 117–125, 1994.

[111] H. Zhang, R.-S. Zhu, G.-J. Wang, K.-L. Han, G.-Z. He, and N.-Q. Lou, "Photodissociation of bromobenzene at 266 nm," *Journal of Chemical Physics*, vol. 110, no. 6, pp. 2922–2927, 1999.

[112] M. Dzvonik, S. Yang, and R. Bersohn, "Photodissociation of molecular beams of aryl halides," *The Journal of Chemical Physics*, vol. 61, no. 11, pp. 4408–4421, 1974.

[113] A. Freedman, S. C. Yang, M. Kawasaki, and R. Bersohn, "Photodissociation of aryl and aryl-alkyl halides at 193 nm: Fragment translational energy distributions," *The Journal of Chemical Physics*, vol. 72, no. 2, pp. 1028–1033, 1980.

[114] I. J. Palmer, I. N. Ragazos, F. Bernardi, M. Olivucci, and M. A. Robb, "An MC-SCF study of the S1 and S2 photochemical reactions of benzene," *Journal of The American Chemical Society*, vol. 115, no. 2, pp. 673–682, 1993.

[115] A. L. Sobolewski and W. Domcke, "Conical intersections induced by repulsive $^1\pi\sigma^*$ states in planar organic molecules: Malonaldehyde, pyrrole and chlorobenzene as photochemical model systems," *Chemical Physics*, vol. 259, no. 2-3, pp. 181–191, 2000.

[116] M. H. Palmer, T. Ridley, S. V. Hoffmann, N. C. Jones, M. Coreno, M. de Simone, C. Grazioli, T. Zhang, M. Biczysko, A. Baiardi, , and K. Peterson, "Interpretation of the photoelectron, ultraviolet, and vacuum ultraviolet photoabsorption spectra of bromobenzene by ab initio configuration interaction and DFT computations," *The Journal of Chemical Physics*, vol. 143, no. 16, pp. 164303–18, 2015.

[117] C. Betram and K. Morgenstern, "Private communication.."

[118] S. C. Silva and J. P. Devlin, "Interaction of acetylene, ethylene, and benzene with ice surfaces," *The Journal of Physical Chemistry*, vol. 98, no. 42, pp. 10847–10852, 1994.

[119] L. Rettig, *Ultrafast Dynamics of Correlated Electrons*. Phd, Fachbereich Physik der Freien Universität Berlin, May 2012.

[120] P. S. Kirchmann, *Ultrafast Electron Dynamics in Low-Dimensional Materials*. PhD thesis, Fachbereich Physik der Freien Universität Berlin, 2008.

[121] A. Zangwill, *Physics at Surfaces*. Cambridge University Press, illustrated, reprint ed., 1988.

[122] M. Meyer, *Ultrafast Electron Dynamics at Alkali/Ice Structures Adsorbed on a Metal Surface*. PhD thesis, Fachbereich Physik der Freien Universität Berlin, Oct., 2011.

[123] E. Knoesel, *Ultrakurzzeit-Dynamik elektronischer Anregungen auf Metalloberfläschen*. PhD thesis, Fachbereich Physik der Freien Universität Berlin, 1997.

[124] D. N. Denzler, *Zur ultraschnellen Reaktionsdynamik von Wasserstoff und Grenzflächenstruktur von Wasser auf der Ru(001)–Oberfläche*. PhD thesis, Fachbereich Physik der Freien Universität Berlin, 2003.

[125] C. N. Berglund and W. E. Spicer, "Photoemission studies of copper and silver: Theory," *Physical Review*, vol. 136, no. 4A, p. A1030, 1964.

[126] C. N. Berglund and W. E. Spicer, "Photoemission studies of copper and silver: Theory," *Physical Review*, vol. 136, no. 4A, p. A1044, 1964.

[127] H. Ueba and B. Gumhalter, "Theory of two-photon photoemission spectroscopy of surfaces," *Progress in Surface Science*, vol. 82, no. 4-6, pp. 193–223, 2007.

[128] G. D. Mahan, "Angular dependence of photoemission in metals," *Physics Review Letters*, vol. 24, no. 19-11, p. 1068, 1970.

[129] G. D. Mahan, "Theory of photoemission in simple metals," *Physical Review B*, vol. 2, no. 11-1, p. 4334, 1970.

[130] S. Hüfner, *Photoelectron Spectroscopy: Principles and Applications*. Springer, Berlin Heidelberg, 3rd ed., 2003.

[131] A. Hotzel, *Elektronendynamik der Adsorbatbedeckten Cu(111)-Ober fäche*. PhD thesis, Freie Universiät Berlin, 1999.

[132] P. S. Kirchmann, L. Rettig, D. Nandi, U. Lipowski, M. Wolf, and U. Bovensiepen, "A time-of-flight spectrometer for angle-resolved detection of low energy electrons in two dimensions," *Applied Physics A: Materials Science & Processing*, vol. 91, no. 2, pp. 211–217, 2008.

[133] P. W. Milonni and J. H. Eberly, *Lasers*. Wiley, illustrated ed., 1988.

[134] A. E. Siegman, *Lasers*. University Science Books, illustrated, revised ed., 1986.

[135] O. Svelto, *Principles of Lasers*. Springer Science and Business Media, US, illustrated ed., 2012.

[136] J.-C. Diels and W. Rudolph, *Ultrashort Laser Pulse Phenomena*. Academic Press, 2006.

[137] E. Riedle, M. Beutter, S. Lochbrunner, J. Piel, S. Schenkl, S. Spörlein, and W. Zinth, "Generation of 10 to 50 fs pulses tunable through all of the visible and the NIR," *Applied Physics B*, vol. 71, no. 3, pp. 457–465, 2000.

[138] C. Rullière, *Femtosecond Laser Pulses: Principles and Experiments*. Springer, Berlin Heidelberg, 1998.

[139] C. Manzoni and G. Cerullo, "Design criteria for ultrafast optical parametric amplifiers," *Journal of Optics*, vol. 18, no. 10, p. 103501, 2016.

[140] R. W. Boyd, *Nonlinear Optics*. 1250 Sixth Avenue, San Diego, CA 92101: Academic Press, October 2013.

[141] G. I. Stegeman and R. A. Stegeman, *Nonlinear Optics: Phenomena, Materials and Devices*. John Wiley and Sons, 2012.

[142] F. Zernike and J. E. Midwinter, *Applied Nonlinear Optics*. Courier Corporation, 2006.

[143] T. Kobayashi and A. Baltuska, "Sub-5 fs pulse generation from a noncollinear optical parametric amplifier," *Measurement Science and Technology*, vol. 13, no. 11, pp. 1671–1682, 2002.

[144] Coherent Laser Group, Coherent Inc., Santa Clara, *Operator's Manual, Verdi V-18 Diode-Pumped Lasers*, 2007.

[145] Coherent Laser Group, Coherent Inc., Santa Clara, *RegA 9050 System Operator's Manual, Preliminary Version 2.1*, 1997.

[146] Coherent Laser Group, Coherent Inc., Santa Clara, *Operator's Manual, The Coherent Modell 9800 Optical Parametric Amplifier*, 1994.

[147] Coherent Laser Group, Coherent Inc., Santa Clara, *Operator's Manual, The Coherent Mira 900-B Laser*, 1993.

[148] C. Schriever, S. Lochbrunner, P. Krok, and E. Riedle, "Tunable pulses from below 300 to 970 nm with durations down to 14 fs based on a 2 MHz ytterbium-doped fiber system," *Optics Letters*, vol. 33, no. 2, pp. 192–194, 2008.

[149] R. Trebino, K. W. DeLong, D. N. Fittinghoff, J. N. Sweetser, B. A. R. Marco A. Krumbügel, and D. J. Kane, "Measuring ultrashort laser pulses in the time-frequency domain using frequency-resolved optical gating," *Review of Scientific Instruments*, vol. 68, no. 9, p. 3277, 1997.

[150] R. Trebino, *Frequency-Resolved Optical Gating: The Measurement of Ultrashort Laser Pulses*. Springer, US, 2000.

[151] F. Salin, P. Georges, G. Roger, and A. Brun, "Single-shot measurement of a 52-fs pulse," *Applied Optics*, vol. 26, no. 21, pp. 4528–4531, 1987.

[152] Z. Bor and B. Rácz, "Group velocity dispersion in prisms and its application to pulse compression and travelling-wave excitation," *Optics Communications*, vol. 54, no. 3, pp. 165–170, 1984.

[153] R. L. Fork, O. E. Martinez, and J. P. Gordon, "Negative dispersion using pairs of prisms," *Optics Letters*, vol. 9, no. 5, pp. 150–152, 1984.

[154] C. Gahl, "Ultrakurzzeitdynamik elektronischer anregungen im adsorbatsystem C_6F_6/Cu(111)," Master's thesis, Fachbereich Physik der Freien Universität Berlin, Nov. 1999.

[155] D. C. Clary and L. Wang, "Influence of surface defects on the adsorption of HCl on ice," *Journal of the Chemical Society, Farady Transactions*, vol. 93, no. 16, pp. 2763–2767, 1997.

[156] P. Y. Cheng, D. Zhong, and A. H. Zewail, "Kinetic-energy, femtosecond resolved reaction dynamics. modes of dissociation (in iodobenzene) from time-velocity correlations," *Chemical Physcs Letters*, vol. 237, no. 5-6, pp. 399–405, 1995.

[157] M. Bockstedte and P. Auburger, "Private communication."

[158] B. J. Hinch and L. H. Dubois, "Stable and metastable phases of water adsorbed on Cu(111)," *The Journal of Chemical Physics*, vol. 96, no. 4, pp. 3262–3268, 1992.

[159] T. Vondrak and X.-Y. Zhu, "Two photon photoemission study of heterogeneous electron transfer: C_6F_6 on Cu(111)," *The Journal of Physical Chemistry B*, vol. 103, pp. 3449–3456, 1999.

[160] R. Hentschke and B. L. Schürmann, "A molecular dynamics simulation of liquid benzene adsorbed on graphite," *Surface Science*, vol. 262, no. 1-2, pp. 180–188, 1992.

[161] K. Ishioka, C. Gahl, and M. Wolf, "Femtosecond dynamics of image potential states of C_6F_6/Cu(111) studied with two-photon photoemission," *Surface Science*, vol. 454-456, pp. 73–77, 2000.

[162] S. Simpson and E. Zurek, "Substituted benzene derivatives on the Cu(111) surface," *The Journal of Physical Chemistry C*, vol. 116, no. 23, pp. 12636–12643, 2012.

[163] J. Björk, F. Hanke, and S. Stafström, "Mechanisms of halogen-based covalent self-assembly on metal surfaces," *Journal of the American Chemical Society*, vol. 135, no. 15, pp. 5768–5775, 2013. PMID: 23506285.

[164] H.-P. Fenzlaff and E. Illenberger, "Low energy electron impact on benzene and the fluorobenzenes. formation and dissociation of negative ions," *International Journal of Mass Spectrometry and ion Processes*, vol. 59, 1984.

[165] C. Gahl, U. Bovensiepen, C. Frischkorn, K. Morgenstern, K.-H. Rieder, and M. Wolf, "Ultrafast electron solvation dynamics in D_2O/Cu(111): influence of coverage and structure," *Surface Science*, vol. 532-535, pp. 108–112, 2003.

Acknowledgements

I would like to take the opportunity to thank all those people who have helped me make this journey to the end of my thesis possible and enjoyable.

Foremost, I would like to express my sincere gratitude to my advisor Uwe Bovensiepen, thank you for giving me the opportunity to this work, for your continuous guidance and motivation. I especially appreciate that you always made time to discuss, even very basic topics. I am also grateful for your encouragement and faith in me, and could not have expected a better mentor.

It is a pleasure to thank our collaborators, Cord Betram, Philipp Auburger, Karina Morgenstern and Michel Bockstedte, for the crucial and detailed discussions. It was an honour working with you all. I would like to thank Karina Morgenstern for also refereeing my thesis. Thank you for your insightful comments, hard questions and encouragement for future endeavours. I especially appreciate the extra effort you put in to finish the referee report much before the official deadline.

I would also like to thank Martina Schmid and Markus Gruner who formed the remainder of the dissertation committee. Thank you for your time, thought provoking questions and the ensuing discussions.

I would like to thank Michael Meyer for making the time to visit Duisburg to train me in sample preparations. I would like thank Lukas Kujawinski from AG Horn von Hoegen's group for fixing the pToF cards and the sputter gun many-many times. A special thank you to Ping Zhou, you taught me everything I know about lasers today. I really really appreciate the long hours you spent with me in the lab developing the NOPA setup and I am very grateful to you for your patience and guidance.

I would also like to thank Mrs. Christina Boese, you always helped me out with my last minute bureaucratic/administrative tasks. You always came through with a solution and sorted out the various complications that were mostly of my own doing. I would also like to thank Roland Kuhn for his support with computer, especially when the lab computers refused to start up during measurements. I would also like thank Michael Bieske for his support in the mechanical realm.

The thesis would not be possible without the support and experiences of the past and present members of the AG Bovensiepen's group. I would like to thank you all: Mahdi Afshari, Ljupka Stojcevska Malbasic, Vesna Mikšic Trontl, Shunhao Xiao, Jayabalan, Andre Seyen, Florian Quinn, Frank Meyer, Mathias Sandhoffer, Jens Wieczorek , Carla Streubur, Andrea Eschenlohr, Jinghao Chen, Isabella Avigo, Abdul Samad Syed and Manuel Ligges, for the valuable discussions, troubleshooting support, pleasant conversations, and for creating a very friendly and lively work atmosphere. In particular, I would like to acknowledge Isabella, Samad and Manuel for teaching me everything about the lab and photoemission, for personnel and professional guidance, for always having my back, and the list goes on. A special thank you to Bedatri Moulik for looking out for me here in Duisburg and being my surrogate sister here.

Finally, I would like to thank my family for their loving support. You never gave me a chance to feel guilty about leaving home to pursue my dreams, even when we faced some tough moments in the past couple of years. I would like to thank my fiancé, Michael Kemeny. Your theoretician's solution to an experimental problem ;) were one of the things that made this journey enjoyable. Jokes apart, I am grateful for your never faltering support and understanding, especially in the past few months.